DOPED ALKALINE EARTH (NITRIDE) HYDRIDES

Maarten Christiaan Verbraeken

A Thesis Submitted for the Degree of PhD
at the
University of St. Andrews

2009

http://hdl.handle.net/10023/714

Doped alkaline earth (nitride) hydrides

A thesis presented for the degree of Doctor of Philosophy

by

Maarten Christiaan Verbraeken

University
of
St Andrews

Supervised by Prof. J.T.S. Irvine

Submitted February 2009

Declarations

I, Maarten Christiaan Verbraeken, hereby certify that this thesis, which is approximately 40,000 words in length, has been written by me, that it is the record of work carried out by me and that it has not been submitted in any previous application for a higher degree.

I was admitted as a research student in June 2005 and as a candidate for the degree of Doctor of Philosophy in November 2006; the higher study for which this is a record was carried out in the University of St Andrews between 2005 and 2009.

Date:……………….. Signature of candidate:…………………………..

I hereby certify that the candidate has fulfilled the conditions of the Resolution and Regulations appropriate for the degree of Doctor of Philosophy in the University of St Andrews and that the candidate is qualified to submit this thesis in application for that degree.

Date:……………….. Signature of supervisor:………………………….

In submitting this thesis to the University of St Andrews we understand that we are giving permission for it to be made available for use in accordance with the regulations of the University Library for the time being in force, subject to any copyright vested in the work not being affected thereby. We also understand that the title and the abstract will be published, and that a copy of the work may be made and supplied to any bona fide library or research worker, that my thesis will be electronically accessible for personal or research use unless exempt by award of an embargo as requested below, and that the library has the right to migrate my thesis into new electronic forms as required to ensure continued access to the thesis. We have obtained any third-party copyright permissions that may be required in order to allow such access and migration, or have requested the appropriate embargo below.

Access to Printed copy and electronic publication of thesis through the University of St Andrews.

Date:…………………. Signature of candidate:…………………………..

Signature of supervisor:………………………….

Summary

The work in this thesis relates to the preparation and structural and electrical characterisation of calcium and strontium hydrides, imides and nitride hydrides. Conventional solid state methods in controlled atmospheres were used to synthesise these materials.

High temperature neutron diffraction, thermal analysis and conductivity studies performed on calcium and strontium hydride suggest an order – disorder transition in these materials at 350 – 450°C. Disordering is believed to involve rapid exchange of hydride ions across two crystallographic sites. This manifests itself in a lowering of the activation energy for bulk hydride ion conduction. The hydride ion conduction is good in these undoped materials: σ_{total} = 0.01 S/cm for CaH_2 at 1000K; for SrH_2, σ_{total} = 0.01 S/cm at 830K. Doping of SrH_2 with NaH causes a significant increase in the low temperature conductivity, due to presence of extrinsic defects. The high temperature conductivity is negatively affected by NaH doping.

Calcium nitride hydride (Ca_2NH) was obtained as a single phase material by reacting either calcium metal or calcium hydride (CaH_2) in an argon atmosphere containing 5 – 7% H_2 and 1 – 7% N_2. Imide ions substituting for hydride and nitride ions constitute a major chemical defect in this material. Long range ordering of the nitride and hydride ions occurs, giving rise to a double cubic crystal symmetry. This order breaks down at 600 – 650°C. Applying the same reaction conditions to strontium metal results in a mixed phase of strontium nitride hydride and imide. No long range order in the nitride hydride phase could be observed. Doping Ca_2NH with lithium hydride (LiH) causes the appearance of a second calcium imide phase, whereas doping with sodium hydride (NaH) increases the amount of imide ions as a defect in the nitride hydride structure, thereby decreasing the long range ordering of nitride and hydride ions.

Acknowledgements

First of all, I would like to thank Prof. John Irvine for offering me the PhD position in his group on this project. My experience in the field of solid state chemistry prior to this PhD was quite minimal and so was the knowledge and experience within the group on this specific type of chemistry I have been doing, so all your scientific input and support have been ever so helpful in getting this work done. Also your positivism about the usefulness of hydride ion electrochemistry (which possibly not everybody shares) has absolutely been an inspiration.

Thanks also go to the members of the JTSI group, who I've worked with over the past three and a half years. I'd like to especially thank Julie for all the help in the lab, the moral support during glovebox maintenance operations and just everything. Thank you, Sylvia, for always finding slots for me on the thermal analysis equipment and for getting me hooked on Lost. I'd also like to thank the people from the David-Cole Hamilton group for allowing me to use some of their lab space and helping me prepare some chemicals; especially thanks to Simon for spending hours with me trying to prepare sodium hydride (we never managed to do it, but it was fun playing with all those explosive chemicals!!). Big thanks too, to Bobby, George, Jim, Brian and Colin for fixing all sorts of things in your workshops and also for helping me move that glovebox a few times. I couldn't have done this work without your help, guys. The final work related thanks are for Institut Laue Langevin (ILL) in Grenoble, France, for granting me beamtime on their neutron beamline and to Emmanuelle Suard in particular for helping me carrying out my experiments there.

Then there is of course the words of gratitude to the people who helped me get through three and a half years outside the chemistry building. Cheers, Fran and Kelcey for initiating me in the Cellar Bar music quiz, which we've managed to win all of once during my stay here. Thanks Davo for bringing Australian drinking culture to St Andrews and for bringing the thunder on many occasions; Chris, Dave, Steve, Maria, Walter and Davo (again) for putting up with me in the house and for all the banter and shenanigans….and for some reason I can see some more coming up in the near future; Gil for some excellent cooking and some infamous parties; Sneh for endless positive energy and Pierrot for being Pierrot; Mark and Diane for great company and being brilliant beer connoisseurs. Finally a big thank to the jazz gang in the Byre for keeping the groove going on Thursdays and any other gigs.

Switching to Dutch: Bedankt, Pa en Ma voor jullie continue morele en financiele steun de afgelopen jaren. Ik weet dat ik gedurende een lange periode het niet al te zonnig inzag, maar gelukkig kon ik altijd op jullie positieve kijk en vertrouwen rekenen. En nu is het dan toch eindelijk zover: het boekje is klaar!

Contents

1 Introduction

The increasing energy demand posed by rising economies in Asia and the rapid depletion of oil reserves create the biggest challenges of this century. Temporary alternatives will be natural gas and coal, but eventually we will have to resort to both nuclear and renewable energy sources, like wind, solar and tidal to provide for our energy needs. More efficient use of fuels will also be a necessary development. Electrochemical devices such as fuel cells will play an important role here. Based on the same technology, electrolyser cells will provide us with clean hydrogen gas for mobile applications.

Electrochemical devices have long been known to provide efficient means of converting one type of energy (*e.g.* chemical or thermal energy) into electrical energy. Because there are no moving parts in these solid state devices, they offer clean and noiseless electricity. Good examples of such devices are solid state batteries, fuel cells, electrolyser cells and AMTEC (Alkali Metal Thermal to Electric Converter) cells. The existence of mixed ionic and electronic conducting ceramic materials has furthermore opened the way for electrochemical separation membranes, an energy efficient alternative to cryogenic gas separation.

Hydrogen has often been proposed to be the main energy carrier for this new energy era. Two large challenges remain for a successful transition to a hydrogen based economy (from a hydrocarbon based one): clean/renewable hydrogen production and efficient storage of hydrogen. It is envisaged that hydrogen can be produced in a sustainable way by electrolysing water, using highly efficient electrochemical electrolyser cells, powered by renewable energy sources (e.g. hydro or wind). Efficient storage of hydrogen might prove an even bigger challenge, as simply compressing or even liquefying hydrogen is currently highly energy intensive and might take away the benefits of changing to a hydrogen based economy in the first place. Also, these techniques would not store hydrogen with sufficient volumetric density (grams of hydrogen per unit of volume), which is a requirement for efficient hydrogen storage. Again the answer to this issue seems to lie in solid state storage, which clearly offers high volumetric densities of hydrogen. Several solid materials have been studied over the past 20 years for their potential to store hydrogen in their chemical structure. The main candidates are light weight metal hydrides or nitrogen – hydrogen based imides and amides. The light weight metal compounds (*e.g.* lithium, magnesium and calcium based) have the advantage of storing hydrogen with high gravimetric (grams of hydrogen per grams of storage material) as well as high volumetric densities, both requirements for efficient hydrogen storage. Fast and reversible uptake and release of hydrogen at ambient pressures and temperatures is the aim here and the combination of different light weight metals seems to be necessary to achieve this goal.

The work presented in this thesis deals with a relatively unknown family of materials, which is of interest for both electrochemical applications as well as hydrogen storage. Alkaline earth metal hydrides as well as nitrogen – hydrogen based materials (imides and nitride hydrides) will be studied structurally, thermally and electrically in order to learn about the mechanisms for hydrogen transport, uptake and release. Light weight metal nitrogen – hydrogen based materials have become of great interest for hydrogen storage purposes, especially after Chen et al. reported the potential storage of 11.5 wt% hydrogen by lithium nitride [1]. Much work has been done to optimise this system in terms of reversibility at temperatures and hydrogen pressures that are typically needed for vehicular onboard storage systems. Different research groups have modified the lithium system with magnesium and calcium in order to bring down the hydrogen desorption temperatures and elevate the hydrogen pressures [2-9]. Mechanical treatment of the starting compounds by ball milling has also been shown to improve the reversibility of this storage system [10, 11].

Metal hydrides have been studied for their potential as hydrogen storage material for the last 20 years. The early studies focused on $LaNi_5H_6$ and derivatives of this material. This alloy has been popular as an electrode material for nickel – metal hydride batteries and therefore extensive knowledge was already available [12, 13]. The heavy weight metals however prevent this material from being efficient in terms of gravimetric hydrogen densities. Therefore later studies moved towards the use of light weight metal (Li, Na, Mg, Ca, etc.) hydrides and complex hydrides in particular, e.g. $LiBH_4$ and $NaAlH_4$ [14-17]. Complex hydrides generally have lower thermal stability and therefore release their stored hydrogen at more favourable temperatures and hydrogen pressures [18, 19]. Whereas many researchers have studied their potential as hydrogen storage materials, only few have tried exploring metal hydrides' electrochemical properties. Their chemical reactivity and high sensitivity towards moisture and air has probably kept most people from considering them as a viable choice for any electrochemical application. It is the chemical reactivity however that offers great potential, as all sorts of electrochemical reactions that have never even been considered before, might become possible.

Traditionally, solid state electrochemistry involves the use of oxide based materials. The advantages of their use are clear; they often have high chemical and thermal stability and are stable over wide pO_2 ranges. The electrochemical species in oxide materials are generally oxide ions or protons. Typical examples of oxide ion conductors are Yttria Stabilised Zirconia (YSZ), gadolinia doped ceria (CGO) lanthanum gallate [20] and bismuth copper vanadium oxide (BiCuVOx) [21]. The first two materials are widely used in SOFC, oxygen sensors and oxygen pumps [22]. Doped barium cerates and zirconates are good conductors of protons (in fact protonated oxide ions) and are candidates as electrolytes in intermediate temperature fuel cells [23]. Finally, some perovskite materials like $La_{1-x}Sr_xFe_{1-y}Co_yO_{3-\delta}$, show good mixed oxygen ionic and electronic conductivity and are used for oxygen separation from air [24, 25] and in membrane oxidation reactors [26] . Electrochemical cells are of course not limited to the use of oxide ions and protons. There is a number of other ions, which have shown to be mobile within solids, e.g. Li^+, Na^+, Ag^+, F^- and Cl^-. It is debated whether the nitride ion (N^{3-}) is mobile under electrochemical operation. Electrochemical and thermal incorporation of nitride ions in YSZ have been shown and diffusion of the nitrogen could be measured using Secondary Ion Mass Spectroscopy (SIMS) [27-29]. Generally however, the nitride's ion mobility was found to be a few orders of magnitude smaller than the oxide ion's. Therefore its contribution to electrochemical activity can usually be neglected compared to those of other ions present in typical electrolytes, e.g. oxide or lithium ions. Good examples of electrolyte materials that use any of those other ions are Li_3N, Na-β-Al_2O_3, AgI, PbF_2 and $SrCl_2$ [22, 30]. Although most of those mobile ions serve perfectly well in solid electrolytes, they are chemically not very interesting.

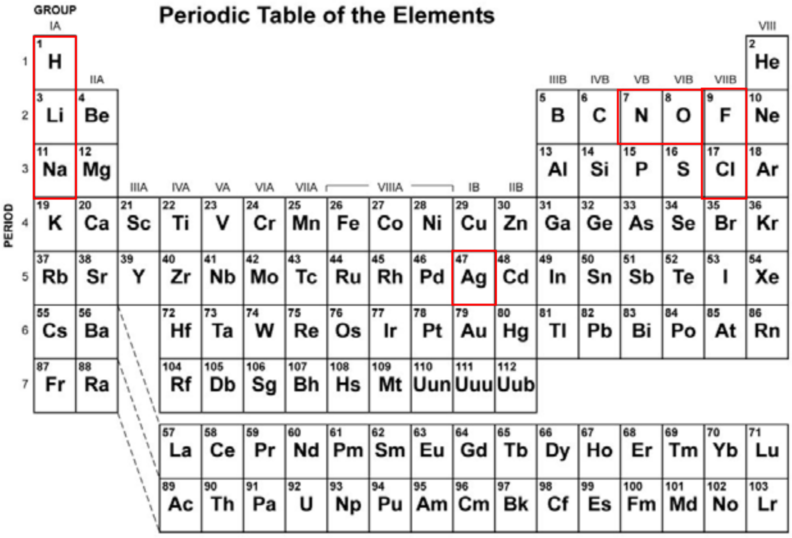

Figure 1-1: Elements known to show mobility in electrochemical applications

The alkaline earth hydrides are ionic compounds and have been reported to be good conductors for negatively charged hydrogen, (H^- or hydride) ions [31]. Whereas for instance fluoride or chloride ions are chemically relatively inert, the hydride ion is a strong reducing agent and of great chemical interest. An electrochemical device based on hydride ions would therefore enable all kinds of highly efficient electrochemical conversion reactions, ranging from hydrogenations to the reduction of fully oxidised compounds (*e.g.* CO_2) into chemically important base products (CO, CH_4, etc.). Also other basic compounds for the chemical industry, like NH_3, which are currently produced using high pressures and temperatures, could be synthesised with high energy efficiency by the simple combination of nitrogen and hydrogen.

1.1 Hydrogen chemistry

Hydrogen is the first element in the periodic table of elements. It is the simplest species, made up of just one proton and one electron (deuterium and tritium have an additional one or two neutrons). Despite this simple composition, its chemistry is versatile. For instance, elementary hydrogen exists in the form of three, more-or-less, stable compounds: protons (H^+), hydride ions (H^-) and hydrogen gas (H_2). In other words, its properties range from being a very strong Lewis acid, to being a strong Lewis base. And although the hydrogen atom has only one single electron, it still can bind to more than one atom simultaneously [32].

1.1.1 Hydrogen – the element

Hydrogen does not fit very well into the periodic table. It is usually placed on top of the Group I alkali metals, because of their mutual one valence electron. From a chemical and physical point of view, this position is not satisfactory, especially because hydrogen is not a metal. Less frequently, hydrogen is placed ahead of the Group 17/VII halogens, since these only need one more electron to fill up their valence shells. And in fact there are some chemical resemblances between hydrogen and the halogens, as we will see later on.

1.1.2 Hydrogen and its ions

Atomic hydrogen ($H^0\bullet$) is a very unstable species. It combines readily with any chemical compound, in order to complete or deplete its 1s valence shell. Accordingly, it forms a proton (generally in combination with a Lewis base), a covalent bond or an ionic bond (as H^-). The electronegativity of hydrogen is 2.2, which is comparable to the electronegativities of B, C and Si, so their E-H bonds are not expected to be very polar. On the other hand, with elements from Group I and II it forms salt-like compounds, in which the hydrogen acquires electron density and is best described as a negatively charged ion, the hydride ion. When combined with electronegative elements on the right hand side of the periodic table, the E-H bond is best regarded as covalent and polar, with the H atom carrying a small positive charge.

The radius of atomic hydrogen ($H^0\bullet$) is with 0.37 Å the smallest found for any atom of the chemical elements. The free hydride ion on the other hand, has a much higher ionic radius of 2.08 Å, which is comparable to the ionic radii of large halides, such as bromide (1.95 Å) and iodide (2.16 Å) anions [19]. The hydride ion and halide ions share the property that they all have a noble gas electron configuration, i.e. a completely filled valence shell. In alkali hydrides and earth alkali hydrides, the ionic radius is 1.42 Å, which is again very similar to the ionic radius of the oxygen ion O^{2-} with a coordination number of six (1.40 Å) [33, 34]. The electron affinity of the hydrogen atom is only –0 .80 eV. This makes that the electron density of H^- is loosely bound to the nucleus and therefore the hydride anion is a strong electron donating species, a strong Lewis base and a potent reducing agent.

The proton, H^+, obviously has an ionic radius close to 0.00 Å, which gives it an extremely high charge/radius ratio. This in turn makes the proton a very strong Lewis acid. In the gas phase it therefore readily combines with other molecules or atoms. In condensed phases it is always found in combination with a Lewis base, from which it spontaneously extracts some electron density. The strong Lewis acidity is also emphasised by the large ionisation energy of the hydrogen atom, i.e. 13.6 eV.

The third form in which elementary hydrogen exists is hydrogen gas, H_2. The covalent bond between the two nuclei is very strong, with an enthalpy of 436 kJ/mol and a bond length of 0.74 Å. The interaction between different hydrogen molecules, on the other hand, is very weak, because of the few electrons in the hydrogen atoms.

1.1.3 Hydrogen compounds

Hydrogen forms stable compounds with the major part of the elements in the periodic table. With the elements on the right-hand side it forms covalent, polar compounds, in which hydrogen normally carries the small positive charge. The compounds range from the electron precise species CH_4, NH_3, H_2O and HX (X = F, Cl, I, B) to electron deficient species as BH_3. With electropositive elements, like the alkalis and earth alkali metals on the left-hand side of the periodic table, hydrogen forms however salt-like compounds in which hydrogen is present as hydride anions. These compounds are stable in dry inert atmospheres, as the hydride anions are highly reducing species that react spontaneously with air and vigorously with water. With most metals from Group 3 – 10, hydrogen can form metal-like materials, in which the hydrogen dissolves as single atoms. In these materials, the hydrogen donates some of its electron density to lower the energy of the metal bands, but still remains most of it hydridic character. These materials are clear intermediates between the saline hydrides and the molecular hydrogen compounds. Finally, hydrogen can form polymeric compounds, despite its single electron. BeH_2 and AlH_3 are known to form polymeric units in their solid state. The structure of AlH_3 is shown in Figure 1-2.

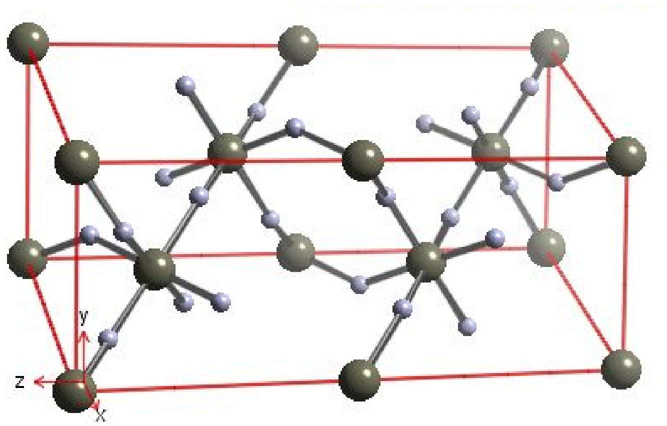

Figure 1-2: Polymeric structure of AlH_3 with the aluminium octahedrally surrounded by hydride ions

1.1.4 The H^-/H_2 equilibrium – the hydrides

In this project we are especially interested in hydrogen transport/exchange in solid materials. From the previous section it becomes clear that we have two options to choose from: either we use the H^+/H_2 equilibrium, or we use the H^-/H_2 equilibrium to transfer hydrogen from gas phase to solid. The first option does not look too appealing, since the proton is a hard and very strong Lewis acid. This is a combination that does not give much hope for reversibility in chemical processes. One of the few well-known electrochemical reactions with H^+ ions that involve hydrogen gas evolution is the reaction of acids with alkali or earth alkali metals. These reactions are highly exothermic (ΔG = -457 kJ/mol for the reaction of metallic Mg with an acids) and have a positive entropic effect (i.e. ΔS > 0), because of the hydrogen evolution. In other words, reversing the reaction would require extremely high temperatures and hydrogen pressures, just to overcome the thermodynamic barrier. Also see equation (1.1).

$$\Delta G = \Delta H^0 - T\Delta S^0 + RT\ln\frac{pH_2 \cdot [Mg^{2+}]}{[H^+]^2} \tag{1.1}$$

The other equilibrium looks a lot better. Since hydrogen has a relatively low electron affinity to form the hydride ion H^-, it is easier to play around with, in a chemical sense. Still the electrochemical potential of the H^-/H_2 couple is -2.25 V, which makes the hydride ion one of the strongest electron donating species, comparable to magnesium (the Mg/Mg^{2+} couple has a potential of -2.37 V). Because of this high absolute standard potential, it only forms saline hydride materials with the alkali and alkaline earth metals, which have a comparable standard potential or are even more electropositive.

1.1.4.1 Saline hydrides

So again, hydrogen forms ionic compounds with the alkali and earth alkali metals. Because these materials are salt-like, they are commonly referred to as the saline hydrides. Exceptions are BeH_2 and MgH_2. In BeH_2 the chemical bond is covalent and the material is in a polymeric form. MgH_2 seems to be a crossover between the saline hydrides and BeH_2 and is therefore called an intermediate hydride. Although from the difference in electronegativities, the ionic character of the bonds seems to decrease from CsH to LiH and from BaH_2 to CaH_2, there is still evidence for a strong ionic bond in all saline hydrides, with electron transfers to the hydrogen atom between 0.8 and 1 electron [35]. Saline hydrides show similarities with their halide analogues, especially concerning brittleness, hardness, optical properties and crystal structure. All the alkali hydrides exhibit the rock salt structure (i.e. the sodium chloride structure), whereas the hydrides of the earth alkali metals have a structure related to the barium chloride structure.

1.1.4.2 Metallic hydrides

With the transition metals, the lanthanides and actinides (see Table 1-1 for an overview of known metal hydrides), which of course have less negative standard potentials, hydrogen can form stable compounds as well. The nature of the chemical bond in these compounds is not very clear, but seems to be a crossover between metallic and ionic bonding. These compounds resemble their respective metals, since they exhibit high electronic (metallic) conductivity and usually have a dull metallic appearance. That is why they are commonly referred to as the metallic hydrides. A more detailed description of their properties follows in section 1.5.

Table 1-1: Known (grey) and unknown (white) hydrides of d- and f-block elements (as adopted from Ref [32].

	Sc	Ti	V	Cr	Mn	Fe	Co	Ni	Cu	Zn
MH			▨	▨				▨	▨	
MH_2	▨	▨	▨	▨						▨

	Y	Zr	Nb	Mo	Tc	Ru	Rh	Pd	Ag	Cd
MH			▨					▨		
MH_2	▨	▨	▨							
MH_3	▨									

	Lu	Hf	Ta	W	Re	Os	Ir	Pt	Au	Hg
MH			▨							
MH_2	▨	▨								
MH_3	▨									

	La	Ce	Pr	Nd	Pm	Sm	Eu	Gd	Tb	Dy	Ho	Er	Tm	Yb
MH_2	▨	▨	▨	▨		▨	▨	▨	▨	▨	▨	▨	▨	▨
MH_3	▨	▨	▨	▨		▨		▨	▨	▨	▨	▨	▨	▨

	Ac	Th	Pa	U	Np	Pu	Am	Cm	Bk	Cf	Es	Fm	Md	No
MH_2	▨	▨				▨	▨	▨						
MH_3			▨	▨		▨	▨							

1.1.4.3 Covalent bound hydrides

Hydrogen forms stable compounds with the first three members of Group III/13, i.e. boron, aluminium and gallium, too. The chemical bond is however not ionic anymore, but covalent. Stable InH_3 and TlH_3 have not been synthesised, yet. When combined with binary hydrides, like LiH or NaH, they can form compounds with a more ionic character, namely $LiAlH_4$ or $NaBH_4$.

1.2 Crystal structures of hydrides

In order to be able to understand the transport properties of a possible hydride ion conducting electrolyte, electrodes or hydrogen storage materials, knowledge of the material's crystal structure is essential. For instance, electrolytes benefit from a structure that promotes fast ionic transport. In that respect, the fluorite structure has shown good results (YSZ, CGO, PbF_2). The alkali hydrides all have the rock salt structure, analogous to their halogenide counterparts. Whereas one would expect the alkaline earth hydrides to have the same structure as their fluoride analogues, this is not the case at low temperatures. CaH_2, SrH_2 and BaH_2 have an orthorhombic structure which is similar to the $PbCl_2$ structure. In this structure, the metal cations are arranged in a distorted hexagonal array, surrounded by four hydride ions of type I and five hydride ions of type II [36, 37]. Interestingly, CaF_2 has this same $PbCl_2$ structure at room temperature when it is exposed to an 8 GPa pressure [38]. MgH_2 forms an exception again in the alkaline earth hydride range, as it has the rutile structure.

Most transition metal hydrides with formula MH_2 have the cubic fluorite structure, in which the hydride ions occupy the tetrahedral sites. Actually, most of these metallic hydrides have this structure in a wide composition range, for instance from TiH to TiH_2. Zirconium and hafnium hydrides only have the cubic structure in a limited composition range of their hydride phase. Beyond this composition limit (for ZrH_x and HfH_x x = 1.61 and x = 1.8, respectively), the structure changes to tetragonal.

Most rare earth elements have both a dihydride and a trihydride. All rare earth dihydrides have a cubic structure, except for EuH_2 and YbH_2, which are isostructural with CaH_2 (orthorhombic structure) [39]. The trihydrides of the light rare earth metals (La, Ce, Nd and Pr) are cubic as well, although for LnH_{2+x}, $\sim 0.25 < x \leq 0.5$ the hydride ions are distorted from their ideal tetrahedral/octahedral positions and form an ordered superlattice, which is better described as body centred tetragonal [40-42]. NdH_3 ($x > 0.7$) and the trihydrides of the heavy rare earth metals, like GdH_3 and SmH_3 usually have hexagonal/trigonal structures [43-45]. This hexagonal structure starts to form at different values of x in LnH_{2+x} for different rare earth metals, but can only be obtained as a single phase at high hydrogen contents, i.e. $x \approx 1$. So often a mixture of the cubic and hexagonal phase is obtained when synthesising the heavy rare earth trihydrides. The composition ranges for these rare earth di- and trihydrides have been listed in Table 1-2, but the lower existence limit for the trihydrides seems to be too low for most rare earths. The reported literature is quite dated and these ranges are very badly reported in more recent research. Whereas the upper existence limit for 'cubic' LnH_{2+x} seems well studied in recent years, it is generally assumed that for LnH_{3-z}, z is always very close to 0. Neutron diffraction studies on LnH_{3-z} do however indicate that z is indeed very close to 0 in most cases. An older study by Perkins and Lundin on the holmium – hydrogen phase system seems to be one of the few that reports a reasonable lower limit for HoH_{3-z}, with z being 0.05 [46]. Yttrium and scandium are transition metals, but their hydride behaviour is very similar to that observed for the hydrides of the rare earth metals. Their hydrides have therefore been added to Table 1-2.

The actinide hydrides show a variety of different crystal structures, ranging from the fluorite structure for actinium and plutonium dihydride to a tetragonal structure for thorium dihydride. The higher actinide hydrides, like Th_4H_{15} and UH_3, have complex cubic structures. A range of compositions with various crystal structures is possible, analogous to the rare earth metal hydrides. As these metal hydrides are not of very practical interest at the moment, their chemistry is beyond the scope of this thesis.

Table 1-2: Crystal structures of rare earth metals and actinides, adopted from Ref [35]

Metal hydride	Structure	Existence range (H/M)	Reference
LaH_2	Cubic		[42]
CeH_2	Cubic		[42]
PrH_2	Cubic		[42]
LnH_3 (Ln = La, Ce, Pr)	Cubic		[41]
NdH_2	Cubic	2 – 2.61 (2.87)	[45] ([47])
NdH_3	Hexagonal/trigonal	~3	[45, 47]
SmH_2	Cubic	1.93 – 2.40	[47]
SmH_3	Hexagonal/trigonal	2.59 – 3	[35, 48]
EuH_2	Orthorhombic		[39, 49]
GdH_2	Cubic	1.82 – 2.3	[50]
GdH_3	Hexagonal/trigonal	2.85 – 3	[43]
TbH_2	Cubic	1.90 – 2.25	[51]
TbH_3	Hexagonal	2.81 – 3	[48]
DyH_2	Cubic	1.94 – 2.23	[52]
DyH_3	Hexagonal	2.86 – 3	[48]
HoH_2	Cubic	1.95 – 2.12	[47]
HoH_3	Hexagonal/trigonal	2.95 – 3	[46]
ErH_2	Cubic	1.95 – 2.10	[47]
ErH_3	Hexagonal	2.82 – 3	[48]
TmH_2	Cubic	1.99 – 2.06	[47]
TmH_3	Hexagonal	2.76 – 3	[48]
YbH_2	Orthorhombic		[39]
YbH_{2+x}	Cubic	2 – 2.55	[53]
YbH_3	Hexagonal/trigonal	Max $YbH_{2.67}$	[54]
LuH_2	Cubic	1.85 – 2.03	[47]
LuH_3	Hexagonal	2.78 – 3	[48]
ScH_2	Cubic		[49]
YH_2	Cubic	1.91 – 2.08	[47]
YH_3	Hexagonal	2.77 – 3	[48]

1.3 Thermodynamics of metal hydrides

The formation of hydrides occurs via simple absorption of either hydrogen gas or hydrogen atoms from an electrolyte. The latter is typical for metal hydride batteries, using a standard hydroxide solution to transfer the hydrogen atoms from one electrode to the other. Absorption/desorption of hydrogen in the metal is typically shown as composition/hydrogen pressure isotherms. These show some generalities and typical isotherms are shown in Figure 1-3. At low pressure, hydrogen is dissolved in the metal lattice and the so called α-phase is formed. During this stage, hydrogen fills octahedral or tetrahedral holes and is present as an interstitial species. When the concentration of hydrogen in the metal increases, nucleation of the real hydride phase starts, called the β-phase and the isotherm reaches a plateau. During this plateau, the α-phase and β-phase coexist. After long enough equilibration times at a certain temperature and hydrogen partial pressure, only the β-phase will remain, with often a substoichiometric hydrogen content. Increasing the hydrogen content further to the metal hydride's stoichiometric value, is now accompanied with high hydrogen pressures. The plateau pressure is actually the dissociation pressure of the non-stoichiometric hydride and is a good measure of its thermal stability. When at a certain temperature the hydrogen pressure above the hydride phase drops below its dissociation pressure, both phases are not in equilibrium anymore and the hydride phase will decompose, releasing hydrogen.

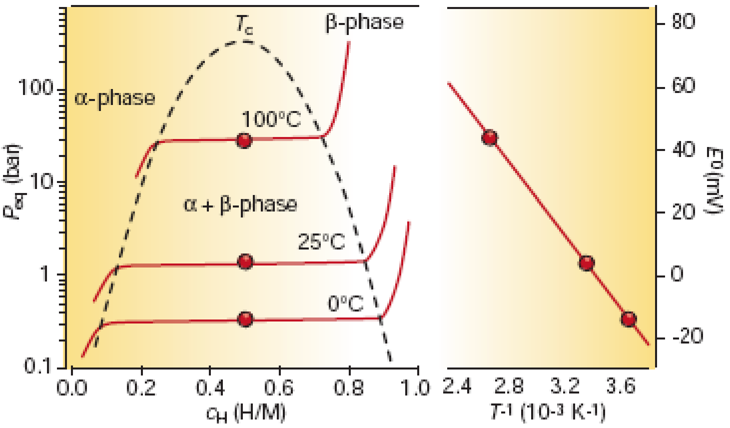

Figure 1-3: General representation of a adsorption/desorption curve for hydrogen in metallic hydrides. Figure adopted from [18]

The logarithm of the dissociation pressure often shows a linear relationship with the reciprocal temperature. The reason for this behaviour can be found in thermodynamics. Consider the next dissociation reaction:

$$MH_x \rightarrow M + \tfrac{x}{2}H_2 \tag{1.2}$$

For the free enthalpy of hydride formation, the following equation holds:

$$\Delta G_f = \Delta G_f^0 + RT\ln Q_p \qquad \text{with } Q_p = \frac{a_{MH_x}}{a_M \cdot pH_2^{\frac{x}{2}}} \tag{1.3}$$

In equilibrium, i.e. with ΔG = 0, this becomes:

$$-\Delta G_f^0 = RT\ln K_p \tag{1.4}$$

Using $\Delta G_f^0 = \Delta H_f^0 - T\Delta S_f^0$ and doing some basic differentiation, this becomes:

$$-\Delta H_f^0 + T\Delta S_f^0 = RT\ln K_p \tag{1.5}$$

$$\frac{\Delta H_f^0}{RT^2} = \frac{\partial \ln K_p}{\partial T} \tag{1.6}$$

The last equation is better known as the Van ‘t Hoff equation. When the metal and metallic hydrides are assumed to be pure solids, their activities become unity. And with $K_p = pH_2^{-\frac{x}{2}}$ the Van ‘t Hoff equation can also be written as:

$$\ln p_{H_2} = \frac{2}{xR}\left(\frac{\Delta H_f^0}{T} - \Delta S_f^0\right) \tag{1.7}$$

From this last equation it can clearly be seen, that the logarithm of the dissociation pressure is linearly dependent on the reciprocal temperature. The slope of the relationship can be used to calculate the enthalpy of formation. Actually, because the metallic hydrides are subject to significant non-stoichiometry that cannot be neglected, the activities of metal and metallic hydride cannot be set to zero and the last equation becomes a bit more complicated. Still it is found that metal hydrides obey an equation of a similar form experimentally:

$$\log p_{H_2} = -\frac{A}{T} + B \tag{1.8}$$

Higher hydrides, for instance GdH_3 or Th_4H_{15} have isotherms with two plateaus. The lower plateau resembles the formation of the lower hydride, whereas the higher hydride starts to form on the higher plateau, coexisting with the lower hydride.

1.4 Saline hydrides

As the name suggests, the bonding in saline hydrides is ionic. Any conductivity in these materials is therefore expected to be purely ionic in nature, which make them of great interest as electrolyte materials. Dependent on the mechanism of ion conduction in the saline hydride materials, doping with higher or lower valence hydrides might increase the ionic conductivity. This is a known fact for materials like ceria and zirconia, which are usually doped with cations of lower valence (Gd or Sm for CeO_2; Y, Sc and Ca for ZrO_2), to improve oxygen ion conductivities. Substitution of the host cations by ions of lower valence causes the creation of oxygen vacancies in the crystal lattice, which enhances conductivity. Alternatively, substitution with elements of higher valence gives rise to interstitial anions. Sorokin and Breiter [55] doped single crystal CaF_2 with different trivalent fluorides (LaF_3, GdF_3, CeF_3, YbF_3, etc.) and managed to enhance the ionic conductivity by several orders of magnitude (up to 0.4 S/cm at 800°C). Highest fluoride ion conduction was obtained for those elements that caused a minimum in the activation energy of migration of the mobile species. Often, a good fit of the dopant element in the host lattice is important, which means that the ionic radii of host and dopant cations should be a good match.

When one applies the same rules to hydride materials, either doping with monovalent or trivalent hydrides might improve the ionic conductivity in MH_2 (M = Ca, Ba, Sr) materials. The ionic radii for different elements are given in Table 1-3. Good candidates for substituting calcium are Li, Na, La, Ce and Nd and Yb, whereas only Na, La and Ce might be large enough to be a good match to strontium. Ytterbium might be a particularly interesting substitution for Ca, as YbH_2 is reported to have the same orthorhombic crystal structure as CaH_2. The higher hydride for ytterbium (YbH_{2+x}, $x \leq 0.67$) suffers from poor thermal stability though, which might mean no interstitial hydride ions are formed upon substitution [49]. The crystal structure also changes into trigonal at higher hydrogen content [54].

Table 1-3: Ionic radii for different cations, adopted from Ref [33]

Cation	Ionic radius in 8-fold coordination (Å)	Ionic radius in 9-fold coordination (Å)
Ca^{2+}	1.12	1.18
Sr^{2+}	1.26	1.31
Li^{+}	0.92	-
Na^{+}	1.18	1.24
Y^{3+}	1.02	1.08
La^{3+}	1.16	1.22
Gd^{3+}	1.05	1.11
Ce^{3+}	1.14	1.20
Nd^{3+}	1.11	1.16
Yb^{2+}	1.13	1.18

1.5 Metallic hydrides

The ‘metallic’ bonding in metallic hydrides gives rise to metallic conductivity. As this is one of the requirements for good electrochemical electrodes, these hydrides are of interest as potential electrode material in a hydride ion electrochemical device. Other requirements for efficient electrodes are electrocatalytic activity towards the electrode reactions, redox stability and chemical and thermal compatibility with the electrolyte. Some degree of ionic conductivity would improve electrode behaviour by extending the active electrode area from the immediate electrode/electrolyte interface a certain distance into the electrode. This does not necessarily have to be ionic transport, as hydrogen could be transported in a different state, e.g. atomic.

Since we are looking for materials that not only show high electronic conductivity, but also fast kinetics for hydrogen uptake, release and transport, it would be interesting to look into hydrides for hydrogen storage as well, as they share most of these properties. Apart from metallic hydrides, complex chemical hydrides like $LiBH_4$ and $NaAlH_4$ are being studied for their hydrogen storage properties and they might be of interest.

1.5.1 Bonding in metallic hydrides

The bonding in metallic hydrides is delocalised and it is argued in which form hydrogen is present in the metal lattice. Different models exist, in which hydrogen is either present as protons, hydride ions or bound covalently [35]. Indications for the protonic model are found in $PdH_{0.6}$, in which the d-band of palladium seems to be filled with electrons from hydrogen. Secondly, hydrogen evolution is observed at the cathode side upon electrolysis. This is however not observed for ‘real’ metallic hydrides, but rather for solid solutions of hydrogen in metal. There are also indications for the hydride anion model. The heats of formation of metallic hydrides and their brittleness resemble those of the saline hydrides, suggesting a certain degree of ionic character in the bonding. Furthermore, the interatomic distances between the metal atoms and hydrogen agree well with calculations using the ionic radii of both metal cations and hydride ions. The high electronic conductivity in such an ionic model can be explained by the fact that metallic hydride compositions usually deviate from the preferred composition of the metal cations (i.e. TiH_2 and ZrH_2 rather than TiH_4 and ZrH_4). This might mean that after bonding with hydrogen, still enough d-electrons are available for the metallic bonding. So despite bonding with hydrogen, enough d-orbital overlap exists to guarantee the metallic conduction. In the last model, in which metal atoms and hydrogen are bound covalently, the hydrogen electrons are delocalised. Since the hydrogen lies much lower in energy than the electronic bands of the metal, hybridisation occurs between the metal and hydrogen orbitals. Due to this hybridisation, the Fermi level can shift downwards, which may result in interesting phase transitions (for example metallic – semi conducting, magnetic – non-magnetic, order – disorder) [18]. This last covalent model seems to agree most with the observed non-stochiometry of metallic hydrides. For instance, in ZrH_x, x can vary between 1.30 and 2.00. Within this range, the compound is clearly a metallic hydride and not just a solid solution of hydrogen in the zirconium metal. Physical properties change as a function of the hydrogen content. Obviously, the electronic structure is very dependent on the amount of hydrogen that is stored inside the metallic lattice.

1.5.2 Electrical properties of metallic hydrides

Except for some of the rare earth hydrides, all metallic hydrides are metallic conductors. A clear relation between the conductivity of the hydride and its pure metal is however not observed. As a matter of fact, some hydrides have higher conductivities than their respective metals. This might seem an indication that the bonding in metallic hydrides is not ionic, since hydride anion formation would lead to a decreased number of metallic electrons. The hydride is however a different material with its own distinct crystal structure. Therefore, the electronic band structure of the hydride, and thus its electronic properties, is expected to be different from that of the metal. The effect of crystal structure becomes clear when the change of conductivity with hydrogen content is observed for both titanium hydride and zirconium hydride. The structure of ZrH_x changes from cubic to tetragonal for $x > 1.61$, whereas TiH_x has the cubic structure for $x > 1$. Whereas the conductivity for tetragonal zirconium hydride decreases with increasing hydrogen content, the conductivity for titanium hydride increases. Thermoelectric measurements have pointed out that the conduction in both cubic materials is of p-type through hole conduction, whereas in the tetragonal structure, electrons are the main current carriers.

As already said, some hydrides of the rare earth elements do not exhibit metallic conduction. This is the case for rare earth hydrides in which the ratio H/M is close to the stoichiometric value of 3. Apart from ytterbium and europium (YbH_2 only has a conductivity of ~3×10^{-5} S/cm), all the rare earth dihydrides are metallic conductors, just like the other metallic hydrides. The lighter lanthanide hydrides (La, Ce, Nd, Pr) with H/M ratios of 2.7 – 2.8 however, were shown to exhibit some interesting electronic properties. At temperatures of 230 – 270 K a transition in the resistivity occurs, which according to Shinar et al. [56] is due to the breakdown of the octahedral H – ordering and tetragonal distortion as discussed in section 1.2. Below the transition the resistivity, ρ, increases with increasing temperature, which is typical for metallic conduction, but above the transition temperature, $\rho(T)$ drops with increasing T and this is thought to be caused by a Variable Range Hopping (VHR) conduction mechanism [57]. Therefore, this transition can be described as a metal – non-metal transition. At stoichiometries close to MH_3 the hydrides increasingly start to behave like semiconductors, as the resistivity now continuously decreases with temperature, showing typical Arrhenius behaviour. Shinar showed this semiconducting behaviour for $LaH_{2.93}$ [56]. The room temperature conductivity of LaH_x drops sharply from 200 S/cm to 2 S/cm when going from $LaH_{2.70}$ to $LaH_{2.93}$, emphasising the changes in the electronic structure of these materials and the transition from metallic to semiconductor behaviour.

Libowitz [35] suggests a plausible model that explains the semiconductor behaviour in rare earth trihydrides. In this model it is assumed that the trihydrides are ionic crystals. In such materials, the electronic band structure would consist of a lower filled 1s valence band, originating from overlapping 1s hydrogen orbitals, and an empty 5d-6s conduction band, formed by the 5d and 6s orbitals of the metal ions. When hydrogen is removed from the ideal trihydride, hydrogen vacancies are formed that act as donor levels in the electronic band structure (appearing just below the conduction band). When the hydrogen vacancy concentration increases, the activation energy decreases by:

$$E_c = E_0 - a(c_D)^{\frac{1}{3}} \tag{1.9}$$

E_c is the activation energy at a certain defect concentration, c_D. E_0 is the activation energy of isolated defects (i.e. low concentration) and a is a constant. It follows that when the defect concentration increases, E_c will become zero and the semiconductor is degenerate. In other words, the material has become a metallic conductor, since the band gap has vanished between the valence band and the conduction band. Apparently, this already occurs at an H/M ratio of just below the stoichiometric value of 3. The observed activation energies at near stoichiometric composition do not have to involve electronic conduction, but could possibly be due to ionic conduction as well. As the H/M ratio increases, the material becomes more ionic in nature, making electronic conduction less favourable.

1.6 Nitride, nitride hydride and imide chemistry of the group I and II elements

Nitride chemistry is, like hydride chemistry, not as widespread as for instance oxide chemistry. Again, the high sensitivity of these nitride materials towards moisture and air is a major drawback in synthesising and analysing them properly. The chemistry of nitrogen is however very rich, with unusual chemical bonding with other elements across the periodic table, resulting in unexpected physical properties (e.g. optical, electrical, etc.). Pure ionic nitride compounds are, analogous to the hydrides, only found in combination with some of the most electropositive elements in the s-block. However, even with many of these elements, there is a variety of chemical bonding possible, including metallic bonding. This section aims to briefly describe some of the, for this research, relevant nitrides of the group I and II elements (lithium, calcium and strontium). It also gives a brief overview of nitrogen – hydrogen chemistry of the same elements, i.e. imides and nitride hydrides.

1.6.1 Lithium nitride, α-Li_3N

Possibly the best described nitride to date is Li_3N. It has received much interest as it is a good conductor of lithium ions, Li^+, already at room temperature, and as such it has great potential as an electrolyte in lithium ion batteries. Lithium nitride forms by combining the elements and does so already at room temperature. However, to obtain a pure, crystalline material, it is preferable to carry out the synthesis by dissolving lithium in molten sodium and reacting the solution with purified nitrogen gas. The crystal structure for Li_3N is unique to the material. Lithium is hexagonally arranged in layers, much like graphite, with nitrogen situated within the centre of the hexagons. The layers are connected by an additional lithium ion, which is situated between the [Li_2N] hexagons. N is therefore 8 coordinated by Li in a hexagonal bipyramidal way. The lithium ions in the hexagonal [Li_2N] layers are coordinated in a trigonal fashion by nitrogen, whereas the interlayer Li ions are linearly coordinated to N. Li_3N is an ionic compound with a highly polarisable N^{3-} ion. Neutron diffraction techniques have shown that a small fraction of the Li2 (intralayer lithium) sites are vacant, caused by some imide ions $(NH)^{2-}$ substituting for the nitride ions. These lithium vacancies actually improve the ionic conductivity, which is predominantly across the hexagonal layers [58].

Lithium nitride reacts with the transition metals and the the p-block elements to form binary nitrides. It also reacts with the halides LiX and lithium hydride, LiH. With LiH, Li_3N forms lithium nitride hydride Li_4NH, which decomposes at ~400°C to form lithium imide, Li_2NH, and depending on the atmosphere LiH or Li_3N [59]. The amides and imides of lithium can be prepared by reacting lithium nitride with ammonia. The resulting amide can thermally be decomposed to yield the imide. The amide and imide of lithium are structurally related, both being based on a distorted cubic closest array of N, with Li occupying the tetrahedral sites [60].

1.6.2 Nitrides of the heavier alkali metals

The existence and stability of the binary nitrides of Na, K, Rb and Cs has long been the subject of much debate. On the basis of thermodynamics of these compounds, only Na_3N has a negative formation enthalpy, which would imply it could be a (meta)stable compound. Indeed a few papers report the synthesis of Na_3N, but only under extreme conditions, using electrically activated nitrogen. The products were however never well characterised and it is believed that sodium azide NaN_3 is formed at the same time as well [58]. Relatively recently, Fischer and Jansen [61] managed to synthesise Na_3N by atomising the elements in a vacuum chamber and codepositing them in a microwave beam on a cooled sapphire substrate. They characterised the product using X-ray diffraction and found an anti-ReO_3 structure, which consists of corner sharing Na_6N octahedra. The structure is thus related to Li_3N, with the difference that N is only 6 coordinated by Na, as opposed to 8 coordinated by Li. Potassium nitride, K_3N has been synthesised and characterised in an analogous manner, although a mixture of phases was obtained in this case [62]. So although a synthesis method is available for some of the heavier alkali nitride, this is not straightforward. The resulting products are also extremely air and moisture sensitive, causing them to decompose within a few weeks even when stored in the protective atmosphere of a glovebox.

1.6.3 Calcium nitrides

Calcium is a unique element, as it is the only elements in the s-block that forms both ionic and subnitrides with nitrogen. For a long time it was believed that there were many compounds in the Ca-N system, including α-Ca_3N_2, β-Ca_3N_2 and γ-Ca_3N_2, calcium pernitride, Ca_3N_4 and a compound of composition $Ca_{11}N_8$. α-Ca_3N_2 is the only compound that has been extensively characterised. It has a distorted form of the anti-bixbyite structure, in which Ca is tetrahedrally coordinated to N, whereas N is octahedrally coordinated to Ca. Recent studies have practically ruled out the existence of all other forms of calcium nitride, just mentioned. These all seem to be some form a calcium nitride cyanamide, $Ca_4N_2(CN_2)$ or $Ca_{11}N_6(CN_2)_2$. The carbon contamination most likely comes from steel in crucibles and reactors or even from the calcium metal.

1.6.4 Subnitrides: Ca_2N and Sr_2N

Although α-Ca_3N_2 seems to be the only ionic compound in the Ca-N system, a subnitride of calcium, Ca_2N, has been properly characterised and shown not to be a contaminated ternary compound. It can be synthesised by heating α-Ca_3N_2 in vacuum. The structure of Ca_2N consists of edge sharing NCa_6 octahedra, in which Ca is only 3 coordinated to N (half fulfilled octahedra). In this way $[NCa_2]^+$ slabs are formed, with large Van der Waals gaps between them. The N-Ca layers are basically ionic in nature, with the excess electron residing in the Van der Waals gaps. Sr_2N was shown to be isostructural with Ca_2N. Strontium does not form the ionic compound Sr_3N_2 and Sr_2N is the only compound that has been properly characterised to date. The excess electron is mobile and gives these subnitride materials electronic conductivity. The electronic conductivity is highly anisotropic and they can therefore be seen as 2D metals, with reasonable conductivity in the direction parallel to the N-A layers [58].

The A_2N subnitrides can be intercalated with hydrogen or halides, resulting in A_2NX compounds (X = H, F, Cl, Br). H^- or X^- will take the place of the excess electron, forming alternating layers of N and H or X [63]. In fact, the ordering Ca_2NH slightly different, but the intercalation is essentially the same. The basic structures of A_2N and A_2NX are shown in Figure 1-4 for comparison.

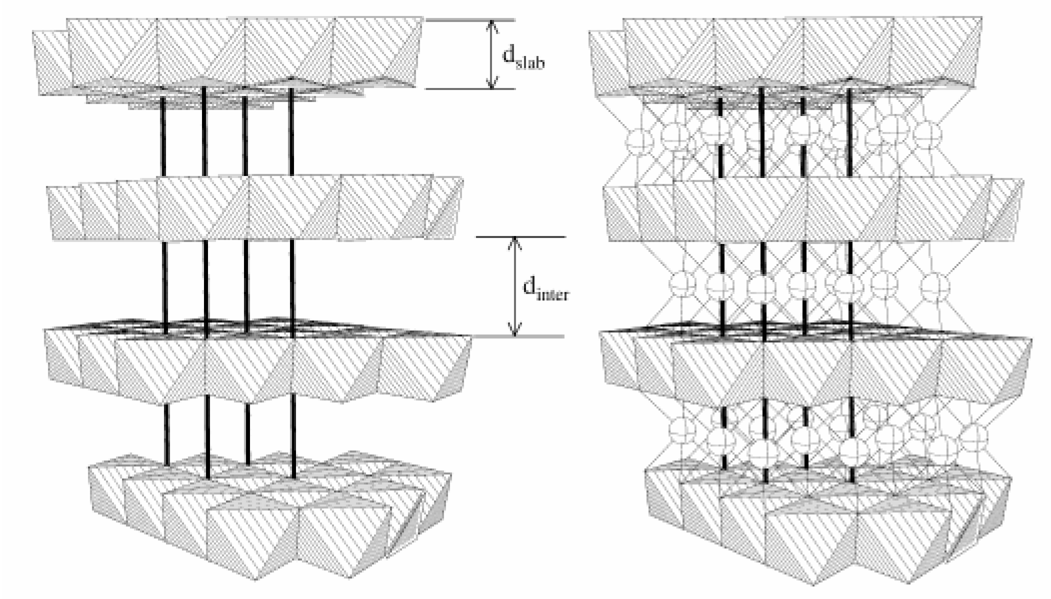

Figure 1-4: Structure of the alkaline earth subnitride A_2N (A = Ca, Sr, Ba) on the left. Structure of the alkaline earth nitride halide/hydride, A_2NX (X = F, Cl, Br, H) on the right. NA_6 octahedra shown as polyhedra, white balls represent X ions. Adopted from Ref [63].

Closely related to calcium nitride hydride, Ca_2NH, are calcium imide, CaNH, and calcium amide, $Ca(NH_2)_2$. Calcium imide has the rocksalt structure, with calcium octahedrally coordinated to nitrogen in a cubic closest packed array of nitrogen ions. Hydrogen is positioned close to the nitrogen ion with a large degree of disorder. Calcium amide has the tetragonal anatase structure, which is closely related to calcium imide [64, 65]. It can roughly be viewed as two imide unit cells stacked on top of each other, with only half of the calcium ions now occupied. The hydrogen in the amide ions was shown to have a large degree of disorder by assuming in and out of plane movements relative to the nitrogen ion [65].

1.7 Nitrogen – hydrogen materials for hydrogen storage

Nitrogen – hydrogen based materials of the light weight metals (group I and II in the periodic table) have become of major interest for hydrogen storage purposes, particularly after Chen et al. reported a potential 10.4 wt% storage of hydrogen by lithium nitride [1]. Their hydrogen storage system involved a two step uptake/release, in which lithium nitride is converted into lithium imide and lithium hydride, which are subsequently converted into lithium amide and more lithium hydride.

$$Li_3N + H_2 \xrightarrow[T=225°C]{pH_2=0.01bar} Li_2NH + LiH \tag{1.10}$$

$$Li_2NH + H_2 \xrightarrow[T=255°C]{pH_2=0.8bar} LiNH_2 + LiH \tag{1.11}$$

The desorption pressure for the first step is generally believed to be too low at T = 255°C to be considered reversible. The second step potentially still stores 6.5 wt% H_2 and therefore researchers have attempted to lower the desorption temperature by destabilising the lithium amide compound. Destabilising was initially carried out by doping lithium amide by magnesium, but later this evolved into the creation of ternary imides. Luo successfully decreased the desorption temperature for reaction (1.11) by 60°C by replacing LiH by MgH_2 [2]. The idea behind substituting LiH with MgH_2 is that MgH_2 has a lower thermal stability than LiH and it would therefore destabilise the desorption process. Overall this resulted in a hydrogen desorption pressure of 32 bar at 200°C.

Chen et al. also reported similar storage behaviour for Ca_2NH, calcium nitride hydride. It could reversibly store hydrogen, but at high temperatures, i.e. 550°C for a desorption temperature of 0.2 bar. Hino et al. studied the Ca-N-H system in more detail and found that calcium amide could be reacted with calcium hydride to form the imide (analogous to equation (1.11)), but that this reaction is irreversible. So finally the Ca-N-H can only store 2.1 wt% H_2 reversibly [9]. Xiong et al. tested the hydrogen absorption characteristics of Ca_3N_2, which shows higher hydrogen pressures at similar temperatures than Ca_2NH [4]. They however also found that only half of the absorbed hydrogen could be released again and that Ca_3N_2 was not reformed. Adding CaH_2 to Ca_3N_2 improved the hydrogen sorption behaviour. This could however be attributed to the formation of Ca_2NH, which does reversibly store hydrogen as mentioned earlier.

Different researchers explored combinations of amides/imides and hydrides to destabilise the binary compounds and thus reduce the desorption temperatures, or alternatively, increase the hydrogen desorption pressure. Combinations of lithium amide with magnesium and calcium hydride so far seem to give the most promising hydrogen storage results and this has resulted in the development of several ternary imides, i.e. $Li_2Mg(NH)_2$, $Li_2Ca(NH)_2$, $MgCa(NH)_2$, etc. [7, 66]. It was found that hydrogen adsorption and desorption temperatures could be reduced by 100°C or even 130°C when LiH was completely substituted by MgH_2 or CaH_2, respectively. The mechanisms for hydrogen absorption/desorption of Li-Ca-N-H and Li-Mg-N-H seem to be quite different as the former only seems to involve 2 formula units of H, whereas the latter involves 4 units. Liu et al. even studied a quaternary compound, $Li_4CaMgN_4H_4$ that they did not structurally characterise, for its hydrogen storage properties [8].

Many additional studies have been performed to elucidate the structure of the ternary system $Li_2Ca(NH)_2$, which should help explain this material's superior hydrogen storage properties as compared to Li_2NH. A combination of XRD, XANES, EXAFS and Li-NMR revealed that the material has the anti-La_2O_3 structure, which is a hexagonal structure in which calcium is octahedrally and Li tetrahedrally coordinated towards nitrogen [3]. A later neutron diffraction study by Wu revealed that the material actually has an ordered structure of CaNH and Li_2NH layers. The hydrogen absorption is now believed to solely occur within the Li_2NH layers, as CaNH is relatively inert towards hydrogen absorption, as stated earlier. Upon hydrogen absorption, lithium imide is basically converted into lithium amide and lithium hydride, leaving three phases (including CaNH). This resulting three phase material however reversibly releases hydrogen again at 140°C and 206°C to form the ternary imide. So although the ternary imide is initially formed by combining lithium amide and calcium hydride, which releases 4 formula units of hydrogen, this involves two conversion steps: formation of lithium imide combined with conversion of CaH_2 into CaNH, which then reacts with Li_2NH to form $Li_2Ca(NH)_2$.

Initial desorption:

$$\begin{aligned} &2LiNH_2 + CaH_2 \longrightarrow Li_2NH + CaNH + 2H_2 \quad \text{4.6 wt\%} \qquad (1.12)\\ &Li_2NH + CaNH \longrightarrow Li_2Ca(NH)_2 \end{aligned}$$

Hydrogen absorption and subsequent desorption:

$$Li_2Ca(NH)_2 + H_2 \rightleftarrows LiNH_2 + LiH + CaNH \quad \text{2.3 wt\%} \qquad (1.13)$$

Kojima et al. and Liu et al. finally showed that many of these hydrogen storage systems suffer from poor kinetics due to slow surface (hydrogen absorption) reactions. The kinetics can be greatly improved by ball milling the materials during the desorption process and Kojima et al. showed that Li_3N and Ca_3N_2 both absorbed a considerable amount of hydrogen (about half of the theoretical value) at room temperature and 1 bar hydrogen pressure. It is probably a combination of intense contact and local temperature rise due to ball impact that causes the improved reaction kinetics [7, 10, 11].

1.8 Aims and objectives

The aim of this work is to get a better understanding of the structural and electrical properties of some alkaline earth hydrides and nitride hydrides. These compounds contain the hydride ion, which is not only of (electro)chemical interest, but also plays an important role in hydrogen storage applications. Understanding the defect chemistry of these materials will be important in understanding the transport mechanisms for hydride ion conduction and hydrogen uptake and release. Modifying this defect chemistry and observing changes in structural and transport properties will be crucial in identifying these mechanisms. Therefore, the host materials in the MH_2 and M-N-H (M = Ca, Sr) systems will be doped with aliovalent elements, like sodium and lithium. The different chapters will have separate introductions that will give specific background information and explain the more technical aspects of doping, ion conduction mechanisms, etc.

2 Experimental techniques

2.1 Synthesis and handling

All the starting materials and compounds that were synthesised in this work are all very air and moisture sensitive and therefore special care had to be taken in the handling and preparation to avoid serious contamination (by oxides and hydroxides) or decomposition. Handling was therefore carried out in an argon filled glovebox. Handling includes powder crushing and mixing, pellet pressing, weighing, loading and unloading of a sealed reactor used for solid state syntheses and filling of glass capillaries used for X-ray diffraction. Some of the analysis techniques required samples to be taken out of the glovebox, but samples were always kept in air tight sample containers. The glass capillaries for X-ray diffraction were temporarily sealed inside the glovebox, using vacuum grease and were permanently sealed in a flame once they were taken out of the glovebox. For the thermal analysis samples had to be transferred from an air tight container to the actual testing equipment, during which the samples were exposed to air. This was unavoidable, but exposure times were kept to a minimum and were never longer than 1 minute.

2.1.1 Hydride compounds

Hydride materials were synthesised in a stainless steel reactor, which was loaded and unloaded in the glovebox and could be sealed, allowing safe transferral between glovebox and a furnace out with the glovebox. Prior to the solid state reaction, the reactor was purged thoroughly with argon gas (BOC zero grade, 99.998%) to get rid of possible nitrogen (and oxygen and water) impurities in the glovebox gas. The argon flow was subsequently swapped for hydrogen gas (BOC High Purity, 99.995%) to create a pure hydrogen atmosphere. Pure hydride compounds (calcium and strontium hydride) were synthesised under flowing hydrogen conditions, whereas the solid state reactions between these parent materials and some alkali metal hydrides (NaH and LiH) were performed in a closed atmosphere of pure hydrogen. Deuterided compounds were obtained in an identical manner, with the exception that deuterium gas (Spectra gases, 99.995% chemical purity, 99.7% isotopic purity) was used instead of hydrogen. Molybdenum metal was used as crucible material. More details about the starting materials and resulting phases will be given in chapters 3 and 4.

2.1.2 Nitrogen – hydrogen compounds

The nitrogen – hydrogen containing compounds that will be discussed in chapters 6 and 7 were synthesised by combining the elements using the glovebox atmosphere. To this extent, 5% H_2 (BOC High Purity, 99.995%) and 1 – 2% N_2 (BOC, 99.998%) had been added to the argon atmosphere in the glovebox. Oxygen and moisture purifiers in the glovebox dri-train prevented oxide and hydroxide contamination during synthesis. Calcium and strontium metal and calcium hydride were subsequently fired in a small tube furnace within this glovebox, using an open alumina furnace tube at temperatures between 600°C and 900°C. Molybdenum metal was used as crucible material. More details about the used starting materials as well as the resulting phases will be discussed in chapters 6 and 7.

2.2 Analysis – diffraction techniques

When electromagnetic radiation comes into contact with small openings (an aperture, grating, slit, etc.), this will generate secondary wave fronts which scatters the incident beam in different directions. When a coherent light source is shone on a single aperture, the diffracted beams can be seen as diffuse rings around the primary dot, called the Airy disc. When there are multiple apertures close to each other, the secondary wavefronts from each aperture will interfere with each other and depending on the angle of the diffracted beam, this interference will be either constructive or destructive. When the beams from different apertures are in phase with each other they will interfere constructively and the diffracted beam can be observed. The spacing between two apertures generally has to be around the same order of magnitude as the wavelength of the electromagnetic radiation, for this phenomenon to occur. For visible light for instance, gratings are typically used with spacings in the order of 10 μm. The spacings in inorganic crystalline materials are of the order of angstroms so a different radiation is needed. X-rays and neutrons are an ideal choice as both have wavelengths of 1 – 2 Å.

For a grating with slit spacing *a*, the following relation for radiation wavelength λ and diffraction angle α can be calculated, for which constructive interference will occur:

$$n\lambda = a \cdot \sin\alpha \tag{2.1}$$

This would result in a pattern with sharp peaks at angles given by equation (2.1). A secondary effect however occurs, caused by the width *d* of the slit. Several wavefronts will be created at every single slit, causing additional interference and diffraction. For the diffraction at a single slit, it can be derived that in order to get destructive interference the following equation holds:

$$\lambda/2 = d/2 \cdot \sin\alpha \Rightarrow \lambda = d \cdot \sin\alpha \tag{2.2}$$

The resulting diffraction pattern for a single slit is therefore a broad peak and some small subsidiary peaks.

Now, a grating with a limited number of slits, *N* with spacing *a* will give a diffraction pattern, which is a combination of the two described above. The primary diffraction peaks will be broadened and have small subsidiary peaks in between them (with *N* minima between them). The more slits the grating has, the larger the difference in intensity between the primary peaks and subsidiary peaks [67]. The intensity of the primary peaks, resulting from equation (2.1) furthermore, is governed by the width of each separate slit, *d*, giving a diffraction profile as shown in Figure 2-1.

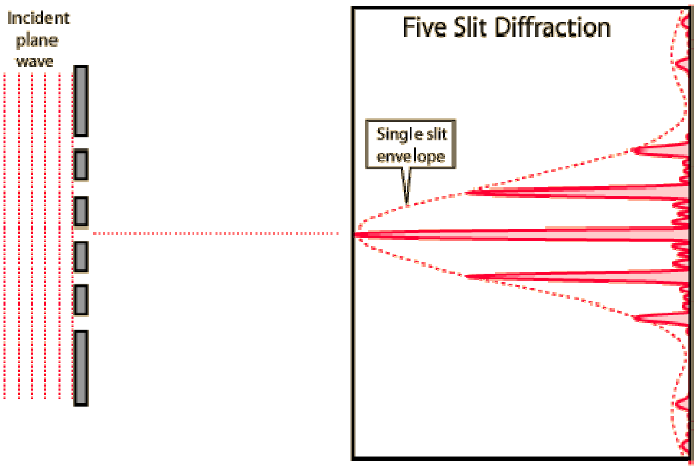

Figure 2-1: Diffraction pattern for a five slit grating

2.2.1 X-ray diffraction

X-ray diffraction for inorganic structures works on the same principle as light diffraction using gratings. Now it is the lattice planes and in particular the electron clouds of the different atoms that cause the X-rays to diffract. Since crystalline materials have, as by definition, ordered structures, with a regular sequence of lattice planes, these planes will now serve as slits for the X-rays. Constructive interference will now occur if the X-ray diffracted from the atom in a certain lattice plane will be in phase with the X-ray diffracted from other planes. This principle was first described by Laue, who however took rows of atoms as the gratings for X-rays. Although this is literally identical to light diffraction, in a 3D crystal this required dealing with six angles (incident and diffracted beam for three lattice parameters), three lattice spacings and three integers, n_x, n_y and n_z for the number of wavelengths in three dimensions. This approach was much simplified by Bragg, who described the diffraction in terms of reflections from crystal lattice planes, which is drawn schematically in Figure 2-2. Treating the diffraction in crystals like this, leads to the well-known Bragg equation. The indices *h, k* and *l*, refer to the Miller indices of the lattice planes [67].

$$n\lambda = 2d_{hkl}\sin\theta_{hkl} \tag{2.3}$$

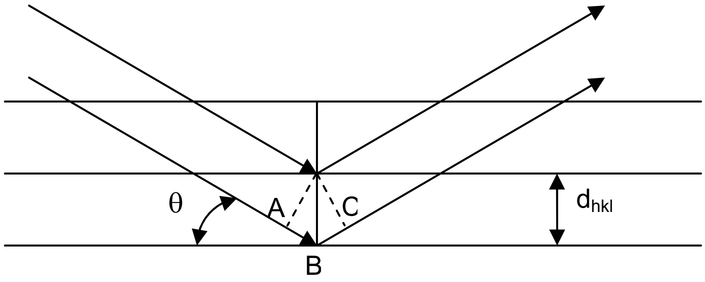

Figure 2-2: Bragg's law, $AB = BC = d_{hkl}\sin\theta$

Using reciprocal space, the following general expression can be derived for the d-spacing and of lattice planes (*hkl*):

$$\boldsymbol{d}^* \bullet \boldsymbol{d}^* = \frac{1}{d_{hkl}^2} = \left(h\boldsymbol{a}^* + k\boldsymbol{b}^* + l\boldsymbol{c}^*\right)\bullet\left(h\boldsymbol{a}^* + k\boldsymbol{b}^* + l\boldsymbol{c}^*\right) \tag{2.4}$$

The superscript * denotes reciprocal vectors. Simple expressions can only be obtained for orthogonal crystal symmetries (cubic, tetragonal and orthorhombic). Because $\boldsymbol{a}^* \bullet \boldsymbol{a}^* = \frac{1}{a^2}$ and due to the orthogonality $a^* \bullet b^* = 0$, etc., equation (2.4) for instance can be rewritten as:

$$\frac{1}{d_{hkl}^2} = \frac{h^2}{a^2} + \frac{k^2}{b^2} + \frac{l^2}{c^2} \tag{2.5}$$

Similarly for the angle between the normals of two lattice planes ($h_1k_1l_1$ *and* $h_2k_2l_2$):

$$\cos\rho = \frac{\boldsymbol{d}^*_{h_1k_1l_1} \bullet \boldsymbol{d}^*_{h_2k_2l_2}}{\left|\boldsymbol{d}^*_{h_1k_1l_1}\right|\left|\boldsymbol{d}^*_{h_2k_2l_2}\right|} \tag{2.6}$$

Again, when substituting $\boldsymbol{d}^*_{hkl}$ with the actual components ($h\boldsymbol{a}^*+k\boldsymbol{b}^*+l\boldsymbol{c}^*$), simple expressions are only obtained for the orthogonal crystal symmetries.

As said earlier, it is mainly the electron cloud around atoms that cause the X-rays to scatter. Therefore, heavier elements are better scatterers for X-rays than the lighter elements. The scattering generally drops with increasing scattering angle, as the interference becomes more destructive between the Z waves, where Z is the atomic number. This effect is stronger for larger ions, hence anions are affected more than cations. This is also the reason, why the intensity in X-ray diffraction patterns drops at high angles. The scattering amplitude for an atom is calculated by summing the contributions of all Z electrons relative to the amplitude of a single electron. This atomic scattering factor, *f*, is normally given as a function of scattering angle (expressed at $\sin\theta/\lambda$).

$$f = \frac{amplitude\ scattered\ by\ atom}{amplitude\ scattered\ by\ a\ single\ electron} \tag{2.7}$$

The scattering in a unit cell is now determined by summing the atomic scattering factors inside the unit cell, taking into account the path and phase difference of the scattered waves, *i.e.* taking into consideration the symmetry of the unit cell. The result of this summation is called the structure factor, F_{hkl}, given by:

$$F_{hkl} = \frac{amplitude\ scattered\ by\ atoms\ in\ the\ unit\ cell}{amplitude\ scattered\ by\ a\ single\ electron} \tag{2.8}$$

F_{hkl} contains information about both the magnitude of the scattering as well as the direction, so it is represented as a vector, in complex format. Now, summing up the scattering contributions of the different atoms can simply be achieved by adding vectors, in mathematical form:

$$F_{hkl} = \sum_{n=0}^{n=N} f_n \exp 2\pi i \left(hu_n + kv_n + lw_n \right) \tag{2.9}$$

where $2\pi(hu_n + kv_n + lw_n)$ is the phase angle of the n^{th} atom with fractional coordinates (u_n, v_n, w_n).

The intensity of diffracted X-rays is now easily calculated from the structure factor by multiplying it by its complex conjugate, F_{hkl}^*. Unfortunately, for centrosymmetric spacegroups this means that the phase information in the structure factor is lost and only the magnitude remains. Still, using equation (2.9), from the obtained intensities, one can determine the atomic positions (u_n, v_n, w_n) for the different elements in the unit cell. The equation is usually expanded to contain such parameters as thermal displacement factors, occupancy, etc., which can all be refined from the intensities of the diffracted X-rays [68].

Broadening of peaks also occurs for X-ray diffraction in a similar way to light diffraction from a grating with a limited number of slits. In small crystallites, only a limited number of lattice planes is available for diffraction and it can be derived that for $\delta\theta$, the deviation from the theoretical angle at which constructive interference would occur, the following relation holds:

$$2\delta\theta = \frac{\lambda}{t\cos\theta} \tag{2.10}$$

In this equation $2\delta\theta$ is usually replaced by β, the width of a diffraction peak at half maximum peak intensity (shown in Figure 2-3), which gives a good approximation for the crystal size t. For polycrystalline materials, a correction factor K is added to give the Scherrer equation:

$$\beta = \frac{K\lambda}{t\cos\theta} \tag{2.11}$$

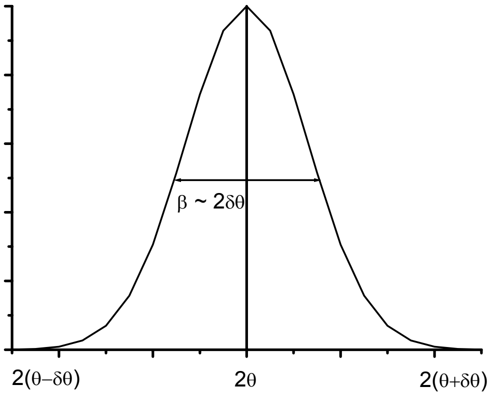

Figure 2-3: Schematic representation of a broadened Bragg peak resulting from crystals with a finite size, with $\beta \approx 2\delta\theta$.

Experimentally, X-ray diffraction patterns on polycrystalline materials are recorded using a fixed wavelength whilst measuring the diffraction angles. This can either be done in reflection or in transmission mode. In this work, the Debye-Scherrer method is used, which has a rod-shaped sample in the centre of the detecting circle. The sample is in fact a glass capillary (diameter ~ 0.5 – 0.7 mm) containing the sample material. The Debye-Scherrer method ensures a relatively good focusing of the diffracted X-rays on the detecting circle, which is an inherent problem for X-ray diffraction on polycrystalline materials [67].

2.2.2 Neutron diffraction

Although X-ray diffraction is a powerful technique, it suffers from some inherent disadvantages. Firstly, little information can be obtained at high diffraction angle, as the destructive interference increases and hence intensity drops. Secondly, the atomic positions and other information of elements with similar atomic number are difficult to determine, as they will diffract X-rays equally strongly. And finally, elements of low atomic number scatter X-rays weakly and especially if they occur in a unit cell together with heavier atoms, their contribution to the X-ray pattern might be negligible and information about these elements can therefore not be obtained. Hydrogen for instance is nearly invisible to X-rays under any circumstances.

This is where neutron diffraction forms a good alternative to X-ray diffraction. Neutrons are uncharged particles and will diffract with the nuclei in the unit cell, rather than with the electron cloud. In fact, as neutrons diffract with the much smaller nuclei, no need for complicated form factors is required, which are used to describe the shape of electron clouds in X-ray diffraction. This is also the reason why the intensity in neutron diffraction does not fall rapidly at high diffraction angle and structural information can still be obtained in this region. Moreover, the neutron scattering length, the neutron diffraction equivalent of the atomic scattering factor, does not increase with atomic number, but rather follows a random dependency as function of atomic number. This means that the diffraction intensity is not predominantly determined by the heavy elements, as it is in X-ray diffraction. In fact, some of the lighter elements have relatively large neutron scattering lengths, making neutron diffraction the ideal tool to determine their positions in crystal structures.

Table 2-1 gives the neutron scattering length of some atoms that are likely to be used in the work described in this thesis. It shows that hydrogen for instance has a negative coherent scattering length of -3.74 fm, which is comparable to the coherent scattering lengths for Ca and Na, so it would contribute well to the diffraction pattern. Unfortunately, hydrogen also has a very large incoherent scattering component (25.27 fm), which causes a large continuous background signal in the diffraction pattern. Therefore it is preferable to use deuterium, D or ^{2}H, which has a large positive neutron scattering length of 6.67 fm, but only a relatively small incoherent scattering component.

Table 2-1: Coherent and incoherent neutron scattering lengths for different elements, adopted from Ref [69].

Atom	Coherent neutron scattering length (fm)	Incoherent neutron scattering length (fm)
H	-3.74	25.27
D	6.67	4.04
^{7}Li	-2.22	-2.49
^{14}N	9.36	2.0
^{23}Na	3.63	3.59
^{40}Ca	4.80	0
Sr	7.02	-
^{139}La	8.24	3.0
Ce	4.84	-
Nd	7.69	-

The experimental setup for neutron diffraction is complete analogous to that for the Debye-Scherrer method in X-ray diffraction. However, since the flux of neutrons from a neutron source is much smaller than the X-ray count from an X-ray generator, the setup needs to be scaled up, to enable one to obtain enough diffraction data within a reasonable time.

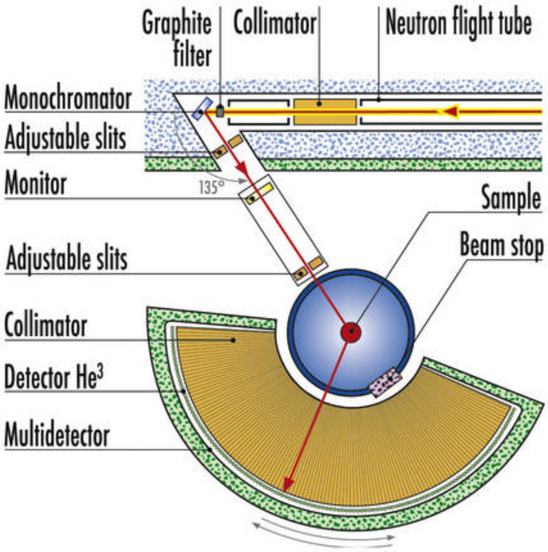

Figure 2-4: Schematic overview of instrument D2B at ILL; this instrument is similar in setup to D1A, which is used in the work presented in this thesis.

2.2.3 Isotopic effect on lattice parameters and thermal expansion

It has been observed that an isotopic effect exists which affects the lattice parameters and the thermal expansion of the crystal lattice. Covington and Montgomery [70] were among the first to experimentally observe this effect in the metal ^{6}Li and ^{7}Li isotopes. The effect is caused by zero-point motion of the atoms, a quantum effect caused by the anharmonicity of the interatomic potential. This zero-point motion causes the atoms in a crystal to vibrate, even at a temperature of absolute zero, because they are slightly displaced from their potential minimum. When the atomic motion is now described in terms of a harmonic oscillator, it follows that its vibration frequency ω is related to the inverse square root of the reduced mass, μ, where k is the spring constant. The reduced mass of a bond between ions A and B is given in equation (2.13). It shows that the reduced mass of isotopes of light elements changes more significantly than that of heavier elements.

$$\omega = \sqrt{\frac{k}{\mu}} \tag{2.12}$$

$$\frac{1}{\mu} = \frac{1}{m_A} + \frac{1}{m_B} \tag{2.13}$$

In a relatively simple approximation using the Debye theory, Ubbelohde [71] showed that for simple ionic crystals (like LiH) the zero-point energy can be calculated using the Debye expression for specific heat, where Θ_D is the Debye temperature, ν_D the Debye frequency, h Planck's constant and k the Boltzmann constant.

$$\Theta_D = \frac{h\nu_D}{k} \tag{2.14}$$

It can further be derived that the number of vibrations between ν + dν is $\frac{9N}{{\nu_D}^3}\nu^2 d\nu$ so for the zero-point energy the next equation holds:

$$E_0 = \frac{9N}{{\nu_D}^3}\int_0^{\nu_D} \frac{h\nu}{2}\nu^2 d\nu = \tfrac{9}{8} nR\Theta_D \tag{2.15}$$

Equation (2.15) shows the dependency of zero-point energy with Θ_D, which is inversely related to the square root of reduced mass again, via ν_D. N is the number of frequencies up to ν_D.

The total energy of the lattice is made up by this zero-point energy and the thermal contribution at T > 0K. The thermal contribution is determined by the specific heat. The Debye theory also shows that the specific heat is inversely related to Θ_D, which means the heat capacity increases for heavier isotopes. So whereas the zero-point energy is higher for the lighter isotopes, the heavier isotopes will have a higher heat capacity and therefore a larger coefficient of thermal expansion, (since the additional energy manifests itself as increased atomic vibrational motion).

Equation (2.16), the Gruneisen relationship, shows how volume expansion, β, relates to the heat capacity C_v, through κ (isotropic compressibility) and γ (the Gruneisen parameter). For T << Θ_D, the following equation (2.17) holds for the specific heat:

$$\beta = 3\alpha = \frac{\gamma\kappa C_v}{3V} \tag{2.16}$$

$$C_V = \frac{\partial U}{\partial T} = \frac{12\pi^4 Nk}{5\Theta_D^3} T^3 \tag{2.17}$$

A similar relation can be derived for the lattice parameter. Anderson et al. [72] showed that the following relation holds at any temperature for the lattice parameter a_0 in LiH:

$$a_0 = A \cdot \mu^{-\frac{1}{2}} + B \tag{2.18}$$

with A and B being different for every temperature. As already discussed, the thermal expansion will be larger for the heavier isotopes and at high temperatures the difference between the lattice parameter of two isotopes will become smaller and smaller.

As this effect is more readily seen for the lighter elements, where the reduced mass changes more significantly with change of isotope, much work has been done on LiH, where both lithium and hydrogen isotopes can be changed [72-74]. More recently, much work is being done on germanium crystals, as this element has a large number of stable isotopes that naturally occur with good abundance [75, 76].

2.3 Thermogravimetric analysis (TGA)

In thermogravimetric analysis (TGA), the weight of a sample is followed, while it is being subjected to a temperature programme. Buoyancy effects, caused by changes in the density of the used gas can be determined by running a correction run in an empty crucible. Its contribution can subsequently be subtracted from the sample's data. Figure 2-5 shows a schematic overview of the Netzsch STA 449 C Jupiter, which was used for the thermal analysis described in this work. This machine is also able to perform differential thermal analysis (DTA), which will be discussed in the next section.

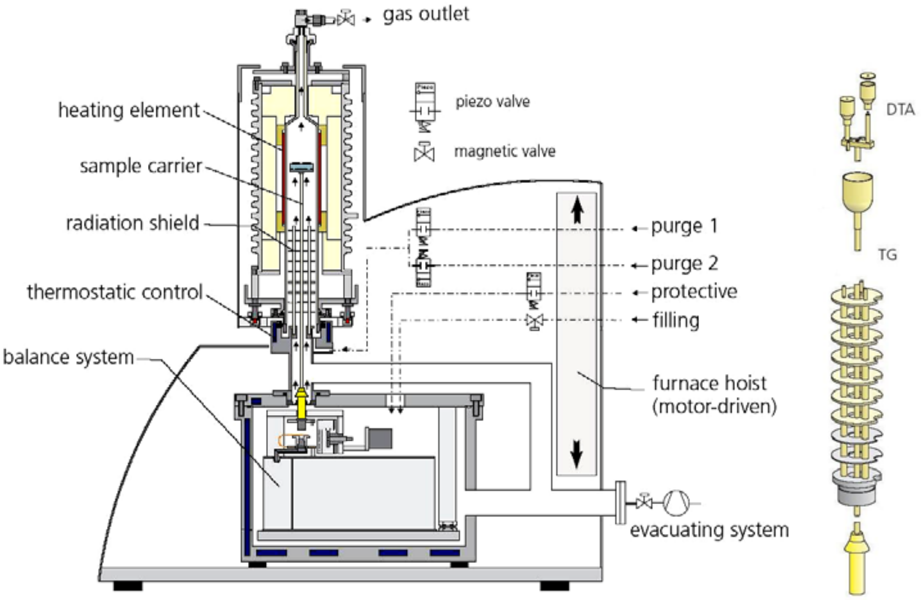

Figure 2-5: Overview of the Netzsch STA 449C Jupiter, with TGA/DTA crucibles

2.4 Differential thermal analysis (DTA)

Differential thermal analysis or DTA measures the temperature difference between a sample and an inert reference material whilst subjected to a heating programme. It is used to measure exothermic and endothermic processes in the sample. Until the occurrence of a thermal event, the temperatures of the sample and the reference (usually an empty crucible/pan) should be zero, but upon a melting, decomposition or other process, the sample temperature will lead or lag that of the reference and a difference can be recorded. To obtain reliable results, the sample and reference are placed close together in a furnace to ensure they are subjected to basically the same temperature programme, with both sample and reference having their own thermocouple. A third thermocouple measures the temperature of the furnace. The output is now generally given as the difference in voltage between the two thermocouples as a function of temperature or time. Quantitative results, like C_p values or thermal events in J/g can only be obtained after calibration of the equipment. Melting of known amounts of a known substance could for instance be used for calibration.

A more direct way for obtaining quantitative results is differential scanning calorimetry (DSC), a technique closely related to DTA. In DSC the sample and reference are again subjected to the same temperature programme, however in two separate compartments with each having its own heating element. The difference in heat that is required to keep sample and reference at the same temperature (or to heat them up at the same heating rate) is now recorded and is a direct measure of the enthalpy change during the different thermal events [22]. Figure 2-6 and Figure 2-7 give a schematic overview of the difference between DTA and DSC.

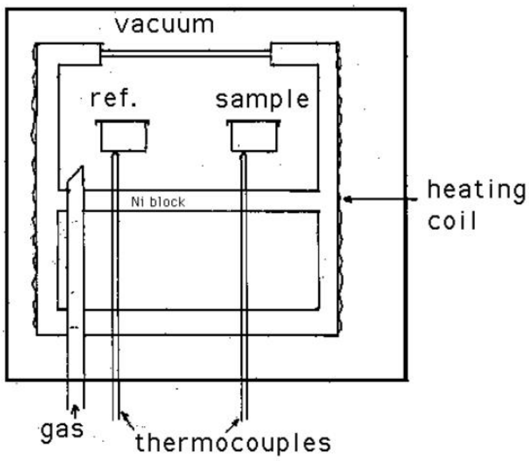

Figure 2-6: Schematic representation of a DTA setup, with sample and reference in one furnace

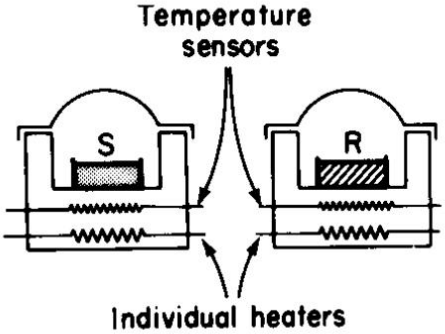

Figure 2-7: Schematic representation of DSC, with sample and reference being heated in separate compartments

2.5 Impedance spectroscopy

Impedance spectroscopy is a powerful tool in the electrochemical analysis of solid-state systems. Rather than measuring relaxation times directly, this technique measures in the frequency domain. This way, processes with a wide range of relaxation times can be measured in parallel within a relatively short time. The technique involves the application of an AC excitation voltage to the studied material at different frequencies and measuring the AC current response. Impedance is a complex vector, so it contains information about both magnitude and direction. The magnitude (amplitude of the AC current) and phase angle (phase shift of the AC current compared to AC voltage) change as a function of the AC frequency, which gives us information about the resistivity and reactivity of the electrochemical system. Different electrical and electrochemical processes have different relaxation times, so each of these processes will become visible at different perturbance frequencies. Different processes can thus be identified by measuring the impedance over a wide range of frequencies. These processes include bulk and grain boundary conduction in electrolytes and electrode processes (charge transfer/double layer capacitance, adsorption/desorption of electrochemical species, etc.).

When a small ac-perturbation, $V_0e^{j\omega t}$, is applied to an electrochemical system, the impedance is given by equation (2.19), where ω is the angular frequency (2πf), j the imaginary unit and φ the phase shift.

$$Z(\omega) = \frac{V(\omega)}{I(\omega)} = \frac{V_0 e^{j\omega t}}{I_0 e^{j(\omega t + \varphi(\omega))}} = \frac{V_0}{I_0}\left(\cos\varphi(\omega) - j\sin\varphi(\omega)\right) \tag{2.19}$$

Because the impedance, $Z(\omega)$ is a complex vector, it is customary to plot the real and imaginary part as a function of each other, with V_0/I_0 being the norm and cos(φ) gving the real and *j*sin(φ) the imaginary part, respectively. Equations (2.20) and (2.21) represent this mathematically, whereas Figure 2-8 explains this graphically. Bode plots, in which the amplitude and phase angle or Z' and Z" are given as a function of frequency are less frequently used, but sometimes offer better insight in relaxation times of overlapping processes.

$$Z_{real} = Z' = |Z|\cos\varphi \tag{2.20}$$

$$Z_{imaginary} = Z" = |Z|\sin\varphi \tag{2.21}$$

$$Z(\omega) = Z' - jZ" \tag{2.22}$$

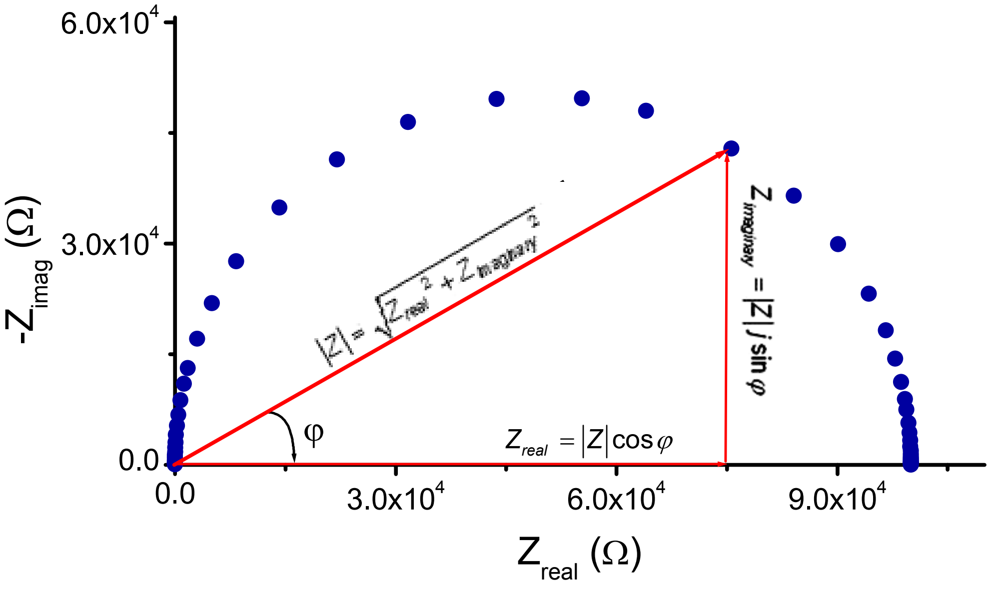

Figure 2-8: Vector representation of complex impedance; real and imaginary parts can be obtained from impedance magnitude and phase angle (φ)

Different representations are sometimes used, like the admittance Y(ω), which is basically the inverse of the impedance:

$$Y(\omega) = \frac{1}{Z(\omega)} = \frac{I_0 e^{j(\omega t + \varphi(\omega))}}{V_0 e^{j\omega t}} = \frac{I_0}{V_0}\left(\cos\varphi(\omega) + j\sin\varphi(\omega)\right) \tag{2.23}$$

For insulating materials, where determining the dielectric properties is important, the permittivity (ε) or modulus (M) representation are commonly used. These are, like impedance and admittance, complex vectors, with the modulus being the inverse of the permittivity [77].

$$\varepsilon = M^{-1} \equiv \frac{Y}{j\omega C_c} = \varepsilon' - j\varepsilon'' \tag{2.24}$$

Analysis of the impedance spectra occurs by fitting the data with a model. The system under consideration is regarded as an electrical circuit, consisting of a number of basic elements (resistances, capacitors, inductances, constant phase elements (CPE's) etc.). The electrical circuit that now represents the real time system can help to understand which processes are playing a dominant role in the impedance behaviour. Figure 2-9 shows an example of such a model. It represents a simplified model for the impedance of a pellet of an ionically conducting material with blocking electrodes. In this model only bulk transport contributes to the impedance. C_{geom} and C_{int} are the geometrical and interfacial capacitances, respectively. The values for R_{ion}, C_{geom} and C_{int} were chosen arbitrarily. Figure 2-10 and Figure 2-11 show the impedance plot and Bode plots for the impedance belonging to this simplified model.

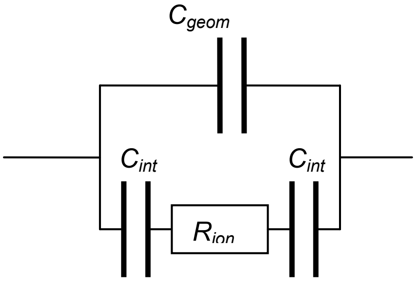

Figure 2-9: Simplified equivalent circuit for the impedance of an ionically conducting pellet with blocking electrodes

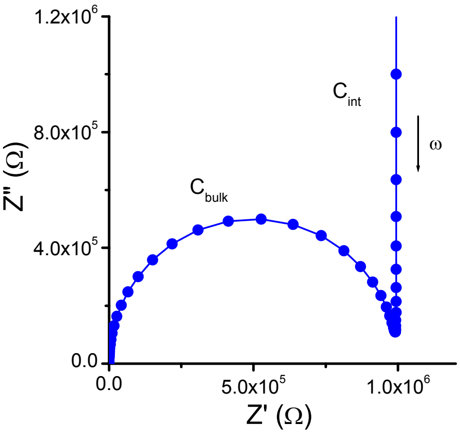

Figure 2-10: Impedance plot for a pellet of an ionically conducting material with blocking electrodes

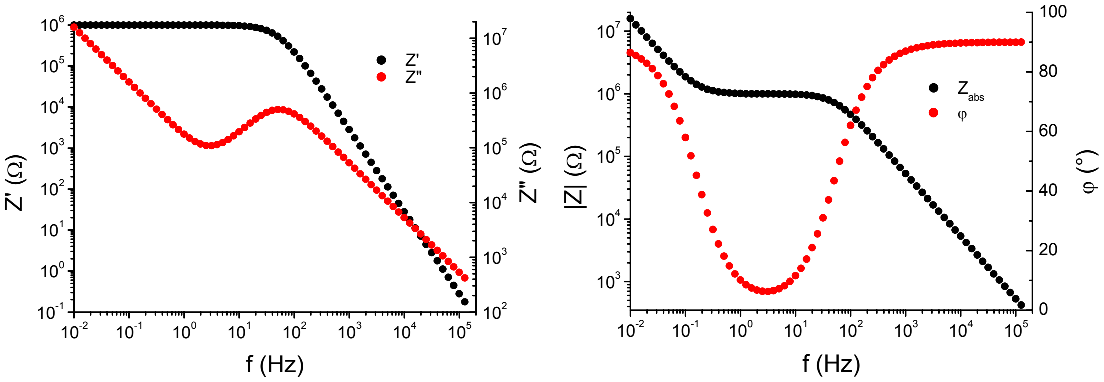

Figure 2-11: Bode plots for the impedance from the equivalent circuit shown in Figure 2-9.

1.1.1. Equivalent circuits

Fitting of the measurement data is performed with the EQUIVCRT software [78]. An equivalent circuit has to be found that fits the measured impedances and can provide a physical explanation of the studied system. For instance, processes that are expected to occur simultaneously or after each other appear typically as parallel or series circuit elements, respectively. Some elements that are typically used in equivalent circuits are listed in Table 2-2, along with their impedances and admittances. *R* is a resistor and *C* is a capacitor. W is a Warburg element, which describes semi-infinite diffusion. *Q* is a constant phase element (CPE) and is in fact a phenomenological element. The exponent α can take any value between -1 and 1. For $\alpha = -1$ the CPE becomes an inductance, for $\alpha = 0$ a resistor, for $\alpha = 0.5$ a Warburg and for $\alpha = 1$ a capacitor. The deviation of α from these ideal values represents the distributed nature of solid state systems (non-homogeneity, rugged surfaces, etc.). Finally, *G* is a Gerischer impedance. The Gerischer element describes an impedance response that originates from an electrochemical process coupled with a chemical side reaction.

Table 2-2: Impedances and admittances of different circuit elements

Element	Description	Impedance	Admittance
L	Inductance	$j\omega L$	$\frac{1}{j\omega L}$
R	Resistance	R	$\frac{1}{R}$
C	Capacitor	$\frac{1}{j\omega C}$	$j\omega C$
W	Warburg	$\frac{Z_0}{\sqrt{j\omega}}$	$Y_0\sqrt{j\omega}$
Q	CPE	$\frac{Z_0}{(j\omega)^\alpha}$	$Y_0(j\omega)^\alpha$
G	Gerischer	$\frac{Z_0}{\sqrt{k+j\omega}}$	$Y_0\sqrt{k+j\omega}$

2.5.1 Conductivity studies using impedance spectroscopy

When conductivity studies are performed, bulk and grain boundary responses are the main features of interest. Therefore they have to be properly extracted from the impedance spectra using equivalent circuits. For ceramics, bulk and grain boundary transport can generally be described by placing a resistor and capacitor in parallel. For such a parallel element, the relaxation time, τ is given by:

$$\tau = \frac{1}{\omega_{summit}} = RC \tag{2.25}$$

Where, ω_{summit} is the summit frequency of the semi circle that is described by the RC parallel element.

When a ceramic is now assumed to behave like a flat plate capacitor (equation(2.26)), it can be seen that the capacitance is determined by its geometry, *A/d* and its dielectric constant, ε_r. Equation (2.26) also includes ε_0, is the permittivity of vacuum, 8.854×10^{-12} F/m. For a typical sintered pellet, *A/d* will be 1 – 10 cm and with a dielectric constant of ~10 it can be seen that bulk or geometric capacitances in the order of 10^{-11} – 10^{-12} F can be expected [79].

$$C = \frac{\varepsilon_r \varepsilon_0 A}{d} \tag{2.26}$$

Now using a simple 'brickwork' model [77, 79] to describe a sintered ceramic it can be derived that for the ratio of bulk and grain boundary capacitances the following equation holds:

$$\frac{C_{geom}}{C_{gb}} = \frac{d_{gb}}{d_{gi}} \tag{2.27}$$

where d_{gi} and d_{gb} describe the length of the grain interior and the grain boundary, respectively, as shown in Figure 2-12. C_{geom} and C_{gb} are the geometric (bulk) and grain boundary capacitances, respectively. It shows that for well sintered ceramics, i.e. when d_{gb}/d_{gi} is small, the grain boundary capacitance increases. Typical grain boundary values lie between 10^{-11} and 10^{-8} F/cm [79].

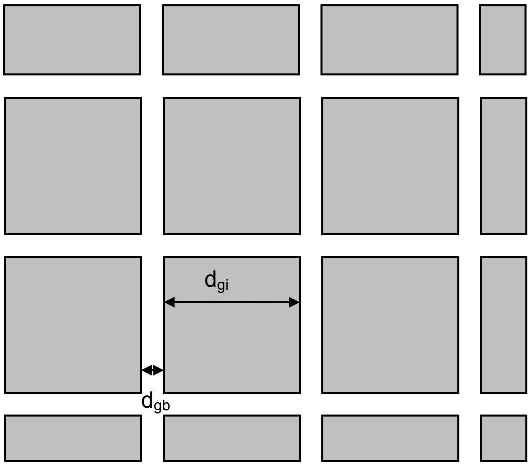

Figure 2-12: Brickwork model for sintered ceramic. Ratio of d_{gi} and d_{gb} determines the order of magnitude of grain boundary capacitance.

Remaining impedance contributions are generally due to electrode processes, like charge transfer/electrochemical double layer, oxidation/reduction processes, adsorption/desorption of electrochemical species, etc. These processes have higher capacitances, with values anywhere between 10^{-6} – 10^{0} F/cm.

3 Calcium and strontium hydride

The chemistry of the alkaline earth metal hydrides (CaH_2, SrH_2 and BaH_2) has not been widely reported so far. Their crystal structure was first studied by Zintl and Harder [80] using X-ray diffraction. They found that the metal ions occupy a distorted hexagonal structure, similar to the $PbCl_2$ structure. The unit cell is however orthorhombic with spacegroup *P n m a*. The positions of the hydride ions were determined later by Bergsma and Loopstra [36] in a neutron diffraction study of CaH_2 and CaD_2. Their findings were basically confirmed and slightly improved in a later study on CaD_2 by Andresen et al. [37]. Recently, two publications discussed the vibrational modes of the hydrides' lattices (phonon modes), which were measured using incoherent inelastic neutron scattering [81] and neutron vibrational spectroscopy [82], respectively. The crystal structure of CaH_2 is shown in Figure 3-1 with Ca-H polyhedra (hydrides coordinating calcium). The calcium ions are nine coordinated by hydrogen (four H1 and five H2).

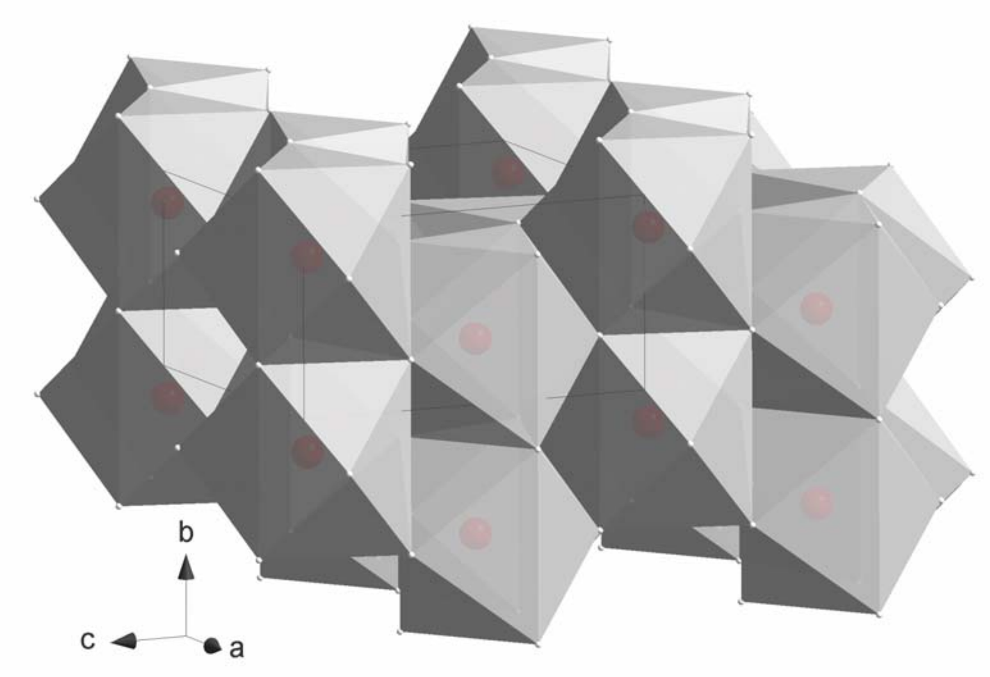

Figure 3-1: CaH_9 polyhedra in the orthorhombic CaH_2 structure. Unit cell edges also shown in dark grey.

Strontium and barium hydride/deuteride have even been less studied. The crystal structure of SrD_2 was studied by Brese et al. [83] using neutron diffraction and Sichla and Jacobs [84] performed single crystal X-ray diffraction on the same compound, but obviously little information on hydrogen positions was obtained in the latter study. The structure of barium hydride/deuteride has only properly been studied by Bronger et al. [85]. It turns out that CaH_2, SrH_2 and BaH_2 are all isostructural.

CaF_2 actually has this same orthorhombic cottunite structure when subjected to 8 GPa pressure [38]. At high pressures, the fluorite structure goes from a cubic packing (ABCABC stacking) into a (distorted) hexagonal one (ABABAB stacking). Figure 3-2 shows how an orthorhombic (cottunite) unit cell can be constructed within a cubic and hexagonal crystal lattice. Upon compression however, the ideal a- and b-axes of the orthorhombic cell contract, whereas the c-axis is elongated. The following relations hold for the ideal orthorhombic lattice parameters in a hexagonal lattice: $a_{orthorhombic} = c_{hexagonal}$, $b_{orthorhombic} = a_{hexagonal}$ and $c_{orthorhombic} = \sqrt{3} \cdot a_{hexagonal}$. It is expected that CaH_2, SrH_2 and BaH_2 adopt the fluorite structure at high temperature [86-88].

This chapter will deal with the structural and thermal properties of calcium and strontium hydride. Structural analysis will involve both X-ray and neutron diffraction studies, whereas the thermal properties are studied using a combination of thermogravimetric techniques and differential thermal analysis.

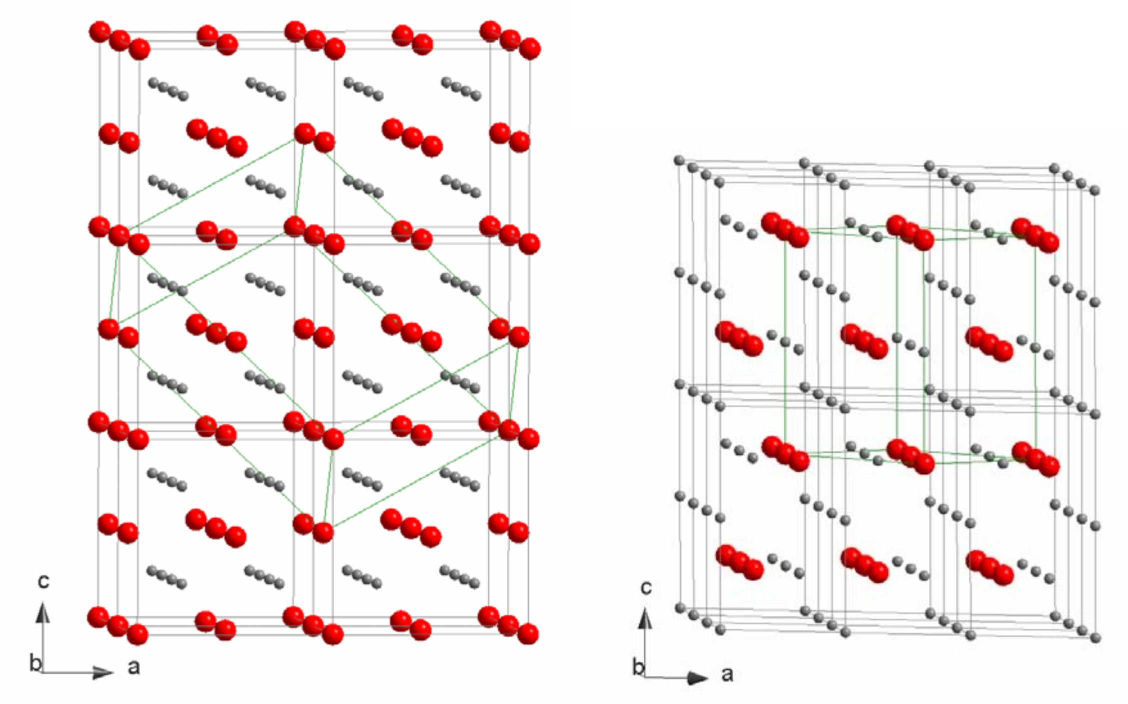

Figure 3-2: Orthorhombic unit cell (in green) within a cubic (left) and hexagonal lattice (right)

3.1 Synthesis

CaH_2 (>97%) was purchased from Fluka. CaD_2 was synthesised by reacting calcium metal (Alfa Aesar, 99.5% metals base) with deuterium gas (Spectra gases, 99.995% chemical purity, 99.7% atom enrichment) at 800°C for 8 hours. Some CaH_2 was also synthesised for diffraction purposes; it was prepared in an identical way CaD_2 was synthesised (using hydrogen gas (BOC, High Purity 99.995%) instead of deuterium gas). SrH_2 and SrD_2 were synthesised similarly, using strontium metal (Sigma Aldrich, 99%) which was reacted at 800°C with hydrogen (BOC, High Purity 99.995%) and deuterium gas, respectively.

3.2 *X-ray diffraction results*

X-ray diffraction patterns were obtained on a STOE transmission diffractometer with Cu Kα1 source, using glass capillaries. Data was recorded in the range $10° < 2\theta < 90°$ with a resolution of 0.02°. Glass capillaries were filled with sample powder inside a glovebox and sealed before the measurements.

3.2.1 CaH_2

The CaH_2 purchased from Fluka was of poor crystallinity and needed a heat treatment at 800°C in pure H_2 atmosphere before a proper diffraction pattern could be obtained. The pattern can be found in Figure 3-3. Diffraction patterns of both as prepared CaH_2 and CaD_2 are shown in Figure 3-4 and Figure 3-5.

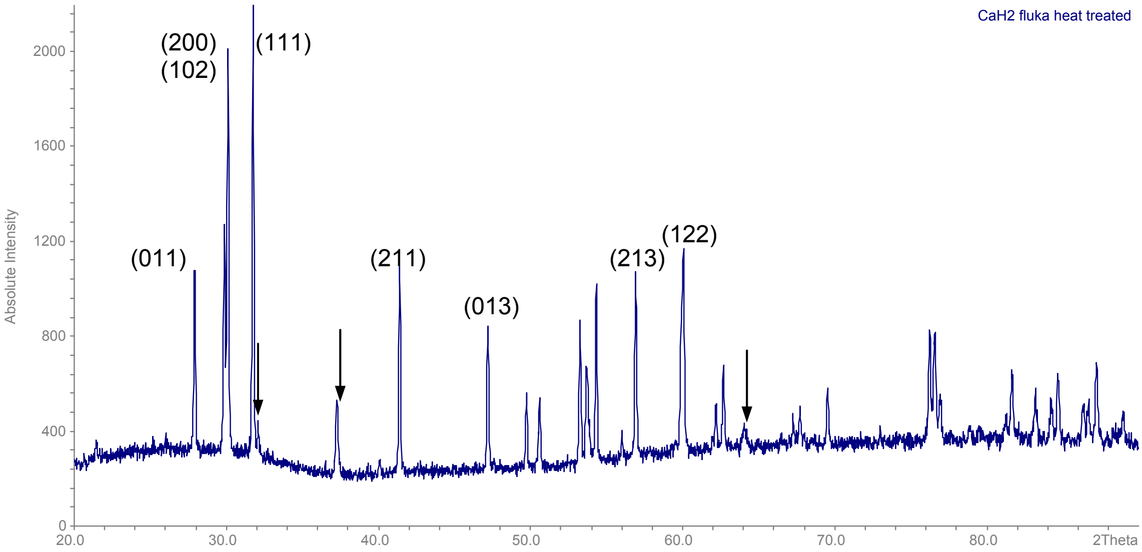

Figure 3-3: X-ray diffraction pattern for CaH_2 (Fluka, >97%). Black arrows show CaO (contamination) peaks

All $CaH(D)_2$ patterns could be indexed and refined using the *P n m a* spacegroup. The as prepared powders additionally contained CaO as a secondary phase (spacegroup *F m 3 m*). Even though care was taken to prevent contamination of the metals and hydride products with air and moisture, it seemed impossible to avoid some oxide formation during the syntheses.

After indexing, the purchased CaH_2 has lattice parameters a = 5.9589(4) Å, b = 3.6002(2) Å and c = 6.8154(5) Å (cell volume 146.21(2) $Å^3$). The as prepared CaH_2 has nearly the same cell volume, i.e. 146.30(16) $Å^3$, with lattice parameters a = 5.960(3) Å, b = 3.602(2) Å and c =

6.814(4) Å. CaD_2 has a slightly smaller cell volume, i.e. 145.4(6) $Å^3$ (a = 5.950(5) Å, b = 3.592(11) Å and c = 6.804(10) Å), for reasons explained in chapter 2, section 2.2.3.

Full pattern refinement, using the Fullprof software, was performed to obtain information about the position of the Ca ions and their thermal displacement. The hydride ion positions were not refined, as they are virtually invisible to X-rays. First of all, it must be noted that the Fullprof refinement resulted in slightly higher values for the as prepared CaH_2 cell volume, i.e. 146.67 $Å^3$. The calcium ions were found to occupy the 4c positions (x, ¼, z). The values for the other refined parameters can be found in Table 3-1. As it can be seen, not all the parameters agree well with each other and some parameters simply do not make any physical sense. The isotropic temperature factor for Ca in CaH_2 is negative for instance. In the case of as prepared CaH_2 it can be explained by the poor quality of the diffraction pattern. There is low signal to noise ratio and the intensities of some peaks are unexpectedly high (see Figure 3-4). Possibly some preferred orientation took place, but mainly X-ray diffraction seems to be nothing more than a technique for quick analysis of these compounds and to obtain the lattice parameters for these phases. The diffraction patterns for the purchased CaH_2 and CaD_2 are of much higher quality, however (Figure 3-5).

Table 3-1: X-ray diffraction refinement results for CaH_2 and CaD_2, in spacegroup *P n m a*

Refinement parameter	CaH_2 (Fluka)	CaH_2 as prepared	CaD_2 as prepared
a (Å)	5.9583 (2)	5.9653 (8)	5.9468 (4)
b (Å)	3.5997 (1)	3.6049 (5)	3.5928 (2)
c (Å)	6.8152 (2)	6.8203 (9)	6.8007 (4)
V ($Å^3$)	146.17 (1)	146.67 (3)	145.30 (1)
Ca, 4c (x,¼,z)			
x	0.2381 (8)	0.2325 (13)	0.253 (11)
z	0.1091 (3)	0.1081 (8)	0.1106 (4)
B ($Å^2$)	-2.71 (5)	-0.9 (2)	0.45 (7)
R_p	5.20	18.6	4.05
R_{wp}	6.46	27.5	5.27
R_{exp}	5.39	9.95	4.30
χ^2	1.43	7.62	1.50

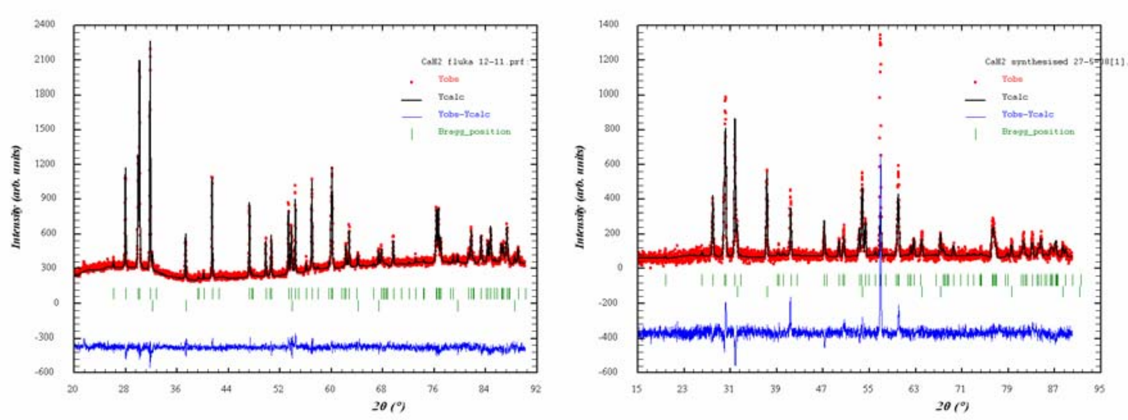

Figure 3-4: X-ray diffraction pattern of purchased (left, Fluka) and synthesised CaH_2 (right). CaO as secondary phase

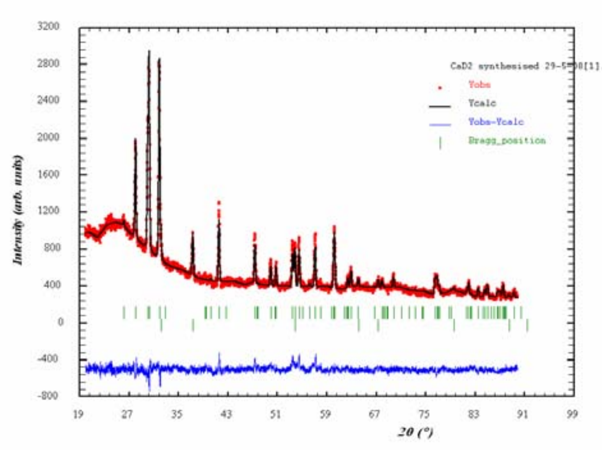

Figure 3-5: X-ray diffraction pattern of CaD_2

3.2.2 SrH_2

The X-ray diffraction pattern for SrH_2 can be found in Figure 3-6. The pattern could be indexed and refined in the *P n m a* spacegroup. A second phase is present, which could be identified as SrO (spacegroup *F m 3 m*). After full pattern fitting using the Fullprof software, the lattice parameters for SrH_2 were found to be a = 6.3888(7) Å, b = 3.8750(4) Å and c = 7.3341(8) Å, which results in a unit cell volume of V = 181.56(3) $Å^3$. The cubic lattice parameter for SrO was found to be 5.1669(4) Å. X-ray diffraction was also performed on SrD_2 and its diffraction pattern can be seen in Figure 3-7. Again, SrO is present as second phase. After refinement, the lattice parameters for SrD_2 are a = 6.3698(4) Å, b = 3.8630(2) Å and c = 7.3119(5) Å, with a resulting unit cell volume of 179.92(2) $Å^3$. Analogous to CaH_2/CaD_2, the lattice parameters for SrD_2 are slightly smaller than those of SrH_2, which is explained by the higher thermal motion of the lighter hydride ions, compared to the deuteride ions. The values for different refinement parameters are given in Table 3-2.

From the R-values given in Table 3-2 it shows again that the diffraction pattern for SrD_2 is of higher quality than that for SrH_2. This is consistent with CaH_2/CaD_2, but it is not understood why this occurs.

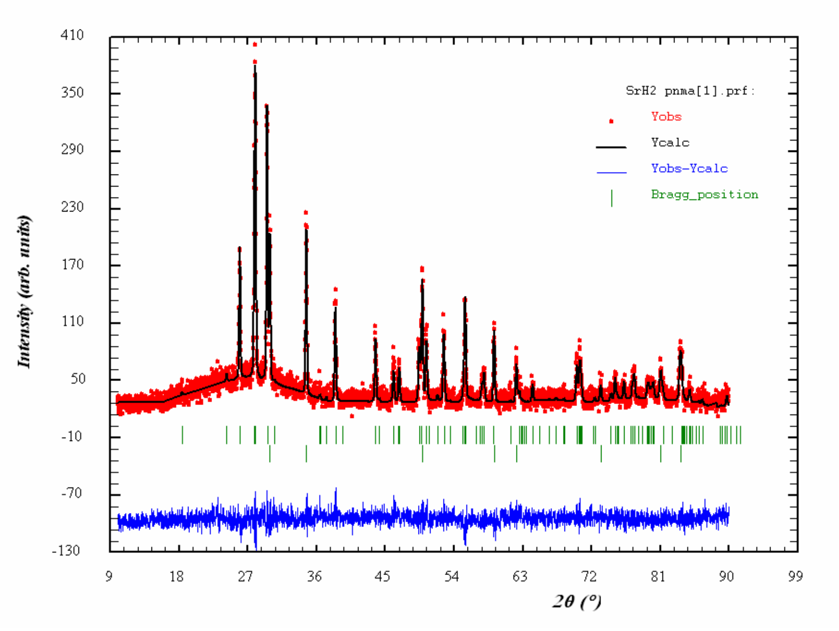

Figure 3-6: X-ray diffraction pattern for SrH_2

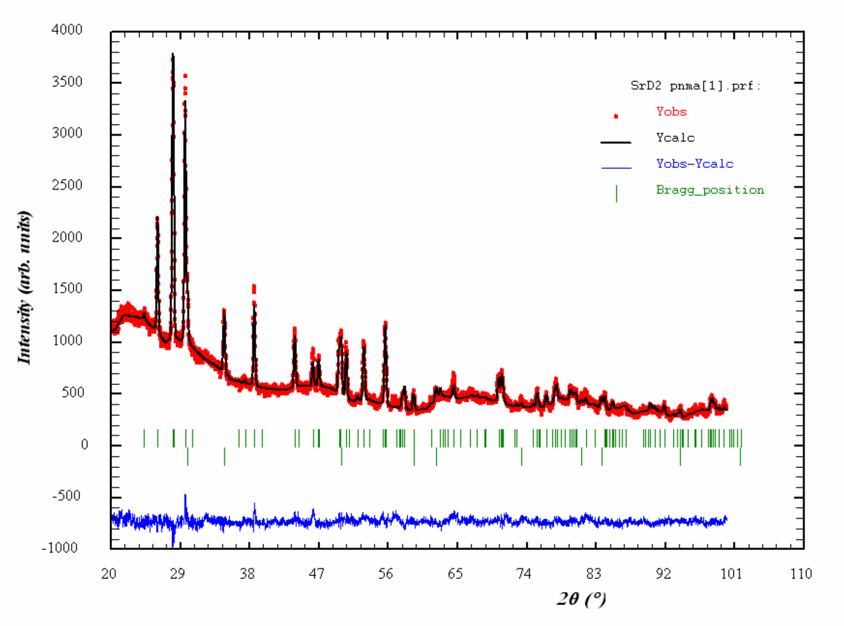

Figure 3-7: X-ray diffraction pattern for SrD_2

Table 3-2: X-ray diffraction refinement results for SrH_2 and SrD_2, in spacegroup *P n m a*

Refinement parameter	SrH_2	SrD_2
a (Å)	6.3888 (7)	6.3698 (4)
b (Å)	3.8750 (4)	3.8630 (2)
c (Å)	7.3341 (8)	7.3119 (5)
V (Å^3)	181.56 (3)	179.92 (2)
Sr, 4c (x,¼,z)		
x	0.2373 (13)	0.2429 (14)
z	0.1095 (6)	0.1096 (3)
B (Å^2)	0.7 (1)	2.22 (9)
R_p	11.7	4.14
R_{wp}	15.2	5.33
R_{exp}	15.63	4.08
χ^2	0.94	1.71

3.3 Neutron diffraction results

Neutron diffraction patterns were recorded on CaD_2 and SrD_2 powder samples. The diffraction experiments were performed on instrument D1A at Institut Laue Langevin (ILL), Grenoble. The neutron wavelength was refined to 1.90946 Å. The powder samples (0.5 – 1.0 g) were loaded into vanadium cans in a glovebox to prevent contamination. An indium wire between the lids and cans operated as a gastight seal to prevent any decomposition during measurements. Neutron diffraction patterns were recorded from $0 < 2\theta < 158°$, with a resolution of 0.05°, measuring for 4 – 5 hours per sample.

3.3.1 CaD_2

The neutron diffraction pattern for CaD_2 is shown in Figure 3-8. The pattern consists of two phases, CaD_2 and CaO. The data could be refined using the Fullprof software with satisfactory R-values. All three ions, Ca, D1 and D2, were set to occupy 4c sites (x, ¼, z), which resulted in good refinement results. Figure 3-8 also shows the calculated pattern and the difference graph of model and data.

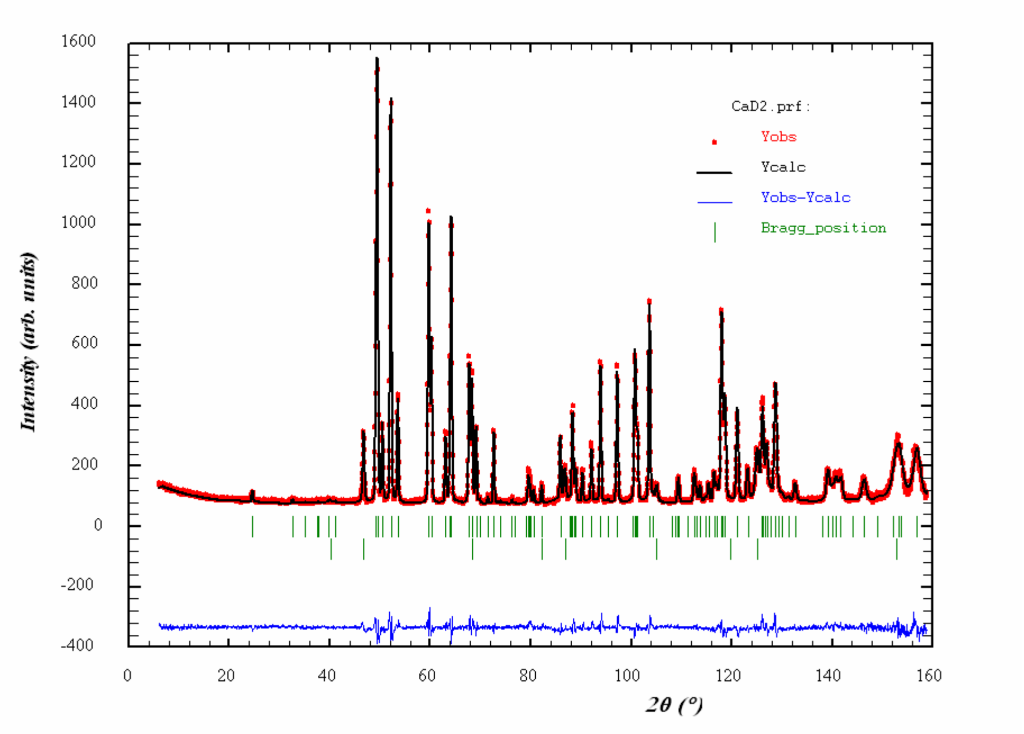

Figure 3-8: Neutron diffraction pattern and refinement of CaD_2 (*P n m a*) with CaO as 2nd phase (*F m 3 m*). Red curve is observed data, black curve is refinement. Blue trail shows residuals after refinement and green ticks show reflections for both phases (lower ticks for CaO)

From the fit in Figure 3-8 it can clearly be seen that the neutron diffraction data is of much higher quality than the X-ray data. This means that more parameters could be refined and more information about the sample could be obtained from the diffraction data. The values of refined parameters are shown in Table 3-3. The refinement results agree well with those found in literature [37, 82]. Also, the occupation for the deuteride ions deviates slightly from stoichiometry (total deuterium content of 1.91 ± 0.02), which can be explained by the reaction temperature of 800°C and considering the pressure – composition isotherms, discussed in chapter 1, section 1.3. Metal (α-phase) and hydride (β-phase) coexist in a two phase system up to near-stoichiometric composition. At this point the hydride exists as a single phase compound but the hydrogen pressure for stoichiometric composition shoots up. The β-phase can pick up more hydrogen at atmospheric pressure at lower temperatures, but kinetically the rate of absorption will be slower at those temperatures. The cooling rate after the hydriding reaction was 1 K/min, but apparently this is still too fast for the product to pick up more hydrogen (deuterium) at lower temperatures. In fact, the deuterium content agrees well with the equilibrium composition for calcium hydride at 800°C reported in literature [86, 89, 90], which is $CaH_{1.90}$. The Ca – CaH_2 phase diagram as composed by Peterson and Fattore is shown in Figure 3-10.

Further it should be noted that the isotropic temperature factor, B, is slightly higher in the case of D2, as compared to D1. Also, the refinement suggests that the hydride (deuteride) vacancies are mainly located on this site. This might be of importance for the conductivity behaviour of CaH_2, but this will be discussed in a later stage. Finally, 13 mol% CaO is present as a second phase, according to the refinement.

Table 3-3: Neutron diffraction refinement results for CaD_2, in spacegroup *P n m a*, λ = 1.90946 Å

Refinement parameter	T = 298K
a (Å)	5.9455 (1)
b (Å)	3.5917 (1)
c (Å)	6.7997 (1)
V ($Å^3$)	145.205 (4)
Ca, 4c (x,¼,z)	
x	0.2407 (3)
z	0.1094 (2)
B ($Å^2$)	0.55 (6)
D1, 4c (x,¼,z)	
x	0.3553 (2)
z	0.4265 (2)
B ($Å^2$)	1.16 (4)
Occ	0.987 (10)
D2, 4c (x,¼,z)	
x	0.9749 (2)
z	0.6756 (2)
B ($Å^2$)	1.33 (5)
Occ	0.926 (10)
R_p	4.24
R_{wp}	5.17
R_{exp}	3.70
χ^2	1.95

When all the atomic positions of the calcium and hydrogen (deuterium) are used in the Diamond software package (Crystal Impact Gpr), a graphical representation of the unit cell can be calculated, which is shown in Figure 3-9. It shows how Ca is 4 coordinated to D1 and 5 coordinated to D2. The CaD_9 polyhedra are prisms of which the faces are the bases of rectangular pyramids. The CaD_9 polyhedra are linked by sharing their pyramidal faces. The software Bond_Str by Rodriguez-Carvajal was used to calculate bond distances and angles. The distances of the Ca-D bonds are shown in Table 3-4.

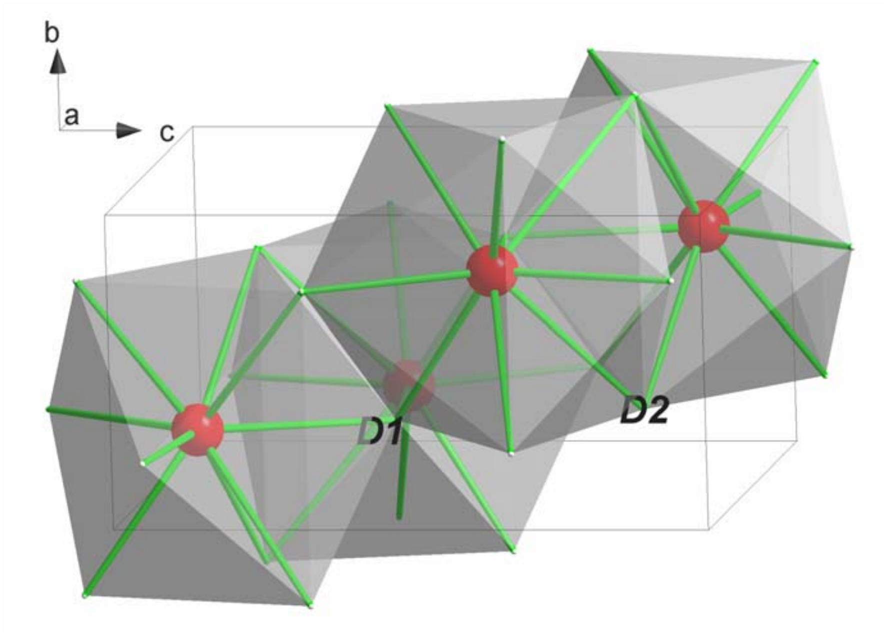

Figure 3-9: Unit cell of CaD_2, which shows the nine coordinated calcium ions in red.

Table 3-4: Ca-D bond distances in CaD_2

N° of bond	Bond type	d (Å)
1	Ca – D1 × 2	2.258 (1)
2	Ca – D1 × 1	2.261 (2)
3	Ca – D1 × 1	2.304 (2)
4	Ca – D2 × 1	2.386 (2)
5	Ca – D2 × 2	2.507(2)
6	Ca – D2 × 2	2.647 (1)

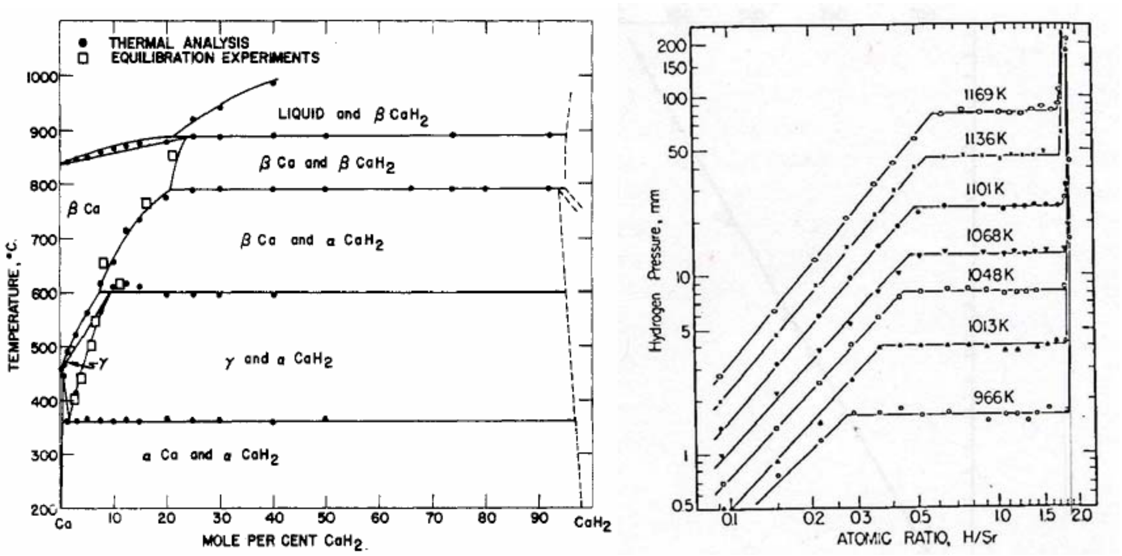

Figure 3-10: Left) Ca – CaH_2 phase diagram as composed by Peterson and Fattore [86]; Right) pH_2 vs. H/Sr composition isotherms as reported by Peterson and Nelson [91]

3.3.2 SrD_2

The neutron diffraction pattern of SrD_2 is shown in Figure 3-11. Again, two phases are present, SrD_2 and SrO, which could be refined using the Fullprof software. Apart from the raw neutron diffraction data, Figure 3-11 also shows the refined calculated pattern and difference plot. The values for the refinement parameters can be found in Table 3-5. Again, analogous to CaD_2, all ions occupy 4c sites (x, ¼, z). On comparison of these refinement parameters with those of CaD_2, it follows that SrD_2/SrH_2 is isostructural with CaD_2/CaH_2 with almost identical atomic parameters. The total deuterium content is 1.90 ± 0.01, which agrees with the equilibrium composition for strontium hydride reported by Peterson et al. [87, 91] at 800°C, i.e $SrH_{1.85}$ – $SrH_{1.95}$. The graph that plots pH_2 vs. H/Sr ratio at different temperatures, as reported by Peterson and Nelson [91], is shown in Figure 3-10. Like CaD_2, there is a slightly lower occupation of deuterium on the D2 site. Also comparable to CaD_2, the isotropic displacement factor, B, for D2 is slightly higher than that for D1. This shows that these differences are not just a modelling uncertainty, but are actually reproducible.

Finally, the refinement suggests that 10 mol% SrO is present as a second phase, which is comparable to the 13 mol% CaO found as a second phase in CaD_2.

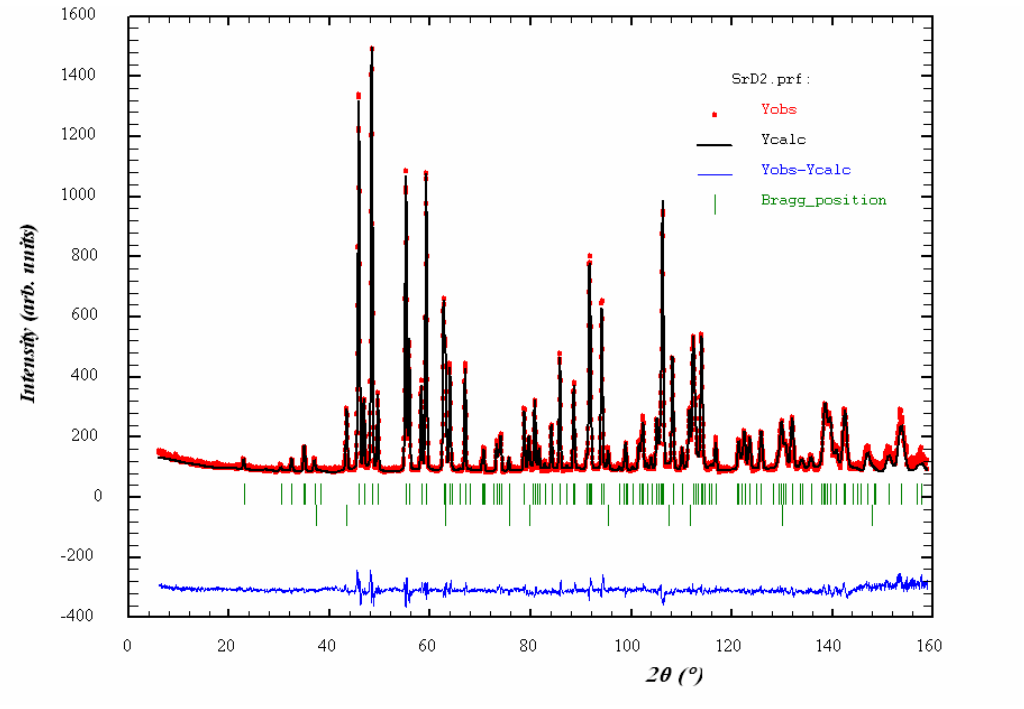

Figure 3-11: Neutron diffraction pattern and refinement of SrD_2 (*P n m a*) with SrO as 2nd phase (*F m 3 m*). Red curve is observed data, black curve is refinement. Blue trail shows residuals after refinement and green ticks show reflections for both phases (lower ticks for SrO)

Table 3-5: Neutron diffraction refinement results for SrD_2, in spacegroup *P n m a*, λ = 1.90946 Å

Refinement parameter	T = 298K
a (Å)	6.3673 (1)
b (Å)	3.8629 (1)
c (Å)	7.3089 (1)
V (Å^3)	179.772 (5)
Sr, 4c (x,¼,z)	
x	0.2399 (3)
z	0.1107 (2)
B (Å^2)	0.45 (4)
D1, 4c (x,¼,z)	
x	0.3542 (3)
z	0.4266 (2)
B (Å^2)	1.14 (5)
Occ	0.965 (7)
D2, 4c (x,¼,z)	
x	0.9742 (3)
z	0.6780 (2)
B (Å^2)	1.51 (5)
Occ	0.937 (6)
R_p	4.92
R_{wp}	5.66
R_{exp}	3.55
χ^2	2.54

Table 3-6 shows the Sr-D bond distances, calculated from the refinement data, by the Bond_Str software.

Table 3-6: Bond distances in SrD_2

N° of bond	Bond type	d (Å)
1	Sr – D1 × 1	2.420 (2)
2	Sr – D1 × 2	2.430 (1)
3	Sr – D1 × 1	2.471 (3)
4	Sr – D2 × 1	2.584 (2)
5	Sr – D2 × 2	2.699 (2)
6	Sr – D2 × 2	2.824 (2)

A second SrD_2 sample was tested at different temperatures, up to 600°C in vacuum. The results are listed in Table 3-7. The occupancy of the deuteride sites was allowed to change freely for the high temperatures, as it is expected that with increasing temperature the partial deuterium pressure in the sample increases and thus some deuterium might be lost from the structure.

Table 3-7: Refinement results for second SrD_2 sample at different temperatures, using spacegroup *P n m a*. Neutron wavelength λ = 1.90896 Å.

Refinement parameter	T = 293K	T = 573K	T = 673K	T = 773K	T = 873K
a (Å)	6.36727 (7)	6.41198 (8)	6.42921 (8)	6.44817 (8)	6.46826 (11)
b (Å)	3.86286 (4)	3.89963 (5)	3.91425 (5)	3.93105 (5)	3.95006 (7)
c (Å)	7.30914 (8)	7.34072 (10)	7.35339 (10)	7.36708 (11)	7.38093 (14)
V (Å^3)	179.775 (3)	183.550 (4)	185.052 (4)	186.741 (4)	188.583 (6)
Sr, 4c (x,¼,z)					
x	0.2399 (2)	0.2405 (2)	0.2405 (2)	0.2404 (2)	0.2408 (3)
z	0.1109 (1)	0.1092 (1)	0.1081 (1)	0.1076 (1)	0.1067 (2)
B (Å^2)	0.96 (3)	1.94 (3)	2.15 (3)	2.51 (4)	3.04 (5)
D1, 4c (x,¼,z)					
x	0.3528 (2)	0.3516 (2)	0.3513 (2)	0.3510 (2)	0.3496 (3)
z	0.4269 (1)	0.4259 (2)	0.4260 (2)	0.4259 (2)	0.4259 (3)
B (Å^2)	1.75 (3)	3.07 (5)	3.42 (5)	4.05 (5)	5.04 (7)
Occ	0.998 (5)	0.988 (5)	0.983 (5)	0.980 (5)	0.983 (6)
D2, 4c (x,¼,z)					
x	0.9738 (2)	0.9751 (3)	0.9762 (3)	0.9770 (3)	0.9780 (4)
z	0.6786 (1)	0.6793 (2)	0.6800 (2)	0.6803 (2)	0.6810 (2)
B (Å^2)	2.31 (3)	3.87 (5)	4.42 (5)	5.09 (6)	6.06 (8)
Occ	0.981 (4)	0.959 (4)	0.959 (4)	0.959 (4)	0.951 (6)
R_p	3.36	3.16	2.96	2.81	2.98
R_{wp}	4.18	3.95	3.58	3.34	3.69
R_{exp}	2.57	2.65	2.61	2.57	2.57
χ^2	2.66	2.22	1.88	1.69	2.06

The deuterium content in this sample is significantly higher than in the previous sample, *i.e.* the composition is now $SrD_{1.98}$. The deuterium flow was kept slightly higher during cooling of the sample, to allow it to absorb more deuterium at lower temperature.

When the lattice parameters and lattice volume are plotted versus temperature, a non-linear increase can be seen. This is shown in Figure 3-12. The largest relative change is seen in the b parameter, which increases with 2.3%. The overall lattice volume expands by 4.9%. These are large changes compared to oxide materials. Yttria stabilised zirconia (YSZ) only shows a 2% volume expansion within the same temperature range [92].

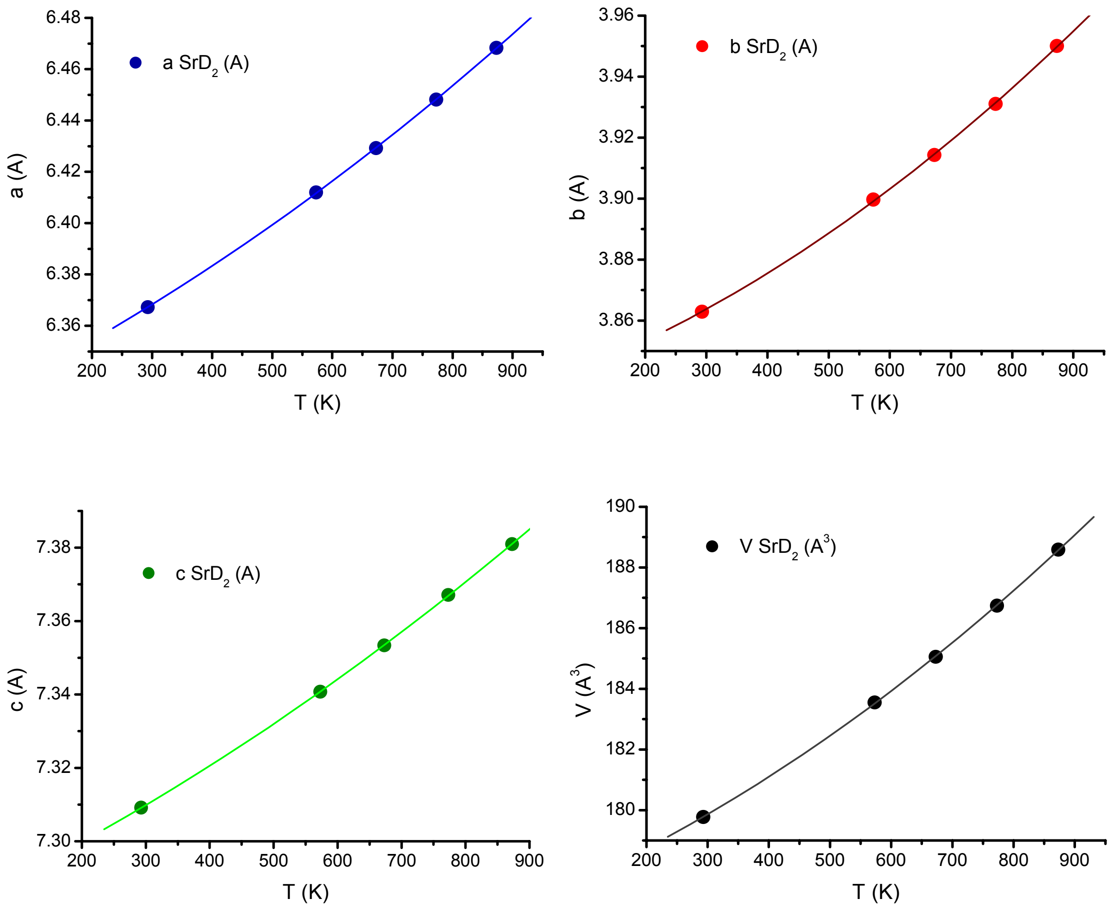

Figure 3-12: Lattice parameters and volume of SrD_2 as function of temperature

The observed non-linear increase in lattice volume may reflect a second order phase transition and could be indicative of short-range disorder, which could explain some of the features observed in the conductivity behaviour for SrH_2 (and CaH_2). This will be discussed in chapter 5. Thermal analysis also shows signs of a secondary phase change (order – disorder) as will be discussed in section 3.4.4. Apart from the non-linear increase in lattice parameters, some trends in the shifting of lattice parameters can be observed as well. In general it seems that the atoms in the unit cell are slowly moving towards the mirror and glide planes (i.e. centres of symmetry). This is probably a very first onset of the transition into the high symmetry cubic (fluorite) structure, which SrD_2 supposedly adopts at 800 – 850°C. Gibson and Irvine related a change in the slope for the isotropic temperature factors vs. temperature to an order – disorder transition in 8 mol% YSZ [92]. The order – disorder transition involved the disappearance of oxygen vacancy – dopant associations at high temperature. The isotropic temperature factors in SrD_2 rather show a non – linear increase (Figure 3-13), much like the lattice parameters/volume. The order – disorder in strontium hydride is not related to any extrinsic defect chemistry and is rather thought to originate from rapid interchange of the two hydride ion sites at high temperatures.

The non-linear behaviour reflects the second-order nature of the phase transition, which is likely to occur over a wide temperature range. Figure 3-14 finally shows the decrease in deuterium content for SrD_2 as a function of temperature.

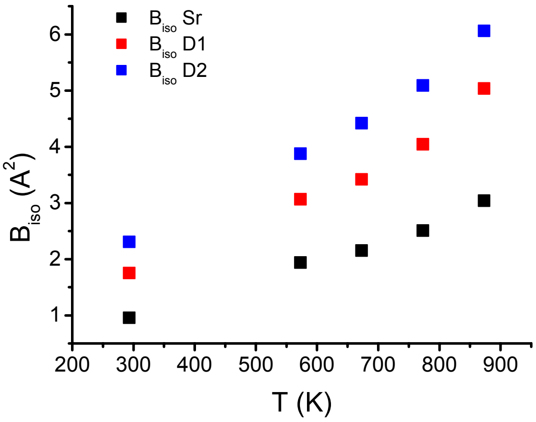

Figure 3-13: Isotropic temperature factors versus temperature

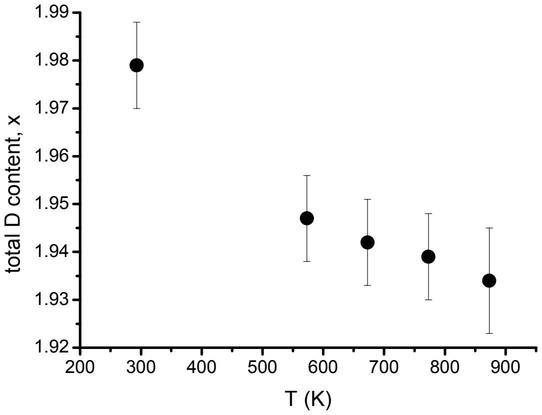

Figure 3-14: Deuterium content in SrD_2 as a function of temperature

It is possible that the small loss of deuterium from the SrD_2 structure contributes to the observed non-linear behaviour of lattice parameters, volume and isotropic temperature factor. The conductivity behaviour however, still supports a (short range) order – disorder transition, as the conductivity tests were performed in hydrogen atmosphere. A loss of hydrogen from the structure is not expected in such an atmosphere and the transition is therefore not caused by changes in stoichiometry.

3.4 Thermal analysis

Thermal properties and the stability of CaH_2 and SrH_2 were analysed using a combination of thermogravimetric analysis (TGA), differential thermal analysis (DTA) and mass spectrometry (MS). All measurements were performed on a Netzsch Jupiter STA449C (TGA/DTA) linked to a Pfeiffer Vacuum Thermostar mass spectrometer.

3.4.1 TGA – CaH_2

Measurements in argon or 5% H_2 in argon all show a similar trend. First there is a small weight loss at low temperature, i.e. 190 – 200°C. This is believed to be a decomposition step of the hydroxides that were formed on the sample's surface during loading into the instrument. The hydroxides decompose into oxides upon releasing water, according to equation (3.1).

$$Ca(OH)_2 \xrightarrow{T\approx 200^{\circ}C} CaO + H_2O \tag{3.1}$$

A large weight loss occurs at higher temperature, which involves the decomposition of the hydride into its elements. In argon, this step occurs at ~675°C, in the mixture of 5% H_2 in argon decomposition occurs at ~760°C. The decomposition temperature of metal hydrides is highly dependent on the partial hydrogen pressure as explained in section 1.3, chapter 1. Thermal analysis could not be performed in pure hydrogen atmosphere, but studies on the calcium – calcium hydride – hydrogen system suggest stability up to 1000°C [89]. Table 3-8 summarises the thermal analysis results obtained for CaH_2.

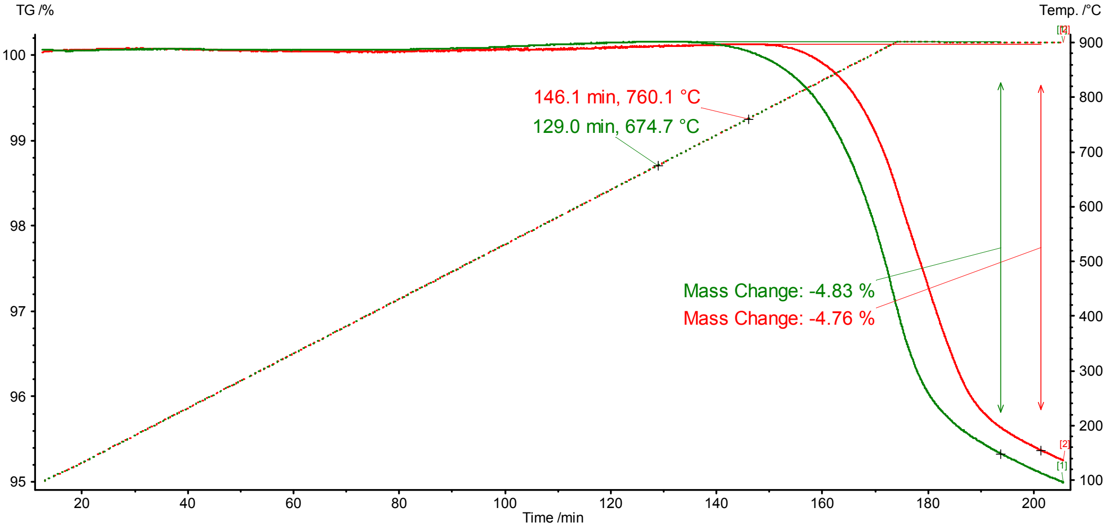

Figure 3-15: TGA for CaH_2 in argon (green) and 5% H_2/argon (red)

Table 3-8: Thermal analysis results for CaH_2

Thermal analysis in argon			
Temperature (°C)	Weight change (wt%)	Ion masses involved	Molecules involved
209	-0.01	m2	H_2
675	-4.83	m2	H_2
Thermal analysis in 5% H_2/argon			
191	-0.04	m2	H_2
760	-4.76	m2	H_2

CaD_2 was also tested for thermal stability under identical conditions to CaH_2. The behaviour in argon was, as expected, very similar to CaH_2, with a slightly lower decomposition temperature, i.e. 635°C. The explanation for this may be found in the slightly higher specific heat of the deuteride as compared to the hydride (chapter 2, section 2.2.3). This means more heat is absorbed by the deuteride and the Ca – D(H) bonds will break at lower temperatures. The weight loss is less than twice the weight loss observed for CaH_2 as the sample contains 13 mol% CaO and the deuterium content is actually less than 2, as explained in the neutron diffraction section in this chapter (actual composition is $CaD_{1.91}$). This results in a weight loss of 7.15 wt%. The behaviour of CaD_2 in 5% H_2 / argon however, is surprisingly different from that of CaH_2. A relatively small weight loss at ~190° is followed by a large weight loss already at ~390°C. The small weight loss probably involves decomposition of surface hydroxides again, although the weight loss is larger than the weight loss observed for CaD_2 in argon at that temperature, i.e. 0.21 wt% instead of 0.04 wt%. Also, two deuterium peaks can be observed in the mass spectrum at this temperature, suggesting that two separate processes occur consecutively. The weight loss at 390°C is 2.63 wt%, which is significantly smaller than the theoretical weight loss of 7.15 wt%, but it is followed by another large weight loss at 765°C, i.e. 4.11 wt%. This thermal behaviour suggests that deuterium – hydrogen exchange is taking place in two steps at intermediate temperatures (i.e. 270°C and 390°C). This process does however not complete and full decomposition of CaH_2/CaD_2 occurs at 765°C, as observed earlier. The fact that deuterium – hydrogen exchange does not complete in 5% H_2 atmosphere can readily be seen in Figure 3-16: the weight loss at 390°C does not reach a plateau and is seamlessly followed by the weight loss at 765°C, belonging to CaH_2 decomposition. Also, the weight loss at 390°C (and 270°C) does not reach 50% of the theoretical weight loss, which would be expected for complete deuterium – hydrogen exchange. Instead, only 2.77 wt% is lost, as opposed to $\frac{7.15wt\%}{2}$ = 3.57 wt%. To get a clearer picture and see the process of deuterium – hydrogen exchange completed before CaH_2 decomposition, this test was repeated in a richer hydrogen atmosphere, i.e. a mixture of 35% H_2 and 65% argon. The resulting TGA graph can be seen in Figure 3-17. Now the weight of the sample reaches a plateau, after a loss of 3.34 wt% at 375°C. Together with the smaller loss at 275°C, this comes to 3.50 wt%, which is very close to half the theoretical weight loss, i.e. 3.57 wt%. In this atmosphere, the decomposition of CaH_2 is shifted to higher temperatures and only starts at ~805°C. Only partial decomposition can be observed, seeing from the weight loss of only 0.24 wt%. This suggests that after losing 0.12 units of H in $CaH_{1.90}$, the resulting compound $CaH_{1.78}$ is stable up to 900°C (at least kinetically). Figure 3-18 finally shows the ion current of mass 3 that was recorded during the TGA of CaD_2 in 35% H_2. It clearly shows a large peak at the main weight loss, meaning that the compound loses deuterium to form HD molecules (resulting from deuterium ions recombining with hydrogen from the atmosphere). The TGA results for CaD_2 in argon, 5%/95 % H_2/argon and 35%/65% H_2/argon are summarised in Table 3-9.

The observed isotope exchange can at least partly be attributed to surface exchange, as the tested material was a powder and surface areas should be high in this case. The exchange, which already starts at temperatures below 400°C, is however very quick and completed within a 300°C temperature range in the case of 35% H_2 atmosphere. As isotope exchange is usually a statistical process, which takes long times at high temperatures, it is believed that CaH_2/CaD_2 acts as a catalyst for this process. The exchanges rates observed here are unusually high and might have large implications in terms of membrane applications.

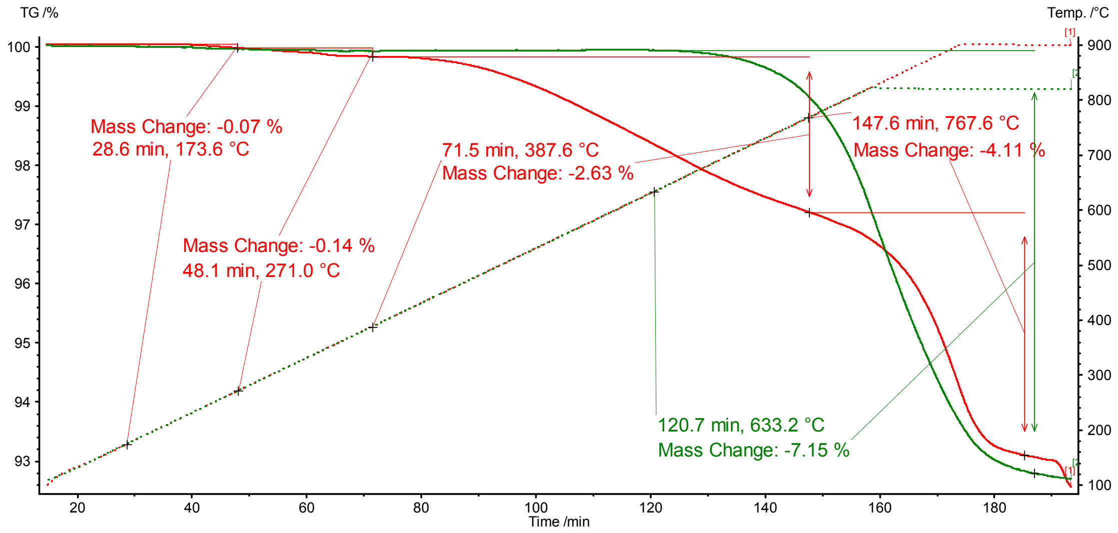

Figure 3-16: TGA for CaD_2 in argon (green) and 5% H_2/argon (red)

Table 3-9: TGA results for CaD_2

Thermal analysis in argon			
Temperature (°C)	Weight change (wt%)	Ion mass involved	Gas involved
197	-0.07	m4	D_2
637	-7.30	m4	D_2
Thermal analysis in 5% H_2 – 95% argon			
189	-0.07	m3	HD
271	-0.14	m3	HD
388	-2.63	m3	HD
768	-4.11	m3	HD $(H_2)^a$
Thermal analysis in 35% H_2 – 65% argon			
186	-0.11	m3	HD
276	-0.16	m3	HD
375	-3.34	m3	HD
807	-0.24	-	- $(H_2)^a$

[a]) No significant mass 2 peaks could be observed, due to the high background level in 5% and 35 % H_2 atmospheres.

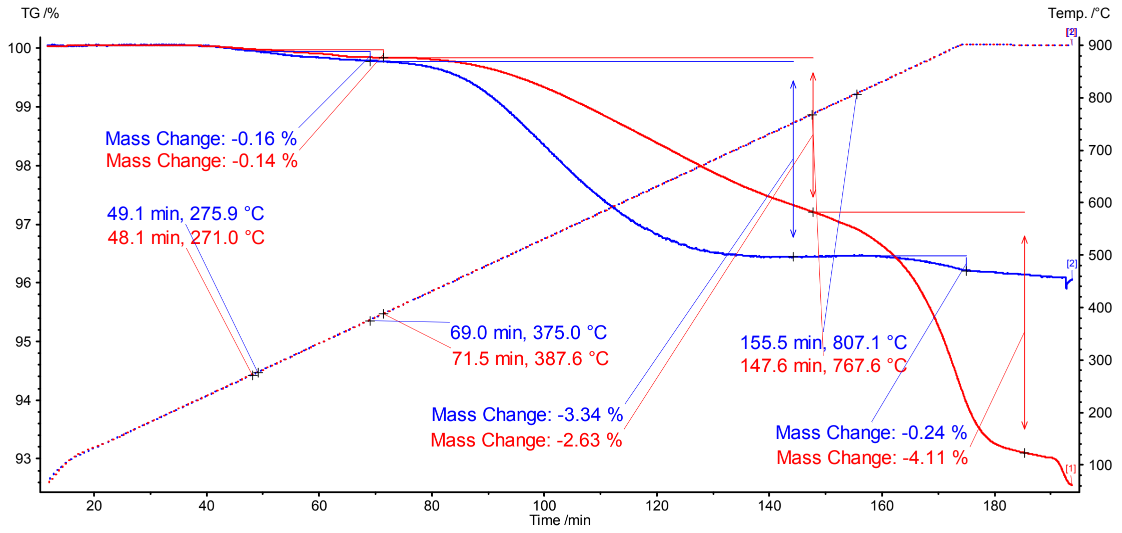

Figure 3-17: TGA for CaD_2 in 5% H_2/argon (red) and 35% H_2/argon (blue)

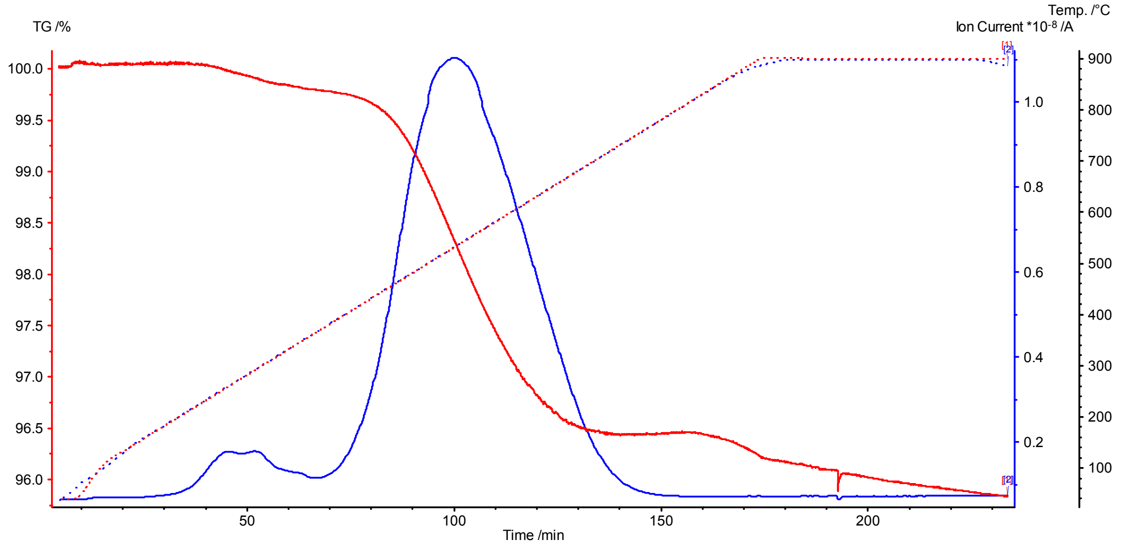

Figure 3-18: TGA for CaD_2 in 35% H_2/argon showing ion current for mass 3 (HD)

3.4.2 DTA – CaH_2

The differential thermal analysis graph for CaH_2 is harder to interpret. It is shown in Figure 3-19. The slopes of the curves change at 469°C and 536°C in 5% H_2/argon and argon, respectively. This change in slope could be caused by a second order phase change which involves disordering of the hydride ions. This change will be discussed in more detail after showing the conductivity results for CaH_2. Fast exchange with atmospheric hydrogen seems to affect this change, causing the change in temperature found for 5% H_2 atmosphere. Comparison with the

DTA data for CaD_2 (discussed below) however, suggests that the transition temperature of 469°C in 5% H_2 might be incorrect.

An endothermic process can be observed around 780 – 790°C. The temperature range agrees well with the orthorhombic to cubic phase transformation, as mentioned by Peterson and Fattore [86]. This transition was initially determined for BaH_2 at 550°C, both crystallographically and using DTA [88], but could only be found using thermal analysis in the case of CaH_2. This phase transformation should however not be observed for CaH_2 in argon, as it has already decomposed at 675°C. Even in 5% H_2 atmosphere the internal partial hydrogen pressure is probably too high for this transition to be observed. It is therefore more likely that this process is simply a reaction of calcium metal, originating from the decomposition reaction, with the alumina crucible.

The DTAs for CaD_2 have been recorded in three different atmospheres: argon, 5% H_2 in argon and 35% H_2 in argon. The DTA for CaD_2 in argon looks similar to that of CaH_2 in argon. CaD_2 in 5% H_2 looks slightly different from its hydrided counterpart. The clear change in slope which was observed for CaH_2 at 469°C cannot be observed at that temperature and seems to have shifted to much higher temperature, i.e. 589°C. Furthermore, the temperature at which this change in slope is observed seems to be dependent on the partial hydrogen pressure of the atmosphere: with increasing pH_2 an increase in temperature from 560°C to 628°C can be seen. The difference in the DTAs for CaH_2 and CaD_2 in 5% H_2 is surprising, because CaD_2 undergoes isotope exchange in hydrogen containing atmospheres, which should result in nearly identical DTAs above ~400°C. All DTA results are consistent however, when it is assumed that the DTA for CaH_2 in 5% H_2 is slightly out of order.

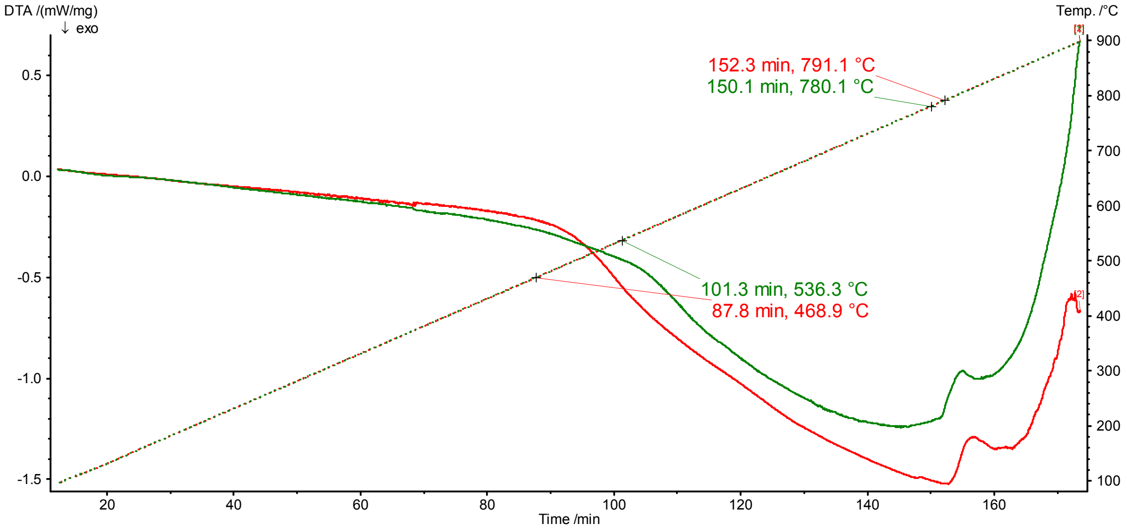

Figure 3-19: DTA for CaH_2 in argon (green) and 5% H_2/argon (red)

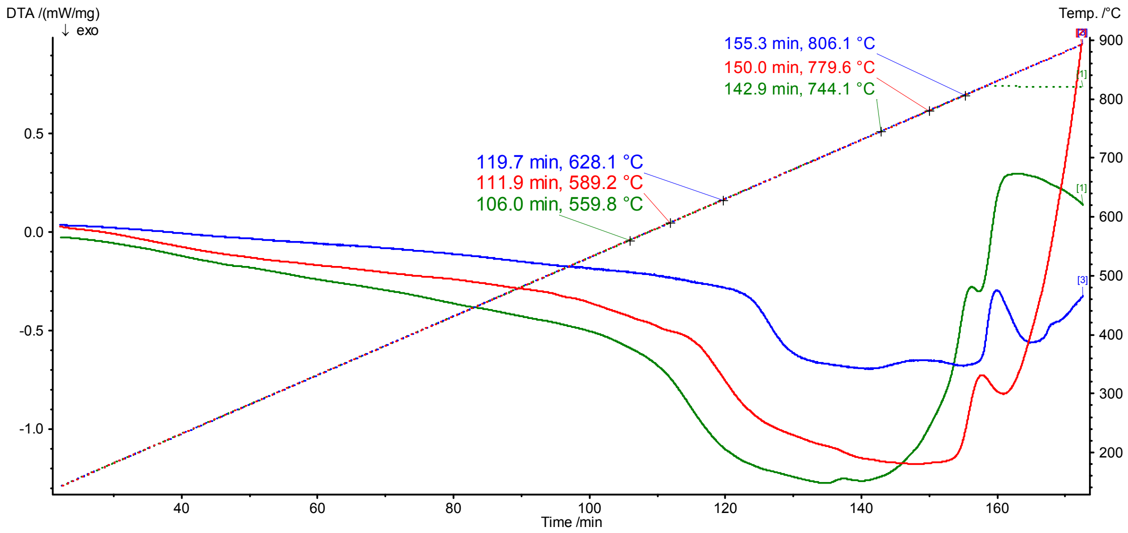

Figure 3-20: DTA for CaD_2 in argon (green), 5% H_2/argon (red) and 35% H_2/argon (blue)

3.4.3 TGA – SrH_2

The TGA for SrH_2 in argon and 5% H_2/argon is shown in Figure 3-21. The behaviour is very similar to CaH_2. A small weight loss, due to decomposition of $Sr(OH)_2$ into SrO, can be observed at ~230°C. This is followed by a large weight loss at ~660°C or ~785°C for argon and 5% H_2 atmosphere, respectively. The second weight loss can furthermore be separated into two stages: first SrH_2 decomposes into strontium metal and hydrogen and subsequently strontium metal starts evaporating. Thus the weight loss seems much larger than that observed for CaH_2. The weight loss due to SrH_2 decomposition amounts to 2.01 – 2.12 wt%, which suggests the presence of 5 – 10 mol% SrO. This agrees with neutron diffraction results.

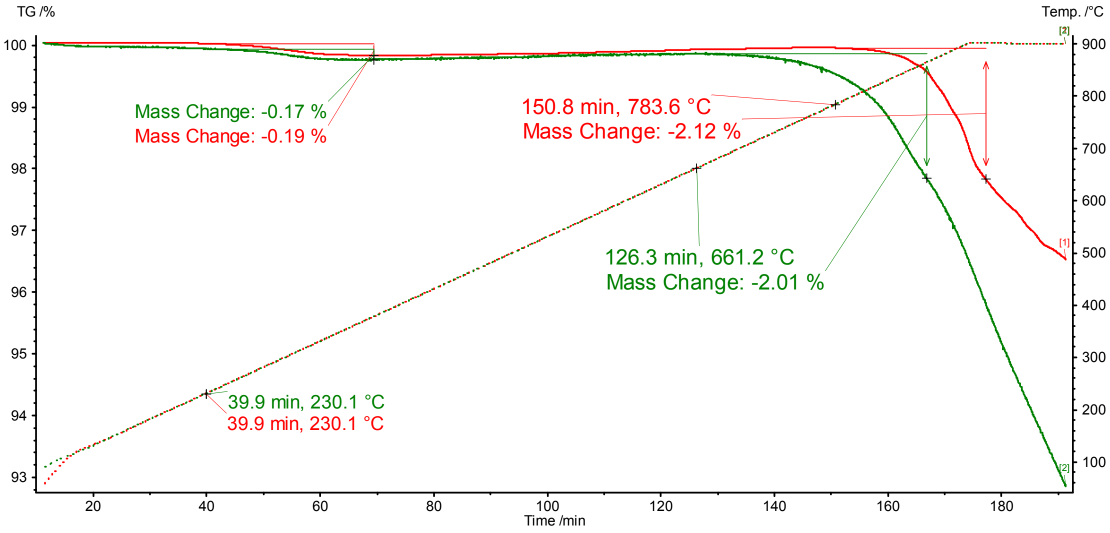

Figure 3-21: TGA for SrH_2 in argon (green) and 5% H_2/argon (red)

Table 3-10: TGA results for SrH_2

Temperature (°C)	Weight change (wt%)	Ion masses involved	Molecules involved
Thermal analysis in argon			
230	-0.17	m2	H_2
661	-2.01	m2	H_2
Thermal analysis in 5% H_2/argon			
230	-0.19	m2	H_2
784	-2.12	m2	H_2

SrD_2 was also thermally analysed. Its TGA in argon and 5% H_2/argon can be seen in Figure 3-22. Analogous to CaH_2/CaD_2 the behaviour in argon is similar for SrH_2 and SrD_2. The large weight loss occurs at only slightly lower temperature: ~653°C as compared to 661°C for SrH_2. The total weight loss amounts to 3.95 wt%, which is very close to twice the weight loss observed for SrH_2, i.e. 2.01 wt%. It also agrees well with the calculated weight loss for a sample containing 10 mol% SrO and a deuterium stoichiometry of 1.91.

Also analogous to CaD_2, in 5% H_2 atmosphere the total weight loss occurs in two major steps. A smaller weight loss at 170°C (0.35 wt%), which again seems to consist of two separate processes, is followed by a significant weight loss at ~330°C (1.44 wt%). Another large weight loss of 2.32 wt% occurs at 753°C. This behaviour is very similar to CaD_2 in a 5% H_2 atmosphere, which is expected as the materials are chemical analogues. A deuterium – hydrogen exchange takes place in two steps at 260°C and 330°C, followed by decomposition of the thus formed SrH_2 at 753°C. These weight losses add up to a total loss of 3.98 wt%, which is in excellent agreement with the weight loss observed for SrD_2 in argon atmosphere. The final decomposition temperature of 753°C is lower than the one observed for pure SrH_2 in 5% H_2 atmosphere, which can be explained by the presence of some residual SrD_2 which decomposes at slightly lower temperature. Also, the TGA run on this particular sample was quite noisy making accurate estimates of decomposition temperatures harder. Unlike CaD_2, the deuterium – hydrogen exchange seems to reach a plateau before decomposing completely at ~750°C. The weight loss due to this exchange is however slightly lower than the theoretical weight loss for this process, i.e. $\frac{3.95wt\%}{2} = 1.98wt\%$.

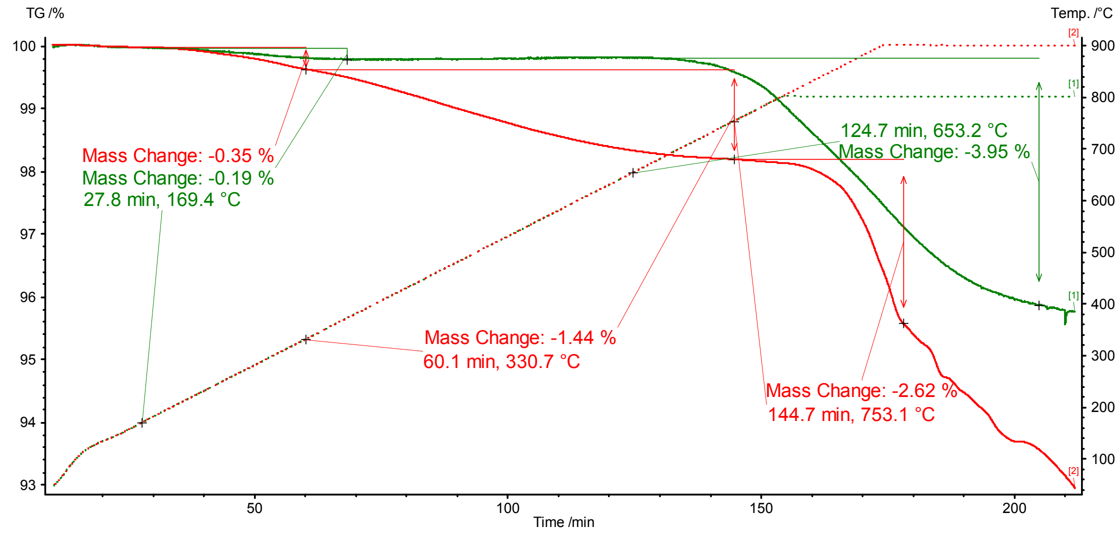

Figure 3-22: TGA for SrD_2 in argon (green) and 5% H_2/argon (red)

In order to see whether complete exchange could be observed, this sample was also tested in a richer hydrogen atmosphere (i.e. 35% H_2 in argon). The results can be seen in Figure 3-23, where SrD_2 in both 5% H_2 and 35% H_2 atmosphere is plotted. It shows that in 35% H_2 the plateau for deuterium – hydrogen exchange is reached more quickly, but that the weight change is almost identical with 5% H_2. Finally, only a small weight loss of 0.26 wt% occurs due to decomposition of SrH_2 at 797°C, showing again that decomposition is strongly dependent on partial hydrogen pressure. Mass spectroscopy (Figure 3-24) further reveals that the main decomposition product in hydrogen atmosphere is HD gas, which forms by combination of deuterium and hydrogen ions. Table 3-11 summarises all TGA results for SrD_2 in different atmospheres.

Table 3-11: TGA results for SrD_2

Thermal analysis in argon			
Temperature (°C)	Weight change (wt%)	Ion mass involved	Molecule involved
169	-0.19	m4	D_2
653	-3.95	m4	D_2
Thermal analysis in 5% H_2 – 95% argon			
169	-0.13	m3	HD
262	-0.22	m3	HD
331	-1.44	m3	HD
753	-2.32	m3	HD
Thermal analysis in 35% H_2 – 65% argon			
169	-0.17	m3	HD
253	-0.40	m3	HD
325	-1.33	m3	HD
797	-0.26	m3	HD

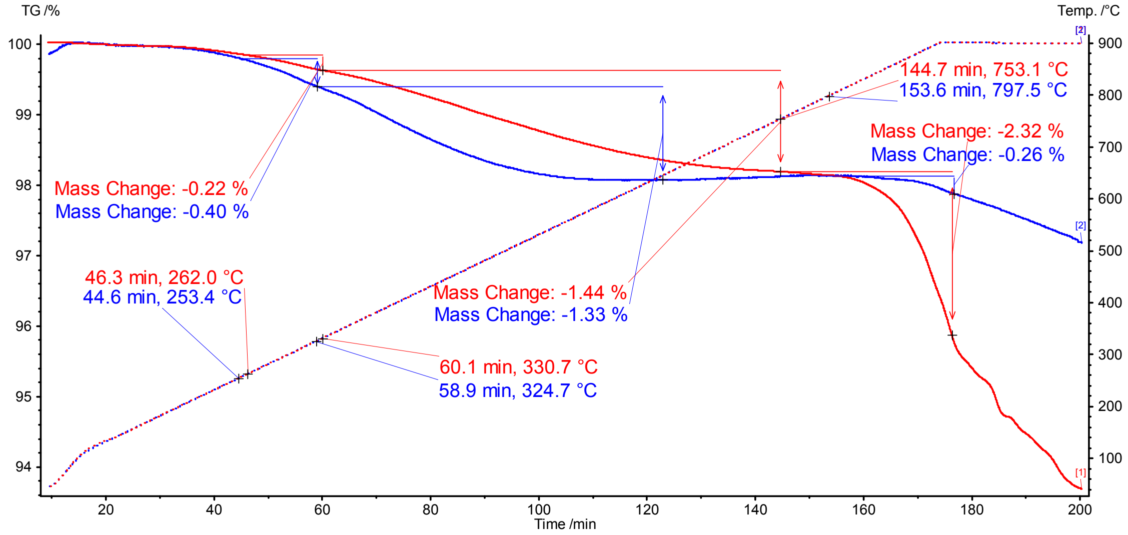

Figure 3-23: TGA for SrD_2 in 5% H_2/argon (red) and 35% H_2/argon (blue)

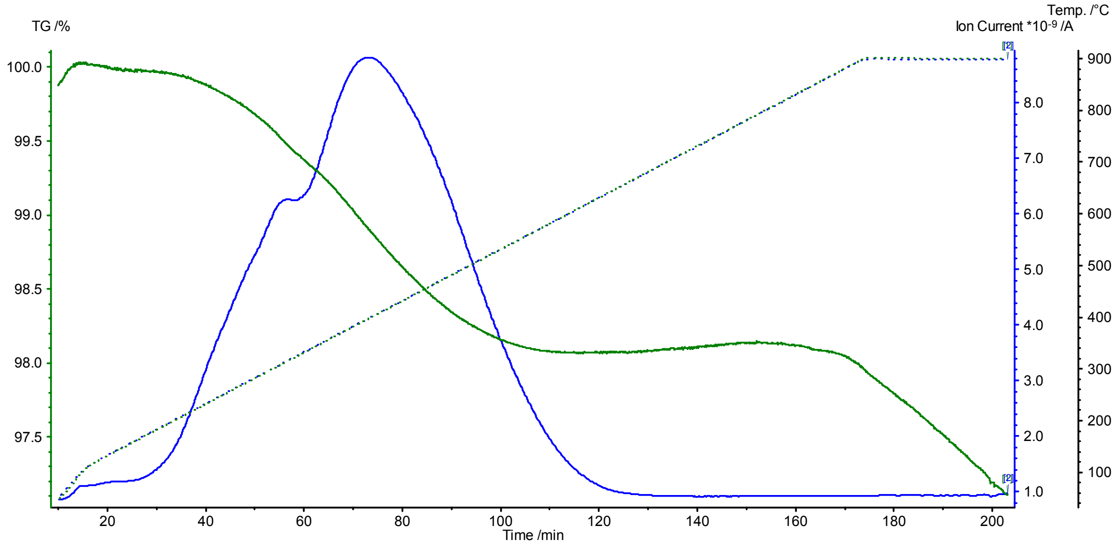

Figure 3-24: TGA and ion mass 3 for SrD_2 in 35% H_2/argon

3.4.4 DTA – SrH_2

The differential thermal analysis of SrH_2 is harder to interpret than its TGA. Several significant changes in slope can be observed, both in argon and 5% H_2 atmosphere, but it is hard to connect them to chemical or physical processes in the materials. Peterson and Colburn suggest a phase change at high temperature, i.e. 800 – 850°C [87]. A peak is visible at ~800°C for both atmospheres, but as this temperatures is beyond the decomposition temperature of SrH_2 in those atmospheres, this probably involves the evaporation of strontium metal, which melts at 777°C. Alternatively, strontium metal might react with the alumina crucible at this temperature. It is further thought that some order – disorder transition might take place in the orthorhombic structure, which could account for some of the more gentle changes in the slopes. The DTA graphs for SrH_2 are shown in Figure 3-25.

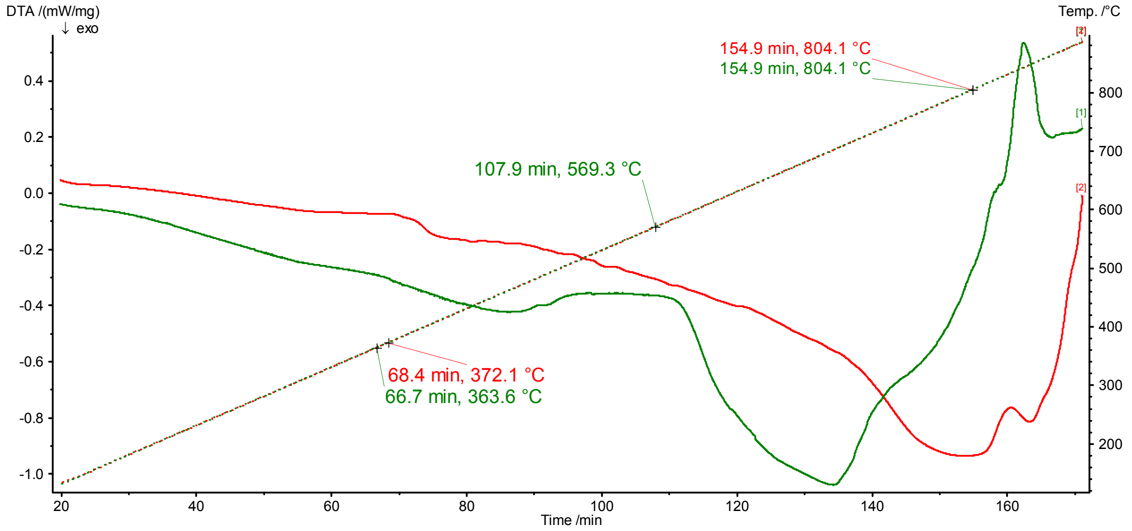

Figure 3-25: DTA for SrH_2 in argon (green) and 5% H_2/argon (red)

Similar DTAs were obtained for SrD_2, shown in Figure 3-26. The DTAs for three different atmospheres are shown: argon, 5% H_2/argon and 35% H_2/argon. It can be seen that the DTA appears flatter when the atmosphere becomes richer in hydrogen, or alternatively when the hydrogen partial pressure increases. Unlike the DTAs obtained for SrH_2, some of the temperatures at which the slopes change agree well with observed changes in conductivity behaviour as explained in chapter 5. It is assumed that these changes are due to an order – disorder transition and the temperatures at which they occur actually show an interesting trend as a function of pH_2. The onset of the order – disorder process (around 330°C) is shifted to lower temperatures for higher pH_2, whereas the completion (~600°C) is shifted to higher temperatures. The onset temperatures in the hydrogen containing atmospheres are also nearly identical to the temperatures at which the second step of deuterium – hydrogen exchange takes place. The change in slope is however reproducible in argon atmosphere (no isotope exchange possible), so it must at least partly relate to a transition that does not involve isotope exchange. An event is also observed for SrH_2 in 5% H_2 atmosphere at slightly higher temperature, i.e. 370°C, confirming that isotope exchange is not the only contributor, if at all. The peaks at higher temperature (~800°C) are probably due to strontium metal evaporation or reaction with the alumina crucible, as discussed before. Melting/reaction however, does not occur until SrD_2/SrH_2 has decomposed, hence the increase in temperature when the pH_2 is increased.

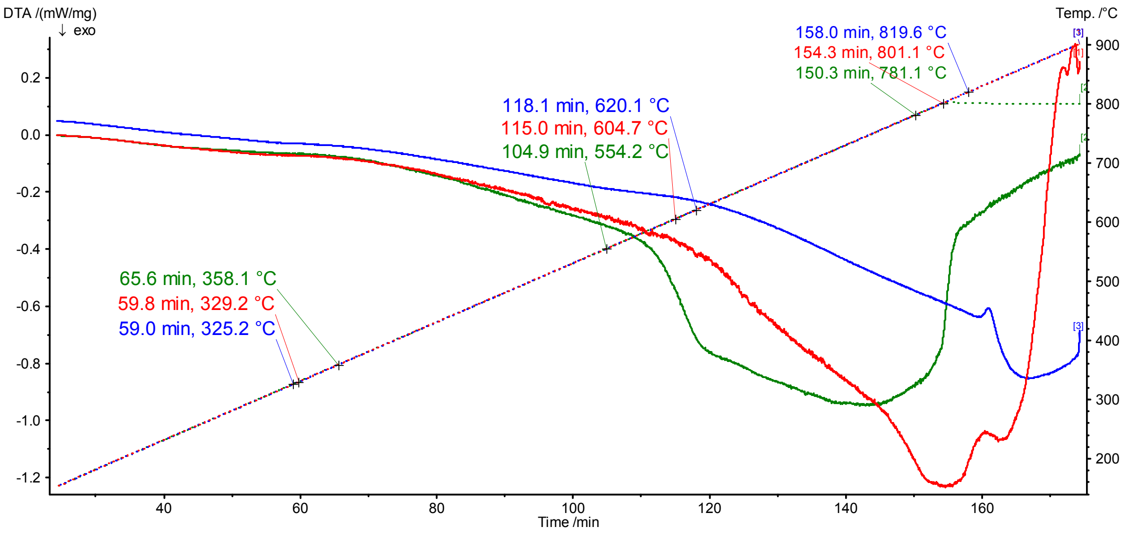

Figure 3-26: DTA for SrD_2 in argon (green), 5% H_2/argon (red) and 35% H_2/argon (blue)

3.5 Future suggestions

For the synthesis of single phase hydride and deuteride materials, gas purification (e.g. oxygen scrubber and molecular sieve) might be required to prevent contamination of the product with oxides. Alternatively, very pure hydrogen could be obtained by decomposing a metal hydride that is stable up to intermediate temperatures, for instance MgH_2 or TiH_2. This is not an economical solution for the synthesis of deuterides.

3.6 Atmospheric exchange – H/D disordering

As will be shown in chapter 5, the conductivity behaviour for CaH_2 and SrH_2 suggests an order – disorder phase transition taking place at ~450°C and ~320°C, respectively. Thermal analysis supports this second order transition and high temperature neutron diffraction suggests the transition is of short range nature. High atmospheric exchange rates for hydrogen/deuterium were observed as well, within a similar temperature range, at which disordering takes place, suggesting that these processes are correlated. The high isotopic exchange rates point to very large chemical diffusivities for these species and this makes these materials of great interest in membrane applications.

4 Structural properties and thermal stability of Na and Li doped CaH_2 and SrH_2

Doping of CaH_2 and SrH_2 with heterovalent ions (i.e. Li, Na, La or Y) is interesting from an application point of view, as this type of doping is expected to introduce extrinsic defects into the host material. The introduction of extrinsic defects for instance, has proven to enhance the conductivities of many materials (eg. Y_2O_3 doping in ZrO_2, Na_2SO_4 doping in Na_3PO_4 or NaF doping in CaF_2 [93-97]). The enhancement in such properties however, generally has a structural cause. Doping zirconia with yttria is an extreme example as the doping causes a stabilisation of the high temperature cubic phase of zirconia at room temperature. This results in a highly conductive phase at lower temperatures. Although often structural changes are not this dramatic, even small changes are at least indicative for successful doping. Or in other words: extrinsic defect chemistry is occurring. Typical structural changes caused by extrinsic defects are change of lattice parameter, displacement of ions in the crystal structure, change in cation/anion occupancy and change in thermal displacement factors for the different ions. Changes in thermal behaviour can also be expected. First and second order transition temperatures are likely to shift upon doping.

Gorelov and Pal'guev already reported doping of CaH_2 with LiH. They claimed to have doped up to 31 mol% LiH into CaH_2, thereby improving the conductivity of CaH_2 below the cubic phase transition markedly. They noted though that the phase analysis was done by X-ray diffraction only and that any second phase LiH might have been invisible due to the light lithium and hydride ions.

In this chapter, doping of CaH_2 and SrH_2 with monovalent ions (Li, Na) is discussed. Li and Na were chosen as dopant ions purely on the basis of their ionic radius. A close match of the ionic radii of dopant and host is important in creating solid solutions as this ensures retention of the crystal coordination and symmetry of the host material. Also, it would prevent the occurrence of strains and distortions of the host lattice. A similar relationship also holds for the ionic conductivity of doped materials, as shown by Sorokin and Breitner, who studied CaF_2 doped with various lanthanides [55]. An optimum in the ionic conductivity and concomitant minimum in the activation energy was observed for doping with Gd and Dy, with slightly lower conductivities for the lighter and larger lanthanides (La, Ce, Pr and Nd). The heavier lanthanides all performed significantly worse, which was explained by a change in the defect clusters. The ionic radii of the dopant and host ions are shown in Table 4-1. The ionic radii of both 8-coordinated ions as well as 9-coordinated ions as reported by Shannon [33] are given. The metallic radii of the close packed metals are also given [98]. The structural and thermal behaviour of the so formed doped materials will be compared to those of the undoped host materials. It is expected that the monovalent doping will affect the electrical properties of its host materials. This will be discussed in a different chapter however.

Table 4-1: Ionic radii of host and dopant ions [33] and metallic radii [98]

Cation	Ionic radius, 8-coordinated (Å)	Ionic radius, 9-coordinated (Å)	Metallic radius, 12-coordinated, ccp (Å)
Ca	1.12	1.18	1.76
Sr	1.26	1.31	1.95
Li	0.92	-	1.28
Na	1.18	1.24	1.66

4.1 Synthesis of Na and Li doped CaH_2 and SrH_2

Li and Na doped CaH_2 and SrH_2 were prepared by solid reaction. LiH was only reacted with CaH_2, NaH was reacted with both CaH_2 and SrH_2. First, powders of alkali hydride were mixed with the alkaline earth hydride powders, using mortar and pestle. The mixed powders were pressed into pellets at 200 MPa. The pellets were subsequently fired in a closed stainless steel reactor, filled with a mixture of hydrogen and argon. The solid state reaction of LiH and CaH_2 was carried out in one stage: 16 hours at 600°C. The solid state reaction with NaH was carried out in two stages, 16 hours at 330°C and 16 hours at 600°C. The first stage temperature is just below the decomposition temperature of NaH in 5% H_2 / 95% argon atmosphere and is used to initially stabilise the NaH in the CaH_2 matrix. Thermal analysis and X-ray diffraction however, showed that the thus formed product is still two phases, so another reaction stage was added. After the reaction with NaH at 600°C, the sample colour has changed from white to blue, which is slightly more intense for SrH_2. No colour change occurs for the CaH_2 reaction with LiH.

4.2 X-ray diffraction

The synthesised LiH – CaH_2, NaH – CaH_2 and NaH – SrH_2 compounds were first analysed using X-ray diffraction. The occurrence of possible second phases should be apparent from the diffraction pattern. A possible second LiH phase might however remain invisible, since the light lithium ion diffracts X-rays very weakly and hydrogen is practically invisible for X-rays. X-ray diffraction patterns were obtained on a STOE diffractometer in transmission mode, using Cu $K\alpha 1$ radiation.

4.2.1 LiH – CaH_2

The diffraction pattern for LiH doped CaH_2 (5 mol% doping) is shown in Figure 4-1. Only the 2θ range between 27° and 48° was measured. Since X-ray diffraction is generally not sufficient to properly analyse hydride compounds, it was only used to see whether a single phase compound had been synthesised during the solid state reaction. In the diffraction pattern of LiH, shown in Figure 4-2, strong reflections are observed at 38.2° and 44.4°. These reflections are absent in the pattern of LiH – CaH_2, so apparently a single phase compound has been synthesised, namely $Ca_{0.95}Li_{0.05}H_{1.95}$. Neutron diffraction will however be required to confirm these results, since LiH diffracts X-rays weakly and a possible second phase might not appear in the X-ray pattern.

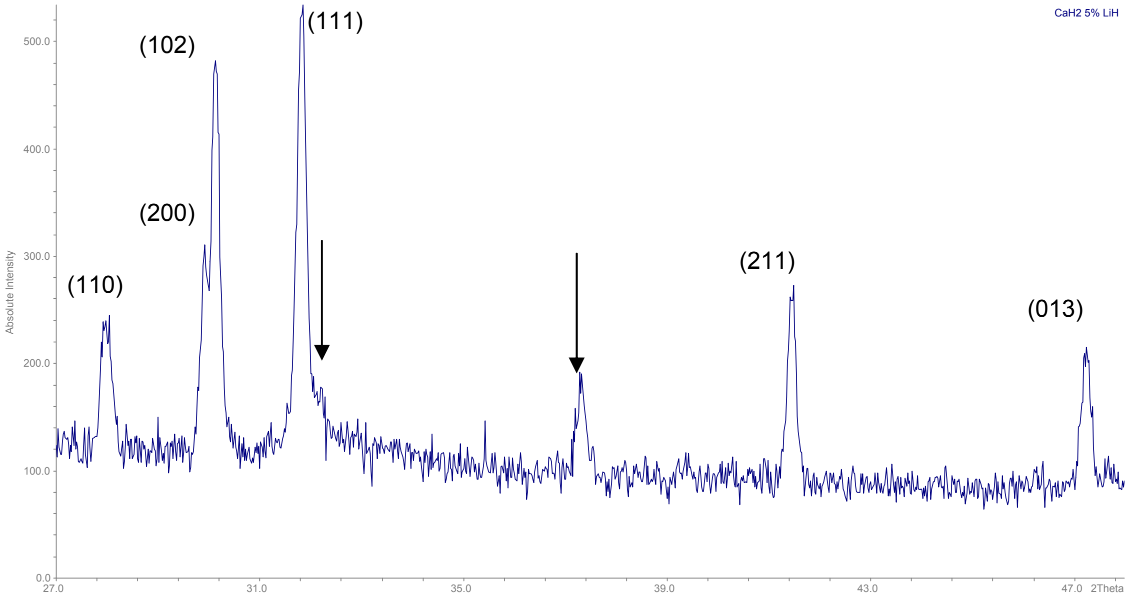

Figure 4-1: X-ray diffraction pattern for LiH – CaH_2 (5 mol% doping). Black arrows indicate CaO contamination

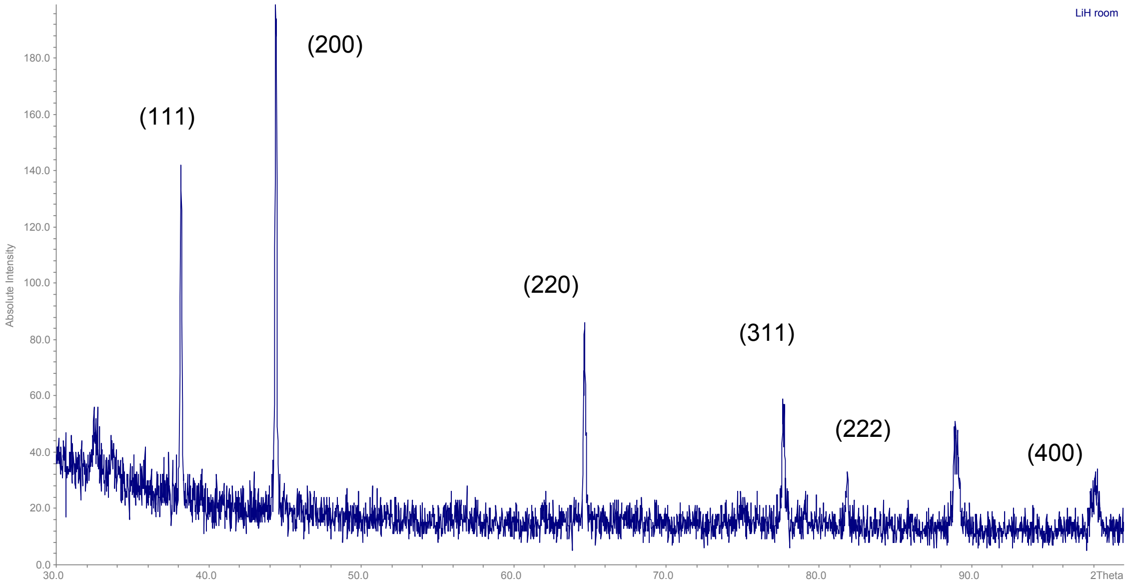

Figure 4-2: X-ray diffraction pattern for LiH

4.2.2 NaH – CaH_2

The X-ray diffraction pattern for NaH – CaH_2 (2 mol% doping) can be found in Figure 4-3. None of the reflections found for NaH (pattern shown in Figure 4-4) can be observed in this pattern, which suggests a single phase compound was synthesised. The weight of sample before and after solid state reaction was taken and a large weight loss was observed, however. Also, a NaH precipitate was found in the cold zone of the stainless steel reactor, indicating that a large fraction of the NaH evaporated from the sample. The colour change, from white to indigo, indicates though that some reaction has definitely taken place. The actual Na content in the product after solid state reaction was checked using Atomic Absorption Spectroscopy (AAS). This confirmed that only a small amount of NaH was doped into CaH_2, namely 0.02 mol%.

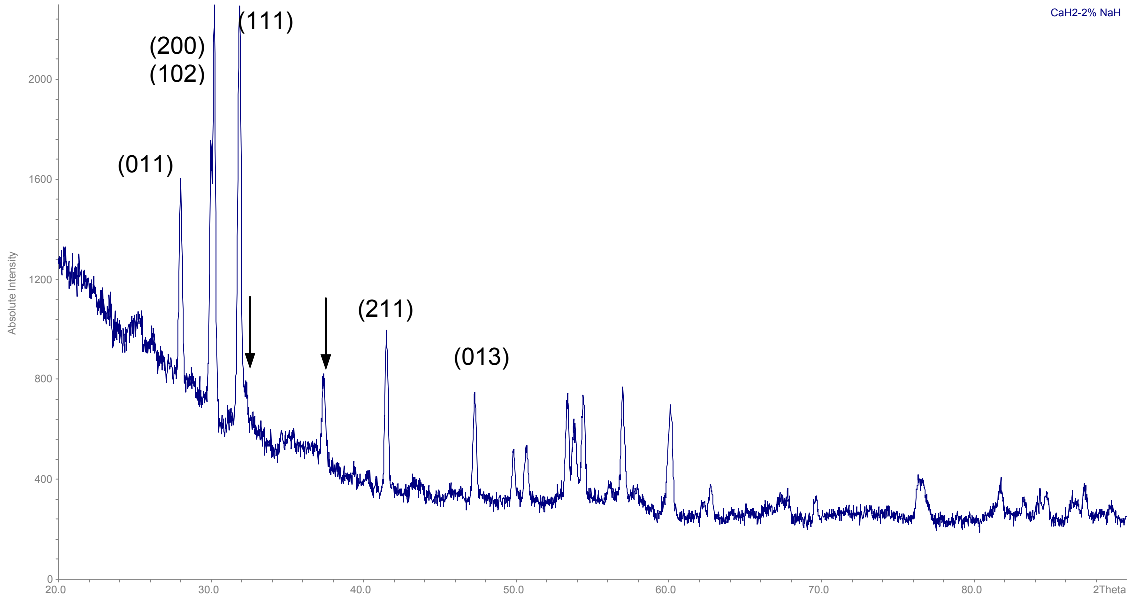

Figure 4-3: X-ray diffraction pattern for NaH – CaH_2 (2 mol% doping). Black arrows indicate CaO contamination

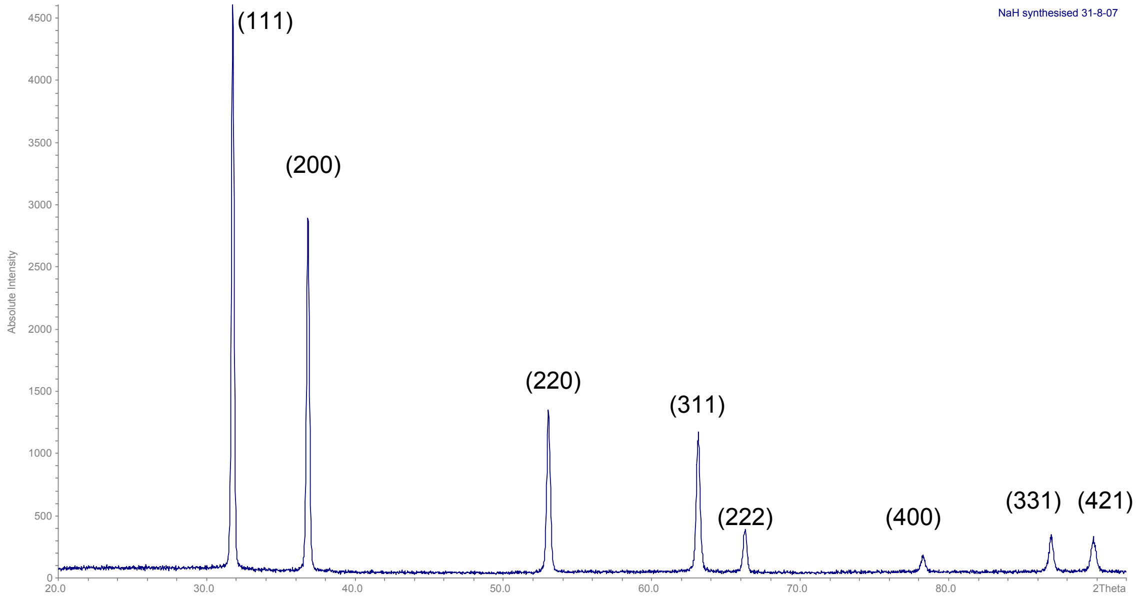

Figure 4-4: X-ray diffraction pattern for NaH

4.2.3 NaH – SrH_2

Similar X-ray experiments were performed for Na-doped SrH_2. Figure 4-5 shows the diffraction pattern for NaD-doped SrD_2 (2 mol% substitution) and no NaD reflections can be observed. As observed for the NaH – CaH_2 solid state reactions however, significant sodium evaporation took place and only small amounts of sodium were actually contained in the product material, i.e. 0.1 mol% of the metal content. A clear colour change from white – pink to light blue indicates a reaction however. Whether this is due to hydride ion vacancy creation or electronic defects will be discussed later.

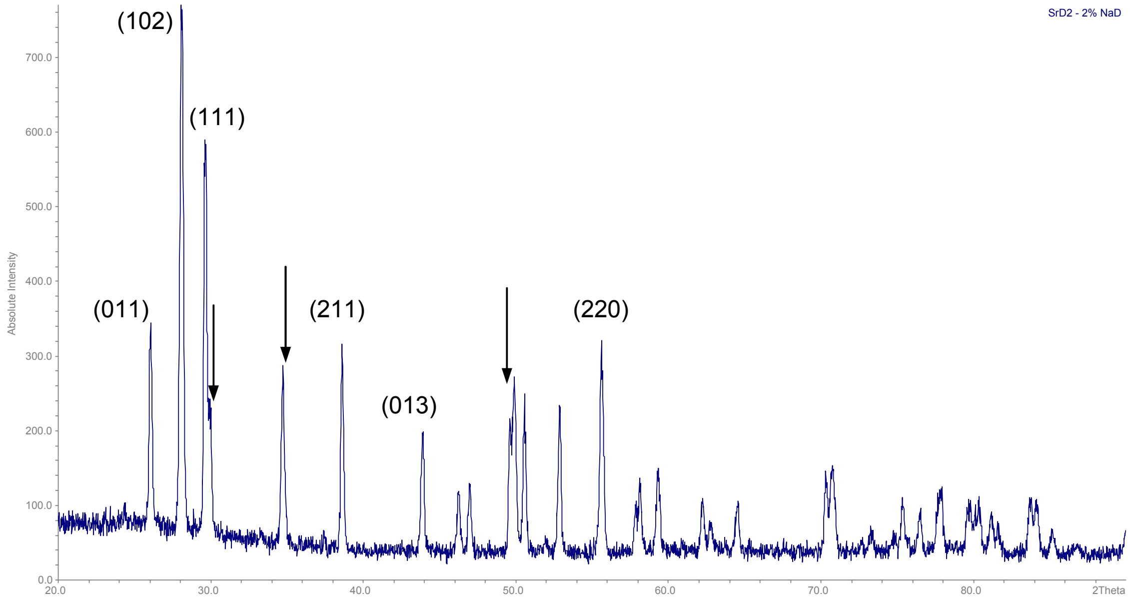

Figure 4-5: X-ray diffraction pattern for NaD – SrD_2 (2 mol% doping). Black arrows indicate SrO contamination

4.3 Neutron diffraction

To analyse the newly formed phases accurately, neutron diffraction was carried out on the deuterided samples. Experiments were performed on instrument D1A at Institut Laue Langevin (ILL) in Grenoble (France). The neutron wavelength was refined to 1.90946 Å. The powder samples (0.5 – 1.0 g) were loaded into vanadium cans in a glovebox to protect the materials from moisture and air. An indium wire between the lids and cans operated as a gastight seal to prevent any decomposition during measurements. Neutron diffraction patterns were recorded from $0 < 2\theta < 158°$, with a resolution of 0.05°, measuring for 4 – 5 hours per sample, all at room temperature.

4.3.1 LiD – CaD_2

The neutron powder diffraction pattern for the LiD – CaD_2 system (5 mol% substitution) can be seen in Figure 4-6. It shows that apart from the orthorhombic CaD_2 phase and the cubic CaO phase, another phase is present. This phase could be indexed as cubic (*FM3M*) with lattice parameter 4.069 Å, which identifies this phase as LiD. From Rietveld refinement analysis it can further be seen, that its phase content is 0.85 wt%, which is slightly less than the 1.1 wt%, which was attempted to be doped into the host material. Some doping might thus have occurred, but actual Ca substitution with Li will not be more than 1.7 mol%. Another sample, which nominally contained 2 mol% LiD in CaD_2 was tested. Here again, a LiD phase could be observed (phase content 0.26 wt% as compared to the nominally doped 0.42 wt%); in this case, not more than 1 mol% Ca substitution with Li is to be expected. Small changes in the orthorhombic structure of CaD_2 actually do take place, indicating that some Li might have entered the structure. The changes however do not seem to follow any trend. A decrease in the thermal displacement parameter for Ca/Li and an increase in the same parameter for D1 seem to be the only consistent changes for the two Li doped samples. The refinement results are summarised in Table 4-2.

Table 4-2: Neutron diffraction refinement results for Li – doped CaD_2, using spacegroup *P n m a*, λ = 1.90946 Å

Refinement parameter	CaD_2	"$Ca_{1-x}Li_xD_{2-x}$", 2 mol% nominal substitution	"$Ca_{1-x}Li_xD_{2-x}$", 5 mol% nominal substitution
a (Å)	5.9455 (1)	5.9458 (1)	5.9448 (1)
b (Å)	3.5917 (1)	3.5920 (1)	3.5913 (1)
c (Å)	6.7997 (1)	6.7996 (1)	6.7987 (1)
V (Å^3)	145.205 (4)	145.221 (4)	145.151 (4)
Ca/Li, 4c (x,¼,z)			
x	0.2407 (3)	0.2400 (4)	0.2415 (4)
z	0.1094 (2)	0.1092 (3)	0.1095 (3)
B (Å^2)	0.55 (6)	0.43 (8)	0.37 (7)
D1, 4c (x,¼,z)			
x	0.3553 (2)	0.3561 (3)	0.3549 (2)
z	0.4265 (2)	0.4270 (2)	0.4262 (2)
B (Å^2)	1.16 (4)	1.21 (5)	1.25 (5)
Occ	0.987 (10)	0.988 (13)	1.000 (12)
D2, 4c (x,¼,z)			
x	0.9749 (2)	0.9753 (3)	0.9757 (3)
z	0.6756 (2)	0.6760 (2)	0.6758 (2)
B (Å^2)	1.33 (5)	1.39 (6)	1.21 (5)
Occ	0.926 (10)	0.945 (13)	0.915 (11)
Phase content LiD (wt%)	-	0.85	0.26
R_p	4.24	4.87	4.31
R_{wp}	5.17	5.78	5.29
R_{exp}	3.70	4.65	4.16
χ^2	1.95	1.54	1.62

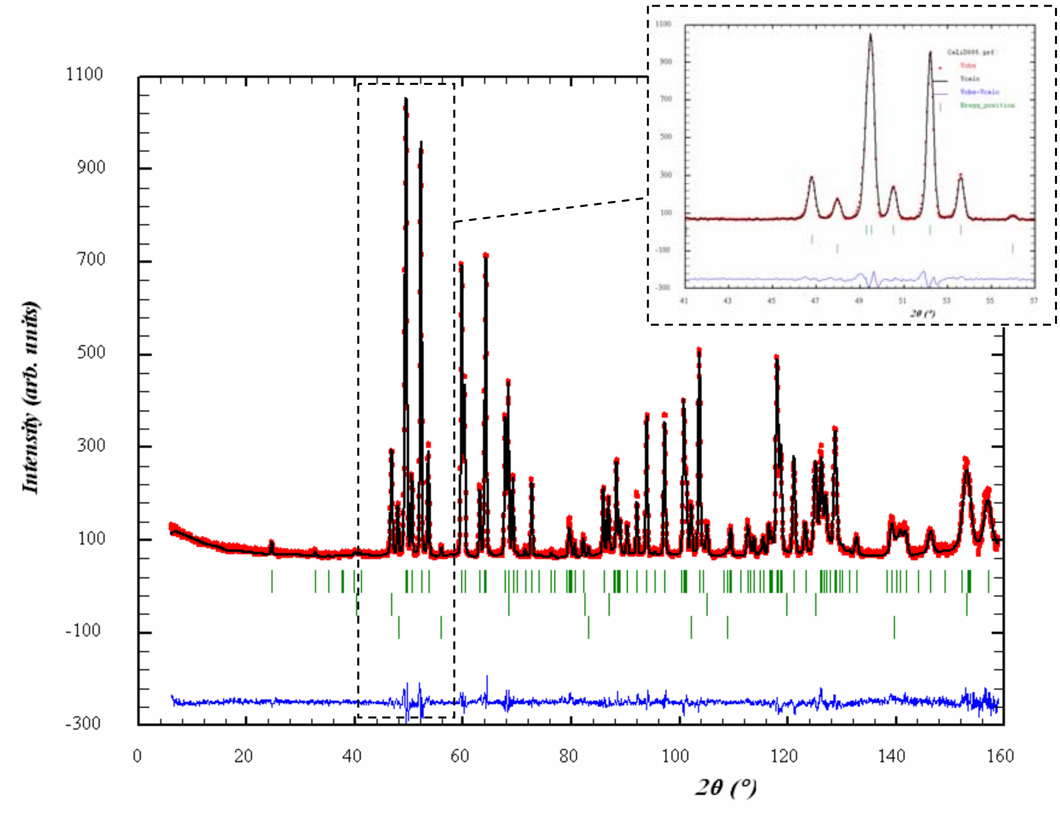

Figure 4-6: Neutron diffraction pattern for Li doped CaD_2 (red curve) and its refinement (black curve). Three phases: $Ca_{1-x}Li_xD_{2-y}$ (spacegroup *P n m a*), CaO (spacegroup *F m 3 m*) and LiD (spacegroup *F m 3 m*). Blue trail shows residuals after refinement; green ticks show reflection positions of the three phases

4.3.2 NaD – CaD_2

Figure 4-7 shows the neutron diffraction pattern for both CaD_2 and $Ca_{1-x}Na_xD_{2-x}$ (x = 0.05, nominally). No shifting of the peaks can be observed, indicating that no changes in the lattice parameters occurred due to the doping. Small changes in the intensity however, can be seen. This is most obvious from the combination of (210)/(112) and (211) peaks and the (013) and (301)/(212) peaks, which can be seen enlarged in the top right corner of Figure 4-7. It shows that after doping these peaks have more equal intensities, whereas before doping a larger difference in their intensities could be seen. The most likely causes for these changes in intensity are shifts in atomic position, changes in the thermal displacement of the atoms or changes in the atomic content of the unit cell. From Table 4-3 it can be seen that no shift in atomic positions take place upon doping. There are however changes in the thermal displacement factors and the occupancies of the deuterium sites. All thermal displacement factors increase and on both deuterium sites deuterium is lost from the structure. The chemical formulae are $Ca_{1-x}Na_xD_{1.77}$ and $Ca_{1-x}Na_xD_{1.82}$ after reaction with 2 mol% and 5 mol% NaD, respectively. The loss of deuterium is much larger than would be anticipated from the actually incorporated amount of sodium (0.02 mol%, as measured with AAS), if it is assumed that substitution is compensated by hydride ion vacancy creation. The change of deuterium content was further checked using thermal analysis as discussed later in this chapter. More discussion will follow to explain this phenomenon.

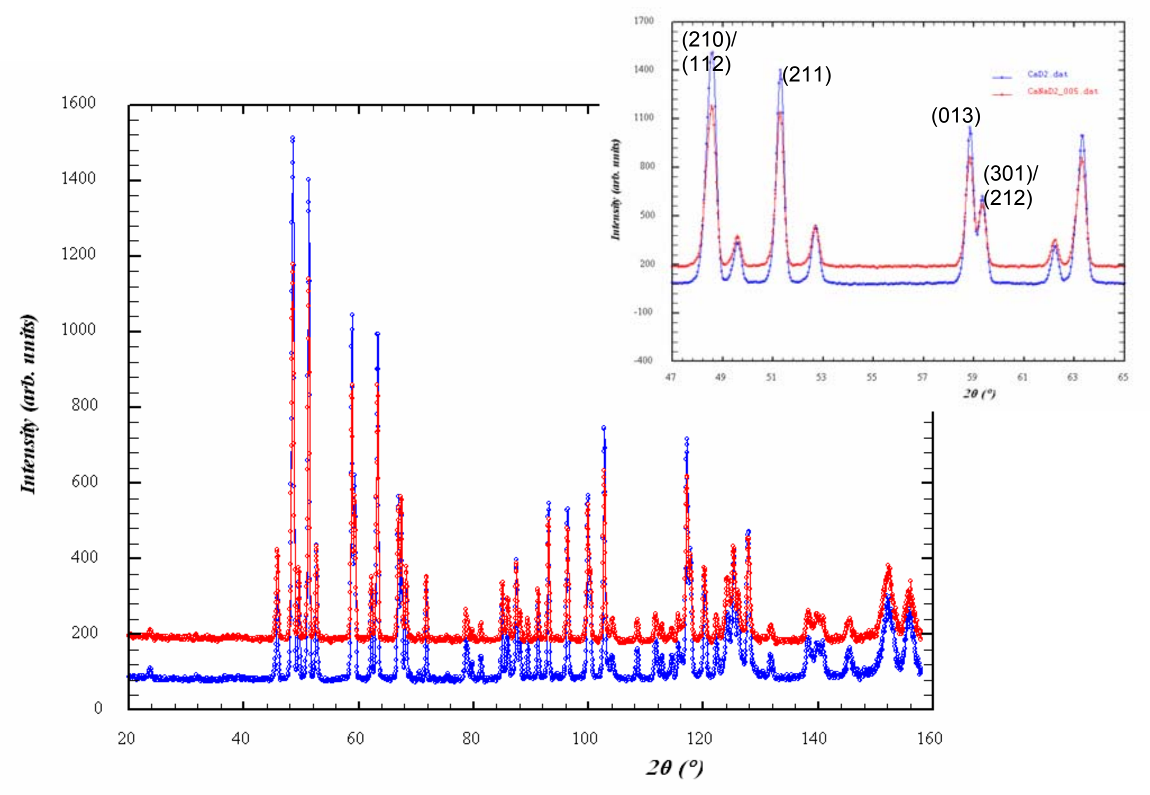

Figure 4-7: Neutron diffraction pattern of CaD_2 (blue) and $Ca_{1-x}Na_xD_{2-x}$ (x = 0.05, nominally) (red). Inset: zoomed section of 2θ = 47 – 65°

Table 4-3: Neutron diffraction refinement results for Na – doped CaD_2, spacegroup *P n m a*, λ = 1.90946 Å

Refinement parameter	CaD_2	"$Ca_{1-x}Na_xD_{2-x}$", 2 mol% nominal substitution	"$Ca_{1-x}Na_xD_{2-x}$", 5 mol% nominal substitution
a (Å)	5.9455 (1)	5.9464 (1)	5.9456 (1)
b (Å)	3.5917 (1)	3.5925 (1)	3.5919 (1)
c (Å)	6.7997 (1)	6.8000 (1)	6.7992 (1)
V (Å^3)	145.205 (4)	145.265 (4)	145.204 (4)
Ca/Na, 4c (x,¼,z)			
x	0.2407 (3)	0.2405 (4)	0.2400 (4)
z	0.1094 (2)	0.1096 (3)	0.1092 (3)
B (Å^2)	0.55 (6)	0.58 (7)	0.64 (7)
D1, 4c (x,¼,z)			
x	0.3553 (2)	0.3551 (2)	0.3552 (2)
z	0.4265 (2)	0.4264 (2)	0.4269 (2)
B (Å^2)	1.16 (4)	1.33 (5)	1.33 (5)
Occ	0.987 (10)	0.922 (11)	0.944 (12)
D2, 4c (x,¼,z)			
x	0.9749 (2)	0.9751 (3)	0.9752 (3)
z	0.6756 (2)	0.6762 (2)	0.6762 (2)
B (Å^2)	1.33 (5)	1.50 (5)	1.43 (6)
Occ	0.926 (10)	0.850 (10)	0.871 (11)
R_p	4.24	3.51	4.17
R_{wp}	5.17	4.18	5.07
R_{exp}	3.70	2.60	3.83
χ^2	1.95	2.59	1.75

4.3.3 NaD doped SrD_2

SrD_2 was doped with nominally 5 mol% NaD only. Actual sodium contents as measured by AAS are 0.1 mol%, the remainder evaporates during the synthesis and a deposit of NaD can be found in the cold zone of the stainless steel reactor. Like for NaD doped CaD_2, no clear changes in unit cell parameters could be observed after reaction with NaD, which can be explained by the small doping levels. Also, no clear changes in the atomic fractional coordinates can be seen. Analogue to Na doped CaD_2 changes in the thermal displacement parameters and D occupancies can be seen though. B_{iso} factors for all atoms increase upon reaction with NaD and the occupancies for both D sites decrease, although the decrease in D content is smaller than for the CaD_2 analogue. The resulting composition is $Sr_{1-x}Na_xD_{1.87}$. The refinement results are summarised in Table 4-4 and the diffraction pattern, along with its refinement and difference plot is shown in Figure 4-8.

Table 4-4: Neutron diffraction refinement results for NaD doped SrD_2, spacegroup *P n m a*, λ = 1.90946 Å

Refinement parameter	SrD_2 at 298K	$Sr_{1-x}Na_xD_{2-y}$ at 298K
a (Å)	6.3673 (1)	6.3673 (1)
b (Å)	3.8629 (1)	3.8635 (1)
c (Å)	7.3089 (1)	7.3081 (1)
V (Å^3)	179.772 (5)	179.777 (4)
Sr/Na, 4c (x,¼,z)		
x	0.2399 (3)	0.2398 (2)
z	0.1107 (2)	0.1106 (1)
B (Å^2)	0.45 (4)	0.58 (3)
D1, 4c (x,¼,z)		
x	0.3542 (3)	0.3538 (2)
z	0.4266 (2)	0.4267 (2)
B (Å^2)	1.14 (5)	1.39 (4)
Occ	0.965 (7)	0.955 (5)
D2, 4c (x,¼,z)		
x	0.9742 (3)	0.9736 (3)
z	0.6780 (2)	0.6782 (2)
B (Å^2)	1.51 (5)	1.92 (4)
Occ	0.937 (6)	0.912 (5)
R_p	4.92	3.19
R_{wp}	5.66	4.04
R_{exp}	3.55	2.51
χ^2	2.54	2.58

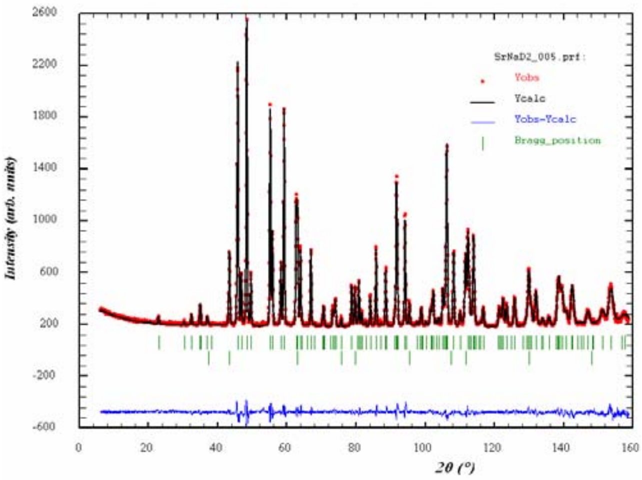

Figure 4-8: Neutron diffraction pattern for $Sr_{1-x}Na_xD_{2-y}$ (red curve), refinement (black curve) in *P n m a*, and difference plot (blue trail). Green ticks show reflection positions for $Sr_{1-x}Na_xD_{2-y}$ and SrO (*F m 3 m*) phase

4.4 Thermal analysis

Figure 4-9 shows the TGAs for CaD_2 and Na doped CaD_2. As the neutron diffraction refinements showed, the sample reacted with NaD had lower deuterium content. This loss should be reflected in the TGA for both compounds. It can be seen that CaD_2 loses 7.28 wt%, which is in excellent agreement with neutron diffraction results, where a phase content of 84.41 wt% for CaD_2 was suggested (CaO being the secondary phase). In that case the weight loss indicates 1.88 formula units of D per CaD_x unit compared to neutron refinement values of $CaD_{1.91}$. For CaD_2 reacted with NaD, the weight loss amounts to 6.61 wt%, which includes a small weight loss of 0.27 wt% at 210°C. Again assuming the phase contents as given by the neutron diffraction refinement are correct, this weight loss agrees with a deuterium content of 1.76 formula units, which is reasonably close to the deuterium content predicted by neutron diffraction ($CaD_{1.82}$). In any case, TGA shows that reacting CaD_2 with NaD causes a significant loss of deuterium from the structure. Figure 4-9 also shows the MS trail for ion mass 4 (D_2), confirming that the weight losses are definitely due to the loss of deuterium.

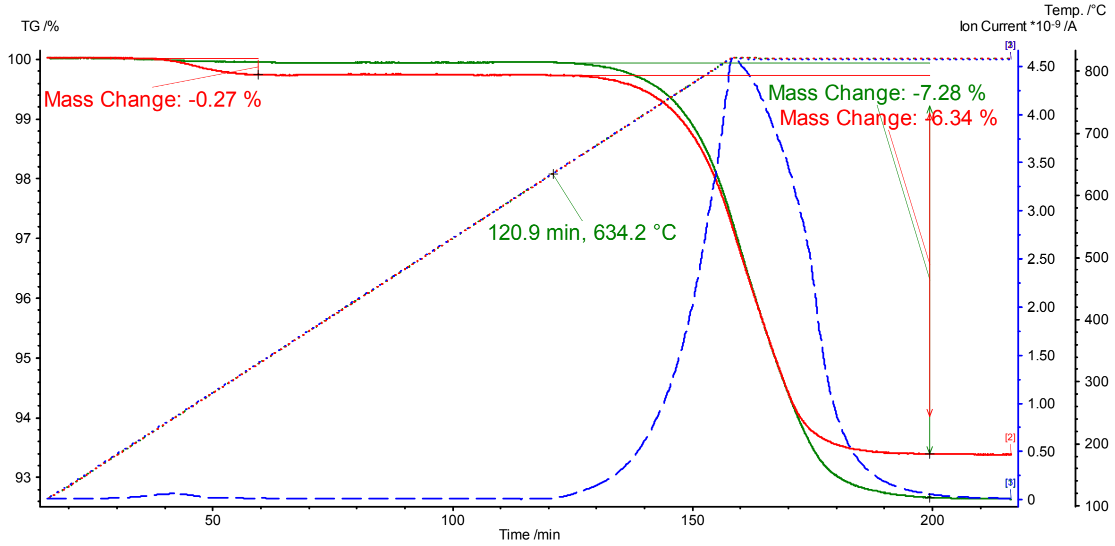

Figure 4-9: TGA for CaD_2 (green) and $Ca_{1-x}Na_xD_{2-y}$ (red); blue dashed line is ion mass 4 on MS showing release of D_2

Similar behaviour can be observed for SrD_2 reacted with NaD. A decrease in weight loss is observed after the reaction with NaD and this change cannot be attributed to an increase in the SrO content only. The absolute values do not agree with the values for the deuterium content as predicted by neutron diffraction, but the actual change in weight loss is in excellent agreement. The actual weight losses for undoped and doped SrD_2 are larger than the calculated ones, which is probably caused by some evaporation of strontium metal, even though temperatures did not exceed 800°C. The values for deuterium contents, as suggested by TGA and as calculated by neutron diffraction refinements, are tabulated in Table 4-5.

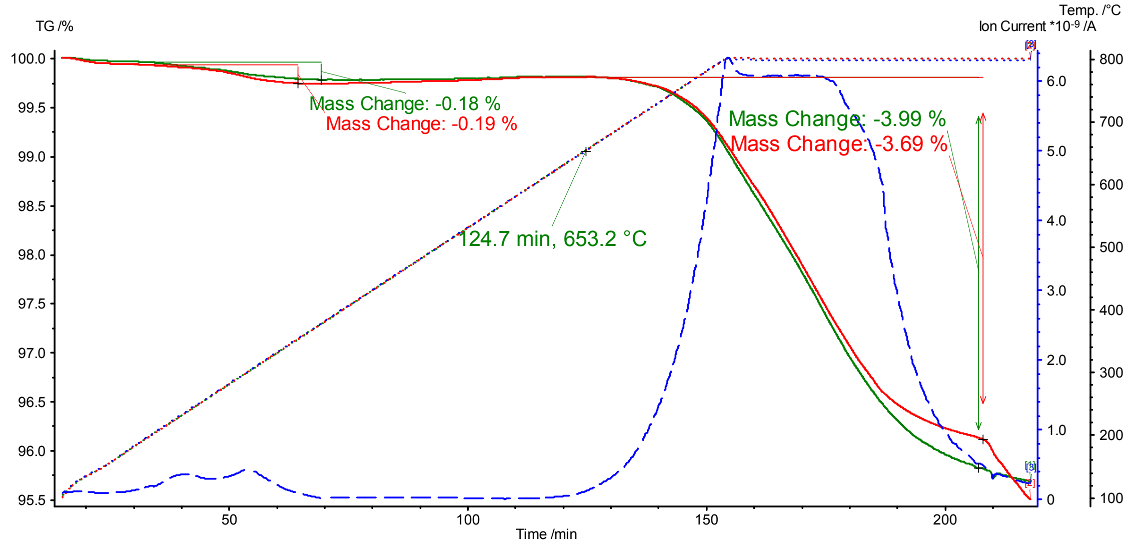

Figure 4-10: TGA for SrD_2 (green) and $Sr_{1-x}Na_xD_{2-y}$ (red); blue dashed line is ion mass 4 on MS

Table 4-5: Phase contents and deuterium content as found by TGA and neutron diffraction refinement

Compound	*Neutron diffraction*		*Thermogravimetric analysis*
	MD_x phase content (wt%)	x in MD_x	x in MD_x
CaD_x	84.41	1.91	1.88
$Ca_{1-y}Na_yD_x$	81.06	1.82	1.76
SrD_x	89.32	1.90	2.04
$Sr_{1-y}Na_yD_x$	83.70	1.87	2.01

4.5 Electron Paramagnetic Resonance spectroscopy (EPR)

Electron Paramagnetic Resonance spectroscopy (EPR) is a technique that is related to Nuclear Magnetic Resonance (NMR) in the sense that it involves particles with a magnetic moment (spin) that can absorb electromagnetic radiation. In NMR these particles are nuclei with a net magnetic moment (spin quantum number $I = \frac{n+1}{2}$, with n = integer), which are separated in a spin up and spin down energy level by applying a strong magnetic field (Zeeman effect). As the upper energy level is slightly less occupied than the lower energy level, the lower energy state nuclei can absorb electromagnetic radiation to flip spin and occupy the high energy level. The frequency of the electromagnetic radiation in NMR is typically in the order of MHz (radio waves). In EPR it is unpaired electrons that are studied. Unpaired electrons have a magnetic moment and spin quantum number ½ and can therefore be split into two energy levels in a similar way. The energy difference between the two levels when applying an external magnetic field, is given by $\Delta E = h \cdot \nu = g_e \cdot \mu_B \cdot B_0$, where g_e the electron's g-factor, μ_B the Bohr magneton and B_0 the magnetic field. It can be seen that the energy required for changing spin state is directly proportional to the magnetic field. For EPR the required magnetic fields are much smaller than for NMR though and the electromagnetic radiation that will typically be absorbed is of higher energy, i.e. ν ~ 10 GHz frequency.

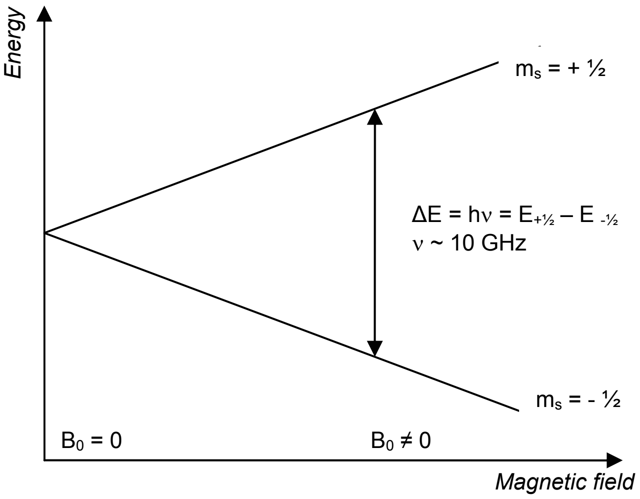

Figure 4-11: Representation of electron spin energy splitting when subjected to a magnetic field

As unpaired electrons have a chemical or electronic surrounding in materials, they experience some magnetic shielding and therefore a different magnetic field than the externally applied field. This can be expressed by formula (4.1). The energy required for changing spin state therefore changes slightly as well. This is finally represented by the overall *g-factor*, which accounts for the unpaired electron's electronic environment.

$$B_{eff} = B_0 \cdot (1-\sigma) \tag{4.1}$$

$$h\nu = g_e \mu_B B_{eff} = g_e \mu_B B_0 \cdot (1-\sigma) = g \mu_B B_0 \tag{4.2}$$

Because EPR is sensitive to unpaired electrons it is the ideal technique to study electronic defects in ceramic materials. The loss of hydrogen/deuterium that was observed in both neutron diffraction and thermogravimetric analysis as well as the colouration after reaction with NaH(D) suggests we might have incorporated electronic defects, namely F-centres. F-centres are unpaired electrons occupying anion sites. This would explain the remaining loss of hydrogen/deuterium apart from the creation of a small amount of hydride ion vacancies. In this case sodium will have acted as a hydrogen getter and the following defect reaction (equation (4.3)) would take place.

$$H_H^x \xrightarrow{Na} \tfrac{1}{2}H_2(g) + e_H^x \tag{4.3}$$

EPR was performed on a sample of NaD doped SrD_2 and as shown in Figure 4-12 it does show a typical F-centre response at g = 3416 – 3418 Gauss. There is actually a small shoulder on the peak and so it seems there are two unresolved peaks that resemble the two hydride ion sites, occupied by unpaired electrons. It must be noted that the response was very weak and the signal had to be boosted. A detailed analysis of the electronic defect structure was beyond the scope of this thesis and so no further studies have been performed. The result however does show F-centre formation and this seems a satisfactory explanation for the large deuterium/hydrogen losses observed after reactions with sodium.

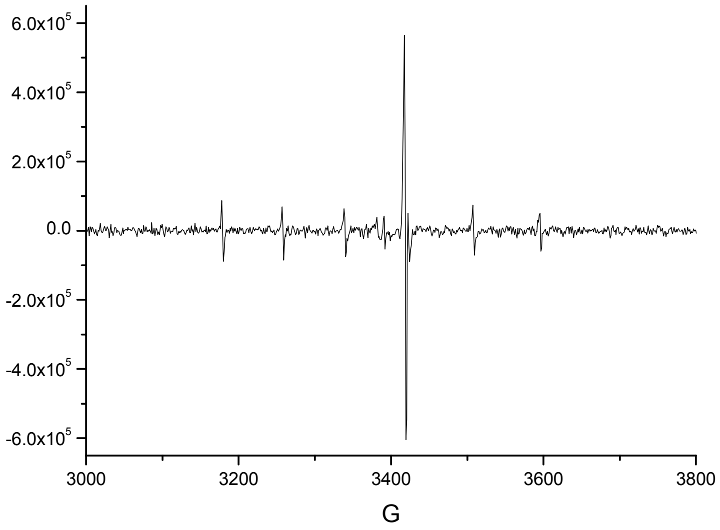

Figure 4-12: EPR spectrum for $Sr_{1-x}Na_xD_{2-y}$, showing an F-centre at 3418 – 3420 G

5 Electrical properties of doped CaH_2 and SrH_2

Whereas there are only few papers reporting structural properties of alkaline earth metal hydrides, the electrical properties of these hydrides have been even less studied. CaH_2 has been reported to be an ionic conductor of hydride ions. Gorelov and Pal'guev [31] studied the conductivity of CaH_2 doped with LiH and CaF_2 using DC techniques. They claimed hydride ion conductivities up to 10 S/cm above 780°C at which temperature CaH_2 supposedly adopts the fluorite structure. Further they report that they were able to dope CaH_2 with up to 31 mol% LiH, which causes the phase transition to shift to lower temperatures. Some ambiguous publications by Zhu [99-101] further suggest good hydride ion conductivity in CaH_2, but this was showed only by direct fuel cell testing, rather than conductivity tests on single phase materials. Strontium and barium hydride have been studied for their electrical resistances under high pressure by Wakamori et al [102], but to the author's knowledge not under ambient pressures. None of the papers thoroughly study the conduction mechanism of those materials and prove pure hydride ion conductivity.

In this chapter it is tried to get a better understanding about the electrical properties of CaH_2 and SrH_2 in general and about the hydride ion conduction mechanism specifically, by creating extrinsic defects. To achieve this, both calcium and strontium hydride have been doped with sodium hydride to create hydride ion vacancies. The electrical properties of both undoped and sodium doped calcium/strontium hydride were tested to see the effect of the presence of hydride ion vacancies.

5.1 Conductivity results

Pellets of CaH_2 and SrH_2 were pressed at 200 MPa and subsequently sintered at 800°C for 2 hours in pure hydrogen. Palladium paint was applied on both sides of the sintered pellets after which the electrodes were annealed overnight at 535 – 595°C in a 5% H_2 in argon atmosphere. Impedance spectra in the frequency range of 13 MHz – 5 Hz were recorded with an HP4192 impedance analyser, using an AC perturbation voltage of 100 mV. All testing was performed in a gas mixture of 5% H_2 and 95% argon. The validity of the impedance data was tested by performing the Kronig Kramers transformation. Kronig Kramers validation ensures the impedance response is within the linear regime and the measured cell is in equilibrium [78, 103]. After validation, the impedance data was analysed using the EQUIVCRT software by Boukamp [104].

5.1.1 CaH_2

Figure 5-1 shows two typical impedance spectra obtained for CaH_2 at 315°C and 586°C. The bulk, grain boundary and electrode responses could be separated, using an equivalent circuit consisting of a simple series of (RQ) elements. The used equivalent circuits are given in equations (5.1) and (5.2), which adopt Boukamp's equivalent circuit representation [104].

$$\left(R_{bulk}Q_{bulk}\right)\left(R_{gb}Q_{gb}\right)Q_{electrode} \qquad < 360°\text{C} \qquad (5.1)$$

$$LR_{bulk}\left(R_{gb}Q_{gb}\right)\left(R_{electrode}Q_{electrode}\right) \qquad > 360°\text{C} \qquad (5.2)$$

Here L represents an inductance, R a resistor and Q a constant phase element (CPE), which is defined as:

$$Y_{CPE} = Y_0 \cdot \left(j\omega\right)^n \qquad 0 \le n \le 1 \qquad (5.3)$$

The subscript *gb* in (5.1) stands for 'grain boundary'. The inductance only appears at higher temperatures (>360°C). The bulk capacitance is only visible below 360°C, above this temperature the bulk response is a simple series resistance. Furthermore, the electrode response got very noisy below ~400°C, so only the start of its semicircle was fitted at those temperatures using a single CPE without a resistor in parallel.

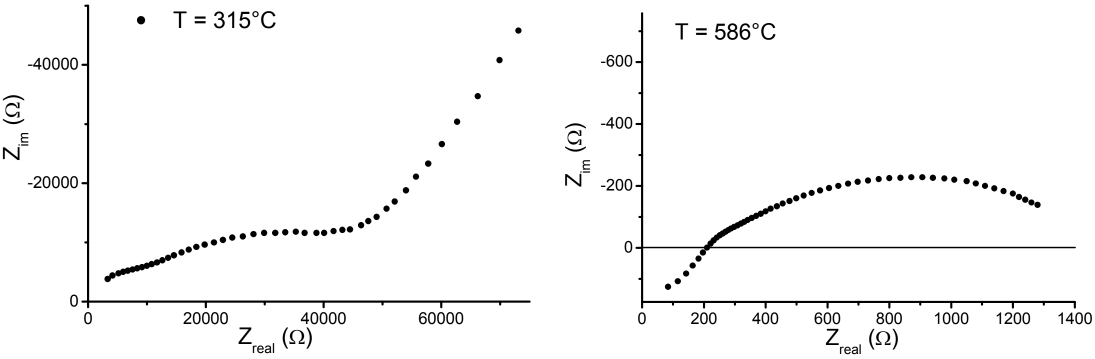

Figure 5-1: Two impedance plots for CaH_2 at T = 315°C (left) and T = 586°C

The large electrode response for CaH_2 at low temperatures, which starts to resemble Warburg behaviour as seen from the 45° angle in Figure 5-1 (T = 315°C), is indicative for hydride ion conduction. The Pd electrodes will become saturated with hydrogen at low temperatures, due to the formation of $PdH_{0.6}$. A mass transport limitation will occur, causing the Warburg response. So it seems that the conductivity is mainly ionic in nature, at least at low temperatures. Table 5-1 lists the values for the different equivalent circuit elements at 315°C and 586°C.

Table 5-1: Equivalent circuit element values for CaH_2

Equivalent circuit element	T = 315°C	T = 586°C
L (H)	-	7.3×10^{-6}
R_{bulk} (Ω)	6.0×10^{3}	1.4×10^{2}
Q_{bulk} ($\Omega^{-1}s^{n}$)	1.2×10^{-11}	-
n_{bulk}	1.0	-
R_{gb} (Ω)	3.6×10^{4}	71
Q_{gb} ($\Omega^{-1}s^{n}$)	1.3×10^{-8}	1.9×10^{-8}
n_{gb}	0.63	0.85
$R_{electrode}$ (Ω)	-	1.4×10^{3}
$Q_{electrode}$ ($\Omega^{-1}s^{n}$)	3.5×10^{-7}	2.8×10^{-5}
$n_{electrode}$	0.59	0.41

The conductivity σ of solids can generally be described using the Arrhenius formula:

$$\sigma T = A \cdot e^{-\frac{E_a}{kT}} \tag{5.4}$$

In this formula *A* is the conductivity prefactor, E_a the activation energy and *k* the Boltzmann constant. When the conductivity of CaH_2 is plotted vs. temperature, Figure 5-2 is obtained. The total conductivity comprises both bulk and grain boundary conductivity. Bulk and grain boundary conductivities are drawn separately in Figure 5-3. The activation energies for the different regimes and conductivities in these plots have also been summarised in Table 5-2.

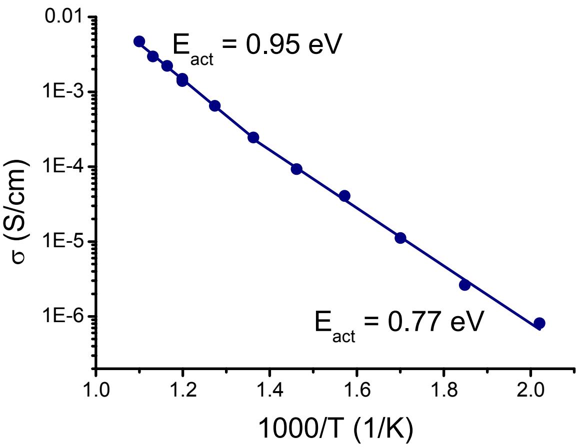

Figure 5-2: Arrhenius plot for the total conductivity for CaH_2

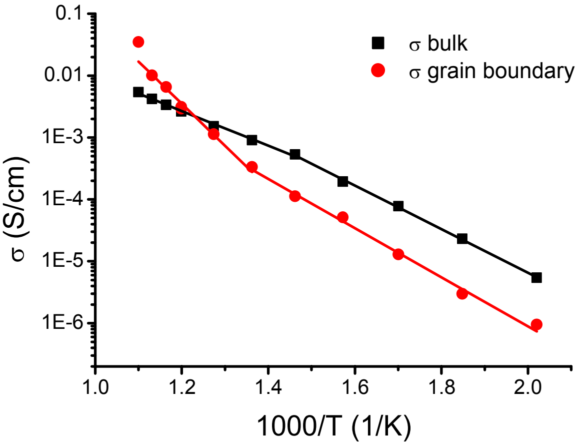

Figure 5-3: Bulk and grain boundary conductivities for CaH_2

Two regimes can be observed. Below ~460°C the activation energy is 0.77 eV, whereas for temperatures above 460°C, the activation energy increases to 0.95 eV. The transition temperature agrees well with the transition found in DTA (469°C) and it likely involves an order – disorder transition of the hydride ions. This type of transition, which is best described as a second order phase change, is often found in ionic conductors [93] and can involve three conductivity regimes: an ordered regime at low temperatures, a regime where the order – disorder transition takes place at intermediate temperatures and finally a completely disordered regime at high temperature. The transition is a thermally activated process and the amount of disorder increases gradually over temperature up to the point where all ions are disordered. As this type of transition is of structural nature, it is best to correlate this with the behaviour of the bulk conductivity. The bulk conductivity actually shows a decrease in activation energy at 460°C from 0.70 eV to 0.56 eV, which probably means that full hydride ion disorder is reached at this temperature. Whereas the activation in the ordered and disordered regime only consist of a migration term, in the transition regime it consists of both migration and defect creation terms, causing the activation energy to be higher in this regime. The activation energy in the disordered regime is lowest, as the disordered hydride ions move more freely than the ordered ones. Therefore, the two regimes observed for CaH_2 are believed to be the order – disorder transition regime (< 460°C) and the disordered regimes (> 460°C). The increase of activation energy in the total conductivity at 460°C must therefore be due to changes in the grain boundary conductivity.

5.1.2 NaH doped CaH_2

CaH_2 was doped with NaH in order to create hydride ion vacancies, which could enhance conductivity, if hydride ion conduction is via a vacancy mechanism. Hydride ion vacancies would be created according to the following Kröger – Vink reaction:

$$NaH \xrightarrow{CaH_2} Na'_{Ca} + H_H^x + V_H^{\bullet} \tag{5.5}$$

It is assumed that hydride ion vacancies are the main defects and no interstitial sodium ions are built into the CaH_2 structure.

The total conductivity for both CaH_2 and $(Ca_{1-x}Na_x)H_{2-x}$ (x = 0.05) is given in Figure 5-4. It can be readily seen that the conductivity behaviour of both compounds is nearly identical. A small increase in the activation energies for both regimes can be observed as well, as listed in Table 5-2. Apart from that, the conductivity behaviour looks almost identical. Activation energies for the different conductivities can be found in Table 5-2. The activation energies for bulk and grain boundary conductivity in $(Ca_{1-x}Na_x)H_{2-x}$ are ambiguous, since they do not show the same order – disorder transition temperature that is found for the total conductivity. From the total conductivity arrhenius plot a small shift in the order – disorder transition temperature can be seen, i.e. 500°C for $(Ca_{1-x}Na_x)H_{2-x}$ as compared to 460°C for CaH_2. The bulk conductivity of $(Ca_{1-x}Na_x)H_{2-x}$ shows this transition temperature however already at 360°C, whereas for the grain boundary conductivity the transition seems to take place at 460°C. The bulk and grain boundary conductivities for undoped CaH_2 and doped CaH_2 are shown in Figure 5-5. Based on Figure 5-4 and Figure 5-5, differences in conductivity behaviour between doped and undoped CaH_2 seem very small, if present.

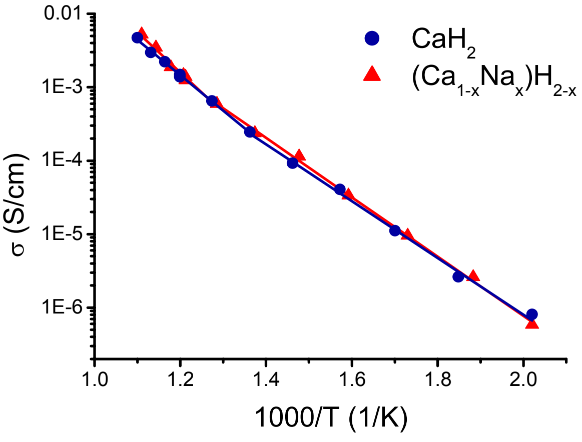

Figure 5-4: Total conductivity for $Ca_{1-x}Na_xH_{2-y}$ and undoped CaH_2

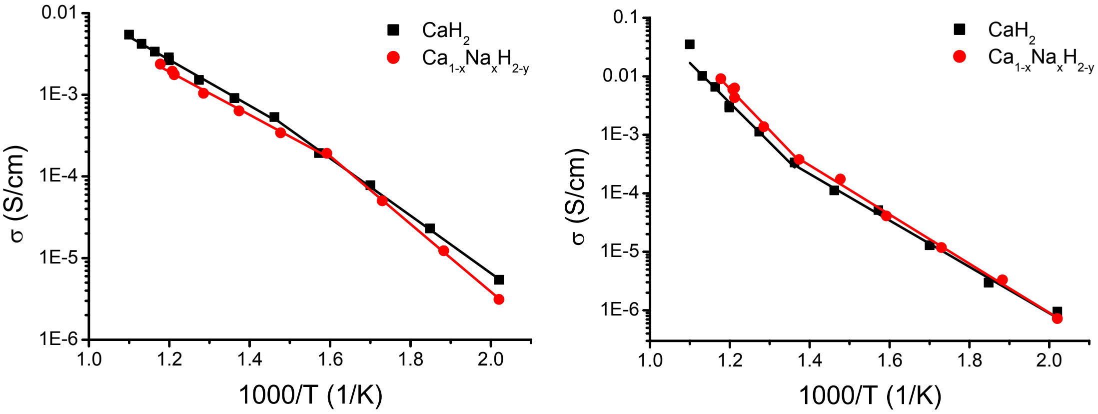

Figure 5-5: Bulk (left) and grain boundary (right) conductivity for $Ca_{1-x}Na_xH_{2-y}$ and undoped CaH_2

Table 5-2: Activation energies for doped and undoped CaH_2

	CaH_2		$Ca_{1-x}Na_xH_{2-y}$, (x = 0.05, nominally)	
Conductivity, σ	E_{act} (eV) < 460°C	E_{act} (eV) > 460°C	E_{act} (eV) < 500°C	E_{act} (eV) > 500°C
Total	0.77	0.95	0.80	1.08
Bulk	0.70	0.56	0.83[a]	0.52[a]
Grain boundary	0.79	1.35	0.83[b]	1.42[b]

[a]) Transition observed at 360°C

[b]) Transition observed at 460°C

The structural and thermal analyses have been described in chapter 4. The elemental analysis of the doped samples has also been given in this chapter. This revealed that only 0.02 mol% Na could be introduced into CaH_2, so very few (if any) free hydride ion vacancies are created. Also, the remaining understochiometry of H could be explained by the creation of F-centres, which are not likely to be mobile. The presence of immobile F-centres and the small increase in the amount of hydride ion vacancies, could account for the lack of change in conductivity. However, Natsuhara et al. did conductivity tests on NaF doped CaF_2 and could only dope 1.7 mol% NaF into the host material. They however found an increase in conductivity by 3 to 5 orders of magnitude [95]. This means small changes in the amount of hydride ion vacancies could improve conductivity significantly. So based on these results, it seems that hydride ion conduction is hardly vacancy mediated.

5.1.3 SrH_2

Two impedance plots for SrH_2 are shown in Figure 5-6. They show good similarities with the impedance spectra recorded on CaH_2, confirming the chemical and structural similarity of these two compounds. Modelling the data was done with similar equivalent circuits as used for CaH_2, given in equations (5.1) and (5.2). Bulk and grain boundary conductivities could only be separated below 420°C, as the grain boundary response is absent at higher temperatures. At those higher temperatures, the first series resistance represents the total conductivity of SrH_2.

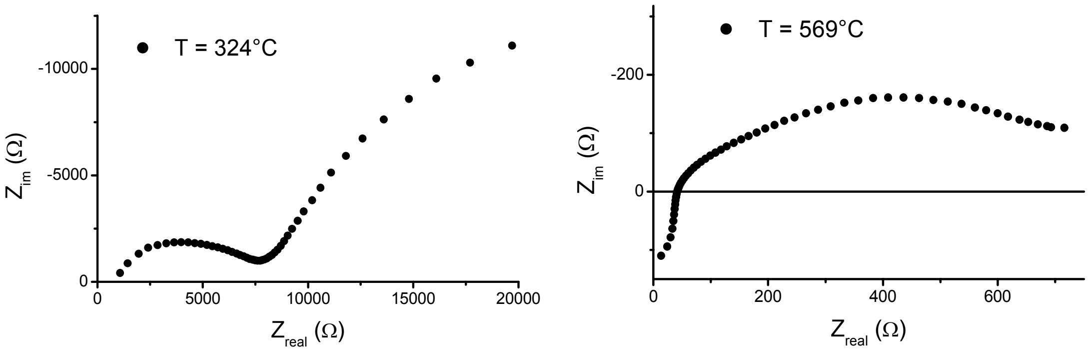

Figure 5-6: Impedance spectrum for undoped SrH_2 at 324°C (left) and at 569°C (right)

The Arrhenius plot for the total conductivity of undoped SrH_2 (Figure 5-7) shows similarities with that of CaH_2, however three regimes can now be distinguished. The low temperature regime has an activation energy of 0.76 eV, which increases to 0.99 eV at 320°C and finally drops again to 0.67 eV at high temperature (> 570°C). This is consistent again with the theory for an order – disorder transition taking place, involving the hydride ions. According to these results, the process of disordering starts at 320°C and is complete at 570°C. Since movement of the hydride ions in the disordered SrH_2 is easier, the activation energy drops to the lower value of 0.67 eV. The separate bulk and grain boundary conductivities can be found in Figure 5-8. The grain boundary response for SrH_2 could only be separated below 420°C, so there are only few data points for the bulk and grain boundary conductivity. They do show a transition at 320°C, as observed for the total conductivity. The activation energy of the bulk conductivity drops again, however, suggesting the material goes from a partly disordered structure into a fully disordered one. The increase and drop in activation energy in the total conductivity therefore seem to be related again to changes in the grain boundary conductivity. Unfortunately there is no more information about the bulk and grain boundary conductivity at temperatures above 420°C. The activation energies for the different regimes for total, bulk and grain boundary activity can be found in Table 5-3.

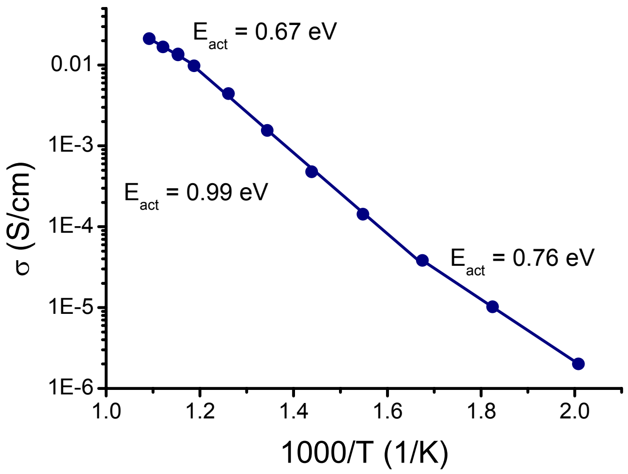

Figure 5-7: Total conductivity for undoped SrH_2

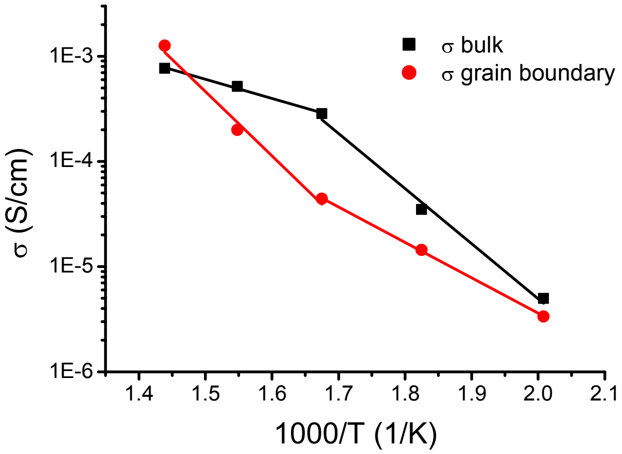

Figure 5-8: Bulk and grain boundary conductivity for undoped SrH_2

5.1.4 NaH doped SrH_2

Doping SrH_2 with NaH leads to the formation of hydride ion vacancies again, according to equation (5.5). Formation of interstitial Na ions is assumed not to take place. The Arrhenius plots for the total conductivity of doped and undoped SrH_2 are given in Figure 5-9. Unlike NaH doped CaH_2, the behaviour for NaH doped SrH_2 is significantly different from undoped SrH_2. The low temperature conductivity is increased by half an order of magnitude and the onset temperature for order – disorder in the hydride ions is increased by ~100°C. From the bulk and grain boundary conductivities (shown in Figure 5-10) it could also be concluded that the material is already fully disordered ~200°C, causing the activation energies to drop significantly, as the term for defect creation has disappeared.

Furthermore, the high temperature conductivity, in the disordered regime, for NaH doped SrH_2 has decreased slightly compared to undoped SrH_2. This behaviour is commonly observed for doped systems. Whereas the low temperature conductivity is dominated by extrinsic defects, the high temperature conductivity is dominated by intrinsic defect chemistry, in this case hydride ion disordering. The Na doping must have a negative entropic effect on the hydride ion disordering at high temperatures, causing the conductivity to drop slightly.

The activation energies in NaH doped SrH_2 have all decreased as compared to undoped SrH_2. They can be found in Table 5-3.

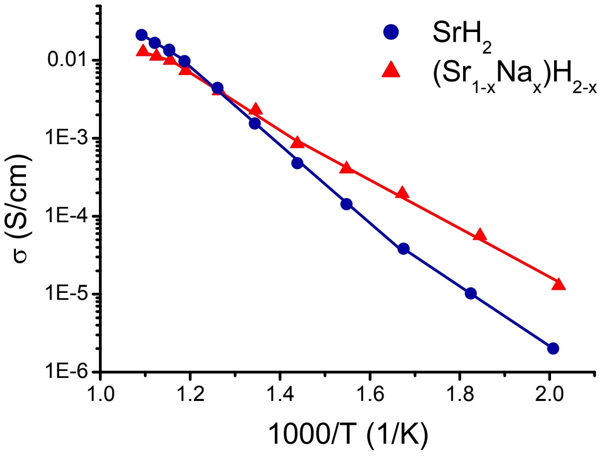

Figure 5-9: Arrhenius plot for total conductivity of $Sr_{1-x}Na_xH_{2-y}$ and undoped SrH_2

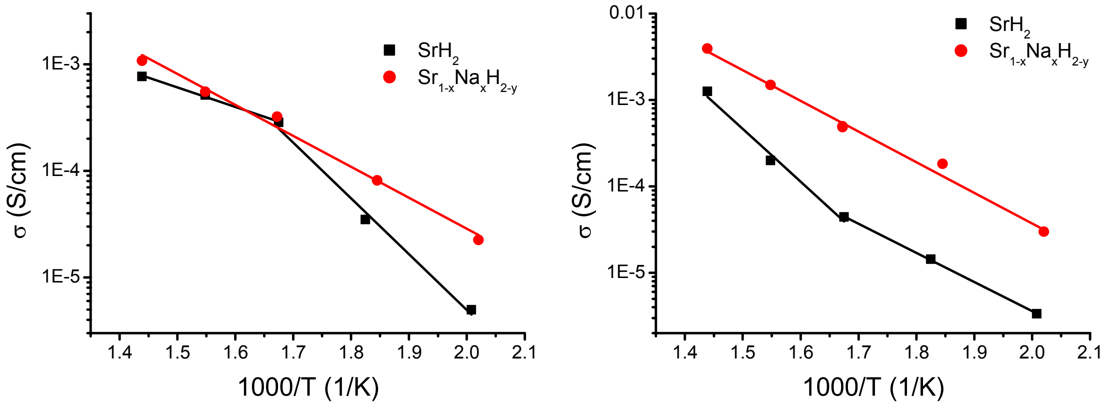

Figure 5-10: Bulk (left) and grain boundary (right) conductivity for $Sr_{1-x}Na_xH_{2-y}$ and undoped SrH_2

Table 5-3: Activation energies for undoped SrH_2 and $(Sr_{1-x}Na_x)H_{2-x}$

		SrH_2	
Conductivity, σ	E_{act} < 320°C (eV)	320°C < E_{act} < 570°C (eV)	E_{act} > 570°C (eV)
Total	0.76	0.99	0.67
Bulk	1.04	0.36	-
Grain boundary	0.67	1.21	-

		$Sr_{1-x}Na_xH_{2-x}$, (x = 0.05, nominally)	
Conductivity, σ	E_{act} < 420°C (eV)	420°C < E_{act} < 590°C (eV)	E_{act} > 590°C (eV)
Total	0.62	0.73	0.35
Bulk	0.58	-	-
Grain boundary	0.70	-	-

5.2 *Further discussion*

It was tried to electrically test CaH_2 at higher temperatures, i.e. up to 825°C, to observe the high temperature phase change from orthorhombic to cubic fluorite. A sudden drop in the impedance with a factor of ~10 could be seen in fact at T = 822°C (shown in Figure 5-11), however the electrode degradation was too high to obtain noise free and reproducible data above 700°C. The electrode degradation also prevented us from doing tests in different hydrogen atmospheres to see the effect on electrode behaviour. It is reasoned that for pure ionic conductors, the electrode impedance should improve with higher hydrogen partial pressures. This effect was however overshadowed by the degradation.

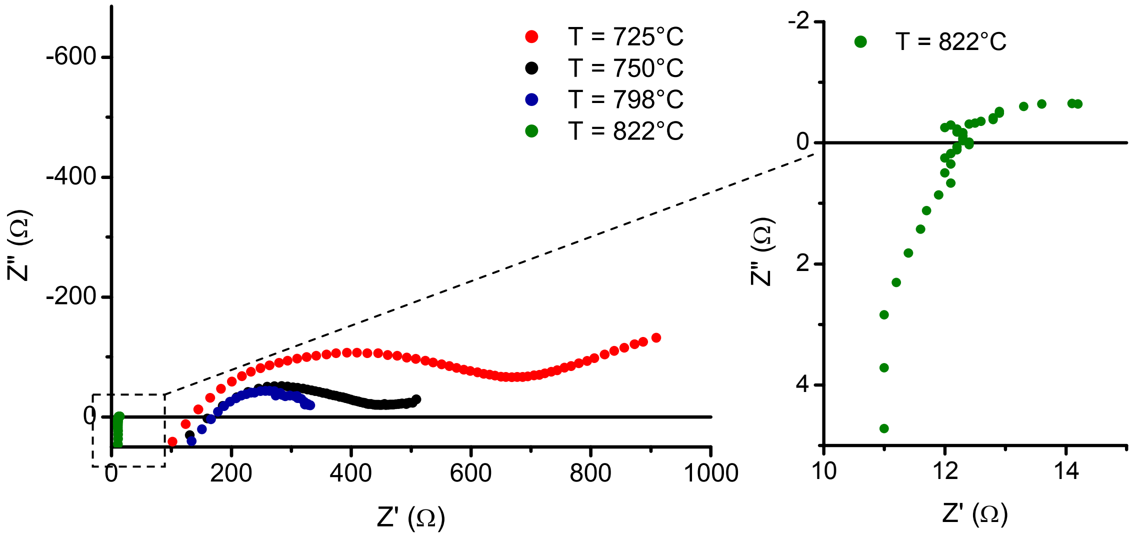

Figure 5-11: Impedance for CaH_2 T > 700°C; sudden drop in impedance at T = 822°C

Painted palladium electrodes are clearly not the ideal electrodes, which could be caused by the organics that cannot be burnt off in the reducing atmospheres. At higher temperatures, carbon residues might start reacting with CaH_2 to form CaC_2 interfacial layers, which could account for the increasing impedances at those temperatures. A more suitable electrode should be looked for, which shows longer term stability, so partial hydrogen pressure dependent studies can be performed. These should shed more light on the nature of the measured conductivity (ionic and/or electronic).

6 The Ca-N-H(D) and Sr-N-H(D) systems

Ionic compounds containing both nitrogen and hydrogen often have these elements present in one shared complex ion, an imide, amide or ammonium ion. The chemical formulas for these complex ions are NH^{2-}, NH_2^- and NH_4^+ for the imide, amide and ammonium ion, respectively. The bonding is mainly covalent, but obviously the bonds are polarised, giving the nitrogen a net negative and the hydrogens a slight positive charge. In fact, amides and imides are used as bases in organic chemistry and the ammonium ion is a weak acid, emphasising the protonic nature of hydrogen in these ions even more. With some cations from group II (the alkali earth elements) however, nitrogen and hydrogen form ionic compounds, in which both hydrogen and nitrogen are present as negatively charged ions and do not form complex ions. In other words, the hydrogen in the structure is a hydride ion and is bound to both the nitrogen and metal ions. Nitride hydrides of calcium, strontium and barium have been reported so far [63, 105-107]. It turns out that the crystal structures of the nitride hydrides of calcium, strontium and barium are very similar to the imides of the same metals. Wegner et al. [106] reported that barium nitride hydride is a good conductor of hydride ions and the nitride hydrides of these alkaline earth metals might therefore be of practical interest in electrochemical applications. This chapter deals with the synthesis and structural, thermal and elementary analysis of some calcium and strontium compounds containing hydrogen and nitrogen.

6.1 The Ca-N-H(D) system

Literature reports that calcium imide (CaNH) and calcium nitride hydride have very similar crystal structures. Calcium imide has a rocksalt structure, spacegroup *F m 3 m* in which calcium and nitrogen are octahedrally coordinated to each other. The position of hydrogen is subject of some debate. Andresen et al. [108] first studied this compound using neutron diffraction techniques and concluded that the hydrogen was statistically distributed between calcium and nitrogen. Brese et al. [83] later studied the chemically similar strontium imide (in its deuterided form: SrND) and used a model where the imide ion is treated as a rigid body with its centre of mass placed on the origin of the cubic lattice. They found that using this model the imide ion shows a lot of rotational disorder. They however also calculated a minimum in the electrostatic energy when the hydrogen was positioned on the body diagonal, i.e. in the [111] direction, close to the nitrogen. Energetically this would be the most favourable site, being furthest away from the positively charged Sr ions. Later again, Sichla and Jacobs [109] suggested from single crystal X-ray studies on calcium imide, that the hydrogen site was close to the nitrogen, displaced along one of the unit cell axes (direction [001]), occupying a 24e site (00z). Calcium imide has a cubic lattice parameter of 5.14 Å [109, 110]. Calcium nitride hydride crystallises in the spacegroup *F d 3 m*, with a lattice based on a superstructure derived from the rocksalt structure. Now the hydride ions are on the origin of the unit cell (16c site) and nitride ions on the 16d site (½,½,½), whereas calcium is located on a 32e site (x,x,x), with $x \approx 0.26$, so in distorted octahedral coordination to both hydride and nitride. The unit cell is a double cubic cell, with lattice parameter 10.13 Å, which is just slightly smaller than twice the unit cell of calcium imide [107, 111]. On going from imide to nitride hydride, half of the imide groups are replaced by nitride, the remaining half by hydride ions. The crystal structures of the two compounds are shown in Figure 6-1.

In terms of a close packing approximation, one can consider both structures to be cubic close packed arrays of the alkaline earth with the imide groups occupying all the octahedral holes in the imide structure and hydride and nitride ions each occupying half of these octahedral sites in the nitride hydride structure. In this latter structure the nitrides and hydrides occupy alternate [100] directions of the face centred cubic structure close packed array of Ca. This nitrogen hydrogen site ordering can be considered as a rocksalt type ordering within the anion array.

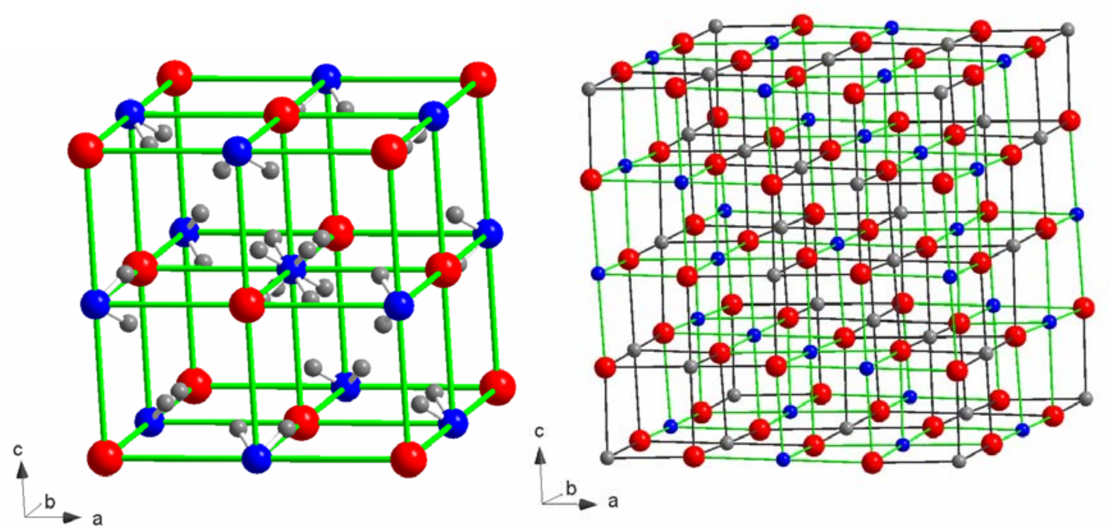

Figure 6-1: Crystal structures of calcium imide (left) and calcium nitride hydride (right); calcium in red, nitrogen in blue and hydrogen in grey. In calcium imide hydrogen is positioned on the body diagonal (note that each H site can only be 12.5% occupied on average.

Ca_2NH has previously been synthesised either by reacting Ca_3N_2 in hydrogen atmosphere [63, 107] or by reacting Ca_3N_2 with CaH_2 in vacuum [107], both at high temperatures.

$$Ca_3N_2 \xrightarrow[T>850°C]{H_2} \tfrac{3}{2}Ca_2NH + \tfrac{1}{4}N_2 \qquad (6.1)$$

$$Ca_3N_2 + CaH_2 \xrightarrow[T=900-1000°C]{vacuum} 2Ca_2NH \qquad (6.2)$$

Calcium imide is traditionally obtained by thermally decomposing calcium amide, which in its turn is obtained by thermally decomposing calcium hexaammonia complex (calcium metal dissolved in ammonia).

$$Ca(NH_3)_6 \longrightarrow Ca(NH_2)_2 + 4NH_3 + H_2 \tag{6.3}$$

$$Ca(NH_2)_2 \xrightarrow{T=400^\circ C} CaNH + NH_3 \tag{6.4}$$

6.1.1 Ca-N-H experimental

Nitrogen and hydrogen containing calcium compounds were synthesised by reacting either calcium metal (Alfa Aesar, 99.5% metals base) or calcium hydride (CaH_2, Fluka, 97%) in an atmosphere of 5% H_2 and 1 – 2% N_2 in argon at temperatures between 600°C and 900°C. Molybdenum was used as crucible material. The reactions were carried out in a small tube furnace within the glovebox using an open furnace tube. Nitrogen levels in the glovebox atmosphere were kept between 1% and 2% for reproducibility purposes. Gas chromatography results have shown however that nitrogen levels between 100 – 1000 ppm still result in nitrogen incorporation in the calcium compounds. This shows the sensitivity of those materials to nitrogen at elevated temperatures. For neutron diffraction, Ca-N-D was synthesised by reacting calcium metal in an atmosphere of 5% D_2 and 2% N_2 in argon at 600°C for 32 hours. Reaction conditions were further identical to those of the hydrided samples. More detail about the synthesis procedures is given in chapter 2. The calcium based samples have a bright, yellow colour, which tarnishes to a darker, slightly green colour after a while.

X-ray diffraction patterns were obtained using a STOE diffractometer in transmission mode with a Cu Kα1 source. Data was recorded in the range $10° < 2\theta < 90°$ with a resolution of 0.02°. Sealed glass capillaries were used to protect the materials from air and moisture.

Neutron diffraction was carried out on a deuterided sample. Neutron diffraction data was obtained on diffractometer D1A at ILL, Grenoble (France). The Ca-N-D powder sample of approximately 1 gram was loaded into a vanadium can in a glovebox. A steel cap was fitted on top of the vanadium can, which prevented the sample from decomposing, whilst transporting the sample to the diffractometer. The neutrons had a wavelength of 1.91 Å (refined to 1.9114 Å). Neutron diffraction patterns were recorded between $0 < 2\theta < 158°$ with a resolution of 0.05°, at room temperature (20°C, RT), 250°C, 450°C and 650°C, all under vacuum. After heating up to the desired temperature, 20 minutes was allowed for equilibration. Data collection times were 4 – 5 hours per sample. Indexing of the patterns was done with the CHECKCELL software. Subsequent Rietveld refinements were carried out using the Fullprof software.

6.1.2 Ca-N-H XRD results

Figure 6-2 shows the XRD patterns of Ca-N-H synthesised from CaH_2 at 600 – 900°C. The compound reacted at 600°C could be indexed in the cubic spacegroup *F d 3 m*, with lattice parameter 10.143(1) Å. The peaks marked with red circles are typical for the double cubic cell and are not observed for the calcium imide phase (see the theoretical pattern for calcium imide, Figure 6-6. Those 'superstructure' peaks seem to disappear, or at least lessen in intensity, when the reaction temperature is increased to 800°C. However at a reaction temperature of 900°C, the peaks reappear. For reaction temperatures >600°C the lattice parameter decreases slightly to 10.138(4) Å. The lattice parameters suggest that Ca_2NH (calcium nitride hydride) is formed and there is no initial indication of calcium imide (CaNH) formation. The change of the relative intensities of many peaks ('superstructure' peaks and for instance (222) and (400) peaks) does however suggest a change of stoichiometry, mainly due to the ratio of Ca : N (as hydrogen is nearly invisible to X-rays). Figure 6-3 shows a zoomed section in which the change of relative intensities of peaks (222) and (400) can clearly be seen.

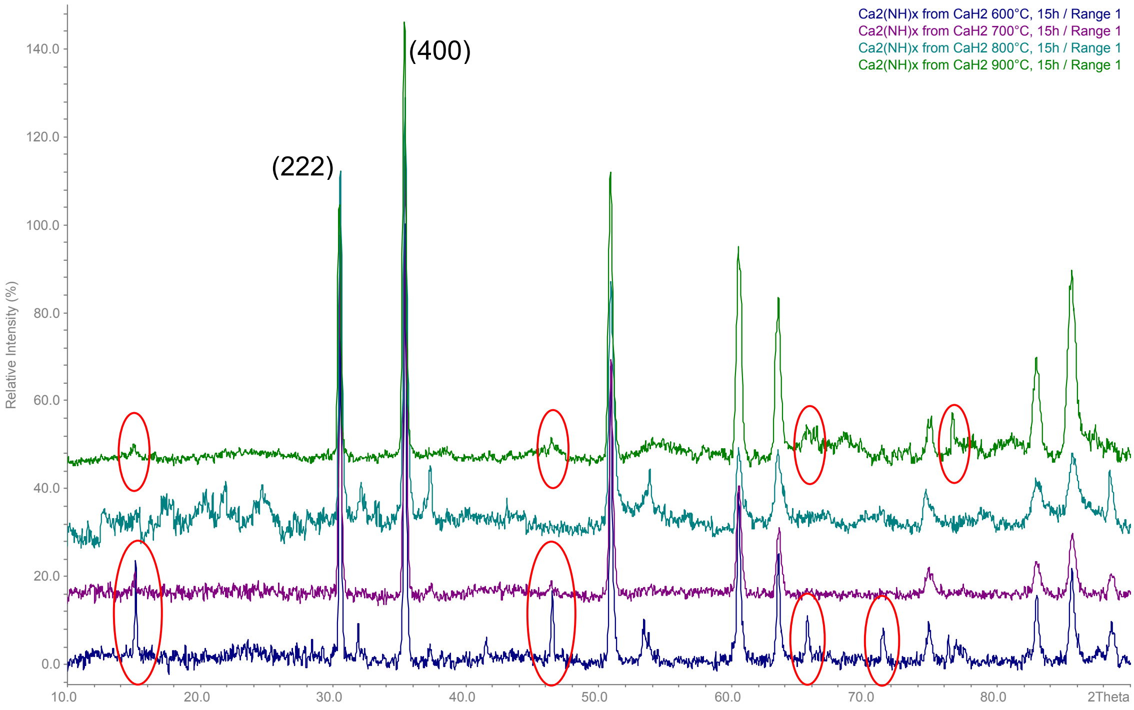

Figure 6-2: XRD pattern of Ca_2NH synthesised from CaH_2 at different temperatures. Red circles mark double cubic cell peaks (all measured at room temperature)

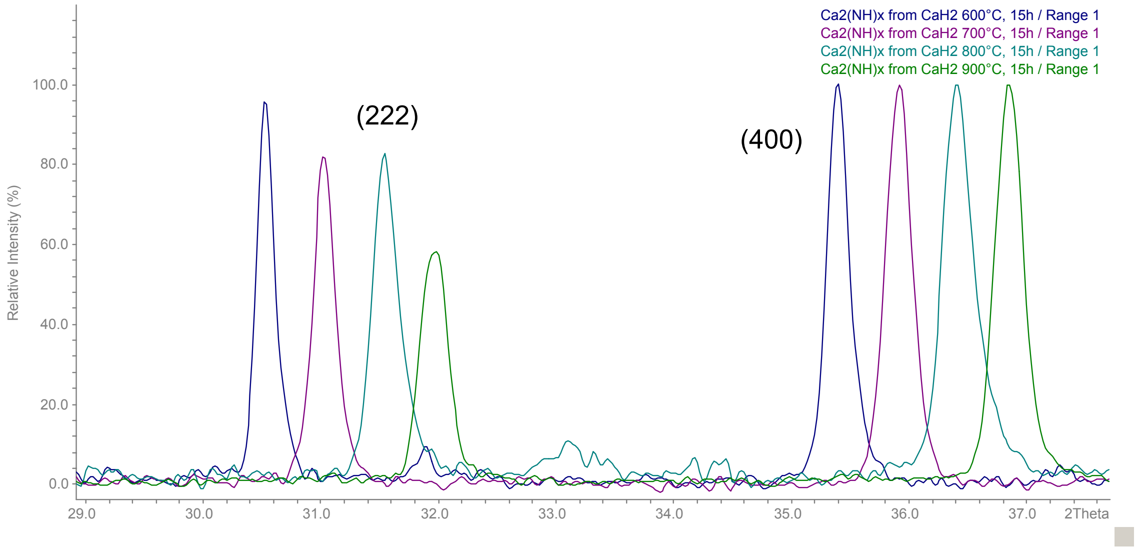

Figure 6-3: Zoomed section of XRD pattern in Figure 6-2; patterns have been staggered in *2θ* to show change in relative intensities

Refinements of the patterns, carried out using the Fullprof software, show a similar decrease in lattice parameter as was observed after simple indexing of peaks. Ca_2NH synthesised at 600°C has a lattice parameter of 10.141(1) Å, decreasing to 10.130(1) Å for a synthesis temperature of 900°C. For the remaining refinable parameters (atomic positions, isotropic temperature factors and occupancies) some comments need to be made first. The refinement software firstly, does not contain a proper scattering factor for the nitride ion (N^{3-}), so instead both scattering factors for the isoelectronic O^{-2} and F^{-1} ions were used. Furthermore, allowing the isotropic temperature factors to change freely, resulted in negative values for these, which does not make any physical sense. Also, temperature factors and occupancies are correlated, so unrealistic B-values are likely to result in bad estimates for the nitrogen occupancies. Therefore, these B-values were fixed to 1 $Å^2$, as approximately found by neutron powder diffraction (discussed in the next section). With these changes made, significant understoichiometry was found on the nitride site. It is therefore proposed that some substitution of both nitride and hydride sites occurs by imide ions (NH^{2-}). Again, as a scattering factor for N^{2-} is unavailable, imide ions were represented by O^{-1} and neutral F in the model, occupying both the nitride (½,½,½) and hydride (0,0,0) sites in equal amounts (there is no evidence of preferential substitution, yet). Table 6-1 shows the resulting values for the refinement parameters, using F^{-1} and neutral F to reflect N^{3-} and NH^{2-} ions. It shows that with increasing synthesis temperature, the substitution by imide ions seems to increase. The same trend is seen when O^{2-} and O^{-1} are used, but higher levels of imide substitution are found (up to 39% NH^{2-} occupancy on hydride and nitride site). Unexpectedly, the lattice parameter decreases with increasing synthesis temperature and increasing imide substitution. The pure imide phase has a slightly larger equivalent lattice parameter and a solid solution of imide in the nitride hydride phase should lead to a larger cell volume. It is stressed, that the X-ray diffraction patterns were of poor quality and that these refinements should be treated with caution. The hypothesis of imide substitution still needs to be confirmed, which will be attempted in the section describing neutron powder diffraction.

Table 6-1: Refinement results for Ca_2NH synthesised from CaH_2. Refinement in spacegroup *F d 3 m*, using F^{-1} for N^{3-} and neutral F for NH^{2-}. Isotropic temperature factors fixed to B = 1 Å^2.

Refinement parameter	*Synthesis Temperature*			
	600°C	700°C	800°C	900°C
a (Å)	10.141 (1)	10.135 (1)	10.137 (1)	10.130 (1)
R_p	24.9	22.0	11.8	25.1
R_{exp}	34.0	17.0	15.7	32.3
R_{wp}	9.41	9.96	8.73	13.6
Ca, 32e (x,x,x)				
x	0.2582 (4)	0.2500 (5)	0.2523 (5)	0.2507 (5)
N^{3-}, 16d (½,½,½)				
Occ	0.91 (3)	0.81 (3)	0.80 (2)	0.71 (2)
NH^{2-}, 16d (½,½,½)				
Occ	0.09 (3)	0.19 (3)	0.20 (2)	0.29 (2)
NH^{2-}, 16c (0,0,0)				
Occ	0.09 (3)	0.19 (3)	0.20 (2)	0.29 (2)

When calcium metal is reacted in nitrogen/hydrogen atmosphere, similar results are obtained. Again, the main product seems to be calcium nitride hydride, Ca_2NH, as the patterns can be indexed in the *F d 3 m* spacegroup with lattice parameters of 10.141(1) – 10.149(1) Å (as obtained from refinement in Fullprof). Unlike what was observed for reacting CaH_2, now the double cubic cell peaks ('superstructure' peaks, marked with red circles) remain observable in the XRD patterns throughout the reaction temperature range. Still, a change in the relative intensities of the main peaks (222), (400) and (440) is observed at the different reaction temperatures. Again this seems to be caused by a change in the chemical composition, as evidenced by a change in the calculated N^{3-} occupancy. The XRD patterns for Ca-N-H are shown in Figure 6-4 and a highlighted section is shown in Figure 6-5, which shows the change of relative intensities of the (222) and (400) peaks (the pattern at 800°C seems to be out of order). The results of the Fullprof refinements are shown in Table 6-2. The same refinement strategy was employed as described for the compounds synthesised from CaH_2. Isotropic temperature factors were fixed to 1 Å^2, scattering factors of F^{-1} and neutral F were used to reflect the nitride (N^{3-}) and imide (NH^{2-}) ion, respectively, and the deviation of nitride occupancy from unity was compensated by substitution by imide ions on both hydride (16c) and nitride (16d) sites. This time however, trends in the Ca position or the imide substitution are not that clear cut, as was observed for the compounds synthesised from CaH_2. Generally, imide substitution still seems to be more pronounced at higher synthesis temperature (>600°C).

Again, it is stressed that the X-ray diffraction patterns were of very poor quality and that these refinement results give rough trends at best. It is anticipated that better data will be obtained using neutron powder diffraction which is discussed in the following section. Figure 6-6 finally shows the theoretical patterns for calcium nitride hydride and calcium imide.

Table 6-2: Refinements for Ca_2NH synthesised from Ca metal. Spacegroup *F d 3 m*, using scattering factors of F^{-1} and neutral F for N^{-3} and NH^{2-}, respectively. Isotropic temperature factors fixed to B = 1 Å^2

Refinement parameter	*Synthesis temperature*			
	600°C	700°C	800°C	900°C
a (Å)	10.143 (1)	10.140 (1)	10.143 (2)	10.149 (1)
R_p	17.4	21.5	19.1	4.72
R_{exp}	14.1	27.7	24.3	6.08
R_{wp}	9.55	12.03	13.80	5.01
Ca, 32e (x,x,x)				
x	0.2519 (5)	0.2585 (4)	0.2529 (9)	0.2531 (4)
N^{3-}, 16d (½,½,½)				
Occ	0.98 (3)	0.83 (3)	0.85 (4)	0.90 (2)
NH^{2-}, 16d (½,½,½)				
Occ	0.02 (3)	0.17 (3)	0.15 (4)	0.10 (2)
NH^{2-}, 16c (0,0,0)				
Occ	0.02 (3)	0.17 (3)	0.15 (4)	0.10 (2)

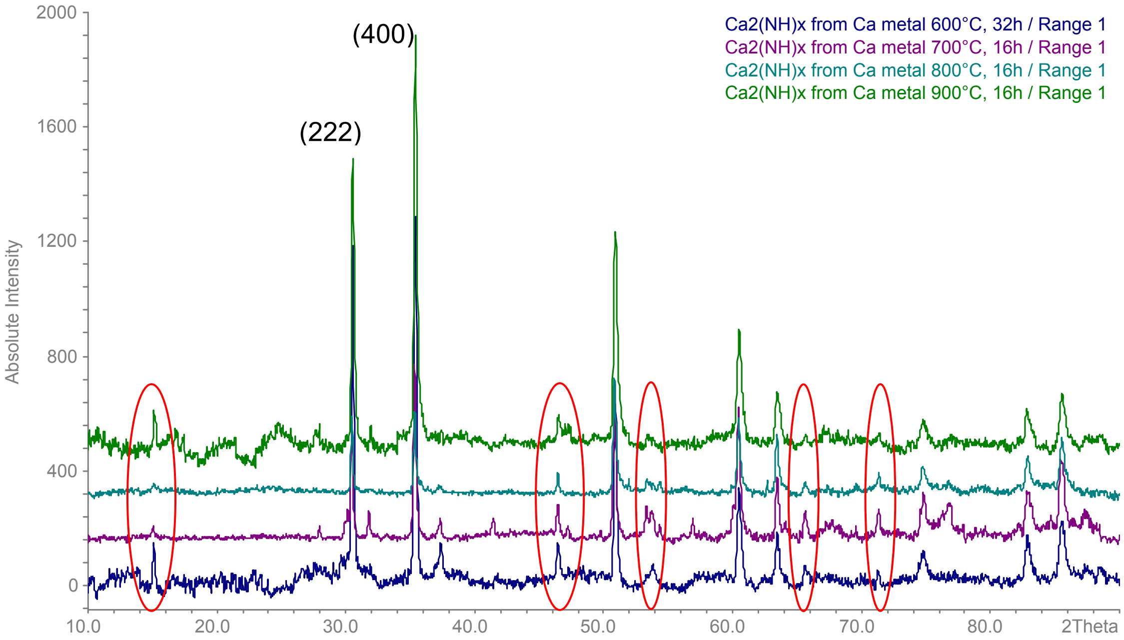

Figure 6-4: XRD patterns of Ca_2NH synthesised from Ca metal at different temperatures. Red circles mark double cubic cell peaks (all measured at room temperature)

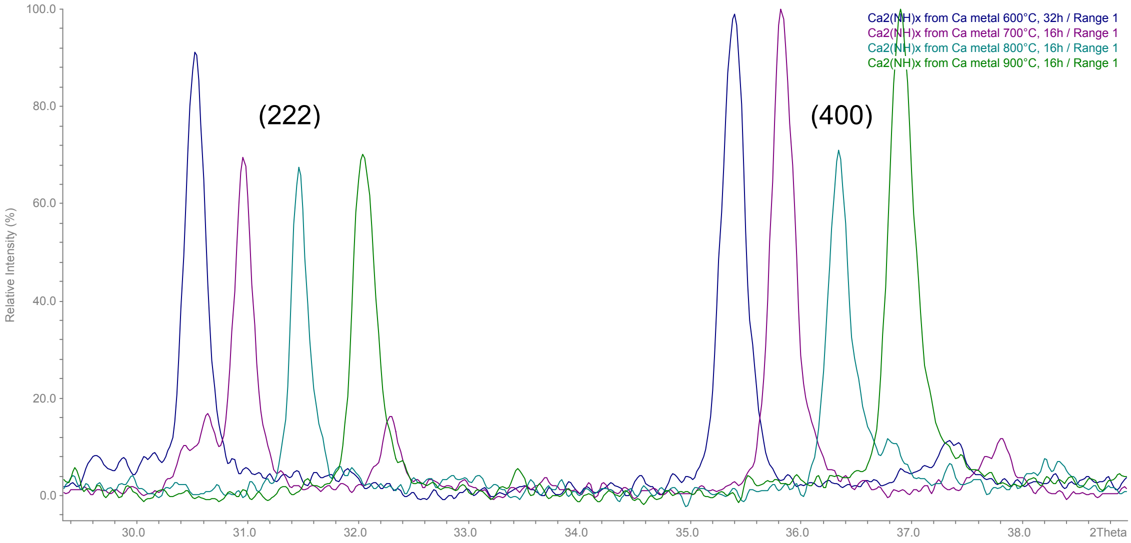

Figure 6-5: Zoomed section of XRD pattern in Figure 6-4; patterns have been staggered in *2θ* to show relative change in intensities

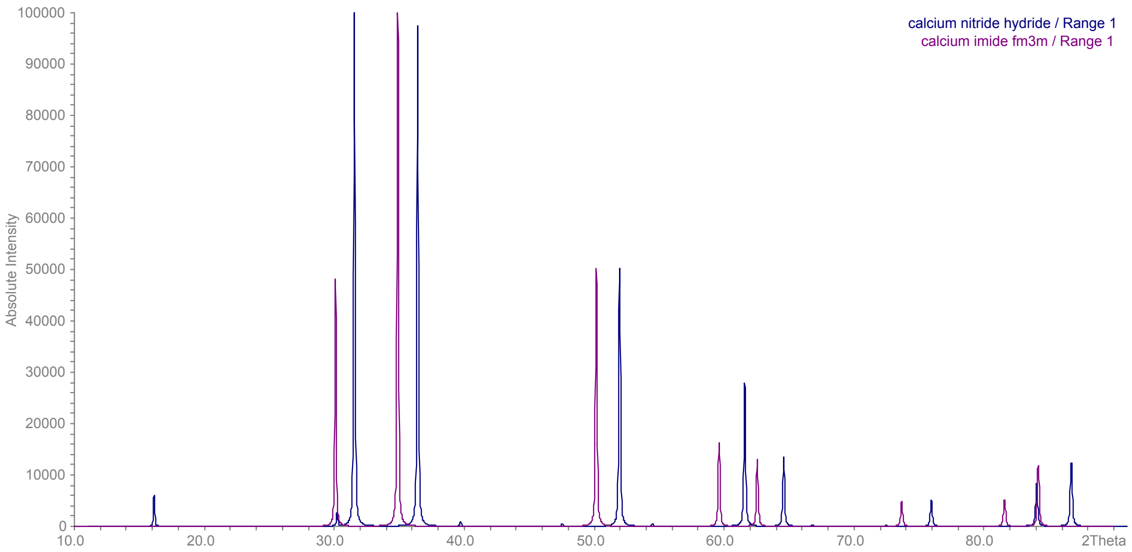

Figure 6-6: Theoretical XRD pattern for calcium imide, CaNH (purple) and calcium nitride hydride (blue), showing difference in relative intensities. Peaks have been staggered in 2θ to show differences more clearly.

6.1.3 Ca-N-H neutron diffraction results

As XRD gives little information about the positions of hydrogen in crystal structures and many XRD patterns were of poor quality anyway, neutron diffraction was carried out on a deuterided sample to get more structural data.

The diffraction pattern at room temperature could be indexed and refined in the *F d 3 m* spacegroup. The cubic lattice parameter of the Ca-N-D phase is 10.1550(2) Å, confirming the nitride hydride (deuteride) phase (Ca_2ND) being the predominant phase. Refinement of the diffraction data was again carried out using the Fullprof software. Initially, a straightforward model was used with spacegroup *F d 3 m* as suggested in literature, in which calcium ions occupy the 32e (x,x,x) sites (*x* being close to 0.25), nitride ions the 16d (½,½,½) sites and deuteride ions the 16c (0,0,0) sites. It was further observed that the background level in the diffraction pattern was slightly too high for a completely deuterided sample and therefore it is assumed that both hydrogen and deuterium are present in the compounds in a ratio of D : H of 9 : 1. Using this simple structural model, a relatively bad fit is obtained, which is mainly caused by a seemingly lower actual neutron scattering length density on the deuteride site. This could also be seen from the large isotropic temperature factor for D, suggesting a partially vacant crystallographic site. When the occupancies for N and D are allowed to change, an occupancy of 0.83 is obtained for D, whereas the nitride occupancy is calculated to be 1.05. Occupancies larger than 1 do not make any sense physically, but in this case it may be explained in terms of imide substitution (as already proposed in the X-ray diffraction section). A general formula $Ca_2N_{1-x}D_{1-y}(ND)_{x+y}$ is suggested.

To see whether imide ions could be present in the Ca_2ND (nitride hydride) structure, Fourier difference plots were made, after refinement in the simple model (fixing the nitride and deuteride occupancy to 1 initially). Fourier difference plots are an ideal tool to spot possible residual neutron scattering length density, after refinement. These Fourier difference plots showed negative scattering length density on the deuteride site, confirming that this site is partially vacant. Furthermore, small positive scattering length density is present around both the 16c and 16d sites, on 96g sites, at a distance of ~1 Å. This suggests that some imide ions might indeed be substituting for the nitride and deuteride ions. To accommodate for these additional imide ions, the structural model was adapted by putting nitrogen on 96g sites around the deuteride site (16c) and deuterium on a similar site around the nitride site (16d). The N-D distances were furthermore fixed to 0.92 Å, a typical bond length in an imide ion. Rather than putting the centre of mass of the imide ion on the ideal crystallographic sites (16c and 16d), it was reasoned that the original ions should stay on their respective sites (D on 16c and N on 16d), to assure retention of the N-D ordering in the cubic structure. The diffraction pattern suggests that ordering is still strong. Obviously, the initially observed vacancy on the deuteride site (16c) could not be compensated by adding extra nitrogen in the vicinity of the site. Therefore the occupancy of this site was fixed to 0.75. This is in agreement with Brice's model [107], with two hydride ion sites, the 16c site being only 75% occupied. The fourier difference plots in this research suggest some residual neutron scattering on the 8a $\left(\frac{1}{8}\frac{1}{8}\frac{1}{8}\right)$ site, which could be where the remaining deuteride ions are situated (see Figure 6-7). The 8a site is tetrahedrally coordinated to both calcium and and deuterium.

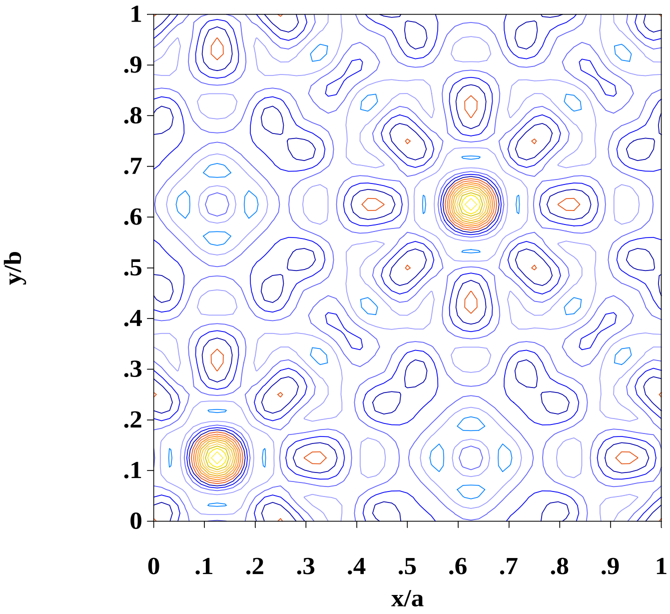

Figure 6-7: Fourier difference map of the x-y plane at z=1/8, showing residual neutron scattering length density on the 8a site

The new model, including imide ions and deuteride ion vacancies on the 16c site, has slightly improved R-values as compared to the first simple model, in which N and D occupancies are allowed to change. A third model, which includes a second deuteride ion site (8a) as suggested by Fourier mapping, has even better R-values. Such a model where additional deuterium is situated in the Ca tetrahedral is in agreement with a neutron diffraction study on Ba_2NH [112]. In the current study, the 8a site is however only 8% occupied, leaving the compound with a net deuterium understoichiometry of 0.79. The results for the refinements using these three different structural models is summarised in Table 6-3. The general formula for the compound is now of the form: $Ca_2N_{1-x}D_{1-y-\delta}(ND)_{x+y}$, where δ stands for the additional D^- vacancies. As can be seen from Table 6-3, imide substitution seems equally distributed over both the nitride (16d) and deuteride (16c) sites, resulting in a net charge neutral defect, as explained by the following Kröger-Vink equation (6.5). From the refinements an imide substitution of $x \sim y \sim 0.08 – 0.10$ is calculated. The positively charged D^- vacancies ($V_D^{\bullet}$) are most likely charge compensated by electronic defects.

$$xN_N^x + yD_D^x + \tfrac{y}{2}N_2 + \tfrac{x}{2}D_2 \longrightarrow xND_N^{\bullet} + yND_D^{'} \tag{6.5}$$

Across the models there is a small variation of the position of the calcium ions. It is however always slightly displaced from the ideal octahedral coordination with both deuterium and nitrogen, such that it is closer to nitrogen than deuterium. This can be explained by the stronger electrostatic attraction from the N^{3-} ion as compared to D^-.

Finally, a secondary phase can be observed, which was identified to be CaO. Whether the CaO originates from impurities in the glovebox atmosphere or in the calcium metal is uncertain. According to abundant crystallographic data on CaO, it is a cubic compound with spacegroup *F m 3 m* and a lattice parameter of 4.81 Å. This information was used to make the secondary CaO phase an internal standard in order to refine the neutron wavelength at 1.9114 Å. Adding another phase to the refinement model, to accommodate a possible calcium imide phase, does not improve the overall refinement. In fact, the Fullprof software quickly sets the content of this third imide phase to zero, indicating that calcium nitride hydride forms as single phase under the reaction conditions (600°C, 5% H_2/D_2, 1 – 2% N_2 in argon), apart from some calcium oxide impurity.

Table 6-3: Neutron diffraction refinement results for Ca_2ND at room temperature, spacegroup *F d 3 m*, λ = 1.9114 Å

Refinement parameter	Standard Ca_2ND model	$Ca_2N_{1-x}D_{1-y-\delta}(ND)_{x+y}$	$Ca_2N_{1-x}D_{1-y-\delta}(ND)_{x+y}$ including 2nd D^- site on 8a
a (Å)	10.1550 (2)	10.1550 (2)	10.1550 (2)
R_p	4.21	4.16	4.08
R_{wp}	5.40	5.32	5.27
R_{exp}	2.79	2.79	2.79
χ^2	3.74	3.65	3.58
Ca, 32e (x,x,x)			
x	0.2572 (2)	0.2579 (3)	0.2581 (3)
B (Å^2)	1.18 (8)	1.30 (6)	1.34 (6)
N1, 16d (½,½,½)			
B (Å^2)	1.25 (5)	1.08 (4)	1.14 (4)
Occ	1.05 (1)	1.00	1.00
D1/H1, 16c (0,0,0)			
B (Å^2)	4.7 (1)	3.7 (1)	3.7 (1)
Occ	0.83 (1)	0.75	0.75
N2, 96g (x,x,z) *imide coordinated to D1/H1*			
x	-	0.061 (4)	0.063 (3)
z	-	0.028 (10)	0.042 (9)
B (Å^2)	-	3.7 (1)	3.7 (1)
Occ	-	0.014 (1)	0.015 (1)
D2, 96g (x,x,z) *imide coordinated to N1*			
x	-	0.562 (1)	0.5686 (8)
z	-	0.477 (10)	0.517 (6)
B (Å^2)	-	1.08 (4)	1.14 (4)
Occ	-	0.016 (4)	0.018 (2)
D4, 8a $\left(\frac{1}{8}\frac{1}{8}\frac{1}{8}\right)$			
B (Å^2)	-	-	3.7 (1)
Occ	-	-	0.081 (4)
d (Ca-N) (Å)	2.468 (2)	2.462 (3)	2.460 (3)
d (Ca-D) (Å)	2.614 (2)	2.620 (3)	2.623 (3)

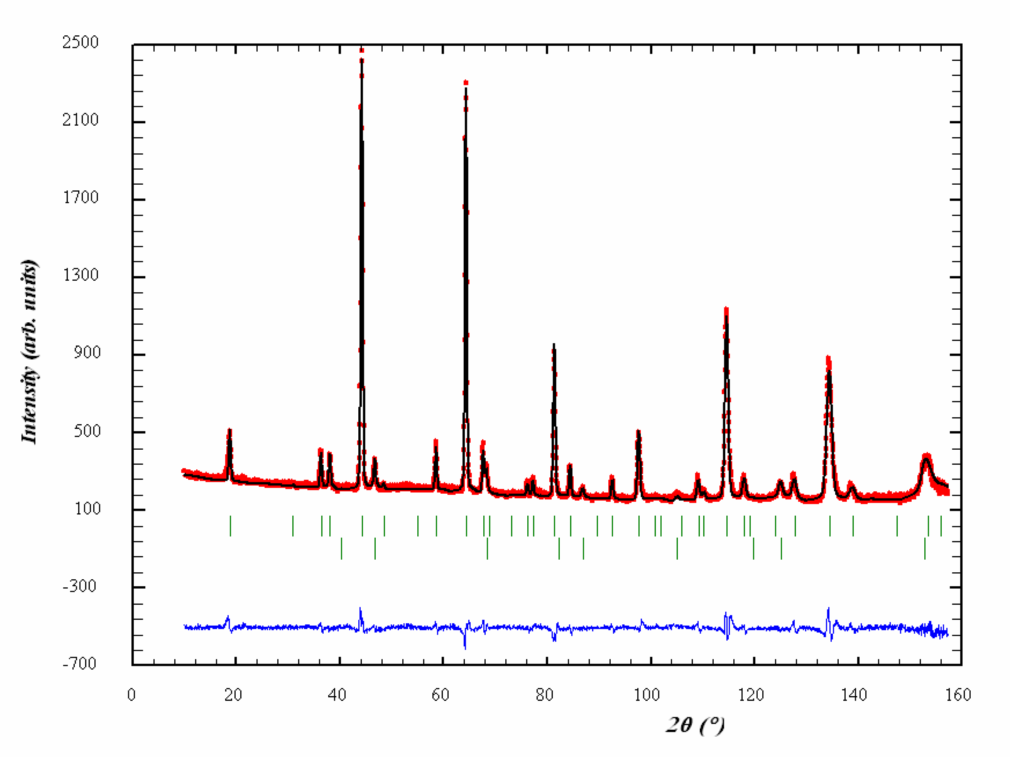

Figure 6-8: Neutron diffraction pattern of $Ca_2N_{1-x}D_{1-y-\delta}(ND)_{x+y}$ at room temperature (red curve); refinement (black curve) in spacegroup *F d 3 m*, using a model with imide substitution and 2nd D^- site on 8a. Second phase is CaO. Blue trail shows residuals (observed – calculated intensiy). Green ticks show reflections

The diffraction patterns of Ca_2ND at 250°C, 450°C and 650°C can be seen in Figure 6-10. They could all be indexed and refined in the *F d 3 m* spacegroup, indicating that there are no first order phase changes over this temperature range. The patterns have been refined using the two models that involve imide ion substitution on both hydride and nitride sites, as these gave the best fits for the sample measured at room temperature. Figure 6-9 shows a linear relationship between the cubic lattice parameter and temperature, indicating that no major distortions of the lattice take place upon heating. A small increase in the imide content was surprisingly observed with increasing temperature. As this seems unlikely in vacuum, where no additional deuterium or nitrogen can be incorporated from the atmosphere, the imide content was fixed for the higher temperatures (450°C and 650°C). On closer inspection of the pattern recorded at 650°C, a significant reduction in the intensity of the superstructure peaks can be observed. This is seen most clearly from the relative intensities of the (311) and (222) peaks and the (533) and (622) peaks, which are shown in detail in the close ups in Figure 6-10. Both the (311) and (533) peaks decrease in intensity compared to their neighbour at higher temperature. This is an indication for a lowering of the N-D ordering in the crystal structure. But as the peaks that are typical for the double cubic cell have not disappeared completely, yet, the pattern cannot be refined in a simple cubic structure with spacegroup *F m 3 m* (where both N and D statistically occupy 50% of calcium's octahedral sites). Instead, some of the nitride and deuteride ions are allowed to cross over to each other's respective sites, to accommodate some disordering. It is expected that at even higher temperatures, or for longer equilibration times at 650°C, Ca_2ND would be completely disordered. Ca_2NF is actually reported to have such a disordered structure at room temperature, with N and F statistically coordinating calcium octahedrally [113]. Recent single crystal X-ray diffraction tests however, suggest N-F ordering in a tetragonal symmetry at room temperature [114].

Also, when refining the additional deuteride site, 8a, the occupancy of this site gradually decreases with increasing temperature. In fact, in the thermal analysis section that will be presented in section 6.1.4, it is shown that some deuterium is lost from the structure at ~580°C. This may mean that the deuterium on site 8a is metastable and disappears at intermediate temperatures.

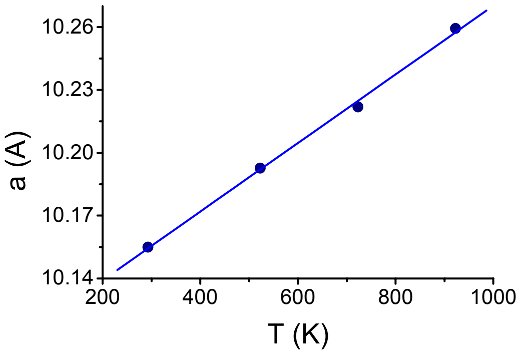

Figure 6-9: Linear relationship of cubic lattice parameter with temperature for $Ca_2N_{1-x}D_{1-y-\delta}(ND)_{x+y}$

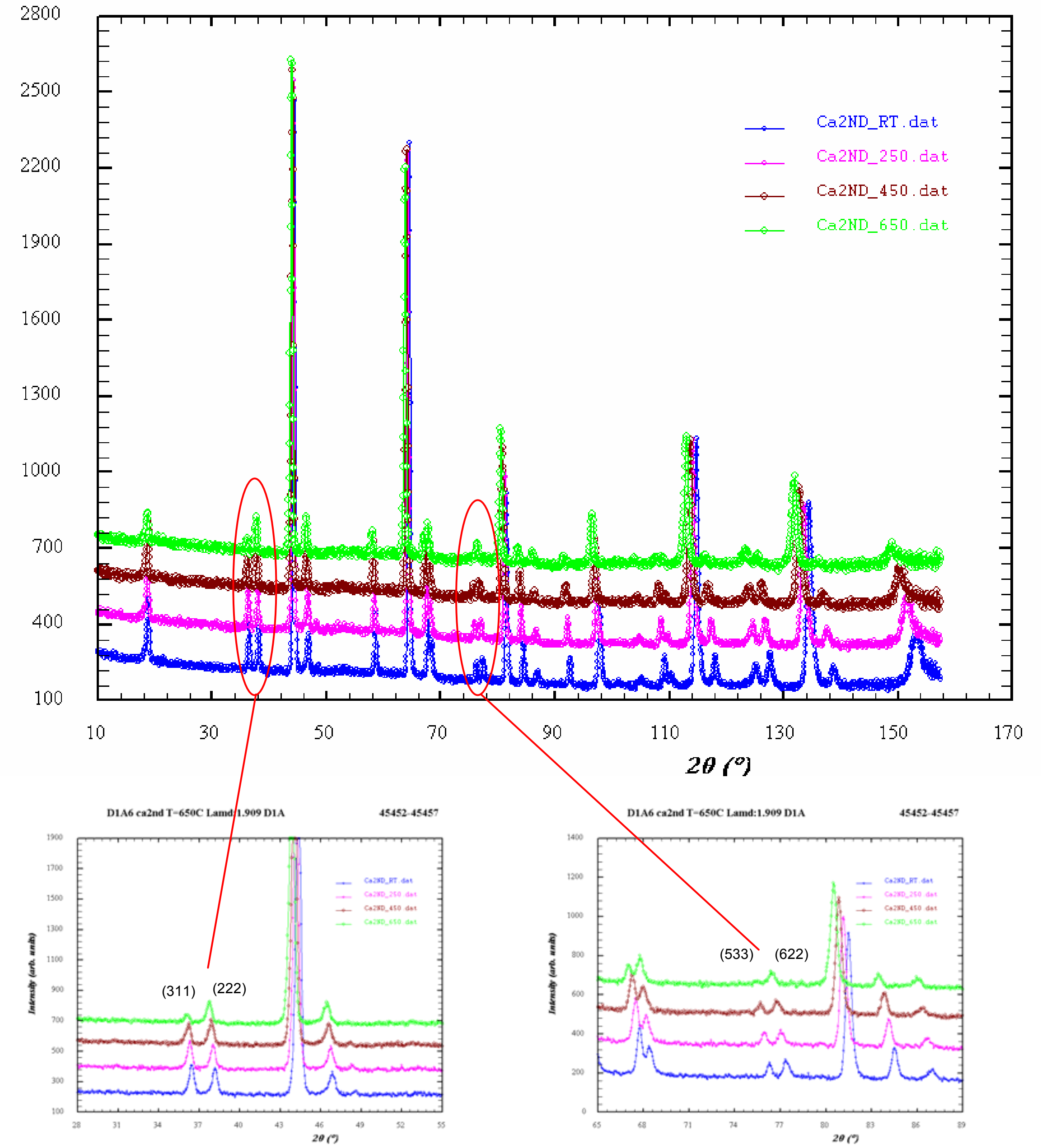

Figure 6-10: Neutron diffraction patterns of Ca_2ND at 20°C (blue), 250°C (pink), 450°C (brown) and 650°C (green) in vacuum. Down left: zoomed section highlighting (311) and (222) peaks. Down right: zoomed section highlighting (533) and (622) peaks.

Table 6-4: Refinement of $Ca_2N_{1-x}D_{1-y-\delta}(ND)_{x+y}$ at different temperatures in spacegroup *F d 3 m*, λ = 1.9114 Å. Structural model includes imide substitution on 16c and 16d sites. Partial N-D disorder takes place at 650°C

Refinement parameter	T = 20°C	T = 250°C	T = 450°C	T = 650°C
a (Å)	10.1550 (2)	10.1927 (2)	10.2219 (2)	10.2567 (2)
R_p	4.16	3.69	3.19	3.15
R_{wp}	5.32	4.76	3.88	3.78
R_{exp}	2.79	2.73	2.69	2.74
χ^2	3.65	3.04	2.07	1.90
Ca, 32e (x,x,x)				
x	0.2579 (3)	0.2589 (3)	0.2597 (2)	0.2559 (3)
B (Å^2)	1.30 (6)	1.52 (8)	1.77 (6)	3.02 (6)
N1, 16d (½,½,½)				
B (Å^2)	1.08 (4)	1.41 (5)	2.16 (5)	2.10 (5)
Occ	1.00	1.00	1.00	0.88 (10)
D1/H1, 16c (0,0,0)				
B (Å^2)	3.7 (1)	4.1 (1)	3.4 (1)	4.7 (1)
Occ	0.75	0.75	0.75	0.74 (10)
N2, 96g (x,x,z) *imide coordinated to D1/H1*	0.061 (4)	0.021 (3)	0.037 (3)	0.039 (4)
x	0.028 (10)	0.085 (2)	0.074 (3)	-0.071 (5)
z	3.7 (1)	4.1 (1)	3.4 (1)	4.7 (1)
B (Å^2)	0.014 (1)	0.018 (1)	0.0167	0.0167
Occ				
D2/H2, 96g (x,x,z) *imide coordinated to N1*				
x	0.562 (1)	0.551 (3)	0.529 (4)	0.545 (3)
z	0.477 (10)	0.446 (6)	0.420 (3)	0.436 (5)
B (Å^2)	1.08 (4)	1.41 (5)	2.16 (5)	2.10 (5)
Occ	0.016 (4)	0.021 (2)	0.0167	0.0167
N3, 16c (0,0,0) partial disorder				
B (Å^2)	-	-	-	4.7 (1)
Occ	-	-	-	0.12 (10)
D3/H3, 16d (½,½,½) partial disorder				
B (Å^2)	-	-	-	2.10 (5)
Occ	-	-	-	0.01 (10)
d (Ca-N) (Å)	2.462 (3)	2.461 (3)	2.460 (2)	2.505 (3)
d (Ca-D) (Å)	2.620 (3)	2.642 (3)	2.658 (2)	2.626 (3)

Table 6-5: Refinement of $Ca_2N_{1-x}D_{1-y-\delta}(ND)_{x+y}$ at different temperatures in spacegroup *F d 3 m*, λ = 1.9114 Å. Structural model includes imide substitution on 16c and 16d sites and an additional D^- site on 8a. Partial N-D disorder takes place at 650°C

Refinement parameter	T = 20°C	T = 250°C	T = 450°C	T = 650°C
a (Å)	10.1550 (2)	10.1927 (2)	10.2219 (2)	10.2567 (2)
R_p	4.08	3.66	3.14	3.11
R_{wp}	5.27	4.72	3.82	3.74
R_{exp}	2.79	2.73	2.69	2.74
χ^2	3.58	2.99	2.01	1.86
Ca, 32e (x,x,x)				
x	0.2581 (3)	0.2591 (3)	0.2603 (2)	0.2559 (3)
B (Å^2)	1.34 (6)	1.47 (8)	1.65 (6)	3.05 (6)
N1, 16d (½,½,½)				
B (Å^2)	1.14 (4)	1.42 (5)	2.24 (5)	2.25 (6)
Occ	1.00	1.00	1.00	0.90 (10)
D1/H1, 16c (0,0,0)				
B (Å^2)	3.7 (1)	4.0 (1)	3.2 (1)	4.5 (1)
Occ	0.75	0.75	0.75	0.75 (10)
N2, 96g (x,x,z) *imide coordinated to D1/H1*				
x	0.063 (3)	0.013 (4)	0.033 (4)	0.037 (4)
z	0.042 (9)	0.088 (1)	0.077 (3)	-0.073 (4)
B (Å^2)	3.7 (1)	4.0 (1)	3.2 (1)	2.25 (6)
Occ	0.015 (1)	0.018	0.018	0.018
D2/H2, 96g (x,x,z) *imide coordinated to N1*				
x	0.5686 (8)	0.551 (3)	0.531 (3)	0.546 (5)
z	0.517 (6)	0.446 (5)	0.422 (3)	0.438 (7)
B (Å^2)	1.14 (4)	1.42 (5)	2.24 (5)	4.5 (1)
Occ	0.018 (2)	0.024	0.021	0.021
N3, 16c (0,0,0) partial disorder				
B (Å^2)	-	-	-	4.5 (1)
Occ	-	-	-	0.10 (10)
D3/H3, 16d (½,½,½) partial disorder				
B (Å^2)	-	-	-	2.25 (6)
Occ	-	-	-	0.00 (10)
D4/H4, 8a $\left(\frac{1}{8}\frac{1}{8}\frac{1}{8}\right)$				
B (Å^2)	3.7 (1)	4.0 (1)	3.2 (1)	4.5 (1)
Occ	0.081 (4)	0.071 (7)	0.066 (3)	0.052 (2)
d (Ca-N) (Å)	2.460 (3)	2.459 (3)	2.455 (2)	2.505 (3)
d (Ca-D) (Å)	2.623 (3)	2.644 (3)	2.665 (2)	2.626 (3)

From Table 6-4 and Table 6-5 it can be seen that the N-D disordering mainly involves nitrogen moving from the 16d site to the partially vacant 16c (D^-) site. This way, the deuteride vacancies become more evenly distributed over the two octahedral sites. Because of this disordering process, calcium moves slightly closer to its ideal site (¼,¼,¼) as the electrostatic forces start to become more averaged out over the 16c and 16d sites.

Because a gradual disappearance of the superstructure peaks is observed in our experiments over a wider temperature range, rather than a sudden transition to a completely disordered structure, this transition seems to be second order in nature. A thermal event in the DTA for both Ca_2ND and Ca_2NH could be observed at ~630°C in argon atmosphere, which is probably the onset of this second order disordering process. The thermal analysis results for Ca_2ND will be presented in 6.1.4.

6.1.3.1 A different Ca_2ND sample

A different Ca_2ND sample was also synthesised, but under different conditions than the sample discussed above. The synthesis was carried out in a quartz reactor, by reacting calcium metal with a flowing mixture of argon, deuterium and nitrogen. The gases were mixed using flowmeters, so that the concentrations of deuterium and nitrogen were 7% in argon each. Importantly the nitrogen concentration is significantly higher than that used for the preparation of the first sample, but the flowmeters did not allow lower gas flows and hence higher gas concentrations for D_2 and N_2 were used. No contamination with H_2 occurred during the preparation of this sample.

Neutron diffraction was carried out on this sample under identical conditions as described previously, apart from the neutron wavelength being 1.9095 Å. As for the previous sample, calcium oxide is present as a secondary phase. A third phase is even present, CaD_2. The lattice parameter of the second sample is significantly smaller than the first sample, *i.e.* 10.1236(2) Å instead of 10.1550(2) Å. A clear change in the intensity of some peaks as compared to the pattern in Figure 6-8 can also be seen. Both these changes can partly be explained by the absence of hydrogen in the structure, due to its higher thermal displacement and negative scattering factor. The overall stoichiometry of the compound however, also plays a large role. This first becomes evident after a quick refinement using the simplest model, as discussed in section 6.1.3, where the occupancies of the nitride and deuteride sites (16d and 16c, respectively) are allowed to change (results shown in Table 6-6). Whereas for the previous sample a large understoichiometry for deuterium was seen, with the D^- (16c) site only 75% occupied, this sample seems to have excess neutron scattering length density on this particular crystallographic site. The nitrogen site for this sample has a small excess scattering density as well, which is comparable to the previous sample. This shows how important the partial hydrogen/deuterium and nitrogen pressures during synthesis are to the resulting composition of these nitride hydride materials. Using the same reasoning as used for the previous refinements, the observed excess neutron scattering length density could be caused by imide ion substitution on the nitride and deuteride sites. Still no sign of a separate imide phase can be observed. Again, the general formula will be of the form $Ca_2N_{1-x}D_{1-y}(ND)_{x+y}$, which for this sample does not contain any deuterium vacancies. Table 6-6 shows the refinement results using the same three structural models that were used for the previous sample. It shows that the large excess neutron scattering length density on site 16c is compensated by a large imide ion substitution (y ~ 0.20). The substitution on this 16c site is twice as large as that for the 16d (nitride) site. The 16c is not partially vacant and additional D^- sites are therefore not necessary. However, Fourier difference maps for this sample still suggest significant residual neutron scattering length density on the 8a site, as found for the previous sample. Therefore, this site was added again in a third structural model to see whether the fit would be improved. As seen from Table 6-6 it does improve the fit, but adding deuteride ions does not make sense chemically. The larger imide substitution on the D^- site (16c) as compared to substitution on the N^{3-} site (16d), already causes a net negative defect (see equation (6.5)) and therefore we should be adding a positively charged defect to the structure to retain charge neutrality. Interstitial calcium ions, $Ca_i^{\bullet\bullet}$ would be such a defect. Interstitial calcium occupancy on the 8a site would then be 0.12(3).

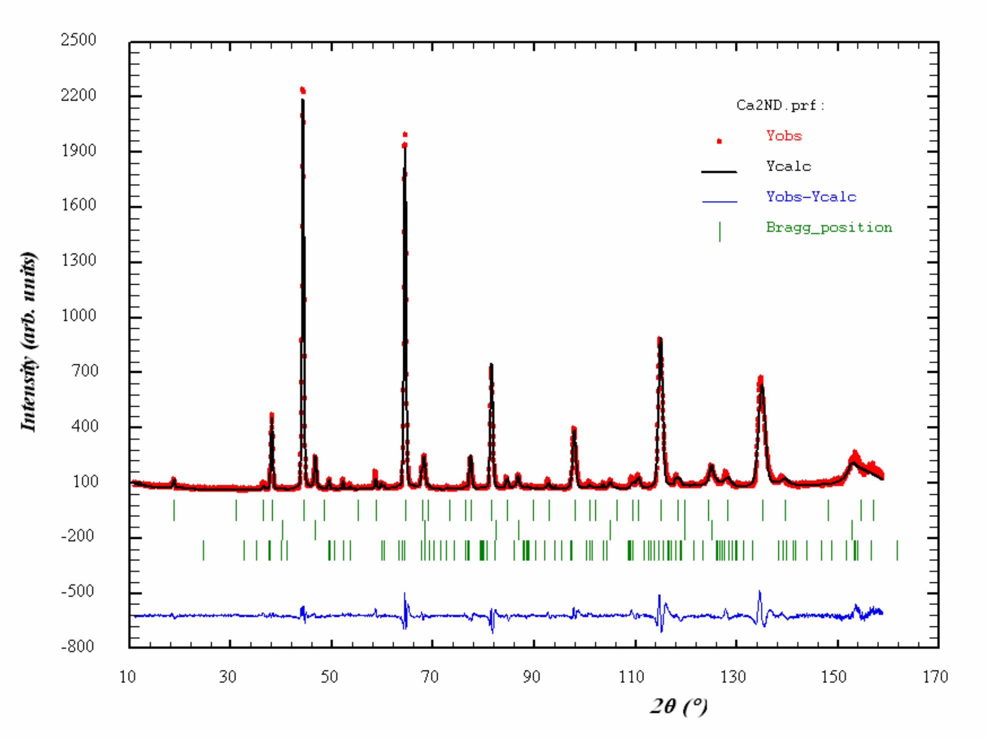

Figure 6-11: Neutron diffraction pattern for a second Ca_2ND without hydrogen contamination (red curve). CaO and CaD_2 are present as a second and third phase, respectively. Refinement (black curve) of Ca_2ND phase in spacegroup *F d 3 m*, including imide ion substitution on sites 16c and 16d. Blue trail shows difference plot for (observed – calculated) intensity. Green ticks show reflections

Table 6-6: Refinement result for 2nd fully deuterided Ca_2ND sample at room temperature, spacegroup *F d 3 m*, λ = 1.9095 Å

Refinement parameter	Standard model Ca_2ND	$Ca_2N_{1-x}D_{1-y-\delta}(ND)_{x+y}$	$Ca_2N_{1-x}D_{1-y-\delta}(ND)_{x+y}$ including 2nd D^- site on 8a
a (Å)	10.1238 (2)	10.1238 (2)	10.1238 (2)
R_p	6.99	6.93	6.77
R_{wp}	9.09	9.22	8.99
R_{exp}	3.94	3.93	3.93
χ^2	5.33	5.49	5.22
Ca, 32e (x,x,x)			
x	0.2558 (4)	0.2569 (5)	0.2583 (5)
B (Å^2)	0.94 (8)	1.54 (7)	1.26 (8)
N1, 16d (½,½,½)			
B (Å^2)	1.08 (5)	1.05 (6)	1.14 (8)
Occ	1.10 (1)	1.00	1.00
D1, 16c (0,0,0)			
B (Å^2)	4.0 (1)	2.4 (1)	2.0 (1)
Occ	1.27 (1)	1.00	1.00
N2, 96g (x,x,z) *imide coordinated to D1/H1*	-	0.0694 (3)	0.0637 (4)
x	-	0.011 (4)	0.012 (5)
z	-	2.4 (1)	2.0 (1)
B (Å^2)	-	0.034 (2)	0.034 (1)
Occ			
D2, 96g (x,x,z) *imide coordinated to N1*	-	0.5697 (5)	0.5641 (6)
x	-	0.506 (12)	0.494 (12)
z	-	1.05 (6)	1.14 (8)
B (Å^2)	-	0.016 (2)	0.019 (2)
Occ			
D3, 8a $\left(\frac{1}{8}\frac{1}{8}\frac{1}{8}\right)$			
B (Å^2)	-	-	2.0 (1)
Occ	-	-	0.092 (7)
d (Ca-N) (Å)	2.474 (4)	2.463 (5)	2.450 (4)
d (Ca-D) (Å)	2.591 (4)	2.603 (5)	2.618 (4)

6.1.4 Ca-N-H thermal analysis

Combined differential thermal analysis (DTA), thermal gravimetrical analysis (TGA) and mass spectroscopy (MS) was performed on the Ca_2ND samples (sample identical to the first material discussed in the neutron diffraction section). The tests were performed on a Netzsch Jupiter STA 449C linked to a Pfeiffer Vacuum Thermostar mass spectrometer in three different atmospheres: argon, 5% H_2/argon and nitrogen. Runs were performed with heating/cooling rates of 5 K/min and an isotherm of 60 minutes at 900°C.

Figure 6-12 shows the DTA graphs for Ca_2ND in argon and 5% H_2/argon. It also shows the DTA for Ca_2NH in argon for comparison. It can be seen that in argon, at 620 – 640°C the slopes of all DTAs change drastically, which is probably due to a second order phase change. As discussed in the neutron diffraction section, this phase change is interpreted as an order – disorder transition resulting in crossover of nitrogen and deuterium/hydrogen in the crystal structure (between site 16c and 16d). A TGA event takes place just below this temperature (570 – 580°C), but this event can be related to the small exothermic dip in the DTA, just before the change of slope. The TGA results are presented in Table 6-7 and Figure 6-13. The minor dip at 570 – 580°C is due to the first deuterium loss from Ca_2ND, which will be discussed shortly. The temperature for the order – disorder transition seems to be in excellent agreement with neutron diffraction results, which show a significant decrease in intensity of the superstructure peaks at 650°C, which can still clearly be observed at lower temperatures.

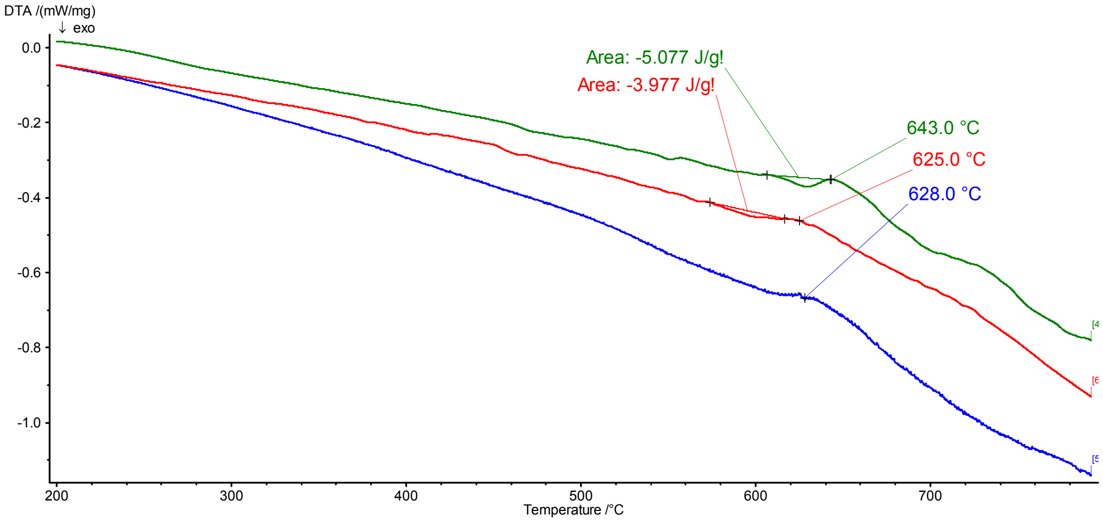

Figure 6-12: DTA graphs for Ca_2ND in argon (green) and 5% H_2/argon (red). Blue graph shows the DTA for Ca_2NH in argon

In the TGA/MS on Ca_2ND in argon (shown in Figure 6-13 and Figure 6-14), four separate weight losses can be observed. The details of these weight losses are listed in Table 6-7. The first weight loss occurs at a low temperature, i.e. 222°C and is not believed to be caused by thermal decomposition of the Ca_2ND. The weight loss is small, ~0.07 wt%, and masses 2, 3, 17 and 18 are the predominant ion masses being recorded by MS. This is indicative for loss of water, which is most probably caused by the thermal decomposition of calcium hydroxide into calcium oxide (see equation (6.6)). The dehydration temperature is in excellent agreement with the value of 215°C reported by Chaix-Pluchery et al., who performed a diffraction study on the dehydration of calcium hydroxide in vacuum [115]. The partial pressure of water in this study (argon atmosphere) will be similar to the one in vacuum. The presence of calcium hydroxide is explained by the short time the Ca_2ND sample is exposed to air, when loading it into the TGA machine.

$$Ca(OH)_2 \longrightarrow CaO + H_2O \tag{6.6}$$

The next weight loss of 0.29% occurs at ~570 – 580°C and involves release of deuterium gas (masses 2, 3 and 4 mainly detected). This weight loss corresponds to a release of only 0.16 formula units of deuterium from the structure and may involve the interstitial deuterium/hydrogen ions on the 8a sites, as found by neutron powder diffraction. Interstitial deuterium/hydrogen only amounts to 0.05 formula units, however. More deuterium release is found at slightly higher temperature, 671°C. This again is not believed to involve Ca_2ND, since this temperature is in perfect agreement with the decomposition temperature of CaH_2 (in argon, as shown in chapter 3, section 3.4.1), which was found to be 675°C. The weight loss of 0.05 wt% suggests a phase content of 1.2% CaD_2 in Ca_2ND. This phase was not observed in either X-ray or neutron diffraction studies. The last weight loss of 1.98% involves both deuterium and nitrogen release and starts at 731°C. In the TGA/MS graph (Figure 6-13 and Figure 6-14) it can be seen that at the isotherm at 900°C, both the nitrogen and deuterium loss seem to be diffusion limited and their release drops rapidly after the isotherm stops. Hence it is believed that the decomposition of Ca_2ND into its elements is not complete.

Table 6-7: Temperatures, weight losses and gasses released when thermally decomposing Ca_2ND in three atmospheres

Temperature (°C)	Weight loss (wt%)	Ion masses involved	Molecules involved
Thermal analysis in Ar			
222	-0.07	m2, m3, m17, m18	H_2O
574	-0.29	m2, m3, m4	D_2 (HD)
671	-0.05	m2, m3, m4	D_2 (HD)
731	-1.98	m2, m3, m4	D_2 (HD)
		m14, m28	N_2
Thermal analysis in 5% H_2/ Ar			
256	-0.12	m2, m3, m17, m18	H_2O
581	-0.74	m2, m3, m4	HD (D_2)
760	-0.98	m14, m28	N_2
Thermal analysis in N_2			
218	-0.06	m2, m3, m17, m18	H_2O
572	-0.20	m2, m3, m4	D_2 (HD)
647	+2.00		
795	-1.08	m2, m3, m4	D_2 (HD)

The TGA/MS data for the runs in 5% H_2/argon and nitrogen are also displayed in Table 6-7 and Figure 6-15, Figure 6-17 and Figure 6-18. They show similarities to the argon run, however some interesting differences are observed. Firstly, all runs show the minor weight loss at 220 – 260°C, explained by dehydration of calcium hydroxide. Secondly, all runs show the first weight loss of Ca_2ND, due to deuterium release at 570 – 580°C. It was anticipated that this decomposition step would be found at a higher temperature in the 5% H_2 run, because of the presence of hydrogen. The atmosphere apparently has not got an influence on the loss of the first deuterium/hydrogen from the structure. This was confirmed by an identical TGA/MS run in 5% H_2/argon using a Ca_2NH sample. For this sample, the first hydrogen was released at even slightly lower temperature, i.e. 540°C. Also, strangely enough, the deuterium loss in 5% H_2 atmosphere is larger (0.39 formula units of D) than in both argon and nitrogen atmospheres (i.e. 0.15 and 0.11 formula units of D, respectively). The release of nitrogen in 5% H_2 atmosphere is found at slightly higher temperature than in argon, i.e. 760°C as compared to 730°C. Moreover, the nitrogen release amounts to 0.98%, so roughly half of the total weight loss found in argon at that temperature. In Figure 6-17 it can be seen, that only nitrogen is released from the structure at 760°C, as the nitrogen peaks (m14, m28) start where the deuterium peak (m4) stops. So at least the second loss does depend on the presence of a hydrogen partial pressure. An alternative explanation for the larger deuterium loss at 570°C is the fact that an isotope exchange takes place. Total isotope H – D exchange would have a weight loss of 0.68 wt%, which is close to the 0.74 wt% which is experimentally found. The initial hydrogen loss, as observed in Ca_2NH at 540°C would bring the total weight loss to 0.82 wt%, which is still close to the experimental value. Isotope exchange will be discussed in further detail after presenting the results for the Sr-N-D system.

Similarly, for the run in nitrogen atmosphere (Figure 6-18), the loss of nitrogen is not observed and is instead replaced by a weight gain. This can either be caused by the formation of a tricalcium dinitride phase, Ca_3N_2, according to equation (6.7) or by the formation of imide ions on the deuteride sites (see equation (6.9) in Kröger-Vink notation). The theoretical weight gain for the first reaction is 4.61%, whereas a completed substitution with imide ions would result in 4.32 wt% weight gain. The actual gain is only 2.00 wt%. Substitution with imide ions is the most likely cause for the weight gain, as it is expected that reaction (6.7) would result in concomitant release of deuterium (Ca_2ND does not fully decomposes into Ca_2N until ~800°C, see Table 6-7, and reaction (6.8) would occur instead at 650°C). No loss of deuterium is observed however in the MS trails, as shown in Figure 6-18. Then at 795°C more deuterium is released; the weight loss is 1.08%. It is assumed that no nitrogen is released under the nitrogen atmosphere (this cannot be confirmed by MS, since the background level is too high). So after a TGA/MS run in three different atmospheres, it seems that the weight loss at 730°C in argon consists of ~1 wt%

N_2 and ~1 wt% D_2. This again would correspond to the loss of 0.08 formula units of N and 0.56 formula units of D in Ca_2ND.

$$Ca_2N + \tfrac{1}{6}N_2(g) \longrightarrow \tfrac{2}{3}Ca_3N_2 \tag{6.7}$$

$$Ca_2ND_{1-\delta} + \tfrac{1}{6}N_2(g) \longrightarrow \tfrac{2}{3}Ca_3N_2 + \tfrac{1-\delta}{2}D_2(g) \tag{6.8}$$

$$N_N^{\times} + 2D_D^{\times} + \tfrac{1}{2}N_2(g) \longrightarrow ND_D^{'} + ND_D^{\bullet} + V_D^{\bullet} + e^{'} \tag{6.9}$$

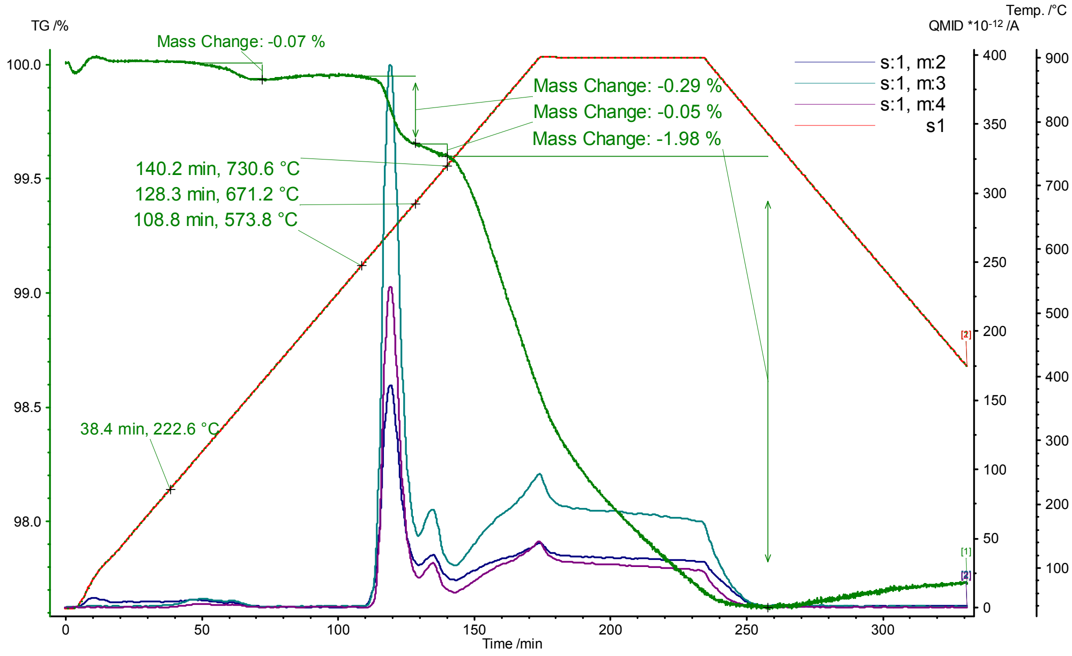

Figure 6-13: TGA/MS of Ca_2ND in argon, showing mass2, mass3 and mass4 (deuterium release)

Reckeweg and Di Salvo [63] performed X-ray studies on $Ca_2ND_{1-\delta}$, and observed the formation of Ca_2N when $\delta > 0.3$. Combining the information from the neutron diffraction refinement and the TGA run in argon, it seems that in our sample the deuterium content goes from 0.69 to 0.64 at 570 – 580°C, releasing interstitial deuterium first. Then at 730°C, 0.07 formula units of N are lost, which most likely involves the release of the imide ions that substitute for nitride and hydride ions. This would agree with the concomitant loss of deuterium at the same temperature. The further loss of deuterium from the structure corresponds to the decomposition of $Ca_2ND_{0.64}$ into Ca_2N.

The compound $Ca_2N_{0.90}D_{0.64}(ND)_{0.20}$, which is formed at 570 – 580°C, relates to the compound in which structural deuterium/hydrogen is lost from the interstitial 8a site, as found by refinement of the neutron diffraction pattern measured at 650°C (section 6.1.3).

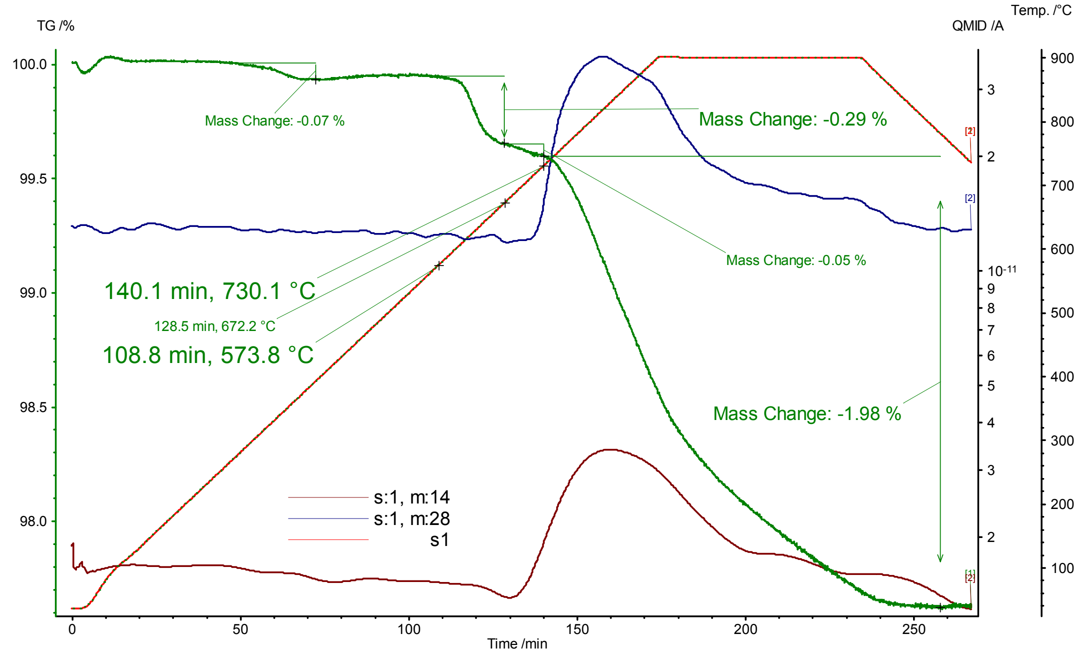

Figure 6-14: TGA/MS of Ca_2ND in argon, showing mass14 and mass28 graph (nitrogen release)

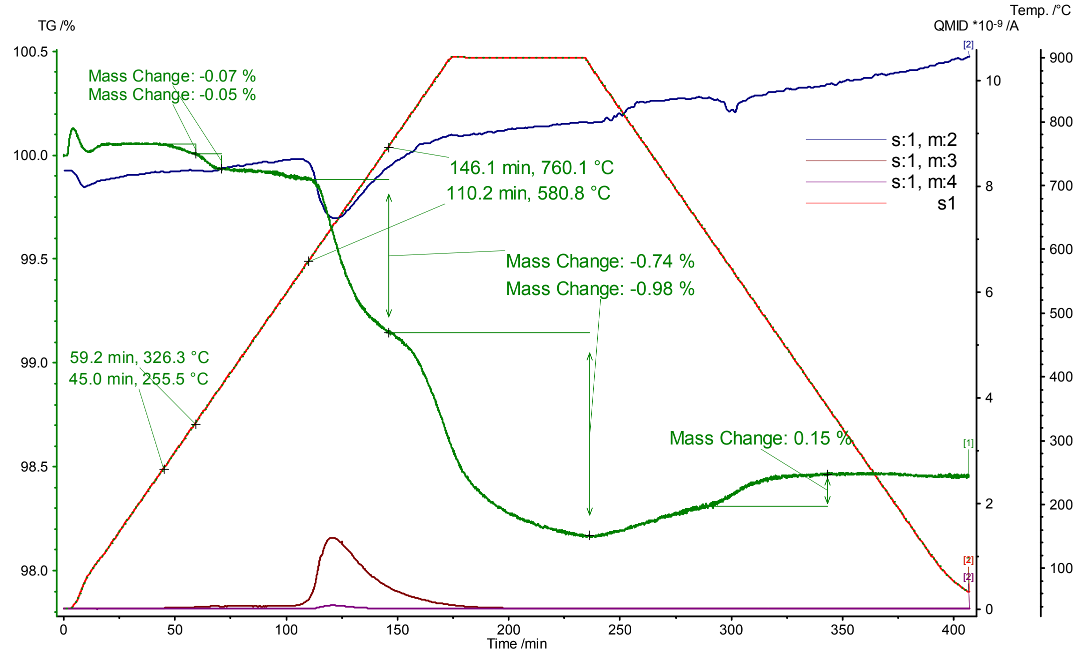

Figure 6-15: TGA/MS of Ca_2ND in 5% H_2/argon, showing mass2, mass3 and mass4 (hydrogen and deuterium)

$$Ca_2N_{0.90}D_{0.69}\left(ND\right)_{0.20} \xrightarrow{T=570-580°C} Ca_2N_{0.90}D_{0.64}\left(ND\right)_{0.20} + \tfrac{0.05}{2}D_2 \tag{6.10}$$

$$Ca_2N_{0.90}D_{0.64}\left(ND\right)_{0.20} \xrightarrow{T=730^\circ C} Ca_2N_{0.90}D_{0.64}\left(ND\right)_{0.12} + \tfrac{0.08}{2}N_2 + \tfrac{0.08}{2}D_2 \tag{6.11}$$

$$Ca_2N_{0.90}D_{0.63}\left(ND\right)_{0.12} \xrightarrow{T=795^\circ C} 0.84Ca_2N + 0.16Ca_2ND_{0.63} + \tfrac{0.84\times 0.67+0.12}{2}D_2 + \tfrac{0.12}{2}N_2 \tag{6.12}$$

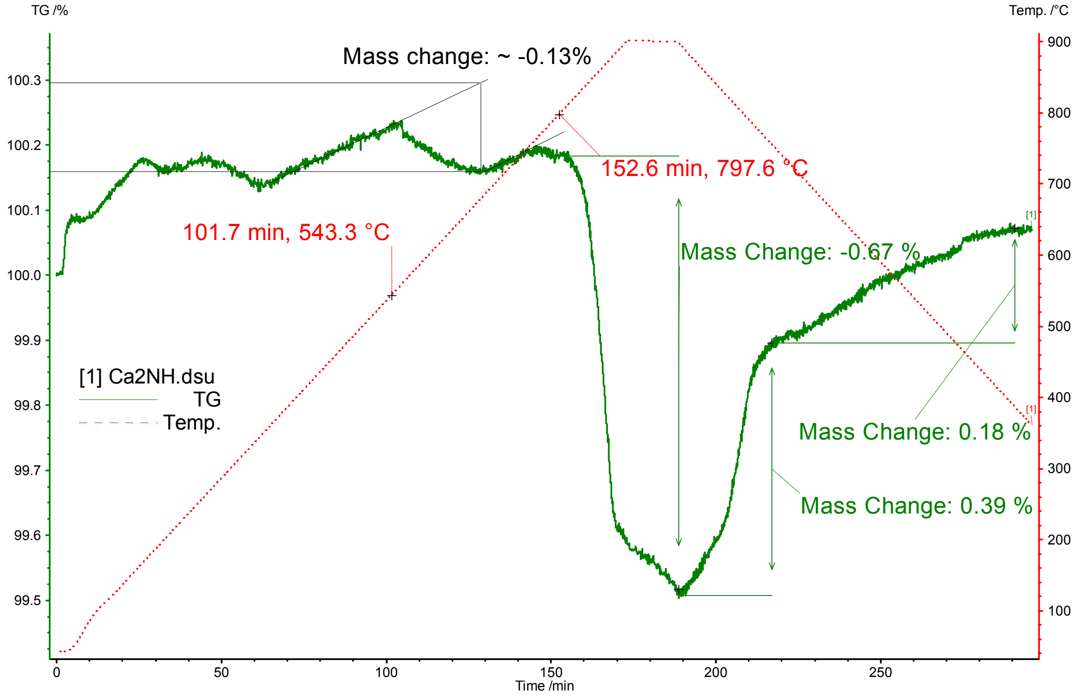

Figure 6-16: TGA of Ca_2NH in 5% H_2/argon

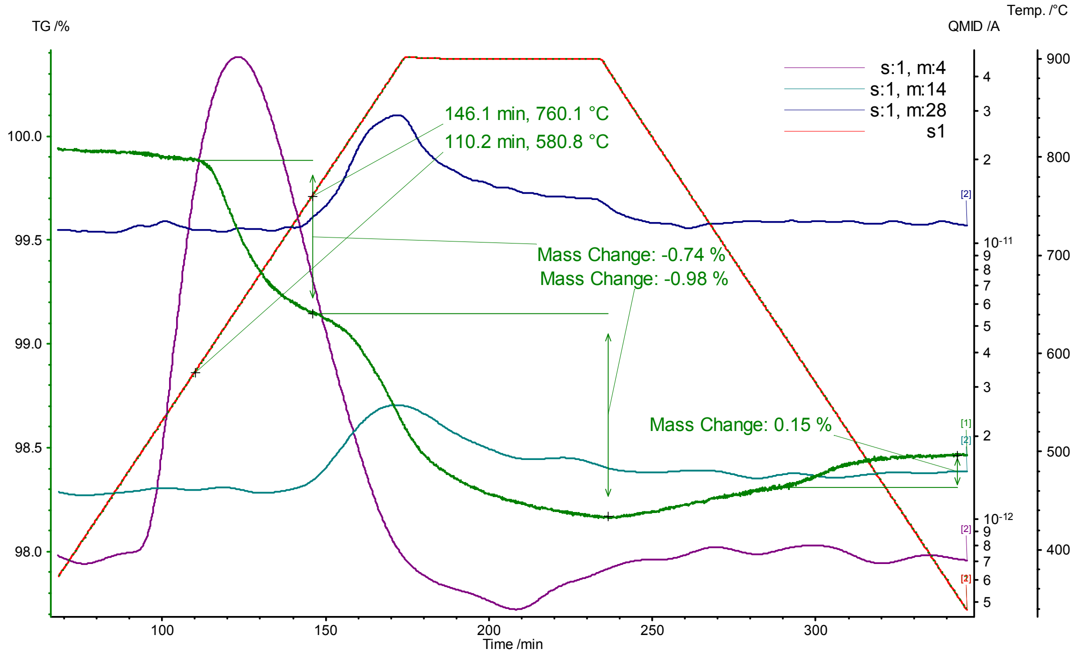

Figure 6-17: TGA/MS of Ca_2ND in 5% H_2/argon atmosphere, showing release of deuterium and nitrogen

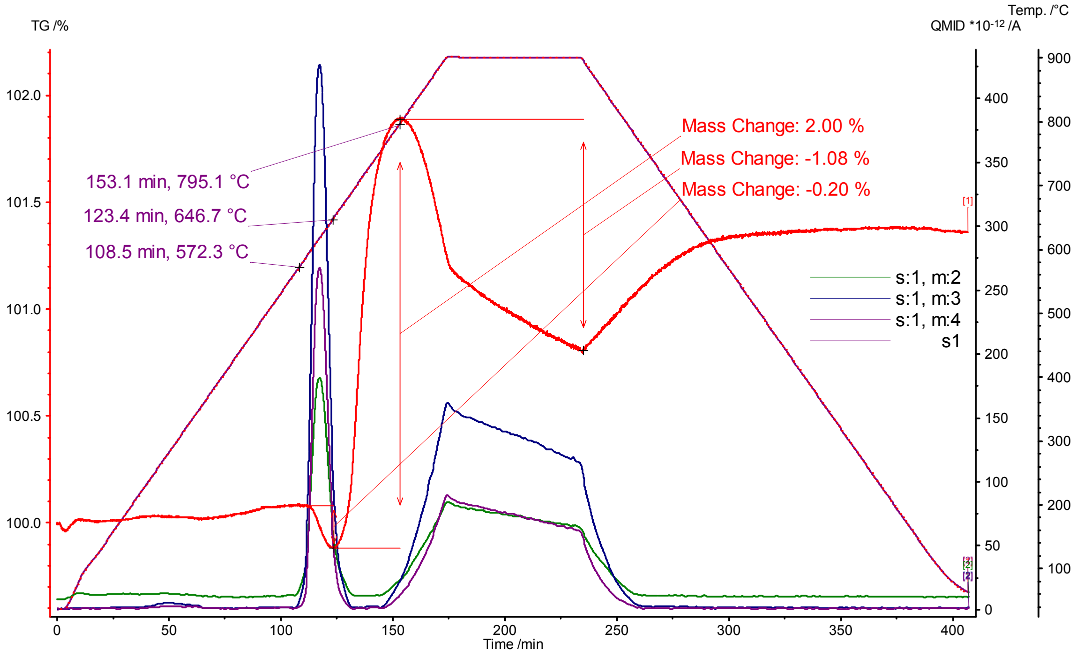

Figure 6-18: TGA/MS of Ca_2ND in nitrogen, showing mass 2, mass 3 and mass 4 (deuterium release)

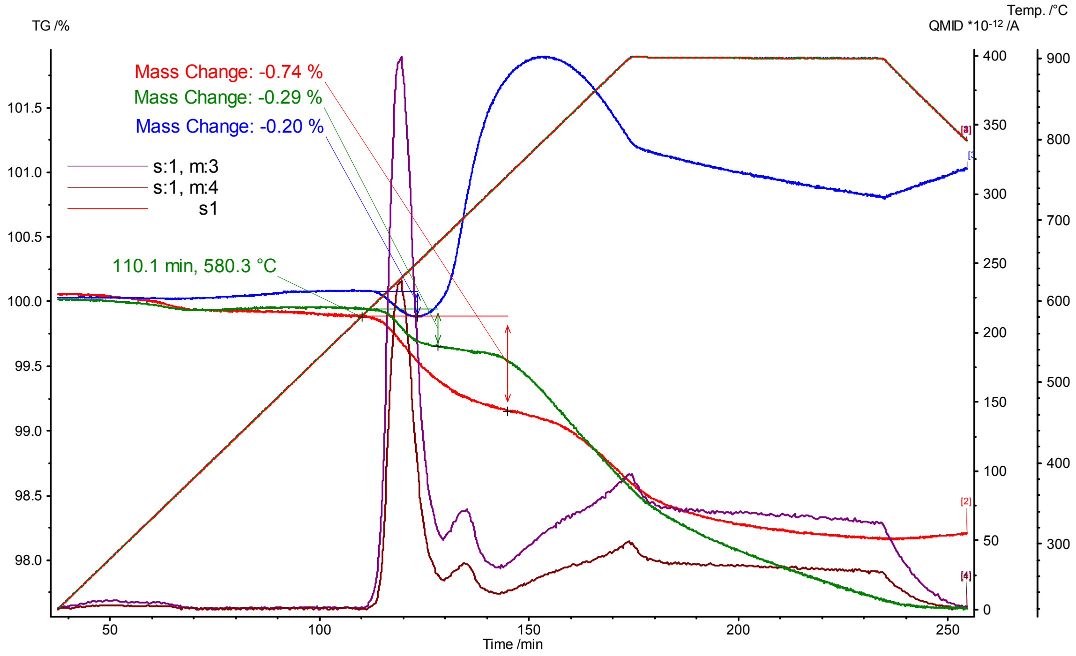

Figure 6-19: TGA/MS of Ca_2ND in argon (green), 5% H_2/argon (red) and nitrogen (blue) and mass3 and mass4 (deuterium release)

6.1.4.1 Different Ca_2ND sample – fully deuterided

The second Ca_2ND sample, which was completely deuterided and described in section 6.1.3.1, was also tested for its thermal behaviour. A slightly different behaviour was observed as compared to the partially hydrided sample. The results are summarized in Table 6-8.

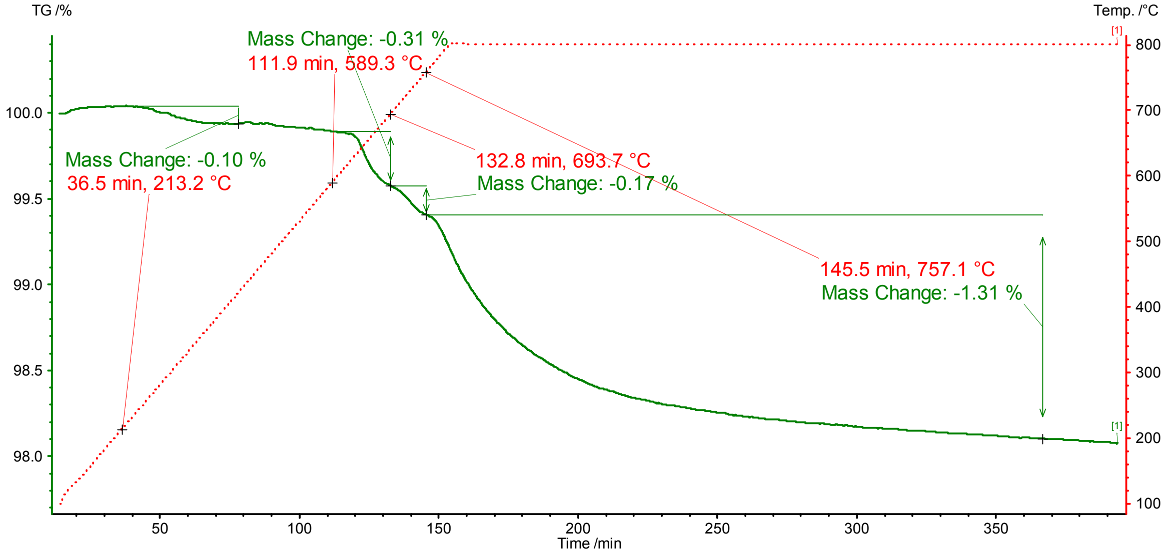

Figure 6-20: TGA for fully deuterided Ca_2ND (section 6.1.4.1)

Table 6-8: Summary of thermal analysis on fully deuterided Ca_2ND sample

Temperature (°C)	Weight loss (wt%)	Ion mass involved	Gas involved
213	-0.10	m18, m4	H_2O, D_2
589	-0.31	m4	D_2
694	-0.17	m4	D_2
757	-1.31	m4, m28	D_2 & N_2

First of all, it becomes clear that the total weight loss is slightly smaller than for the previous, partially hydrided sample. This thermogravimetric test did however not go to temperatures higher than 800°C, so no decomposition into Ca_2N is observed. On the other hand, larger weight losses would have been expected considering the different compositions of the samples. The partially hydrided sample had a composition $Ca_2N_{0.90}D(H)_{0.69}(ND)_{0.20}$, according to Rietveld refinement of the neutron diffraction data. The fully deuterided sample has a calculated composition $Ca_2N_{0.90}D_{0.80}(ND)_{0.30}$, and according to the proposed decomposition mechanism in equations (6.10) – (6.12), a larger weight loss would be expected for this particular sample as it is richer in both nitrogen and deuterium. Also, it contains more imide ions, which are expected to be metastable and should decompose around 730°C. From the weight losses in Table 6-8, together with the released gases found by MS, the following thermal decomposition is proposed for this sample, as described in reactions (6.13) and (6.14). It is assumed that the weight loss at 213°C is caused by decomposition of surface hydroxides and the weight loss at 694°C agrees well with the presences of 5 mol% CaD_2, which was found by neutron diffraction.

$$Ca_2N_{0.90}D_{0.80}(ND)_{0.30} \xrightarrow{T=590°C} Ca_2N_{0.90}D_{0.62}(ND)_{0.30} + \tfrac{0.18}{2}D_2 \qquad -0.31\ \text{wt\%} \qquad (6.13)$$

$$Ca_2N_{0.90}D_{0.62}(ND)_{0.30} \xrightarrow{T=757°C} Ca_2N_{0.90}D_{0.62} + \tfrac{0.30}{2}N_2 + \tfrac{0.30}{2}D_2 \qquad -4.03\ \text{wt\%} \qquad (6.14)$$

Reaction (6.13) is again partial loss of deuterium from the structure to form $Ca_2ND_{1-\delta}$. The resulting D^- content after this decomposition step (i.e. 0.62), agrees well with what was found for the first sample, described previously. The fact that this step occurs, might indicate that some interstitial deuterium is also present in this sample's structure. In reaction (6.14) it is assumed that the imide ions decompose completely, without filling any nitride or deuteride vacancies. The theoretical weight loss for decomposition of the imide ions (4.0 wt%) is however much larger than the observed weight loss. Therefore, it seems that some of the imide ions are converted into nitride ions and protons, after which the protons are released as deuterium/hydrogen gas and the nitride ions incorporated in the left vacancies, resulting in a lower weight loss.

6.1.5 Ca-N-H(D) discussion

It was shown that $Ca_2NH(D)$ was prepared as a single phase compound (apart from slight oxide and hydride contamination during synthesis) when calcium metal was reacted in an atmosphere of nitrogen and hydrogen (deuterium) in argon. X-ray results suggest that no imide phase is formed when the reaction is carried out at temperatures from 600°C to 900°C. Neutron diffraction data obtained on samples synthesised at 600°C confirm this, but there are no neutron diffraction measurements on the samples synthesised at higher temperatures. Also no calcium imide formation could be observed up to nitrogen and hydrogen concentrations of 7% in argon for a reaction temperature of 600°C. It could be seen however, that the actual chemical composition of $Ca_2NH(D)$ is highly dependent on the partial hydrogen and nitrogen pressures and that deviations from the ideal chemical formula are easily obtained. Fourier difference plots from the neutron diffraction data and thermal analysis suggest that some imide ions might have been incorporated into the nitride hydride structure, without the formation of an actual imide phase. It seems that accurate control of pN_2 and $pD(H)_2$ would enable us to prepare materials of known composition. Working in sealed systems with known amounts of nitrogen and hydrogen would further improve obtaining compounds with a known stoichiometry.

Thermal analysis and neutron diffraction also suggest an order – disorder transition, which starts around 630°C. During this transition the N/D order in the nitride hydride crystal structure gradually disappears, resulting in a simple face centred cubic array of calcium ions, in which hydride ions and nitride ions each statistically occupy half of the octahedral holes (taking into account any loss of hydrogen from the structure). The order – disorder within the N/D layers could be closely related to the relatively large weight loss at 570°C, observed for Ca_2ND in 5%

H_2. It was shown that this weight loss agrees well with deuterium – hydrogen exchange with the atmosphere. It is likely that both processes are linked by increased mobility of hydrogen and nitrogen in the structure at ~600°C. A comparison will now be made in the Sr-N-H(D) system and more discussion will follow at the end of this chapter.

6.2 The Sr-N-H(D) system

Analogous to the Ca-N-H system, strontium imide (SrNH) and strontium nitride hydride (Sr_2NH) have similar crystal structures. Again, strontium imide has the rocksalt structure, with strontium and nitrogen coordinating each other octahedrally (spacegroup *F m 3 m*). The cubic lattice parameter of strontium imide is 5.51 Å [83, 105, 110]. Hydrogen is coordinated to nitrogen and different models have been used to describe its position within the lattice. Both sites in the [001] direction and on the faces of the Sr_6 octahedron (in the [111] direction) are suggested as simple ionic models [109]. Treating the imide ion as a rigid body clearly respects the covalent character of the N-D bond and would chemically be more accurate [83]. Literature reports that strontium nitride hydride does not crystallise in the *F d 3 m* spacegroup like its calcium analogue [105, 116]. The structure is similar and involves a distorted cubic closed packed (ccp) array of strontium, with nitride and hydride each occupying the octahedral holes. But whereas in calcium nitride hydride the N/D ordering is such that nitrogen and hydrogen are in a rocksalt configuration (displaced along the [001] direction), in strontium nitride hydride, the anions alternate between the ccp layers of strontium as shown in Figure 6-21. The crystal structure can be described using the rhombohedral spacegroup *R -3 m* with approximate lattice parameters a = 3.88 Å and c = 18.93 Å [105, 116]. Hydrogen is situated on the origin, nitrogen on (00½) and strontium on (00z), with z being close to ¼. The unit cells for both strontium nitride hydride and strontium imide are shown in Figure 6-21.

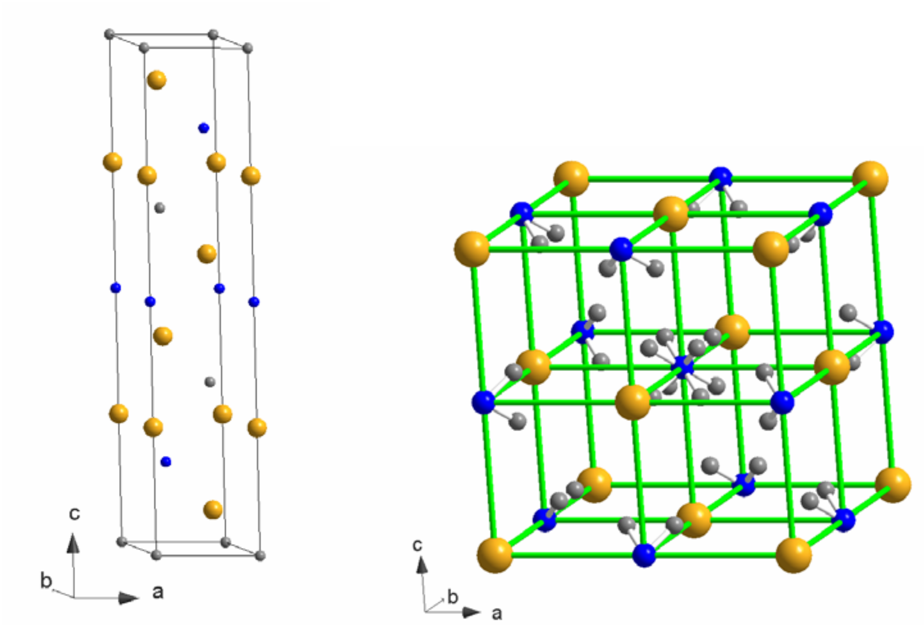

Figure 6-21: Unit cells of strontium nitride hydride, Sr_2NH (left) and strontium imide (right); strontium in yellow, nitrogen in blue and hydrogen in grey [105, 116].

The ordering in Sr_2NH and Ca_2NH is very similar and will be hard to distinguish using diffraction techniques only, as these techniques are sensitive to long range structures only. The ordering causes extra 'superstructure' peaks, but these will have low intensity, adding an additional problem to determining the exact ordering. Going from a cubic to rhombohedral symmetry might result in some broadening or splitting of peaks as the overall symmetry is lowered.

6.2.1 Sr-N-H experimental

Compounds in the Sr-N-H(D) system were synthesised by reacting strontium metal (Sigma Aldrich, 99%) at 600 – 700°C in an atmosphere of 5% H_2/D_2 and 1 – 2% N_2 in argon in an open furnace tube within the glovebox, in molybdenum crucibles. Additional information about the synthesis method can be found in chapter 2. The strontium based samples have a yellow – orange colour, which again turns green after a short while.

X-ray diffraction was carried out on a STOE diffractometer in transmission mode. The radiation is Cu Kα1. Data was recorded in the range $10° < 2\theta < 90°$ with a resolution of 0.02°. Sealed glass capillaries were used to protect the materials from air and moisture.

Neutron diffraction was carried out on instrument D1A at ILL, Grenoble (France) on a sample of Sr-N-D (sample weight ~1 gram). Neutron diffraction data was recorded at room temperature only. All other experimental conditions are identical to those described in section 6.1.1.

6.2.2 Sr-N-H XRD results

X-ray diffraction was performed on the Sr-N-H samples synthesised at both 600°C and 700°C. The sample synthesised at 600°C could be indexed in either the *F m 3 m* spacegroup, or the *R -3 m* spacegroup. The lattice parameter for the cubic spacegroup is 5.4601(4) Å, whereas in the rhombohedral spacegroup a = 3.861(1) Å and c = 18.91(1) Å. A small secondary phase can be detected, which is most likely SrH_2; its content is very small though. Rietveld refinement of the diffraction pattern in Fullprof was performed using three spacegroups: *F m 3 m*, *F d 3 m* and *R -3 m.* All refinements result in almost identical refinement parameters, independent of spacegroup. Also, the reliability factors are practically identical, making a conclusion about the actual compound or its true spacegroup impossible (see Table 6-9). From the lattice parameter in the cubic spacegroup however, it looks like the main phase is the strontium nitride hydride. It is hard to say from X-ray diffraction though, since the strontium ions will have the highest scattering factor, whereas nitrogen is a relatively weak scatterer and will add relatively little information to the diffraction pattern. Hydrogen is practically invisible to X-rays and will therefore not add any information to the pattern. Figure 6-22 shows the XRD pattern and Rietveld refinement using spacegroup *R -3 m* for Sr_2NH and it can be seen that the model does not give satisfactory fitting results. The same poor fits are obtained when *F d 3 m* or *F m 3 m* are chosen as spacegroups.

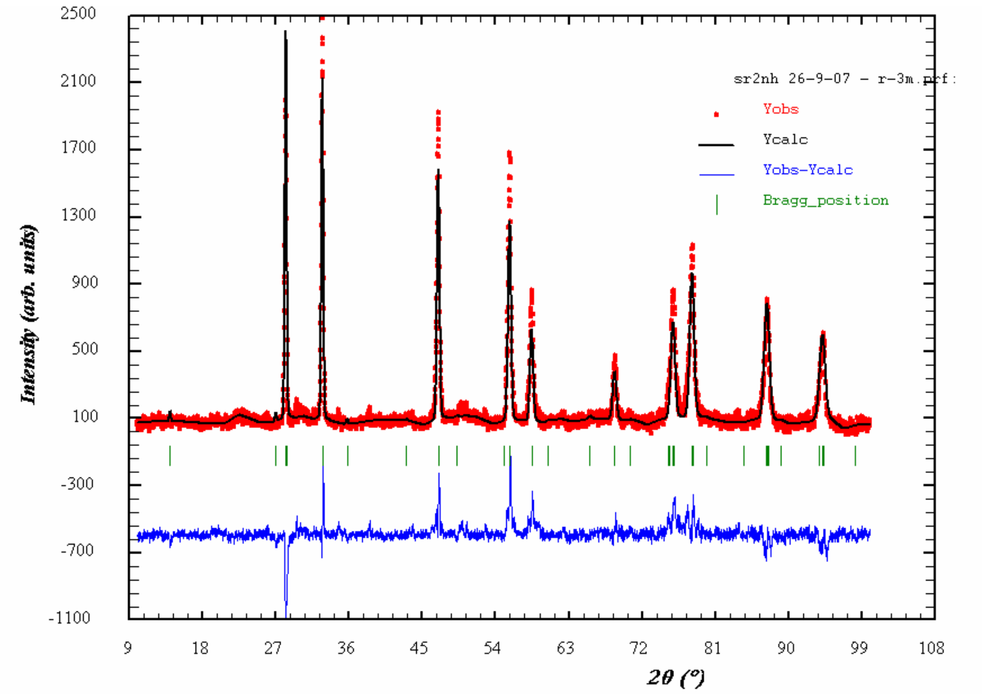

Figure 6-22: X-ray diffraction pattern for Sr-N-H synthesised at 600°C and Rietveld refinement in *R -3 m* spacegroup. Red curve is observed pattern, black curve is calculated pattern. Blue trail shows residuals after refinement, green ticks show position of reflections

Table 6-9: X-ray diffraction refinement parameters for Sr-N-H compound synthesised at 600°C, using three different spacegroups

Refinement parameter	F m 3 m		F d 3 m		R -3 m
a (Å)	5.4646 (5)	a (Å)	10.928 (1)	a (Å)	3.8587 (5)
			-	c (Å)	18.978 (5)
V (Å^3)	163.18 (2)	V (Å^3)	1305.1 (1)	V (Å^3)	244.72 (8)
Sr, 4a (0,0,0)		Sr, 32e (x,x,x)		Sr, 6c (0,0,z)	
		x	0.2488 (3)	z	0.2489 (3)
B (Å^2)	-2.2 (1)	B (Å^2)	-2.3 (1)	B (Å^2)	-2.4 (1)
Occ	0.77	Occ	0.66	Occ	0.67
N, 4b (½,½,½)		N, 16d (½,½,½)		N, 4b (0,0, ½)	
B (Å^2)	-0.8 (5)	B (Å^2)	-4.4 (4)	B (Å^2)	-4.4 (1)
Occ	1.00	Occ	1.00	Occ	1.00
R_p	17.1	R_p	18.2	R_p	18.0
R_{wp}	24.0	R_{wp}	25.3	R_{wp}	25.2
R_{exp}	8.27	R_{exp}	8.26	R_{exp}	8.26
χ^2	8.46	χ^2	9.37	χ^2	9.28

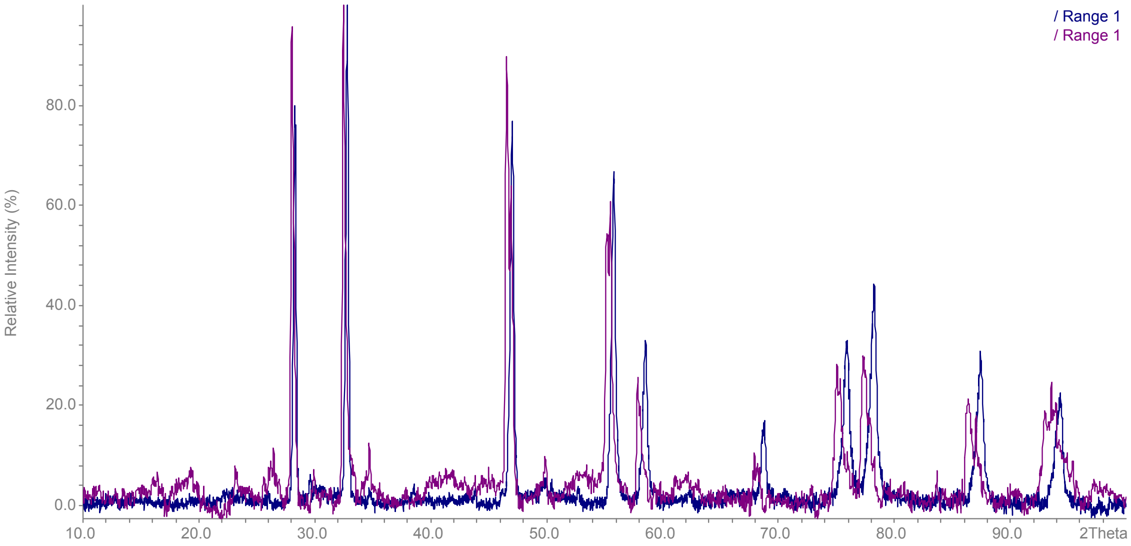

Figure 6-23: XRD patterns for Sr-N-H synthesised at 600°C (purple) and 700°C (blue)

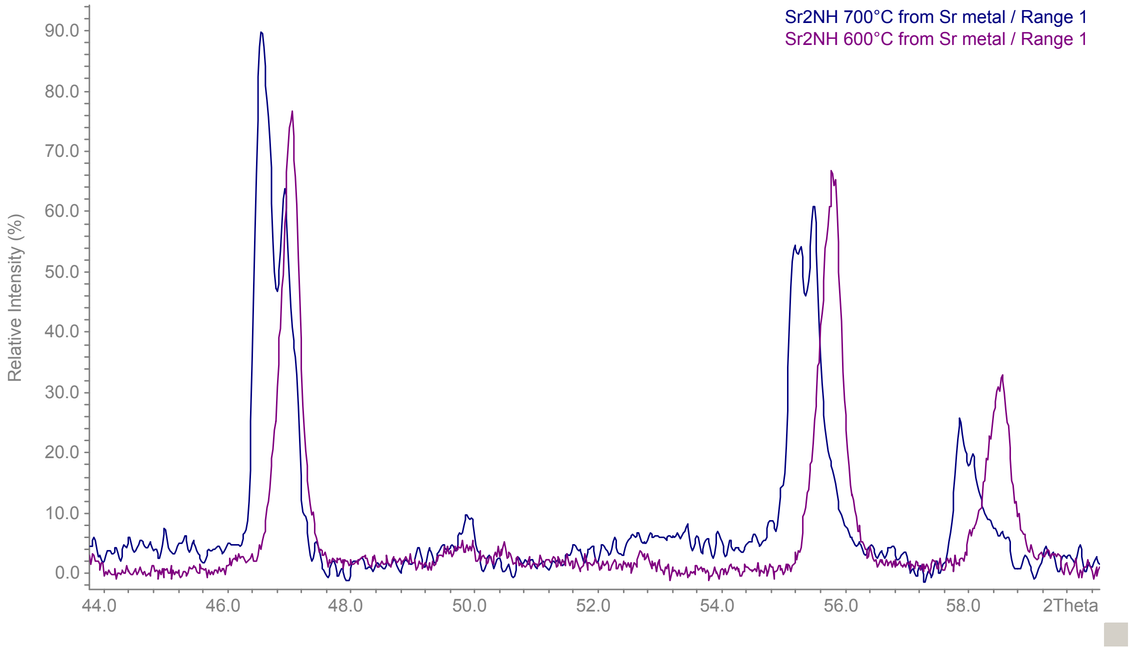

Figure 6-24: XRD patterns of Sr-N-H zoomed section (2θ = 44 – 60°)

In the diffraction pattern of the compound synthesised at 700°C, a second phase emerges with lattice parameters close to the phase already found at the synthesis temperature of 600°C. In fact, this second phase is now the dominant phase and it can be indexed in the *F m 3 m* spacegroup, with lattice parameter a = 5.518(2) Å. The other phase can be indexed in the same spacegroup, with cubic lattice parameter a = 5.489(1) Å. It seems that the strontium imide becomes the dominant phase at higher reaction temperatures, whereas more strontium nitride hydride is present at reaction temperatures < 600°C. This can clearly be seen in Figure 6-23 and Figure 6-24. As the X-ray diffraction pattern of the sample synthesised at 700°C is of relatively poor quality, some information about the nitride hydride and imide phases will be obtained using neutron diffraction first. This information will be used again to refine the X-ray data. This will be presented later on in this chapter in section 6.2.6.

6.2.3 Sr-N-D(H) neutron diffraction results

A deuterided (Sr-N-D) sample was prepared for neutron diffraction, synthesised at 600°C using the conditions given in section 6.2.3 and chapter 2, section 2.1. The weight before and after the reaction was taken to get an estimate of the nitrogen and deuterium uptake by strontium. Analogous to Ca_2ND, it is assumed that hydrogen is present in the structure in a D : H ratio of 10 : 1. The Sr-N-D sample was only tested at room temperature. Neutron diffraction was again carried out at ILL, Grenoble (France) on instrument D1A. The same conditions were used as described for Ca_2ND, which can be read in section 6.1.3.

The diffraction pattern is shown in Figure 6-25. The section at high angle is zoomed and it can be seen that there is splitting of the peaks. This is in fact not a result of the lower symmetry in the rhombohedral Sr_2ND phase as compared to the cubic Ca_2ND, but it is caused by the presence of a second phase, with very similar lattice geometry. So whereas the Sr-N-D(H) compound synthesised at 600°C could be indexed as a single phase in XRD (which seemed to be $Sr_2ND(H)$, strontium nitride hydride), from neutron diffraction it becomes clear that it is in fact a mixed phase of strontium nitride hydride and strontium imide, SrND(H). Refinement of the neutron diffraction data proved to be difficult, as the peaks of the two phases overlap strongly and their phase contents seem to be close to a 1 : 1 ratio. A third phase is even present: SrD_2, but its content is significantly smaller and the peaks do not overlap as much.

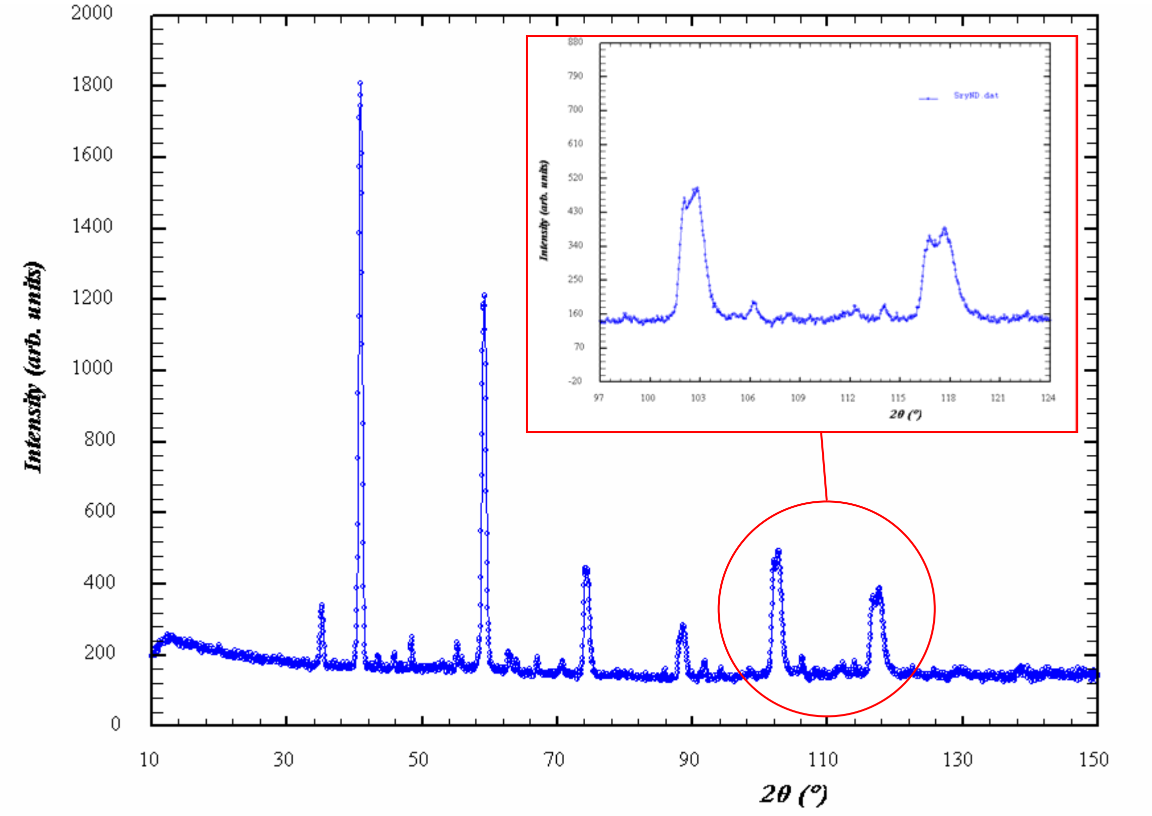

Figure 6-25: Neutron diffraction pattern of the Sr-N-D phase synthesised at 600°C

From initial refinements, in which all parameters were allowed to change freely, the phase contents for Sr_2ND, SrND and SrD_2 are 32 mol%, 56 mol% and 13 mol%, respectively (Sr_2ND : SrND = 36 : 64). These values are actually in good agreement with the observed weight gain after the synthesis (13.5 wt%) and also CHN analysis suggests a similar ratio between the three phases. As there is such strong overlap of peaks in the pattern, the amount of refineable parameters were kept to a minimum. Too many parameters that can change freely increase the chance of divergence and/or meaningless values for different parameters. Therefore the molar phase ratio was fixed to be 31 : 56 : 13 for Sr_2ND : SrND : SrD_2. The occupancies of deuterium and nitrogen were fixed as well, as refining those parameters resulted in divergence of the refinement process. The deuterium site in strontium imide was initially positioned on the body diagonal (32f site) as used by Sichla et al. [105] in a study of a very similar mixed phase. The refinement results can be found in Table 6-10.

Table 6-10: Refinement results of neutron diffraction pattern of Sr-N-D, synthesised at 600°C, λ = 1.9114 Å

Refinement parameter	Phase 1 Sr_2ND	Refinement parameter	Phase 2 SrND
Spacegroup	*R -3 m*	Spacegroup	*F m 3 m*
a (Å)	3.8745 (2)	a (Å)	5.5019 (2)
c (Å)	18.885 (1)		
V (Å^3)	245.52 (3)	V (Å^3)	166.55 (1)
Sr, 6c (0,0,z)		Sr, 4a (0,0,0)	
z B (Å^2)	0.2513 (8) 2.7 (1)	B (Å^2)	3.5 (2)
N, 3b (0,0,½)		N, 4b (½,½,½)	
B (Å^2)	2.8 (3)	B (Å^2)	3.2 (1)
D/H, 3a (0,0,0)		D/H, 32f (x,x,x)	
B (Å^2)	-0.8 (2)	x B (Å^2)	0.418 (5) 13 (1)
Phase content (mol%)	31	Phase content (mol%)	56

	Phase 3 SrD_2			
Spacegroup	*P n m a*			
a (Å)	6.381 (1)			
b (Å)	3.869 (1)			
c (Å)	7.322 (1)			
V (Å^3)	180.77 (6)			
Phase content (mol%)	13			
Atom	x	y	Z	B (Å^2)
Sr, 4c (x,¼,z)	0.246 (3)	0.25	0.107 (2)	-1.2 (2)
D/H1, 4c (x,¼,z)	0.351 (3)	0.25	0.420 (3)	1.3 (4)
D/H2, 4c (x,¼,z)	-0.025 (5)	0.25	0.673 (3)	4.3 (7)

Reliability factors							
R_p	4.20	R_{wp}	5.26	R_{exp}	3.12	χ^2	2.84

As can be seen from Table 6-10, due to the overlapping of peaks, some parameters still have meaningless values. For instance, the isotropic temperature factor (B) for deuterium in the Sr_2ND phase is negative and unreasonably large in the SrND phase. The error estimate in the deuterium position of SrND is also large, suggesting that the deuterium ion is very mobile and perhaps more statistically distributed, as Andresen et al. [108] suggested.

Since the phase content of strontium imide is large and its deuterium position doubtful, it is expected that refining the deuterium on the wrong site will have large implications for the refinement of the Sr_2ND phase as well. To overcome this, a new approach was tried, in which the deuterium position in SrND is initially not refined. The refinement results were then transformed into a fourier difference map that plots neutron scattering length density within the unit cell. Residual neutron scattering length density can thus be correlated to the deuterium in the structure (coherent neutron scattering length for D is +6.67 fm). The xy – fourier difference maps at z = 0.3150, z = 0.3750 and z = 0.5 are shown in Figure 6-26. The analysis shows only one site with a positive neutron scattering length density, on a 96j site (0,y,z). The neutron scattering length density in this site still seems low compared to the Sr and N-sites, but it should be kept in mind that one deuterium ion is occupying 24 crystallographically equivalent sites per N-site and hence the density per single site is low. This 96j site is in fact a good trade-off between the suggested statistically distributed site and a fixed position. The deuteride ion can move over 24 sites per N atom, which is substantially more than 6 or 8 sites as proposed by Sichla and Jacobs. Subsequently, this new deuterium site was tested by including it in the refinement of the diffraction pattern. The models proposed in literature, with deuterium on (0, 0, z) and (x, x, x) were also refined and compared with the new deuterium site. Finally, to improve the refinement procedure, UVW and peak shape parameters were constrained to be the same for all three phases (Sr_2ND, SrND and SrD_2).

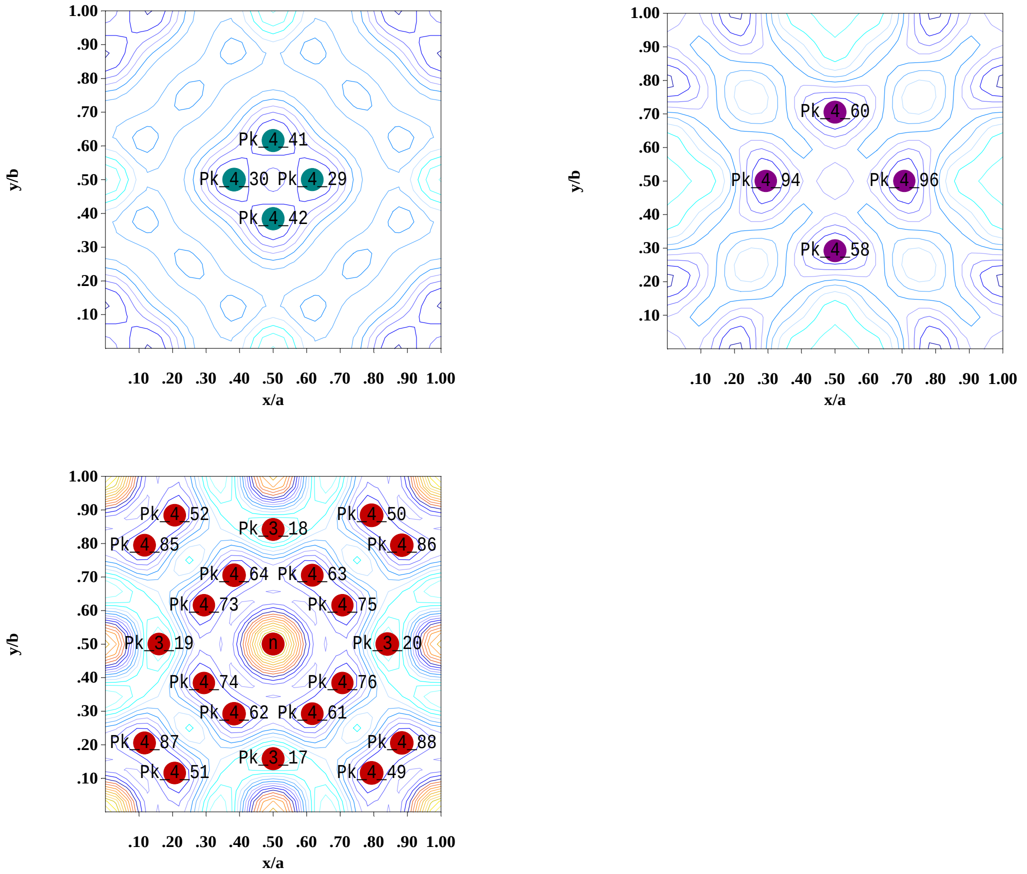

Figure 6-26: Fourier difference maps for SrND, showing positive neutron scattering length density on site 96j (0.294, 0.117, 0). Top left z = 0.3150, top right z = 0.3750, bottom left z = 0.5

Table 6-11: Refinement results for the imide phase, SrND, using different deuterium sites. Spacegroup *F m 3 m*

Refinement parameter	D site on 24e (0,0,z)	D site on 32f (x,x,x)	D site on 96j (0,y,z)
a (Å)	5.5001 (3)	5.4999 (3)	5.5003 (3)
Sr, 4a			
B ($Å^2$)	3.1 (2)	3.1 (2)	3.3 (2)
N, 4b			
B ($Å^2$)	2.9 (1)	2.7 (1)	2.3 (2)
D/H			
x D/H	0	0.417 (5)	0
y D/H	0	0.417 (5)	0.344 (3)
z D/H	0.368 (5)	0.417 (5)	0.090 (3)
B ($Å^2$)	14 (1)	11 (1)	1.6 (9)
d (N-D) (Å)	0.728	0.794	0.989 (8)
γ (Sr-D-N)	180.0°	109.5°	135.3° (5)
R_p	3.97	4.00	3.90
R_{wp}	4.99	5.00	4.89
R_{exp}	3.12	3.12	3.12
χ^2	2.56	2.57	2.45

Table 6-11 summarises the refinement results for the strontium imide phase, SrND, when using three different deuterium sites. It shows that the isotropic temperature factor decreases when the multiplicity of the site increases (24e → 32f → 96j). In case of the 96j site, the B-factor for deuterium is actually lower than those for Sr and N, which is questionable. The N-D distance of the imide ion also increases with increasing multiplicity, whereas the Sr – D – N bond angle finds a minimum for the 32f site, which is expected as it is the energetically most favourable site. The N-D bond length for the 96j site is 0.989 Å, which is very close to the bond length used by Brese et al. in their model, i.e. 1.01 Å [83].

On closer inspection of the neutron diffraction pattern (and also X-ray diffraction pattern) for the Sr-N-D(H) mixed phase, it can be seen that actually none of the superstructure peaks, expected from N-D ordering in $Sr_2ND(H)$, is present. Whereas in Ca_2ND there are clear reflections from the double cubic cell, these are completely absent for the $Sr_2ND(H)$ phase. Not even diffuse peaks can be seen in the patterns. This means that refining the Sr_2ND phase using an ordered supercell is not necessary and going back to a simple single unit cell is preferable. In this disordered cell, nitride and deuteride each occupy half of the same crystallographic site (octahedrally coordinated to strontium). There does seem to be an improvement upon using a rhombohedral unit cell over a cubic cell. The results for the refinements of the Sr_2ND phase using a simple face centred cubic cell, spacegroup *F m 3 m* and a single rhombohedral cell, spacegroup *R -3 m* are given in Table 6-12 and Table 6-13. The occupancy of Sr is allowed to change to account for randomly distributed imide ions within the nitride hydride structure, as found for Ca_2ND. This actually leads to a relatively low occupancy of ~0.67 in the *F m 3 m* spacegroup, which means that about 50% of the nitride and deuteride ions have been replaced by imide ions. This seems too much for the nitride hydride phase to remain unchanged. Also, using these single unit cells has some minor implications for the refinement of the strontium imide phase, so these have also been given in Table 6-12 and Table 6-13.

Table 6-12: Refinement results for Sr$_2$ND using *F m 3 m* spacegroup and SrND phase with D on 96j site and *F m 3 m* spacegroup, λ = 1.9114 Å

Refinement parameter	Sr$_2$ND, *F m 3 m*		SrND
a (Å)	5.4672 (3)	a (Å)	5.4973 (3)
V (Å^3)	163.42 (2)	V (Å^3)	166.13 (2)
Sr, 4a (0,0,0)		Sr, 4a (0,0,0)	
B (Å^2)	0.74 (9)	B (Å^2)	0.74 (9)
Occ	0.67 (1)		
N, 4b (½,½,½)		N, 4b (½,½,½)	
B (Å^2)	3.4 (2)	B (Å^2)	4.7 (1)
Occ	0.50		
D, 4b (½,½,½)		D/H, 96j (0,y,z)	
B (Å^2)	3.4 (2)	y	0.356 (5)
Occ	0.50	z	0.095 (5)
		B (Å^2)	6.6 (10)
Phase content (mol%)	42		58
R$_p$		3.96	
R$_{wp}$		4.95	
R$_{exp}$		3.13	
χ^2		2.51	

Table 6-13: Refinement result for Sr$_2$ND using *R -3 m* spacegroup and SrND phase with D on 96j site, spacegroup *F m 3 m*, λ = 1.9114 Å

Refinement parameter	Sr$_2$ND, *R -3 m*		SrND
A (Å)	3.8729 (3)	a (Å)	5.4997 (3)
C (Å)	9.444 (1)		
V (Å^3)	122.67 (2)	V (Å^3)	166.35 (2)
Sr, 3a (0,0,0)		Sr, 4a (0,0,0)	
B (Å^2)	2.6 (1)	B (Å^2)	2.6 (1)
Occ	0.86 (2)		
N, 3b (0,0, ½)		N, 4b (½,½,½)	
B (Å^2)	1.8 (1)	B (Å^2)	2.3 (2)
Occ	0.50		
D/H, 3b (0,0, ½)		D/H, 96j (0,y,z)	
B (Å^2)	1.8 (1)	y	0.339 (3)
Occ	0.50	z	0.091 (2)
		B (Å^2)	1.5 (7)
Phase content (mol%)	37		63
R$_p$		3.92	
R$_{wp}$		4.90	
R$_{exp}$		3.12	
χ^2		2.46	

A single phase Sr_2ND material was obtained by Chemnitzer et al. [116] and they confirmed N/D ordering in the crystal structure. Obviously, when a second imide phase is present, the long range ordering disappears and the structure can be described in a single unit cell. From the refinement, it seems furthermore that it is also better described using a rhombohedral lattice, rather than a face centred cubic cell. The resulting fit and the difference plot are given in Figure 6-27.

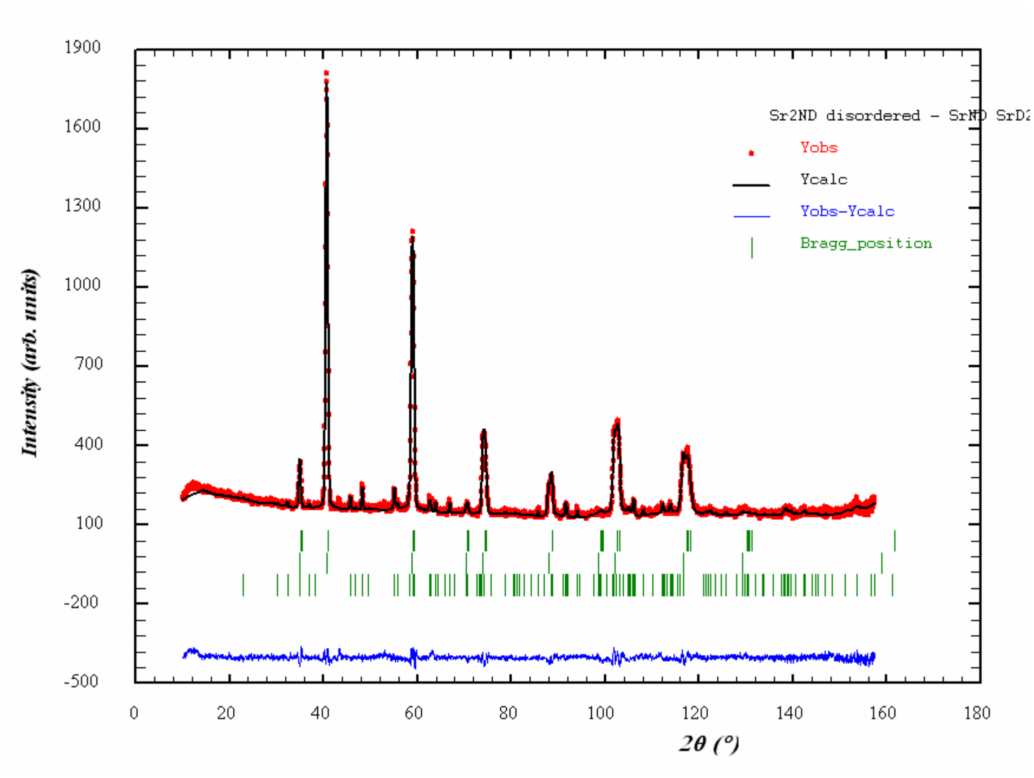

Figure 6-27: Refinement of the mixed Sr-N-D phase: phase 1 is Sr_2ND (*R -3 m*) without N-D ordering, phase 2 is SrND (*F m 3 m*) and phase 3 is SrD_2 (*P n m a*). Blue trail shows residuals after refinement. Green ticks show reflection positions for the three phases

6.2.4 Sr-N-H thermal analysis – results

The Sr-N-D sample that was used for neutron diffraction was also used for thermal analysis, i.e. TGA/DTA combined with mass spectrometry (MS). Similarly to Ca_2ND, the analysis was performed in three atmospheres: argon, 5% H_2/argon and nitrogen. Initially, runs were performed with a heating and cooling rate of 5 K/min and an isotherm of 60 minutes at 900°C.

Figure 6-28 shows the DTA for the Sr-N-D sample in argon. A change in slope can be observed at 430°C (which cannot be related to a thermogravimetric event), but the change is a lot more subtle than observed for Ca_2ND. This can be explained by the presence of a secondary imide phase and the absence of long range ordering for the strontium nitride hydride. There is however still a possibility for short range order and the breaking up of this short range order is probably the reason of the observed second order phase change at 430°C. The temperature for this order – disorder transition is significantly lower than the transition temperature for Ca_2ND. In 5% H_2 atmosphere, a clear change in DTA slope can be observed at roughly the same temperature. Although this might be related to the N/D order – disorder transition, it also occurs in parallel with a thermogravimetric event, involving H-D exchange (see Table 6-14).

In all atmospheres the TG graph of the Sr-N-D sample shows a weight loss again at relatively low temperature, i.e. 200 – 220°C, which is attributed to the dehydration of $Sr(OH)_2$ into SrO, releasing a water molecule. This process is described in more detail in section 6.1.4 and the presence of $Sr(OH)_2$ is explained by exposure of the sample to air during loading it into the TG machine.

The TG graphs of Sr-N-D in the three atmospheres further show striking similarities with their Ca_2ND analogue. First a weight loss, caused by deuterium loss is observed, followed by a loss of nitrogen, combined with more deuterium release. The results for all three atmospheres are summarised in Table 6-14.

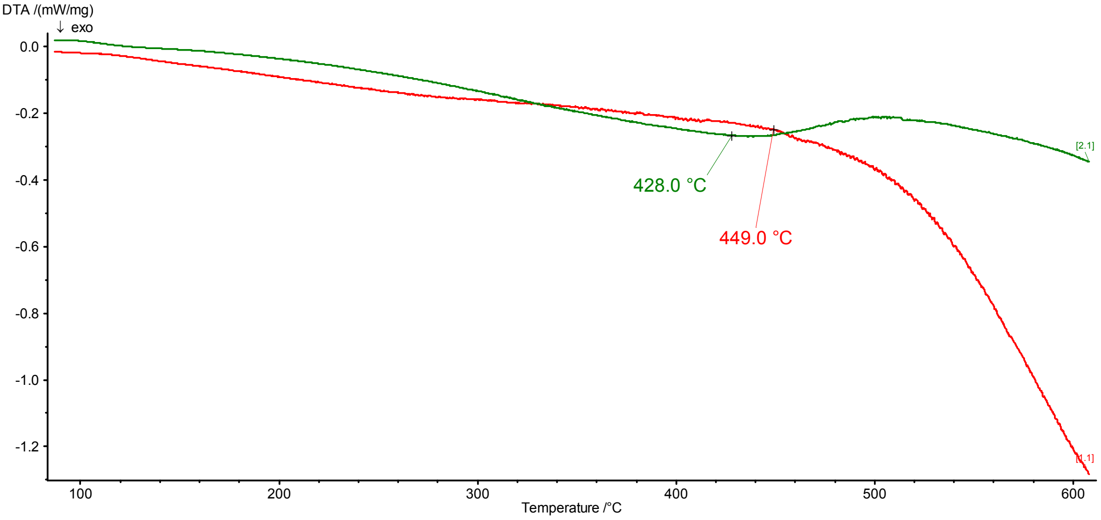

Figure 6-28: DTA of Sr-N-D in argon (green) and 5% H_2/argon (red)

Table 6-14: Thermal analysis of Sr-N-D in three different atmospheres

Temperature (°C)	Weight loss (wt%)	Ion masses involved	Molecules involved
Thermal analysis in argon			
197	-0.11	m2, m3, m17, m18	H_2O
528	-0.44	m2, m3, m4	D_2 (HD)
721	-0.32	m2, m3, m4, m14, m28	D_2 (HD) & N_2
768	-3.34	m2, m3, m4, m14, m28	D_2 (HD) & N_2
900	-5.32	m2, m3, m4, m14, m28	D_2 (HD) & N_2
Thermal analysis in 5% H_2/argon			
211	-0.14	m2, m3, m17, m18	H_2O
495	-0.91	m3, m4	HD
760	-4.29	m3, m4, m14, m28	HD & N_2
653*	+0.68	m2	H_2
Thermal analysis in nitrogen			
221	-0.07	m2, m3, m17, m18	H_2O
440	+0.06	m3, m4	D_2 (HD)
604	+0.15	m3, m4	D_2 (HD)
722	-3.36	m3, m4	D_2 (HD)
900*	+0.94		

*) Cooling down

The thermal analysis in argon shows a weight loss at 510 – 530°C of -0.44 wt%, which is caused by two decomposition steps, which can't separated in the TG graph. First of all there is an initial loss of deuterium from Sr_2ND, analogous to equation (6.10). Secondly, at 660°C, SrD_2 decomposes into its elements. From the weight loss, it can be calculated that 0.12 formula units of deuterium are lost from the Sr_2ND structure.

$$Sr_2ND \xrightarrow{T=510°C} Sr_2ND_{0.88} + \tfrac{0.12}{2} D_2 \tag{6.15}$$

$$SrD_2 \xrightarrow{T=660°C} Sr + D_2 \tag{6.16}$$

Then there are two subsequent weight losses, the last of which continues into the isotherm at 900°C. From the MS it becomes clear that both deuterium and nitrogen are lost from the Sr-N-D sample. And again, like for Ca_2ND, the nitrogen and deuterium release at the isotherm at 900°C seems to be diffusion limited. However the total weight loss after the isotherm at 900°C is 9.07 wt%, which is very large compared to the weight loss for Ca_2ND and is in fact close to the maximum weight loss if the sample would decompose into its elements. It is however not likely that Sr-N-D will decompose into its elements, as Sr_2N is a stable compound which should be stable to high temperatures. The large weight loss is rather caused by evaporation of Sr metal (from SrD_2), which was also observed for a TG run of SrH_2 in argon. As the Sr evaporation is complicating the analysis even more, a second run in argon was performed, with two isotherms of 6 hours at 740°C and at 780°C (to complete the decomposition steps at 721°C ad 768°C, respectively). The results are shown in Table 6-15. From this table it can be seen that weight losses initially found at 721°C and 768°C were actually convoluted and it becomes clear that all nitrogen loss is already occurring at 715 – 740°C.

Table 6-15: Thermal analysis of Sr-N-D in argon, with two isotherms at 740°C and 780°C

Thermal analysis in argon			
Temperature (°C)	Weight loss (wt%)	Ion masses involved	Molecules involved
197	-0.11	m2, m3, m17, m18	H_2O
510	-0.44	m2, m3, m4	D_2 (HD)
715 – 740	-3.38	m2, m3, m4, m14, m28	D_2 (HD) & N_2
768 – 780	-1.08	m2, m3, m4	D_2 (HD)

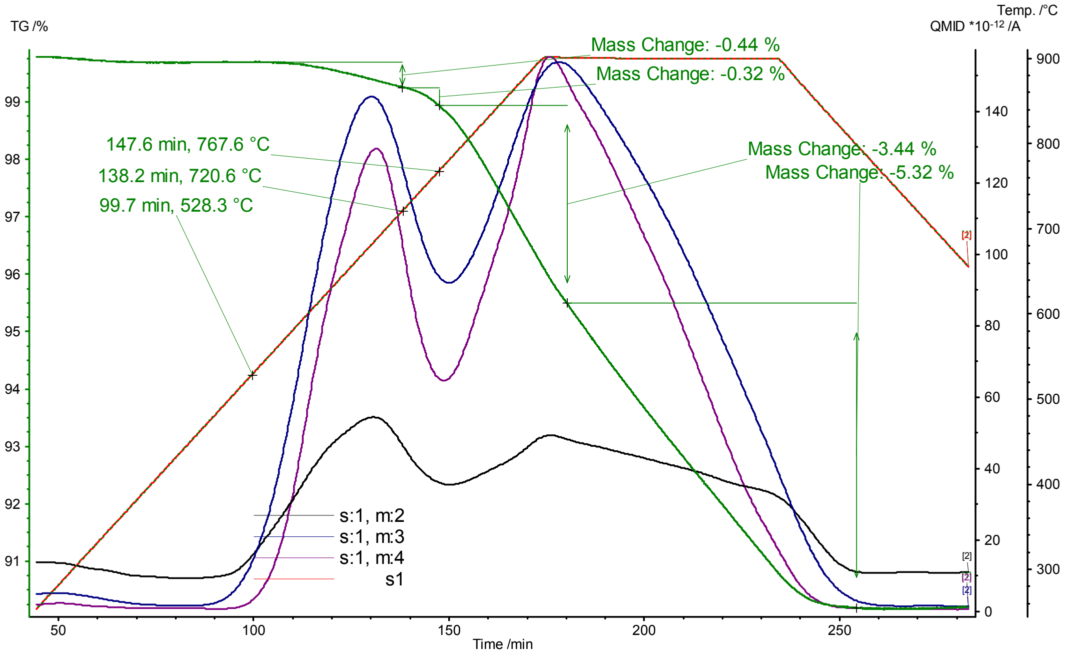

Figure 6-29: TGA/MS of Sr-N-D in argon, showing deuterium release

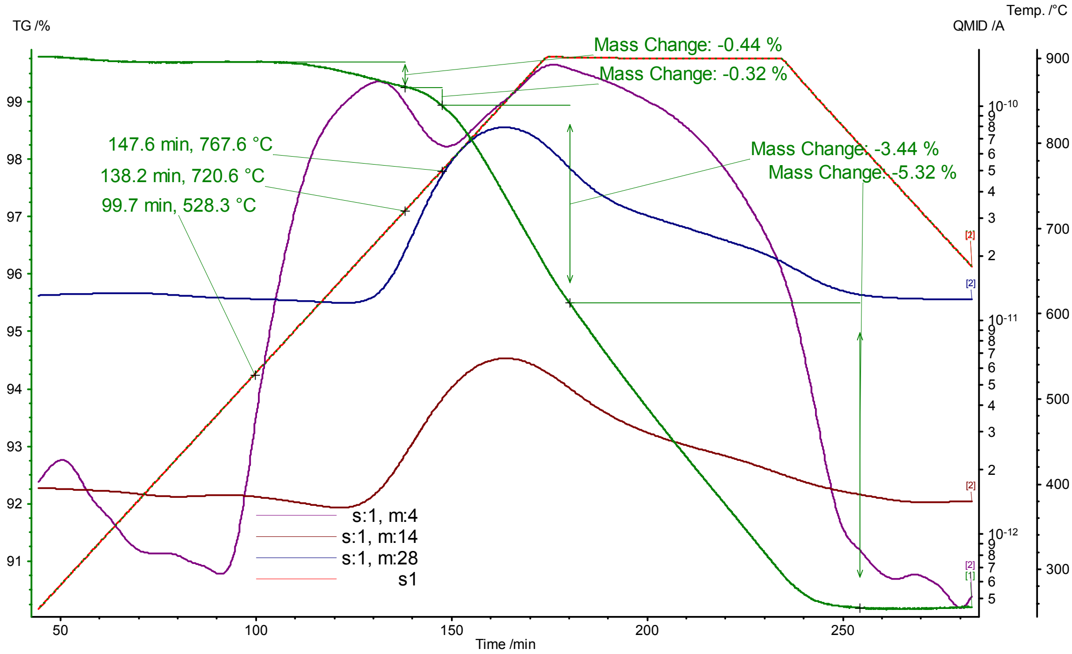

Figure 6-30: TGA/MS for Sr-N-D in argon, showing nitrogen release and mass4

As can be seen from Table 6-14, strontium evaporation is not as pronounced in 5% H_2 and nitrogen atmospheres. In nitrogen atmospheres this is probably caused by the formation of Sr_2N, which should be stable up to high temperatures in nitrogen atmosphere. SrH_2 however is supposed to decompose at ~850°C according to Peterson and Nelson [91]. In fact, as prepared SrH_2 has been tested for thermal stability in 5% H_2 and hydrogen release was observed, already at 798°C. Consequently, large weight losses due to Sr metal evaporation could also be observed for SrH_2.

Again, like in the case of Ca_2ND, the first weight loss at ~510°C is largest in the 5% H_2 atmosphere. The weight loss has even shifted to slightly lower temperature, i.e. 495°C. The weight loss now amounts to 0.91 wt%, which is close to the theoretical weight loss for a sample of pure Sr_2ND, which loses all of its deuterium. However, since it is expected that the sample will not contain more than 50 mol% of the nitride hydride phase, it is likely that some other process takes place at this temperature. On closer inspection of the DTA graph, it seems that there are actually two processes occurring. The first process, starting at 495°C releases 0.44 wt%, whereas the second process starts at 655°C with a weight loss of 0.47 wt%. This was also confirmed by a second run which included isotherms at 680°C and 780°C, yet higher temperatures for both steps were found, i.e. 570°C and 690°C. Since significant hydrogen absorption can be observed in the MS graph, it is believed that isotope exchange is taking place at this temperature. The theoretical weight loss for complete exchange of deuterium with hydrogen is 0.82 wt% for a sample with molar ratios found initially by Rietveld refinement of the neutron diffraction data (Sr_2ND : SrND : SrD_2 = 32 : 55 : 13). A further weight loss of 2.89 wt% at 760°C involves both N_2 and HD release.

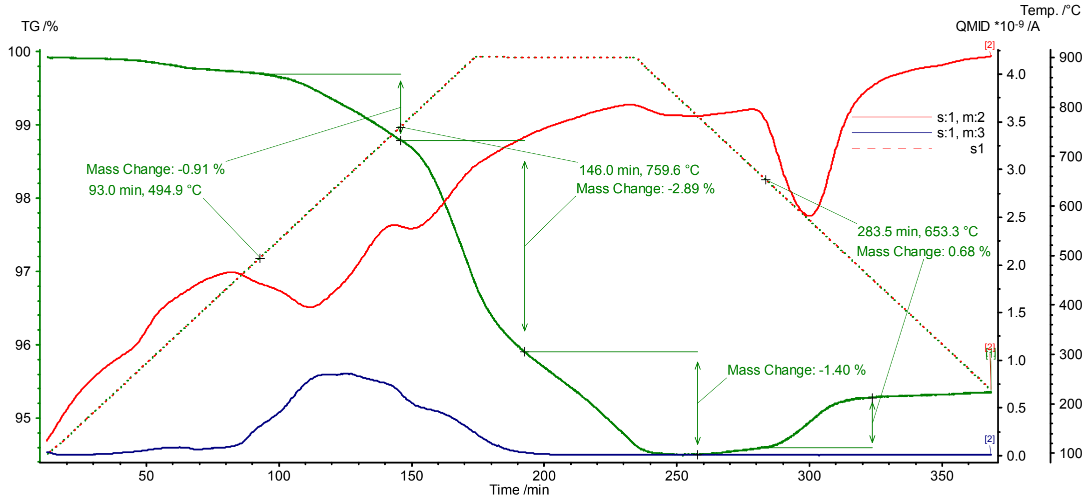

Figure 6-31: TGA/MS for Sr-N-D in 5% H_2/argon, showing mass2 and mass3

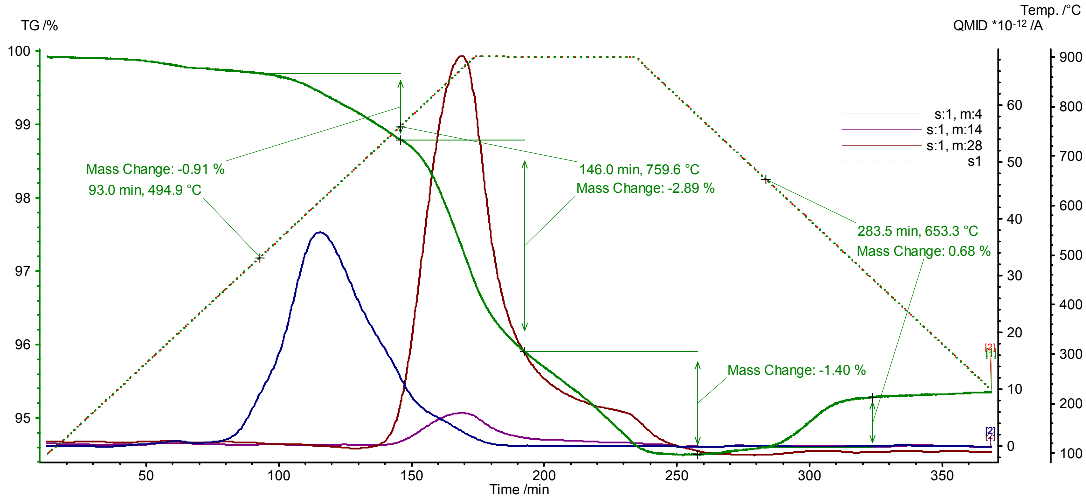

Figure 6-32: TGA/MS for Sr-N-D in 5% H_2/argon, showing mass4, mass14 and mass28

Sr-N-D in nitrogen

For the Sr-N-D sample in nitrogen atmosphere, a continuous deuterium release is observed from 440°C till 900°C, where the release seems to become diffusion limited. Complete loss of deuterium is therefore not expected. The first weight loss of deuterium (at 440°C) involves a weight gain, which can be explained by simultaneous deuterium release and nitrogen pick up by SrD_2. This was confirmed by performing thermal analysis on as prepared SrH_2 in nitrogen.

Nitrogen pick up did indeed start around 440°C. Also, Sr_2ND will release deuterium to form $Sr_2ND_{1-\delta}$, but this is expected to happen at slightly higher temperatures, i.e. 510 – 600°C (analogous to Sr-N-D in argon). At 722°C, a large weight loss is observed, continuing into the isotherm at 900°C. It is expected that all three phases will form Sr_2N, according to equations (6.24), (6.25) and (6.26). The observed weight loss at this temperature is 3.37 wt%.

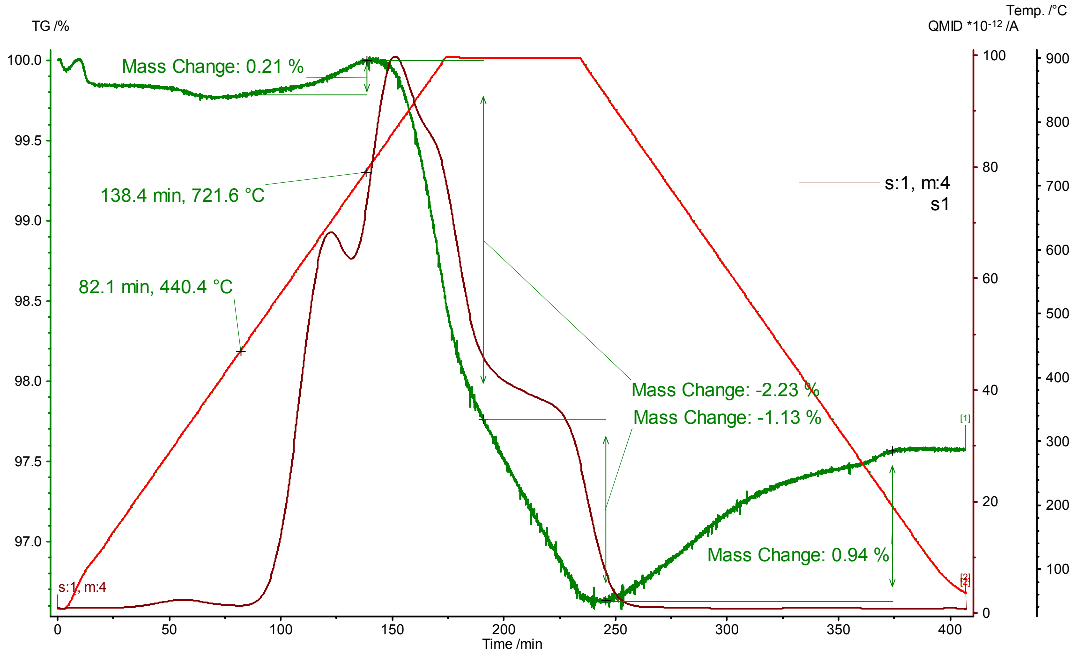

Figure 6-33: TGA/MS for Sr-N-D in nitrogen, showing mass4

6.2.5 CHN elemental analysis

CHN analysis reveals that the Sr-N-D sample, used for neutron diffraction, contained 1.77 wt% D/H and 9.10 wt% N. An assumption must be made for the SrD_2 content of the sample to calculate the phase content ratio of imide and nitride hydride. As the SrD_2 phase did not overlap much in the neutron diffraction pattern, the phase content calculated by Rietveld refinement of the neutron diffraction data was assumed to be fairly accurate. It turns out that when the SrD_2 content is set to 14 mol%, 32 mol% Sr_2ND and 54 mol% SrND are present. This is in fact very close to the values initially obtained from the Rietveld refinement.

6.2.6 X-ray data of Sr-N-H synthesised at 600°C and 700°C

The neutron diffraction data has given information about the phase contents of the imide and nitride hydride, synthesised at 600°C. This information was fed back to the analysis of the X-ray data obtained from the hydrogen containing sample synthesised at 600°C. The initial refinements, as presented in Table 6-9 were carried out using a single phase model. It was therefore tried to optimise the refinement by adding a secondary phase. A third SrH_2 phase can hardly be observed, so there is no need in refining this. The x-ray data is of insufficient quality to differentiate between the rhombohedral structure of Sr_2NH, rather than a cubic geometry and therefore the simpler cubic structure (spacegroup *F m 3 m*) is used to minimise the amount of refinable parameters. The phase ratio obtained from neutron diffraction was used and fixed in the refinement. The result can be seen in Table 6-16. The quality of the refinement does actually not improve upon using the second imide phase. Negative isotropic temperature factors still occur, which do not make any physical sense. The refinement also results in smaller lattice parameters for both imide and nitride hydride phase as compared to their deuterided counterparts. This is not expected and probably means that the hydrogen and deuterium containing phases are not identical enough to compare their data straight away. Small changes in the atmospheres (pH_2 vs. pD_2 and pN_2) can result in relatively large changes in stoichiometry as discussed for $Ca_2NH(D)$.

Table 6-16: Refinement for Sr-N-H synthesised at 600°C, using 2 cubic (*F m 3 m*) phases

Refinement parameter	Sr_2NH phase	SrNH phase
a (Å)	5.456 (2)	5.474 (2)
V ($Å^3$)	162.40 (9)	164.05 (9)
Sr, 4a (0,0,0)		
B ($Å^2$)	-2.3 (5)	-2.4 (3)
Occ	0.67	1.00
N, 4b (½,½,½)		
B ($Å^2$)	-3.7 (3)	-3.7 (3)
Occ	0.50	1.00
Phase content (mol%)	42	58
R_p	17.6	
R_{wp}	24.6	
R_{exp}	8.27	
χ^2	8.82	

The X-ray data obtained on the sample synthesised at 700°C is of even poorer quality, but the same information obtained from neutron diffraction was used to get more information about the two phases that form at this reaction temperature. Again two cubic phases, spacegroup *F m 3 m* are used, with initial lattice parameters obtained from indexing in the CHECKCELL software. The phase ratio is allowed to change, as it is expected that this material is richer in strontium imide. The refinement results can be found in Table 6-17.

Table 6-17: Refinement for Sr-N-H synthesised at 700°C, using 2 cubic (*F m 3 m*) phases

Refinement parameter	Sr_2NH phase	SrNH phase
a (Å)	5.4856(1)	5.515 (1)
V ($Å^3$)	165.06 (4)	167.74 (4)
Sr, 4a (0,0,0)		
B ($Å^2$)	-0.8 (2)	-0.8 (2)
Occ	0.67	1.00
N, 4b (½,½,½)		
B ($Å^2$)	0.9 (10)	0.9 (10)
Occ	0.50	1.00
Phase content (mol%)	22	78
R_p	6.16	
R_{wp}	9.52	
R_{exp}	4.30	
χ^2	4.89	

*) Parameter fixed

It can be seen that indeed the material gets richer in strontium imide phase when higher reaction temperatures are used. On increasing the reaction temperature from 600°C to 700°C, the phase content of the imide phase increase from 58 mol% to 78 mol%. It is therefore likely that the strontium imide phase could be obtained single phase by quickly cooling down a reaction product synthesised at temperatures > 700°C.

6.2.7 Discussion of Sr-N-D(H) results

From the weight gain during the synthesis, the Rietveld refinement and the CHN analysis it is assumed that the phase content ratio of Sr_2ND, SrND and SrD_2 is 31 : 56 : 13. With this ratio, the weight changes observed in the thermal analysis can now be linked to a set of decomposition or conversion steps that take place in the different atmospheres. Table 6-18 shows these steps, along with their observed and calculated weight changes and the ion masses of the released products as found by Mass Spectrometry.

Table 6-18: Decomposition or conversion steps for Sr-N-D in three atmospheres

Temp. (°C)	Decomposition/conversion step	Weight change (wt%)		Ion/gas involved	Eq. No (#)
		Theo.	Obs.		
	Argon				
510 – 520	$Sr_2ND \longrightarrow Sr_2ND_{1-\delta} + \frac{\delta}{2}D_2$, δ = 0.12	-0.06	Total:		(6.17)
660	$SrD_2 \longrightarrow Sr + D_2$	-0.39	-0.44	D_2	(6.18)
715 – 740	$2SrND \longrightarrow Sr_2ND_{1-\delta} + \frac{1}{2}N_2 + \frac{1+\delta}{2}D_2$	-3.40	-3.38	D_2, N_2	(6.19)
768 – 780	$Sr_2ND_{1-\delta} \longrightarrow Sr_2N + \frac{1-\delta}{2}D_2$, δ = 0.12	-0.87	-1.08	D_2	(6.20)
	5% H_2/argon				
495 – 570	$Sr_2ND + SrND + SrD_2 \xrightarrow{H_2} Sr_2NH_{1-\delta} + SrNH + SrH_2$	-0.83	-0.44	HD	(6.21)
660 – 690			-0.47		
760	$2SrNH \longrightarrow Sr_2NH_{1-\delta} + \frac{1}{2}N_2 + \frac{1+\delta}{2}H_2$	-3.28	-2.89	HD, N_2	(6.22)
	Nitrogen				
440	$SrD_2 + \frac{1}{2}N_2 \longrightarrow xSr_2ND + ySrND + \frac{3x+y}{2}D_2$	+0.27*	Total:		(6.23)
510 – 600	$Sr_2ND \longrightarrow Sr_2ND_{1-\delta} + \frac{\delta}{2}D_2$, δ = 0.12	-0.06	+0.21	D_2, HD	(6.17)
730	$2SrND \longrightarrow Sr_2N + D_2 + \frac{1}{2}N_2$	-3.87	Total:		(6.24)
	$Sr_2ND_{1-\delta} \longrightarrow Sr_2N + \frac{1-\delta}{2}D_2$, δ = 0.12	-0.40	-3.37	D_2, HD	(6.25)
	$2SrD_2 + \frac{1}{2}N_2 \longrightarrow Sr_2N + 2D_2$	+0.32**			(6.26)

*) For 30% conversion of SrD_2 into 37% Sr_2ND and 63% SrND

**) 0.32 wt% is theoretical weight gain, assuming no SrD_2 has been converted into Sr-N-D, according to equation (6.23)

The isotope exchange as given in equation (6.21) will be further discussed in the next paragraph. Table 6-18 further contains are a few highly speculative conversion steps, that might not take place, but their theoretical weight losses and decomposition products do agree with the experimental findings. Especially the reactions described in equations (6.19) and (6.22) do not seem to agree with the results discussed in section 6.2.2, where it was noted that with increasing reaction temperature, more strontium imide seems to be formed than strontium nitride hydride. It therefore seems unlikely that strontium imide would again transform into a nitride hydride at high temperatures. The actual atmospheres and partial hydrogen and nitrogen pressures are however also very important for the resulting phases and stoichiometries as already described for Ca_2ND. Therefore these conversion reactions might take place in the absence of nitrogen.

Of course, dealing with a three phase system is not ideal when trying to find out how these materials behave thermally. The only material which has been thermally tested so far is $SrH(D)_2$, but same should be done for SrNH(D) and $Sr_2NH(D)$. Synthesising these materials as a single phase is clearly not straightforward, but SrNH(D) could be prepared by decomposing $Sr(NH_2)_2$. Chemnitzer et al. have described a synthesis route for preparing single phase $Sr_2NH(D)$ [116], but this requires high hydrogen pressures, i.e. 200 bar.

Isotope exchange/exchange with H_2 atmosphere – Ca-N-D and Sr-N-D in H_2

Both Ca_2ND and Sr-N-D have been shown to undergo isotope exchange in a 5% H_2 atmosphere. This can alternatively be viewed as exchange with the atmosphere, which apparently is extremely rapid already at intermediate temperatures. It can be seen that the isotope exchange in both compounds is completed within an hour, which means that these materials have an extremely high exchange rate with their atmosphere. In the Sr-N-D case, weight loss occurs in two consecutive steps. This two step exchange can be thought of as a surface and bulk exchange at lower and higher temperature, respectively. For Ca_2ND these two steps seem to be convoluted. Finally it can be seen that hydrogen/deuterium exchanges as atomic H/D. The ion mass that is mainly found by MS is mass 3, belonging to HD, which forms by recombination of D atoms with H_2 in the atmosphere. These high exchange rates are generally not observed for oxides and certainly not at these relatively low temperatures. It would make the materials interesting for exchange membranes or as catalysts.

The isotope exchange seems to be closely correlated with the order – disorder transition for Ca_2ND and Sr_2ND. Both processes occur at similar temperatures and involve rapid N/D or H-D exchange within the crystal structures. The DTA data for Sr-N-D in argon and 5% H_2 atmosphere confirms this, as both graphs show a clear change in slope. Whereas in argon this change is due to the N/D order – disorder transition, in 5% H_2 it can be correlated to both order – disorder as well as H-D isotope exchange. Similar behaviour was observed in CaD_2 and SrD_2, in which the D/H exchange could also be related to an order – disorder transition. Similar isotopic exchange was in fact also found by Sobolev and Panov in CaH_2, SrH_2 and BaH_2 [117]. These disordering and exchange processes all relate to very mobile hydrogen/deuterium (nitrogen) species within the structure that also exchange with the atmosphere. This points to very large chemical diffusivities for these species and this makes these materials of great interest in membrane applications.

7 Structural and thermal properties of Li and Na doped Ca-N-H(D) and Sr-N-H(D)

Both Ca_2ND and Sr-N-D have been doped with monovalent elements to modify their defect chemistry. It is anticipated that substituting calcium and strontium with these elements would result in negatively charged defects, *e.g.* $Na'_{Ca/Sr}$. This negatively charged defect will have to be compensated by positively charged defects, for the compounds to maintain charge neutrality. Typical defects that might occur are hydride ion vacancies or interstitial cations. Reaction with Na or Li might also destabilise the hydride, creating electronic defects, like F-centres. The occurrence of defects will generally have an effect on both the structure as well as thermal or electrical properties. This chapter studies the structural and thermal properties of $Ca_2NH(D)$ and Sr-N-H(D) doped with small amounts of lithium and sodium. Diffraction techniques were used to analyse the new compounds and to identify important differences between the doped and host materials. Thermal analysis was also performed to see whether changes in thermal stability or in stoichiometry could be observed.

7.1 Experimental

$(Ca_{1-x}Na_x)_2ND_{1-\delta}$ and $(Sr_{1-x}Na_x)$-N-D (nominally $0 < x < 0.10$) were prepared by solid state reaction of Ca_2ND or Sr-N-D with NaD. The respective materials were thoroughly mixed using mortar and pestle and subsequently pressed into pellets. The pellets were fired in two steps; 16 hours at 330°C and another 16 hours at 600°C. NaD was prepared by firing sodium metal in pure H_2 in a stainless steel bomb at 540°C with an initial pressure of $pH_2 = 2.8$ bar. The reaction takes about 48 hours to complete. $(Ca_{1-x}Li_x)_2ND$ ($x = 0.05$) was also prepared in a similar manner, using the fully deuterided Ca_2ND sample as the parent material, described in chapter 6, section 6.1.3.1. To carry out the solid state reaction, pellets of mixed LiD and Ca_2ND were fired at 600°C in pure deuterium in a sealed stainless steel reactor for 16 hours. LiD was prepared by firing lithium metal in pure flowing deuterium gas at 650°C for 8 hours.

The Na doped Ca_2ND samples show a colour change from yellow to green. Na doped Sr-N-D has a beige colour as opposed to the yellow – orange colour of undoped Sr-N-D. These colour changes suggest that at least some reaction takes place.

Neutron powder diffraction was carried out on instrument D1A at ILL, Grenoble (France). Samples were loaded into vanadium cans in a glovebox to protect the sample from moisture and air. Indium wire between the cans and lids further operated as a gastight seal, to protect the samples during measurements. The neutron wavelength was refined to 1.9114 Å and patterns were recorded between $0 < 2\theta < 158°$, with a resolution of 0.05°. All neutron diffraction experiments were carried out at room temperature. $(Ca_{1-x}Li_x)_2ND$ was synthesised from a different parent material (fully deuterided Ca_2ND) and its neutron diffraction pattern was recorded on a different day. All experimental conditions were identical, apart from the neutron wavelength, which was refined to 1.9095 Å.

7.2 Results –Atomic Absorption Spectroscopy (AAS)

Weight losses and material deposition were observed after the solid state reactions of NaD with Ca_2ND and Sr-N-D. It was anticipated that sodium might evaporate at 600°C, so to obtain the actual sodium content of the samples, atomic absorption was carried out. The results can be found in Table 7-1. The actual sodium content is very small and even slightly smaller than the solubility limits of NaF in CaF_2 found by Natsuhara et al. [95] (1.7 mol%). Ure [96] however found a lower value for the solubility limit in the same NaF – CaF_2 system, i.e. 0.6 mol%, which agrees better with the values found in this study.

Table 7-1: AA sodium content result

Compound	x (nominal composition)	x (actual Na content)
$(Ca_{1-x}Na_x)_2ND$	0.02	6.6×10^{-3}
$(Ca_{1-x}Na_x)_2ND$	0.1	7.9×10^{-3}
$(Sr_{1-x}Na_x)$-N-D	0.02	3.1×10^{-3}
$(Sr_{1-x}Na_x)$-N-D	0.05	1.0×10^{-2}

7.3 Na doped Ca_2ND – Neutron diffraction

Neutron diffraction patterns for two Na doped Ca_2ND samples are shown in Figure 7-1. Refinement of the neutron diffraction data of the Na-doped Ca_2ND samples was done using the low temperature (<650°C) model used for undoped Ca_2ND. This model includes imide ion substitution on the 16c and 16d sites (substitution for deuteride and nitride ions, respectively). The refinement results are shown in Table 7-2. The occupancies for both N and D(H) on their respective crystallographic sites have been fixed to 1, as Fourier difference maps revealed excess residual neutron scattering length density, after refinement in the standard Ca_2ND model (as described in chapter 6, section 6.1.3). This confirms again that the actual stoichiometries of these materials are very changeable and strongly dependent on reaction conditions. The residual scattering density further justifies using the structural model, which includes imide ion substitution. Also explained in chapter 6 section 6.1.3, a general formula $(Ca_{1-x}Na_x)_2N_{1-y}D_{1-z}(ND)_{y+z}$ is expected. A third model was used to refine the undoped Ca_2ND samples, which involved an additional interstitial deuteride site on 8a. This has been tried for the Na doped samples as well, but no improvement of the fit could be obtained and moreover, the occupancy of this site was found to be close to 0.0. Since the remaining refinement parameters using this third model were nearly identical to the values that are already listed in Table 7-2, these results have been omitted.

The refinement results show a significant increase in the imide content after doping. In the general formula $(Ca_{1-x}Na_x)_2N_{1-y}D_{1-z}(ND)_{y+z}$, *y* after doping is ~0.24, whereas *z* amounts to 0.15. Before doping, *y* and *z* are only 0.10 and 0.08, respectively. This seems quite surprising, as adding a more electropositive element to the structure, namely Na, would be expected to have a reducing effect, whereby the amount of imide ions should be reduced, whilst leaving more of nitride hydride character.

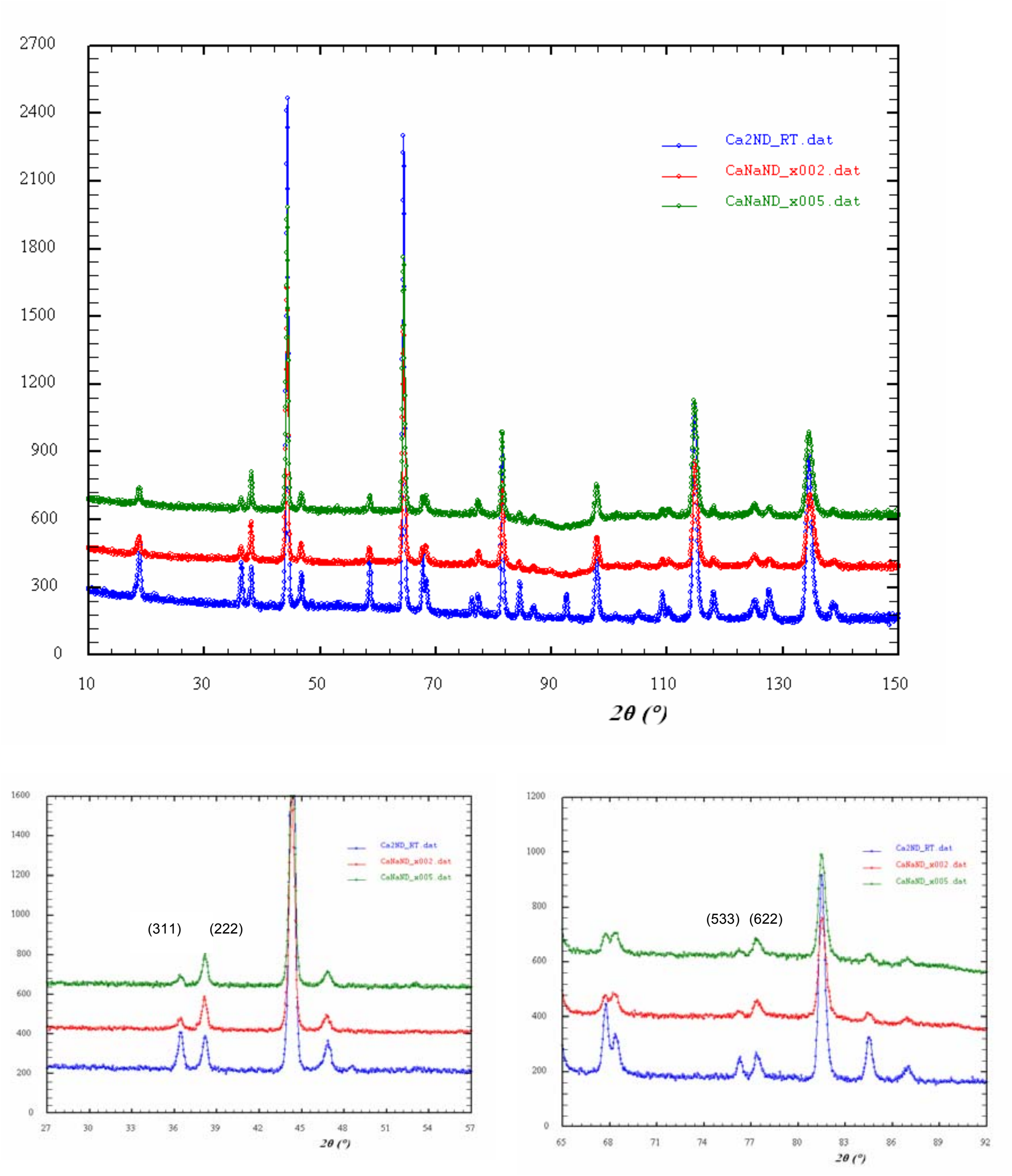

Figure 7-1: Neutron diffraction patterns of $(Ca_{1-x}Na_x)_2ND_{1-\delta}$. Nominal sodium substitution is as follows: blue x = 0, red x = 0.02, green x = 0.05

On closer inspection of the neutron diffraction pattern, a resemblance with the diffraction patterns of the high temperature phase of undoped Ca_2ND can be seen. The neutron diffraction patterns of this high temperature phase were characterised by the change of relative intensities of the (311) and (222) peaks and the (533) and (622) peaks. Similar behaviour is now observed for the Na doped samples at room temperature. It is possible that sodium doping causes disorder in the N and H(D) layers, which was used to characterise the high temperature neutron diffraction data for Ca_2ND. Refinement of the Na – doped data using this model however, does not lead to satisfactory results. In fact, divergence of the refinement model occurs, even after fixing and correlating most parameters. It is therefore not unlikely, that the change in intensities is mainly due to a change in stoichiometry (increase of N and D/H occupancies and imide substitution). Disordering of the overall structure is not unlikely to happen to some extent as well. After all, an increased amount of imide ions are substituting for the nitrides and hydrides, which will affect the ordering. In Sr-N-D we saw a complete disorder in Sr_2ND upon the formation of a second imide phase. Also, the Ca ions are moving more towards the ideal (¼,¼,¼) sites, which is indicative for disorder of the N and D ions, as the difference in electrostatic attraction between N^{3-} and D^- ions is more averaged out in a disordered system.

Table 7-2: Refinement summary for $(Ca_{1-x}Na_x)_2N_{1-y}D_{1-z}(ND)_{y+z}$ in spacegroup *F d 3 m*, λ = 1.9114 Å. Structural model involves imide ion substitution on 16c and 16d sites. No interstitial deuterium on site 8a was refined

Refinement parameter	x = 0	x = 0.02	x = 0.05
Actual Na content, x	0	0.007	0.008
a (Å)	10.1550 (2)	10.1502 (2)	10.1521 (2)
R_p	4.16	5.50	4.27
R_{wp}	5.32	7.28	5.06
R_{exp}	2.79	3.77	3.47
χ^2	3.65	3.72	2.13
Ca, 32e (x,x,x)			
x	0.2579 (3)	0.2545 (5)	0.2555 (4)
B ($Å^2$)	1.30 (6)	1.50 (7)	1.31 (7)
N1, 16d (½,½,½)			
B ($Å^2$)	1.08 (4)	1.27 (6)	1.35 (6)
Occ	1.00	1.00	1.00
D1/H1, 16c (0,0,0)			
B ($Å^2$)	3.7 (1)	2.9 (1)	2.3 (1)
Occ	0.75	1.00	1.00
N2, 96g (x,x,z) *imide coordinated to D1/H1*			
x	0.061 (4)	0.037 (3)	0.039 (4)
z	0.028 (10)	-0.084 (3)	-0.072 (4)
B ($Å^2$)	3.7 (1)	2.9 (1)	2.3 (1)
Occ	0.014 (1)	0.025 (2)	0.023 (2)
D2, 96g (x,x,z) *imide coordinated to N1*			
x	0.562 (1)	0.438 (2)	0.470 (3)
z	0.477 (10)	0.545 (7)	0.580 (2)
B ($Å^2$)	1.08 (4)	1.27 (6)	1.35 (6)
Occ	0.016 (4)	0.041 (3)	0.039 (2)
d (Ca-N) (Å)	2.462 (3)	2.493 (5)	2.483 (4)
d (Ca-D) (Å)	2.620 (3)	2.584 (5)	2.595 (4)

In Table 7-2 and Figure 7-2 it can be seen that the lattice parameter of Ca_2ND changes upon Na doping. The change does not seem to follow Vegard's law, but generally it can be said that the lattice parameter decreases upon Na substitution. Whether it is the Na substitution or the small compositional changes (i.e. change in N and D(H) occupancies) that causes this change in lattice parameter cannot be said. A decrease in lattice parameter is actually quite unexpected as Na has a larger ionic radius than Ca and if it were the Na substitution that is responsible for the lattice parameter change, an increase in lattice parameter would be expected. If the change in stoichiometry would cause the change, an increase in lattice parameter would also be expected. There is a net overstoichiometry of N and D(H) in the structure, which would give the nitride hydride a slight imide character. The imide has a slightly larger lattice parameter than half the nitride hydride's lattice parameter.

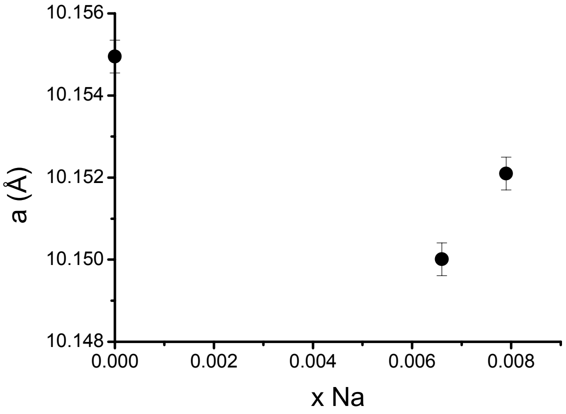

Figure 7-2: Lattice parameter of $(Ca_{1-x}Na_x)_2ND$ vs. x (Na content)

7.4 Li doped Ca_2ND – neutron diffraction

Ca_2ND was also doped with lithium (5 mol% of Ca content), as lithium too has an ionic radius which is relatively close to calcium. The sample that was doped is the sample that is discussed in section 6.1.3.1 in chapter 6 and therefore has only deuterium and no hydrogen in its structure. Furthermore it has excess neutron scattering density on both the nitride (½½½, 16d) and deuteride (000, 16c) site, which is accounted for by substituting these sites partially with imide ions. No secondary imide phase could be observed however.

After doping with lithium, broadening of the peaks at high angle can be observed, analogue to what is observed for the mixed Sr-N-D phase. Refinement of the pattern is possible assuming a mixed phase of calcium imide and calcium nitride hydride. The refinement results are summarised in Table 7-3. No sign of residual LiD could be observed, so it is assumed that all LiD is incorporated into the Ca_2ND and CaND structures. The lattice parameter for the imide phase is 5.0913(2) Å and this seems low compared to literature values (5.14 Å [109, 110]). This could partially be caused by the deuterium in the structure. The calcium imides reported in literature were not deuterided and will have a higher cubic lattice parameter, as described in chapter 2, section 2.1.3. Lithium imide (Li_2ND) reportedly has a cubic lattice parameter of 10.127 Å in spacegroup *F d 3 m* [60], which is two times 5.064 Å when converted to a single face centred cubic cell. Hence lithium doping could also explain the strong contraction of the calcium imide unit cell. The pattern including refinement and difference plot can be found in Figure 7-3.

Li doping clearly has a detrimental effect on the stability of single phase nitride hydride phase. This is possibly caused by the fact that lithium imide is far more easily formed than lithium nitride hydride, which only seems to form upon reaction between LiH and Li_3N [59]. The formation of lithium imide might then trigger the formation of a stable calcium imide phase, instead of having imide ions randomly distributed within the calcium nitride hydride lattice. Lithium (hydride / deuteride) is in this sense a unique dopant, as it is the only alkali metal that reacts directly with nitrogen and hydrogen to form nitrides, amides and imides. Sodium is practically inert towards nitrogen [58]. Therefore similar imide formation is not observed for the Na doped Ca_2ND samples. Doping with sodium does however cause an increase in the imide substitution in Ca_2ND and it also affects the imide/nitride hydride phase ratio in the strontium based samples, as we will see shortly.

Doping Ca_2ND with lithium causes a large increase in lattice parameter of the nitride hydride phase, i.e. from 10.1238(2) Å to 10.1350(2) Å. Again this seems unexpected, as lithium has a smaller ionic radius than calcium. Although a secondary imide phase has formed, there is still excess neutron scattering density on the nitride and deuteride sites in the Ca_2ND structure. This most likely means that still some substitution by imide ions on these sites occurs. Analogous to the Sr_2ND/SrND mixed phase, the order in the Ca_2ND seems to have disappeared completely. This becomes apparent from the absence of any double cubic superstructure peaks in the diffraction pattern. Therefore the doped nitride hydride phase will be treated as a single cubic cell, with spacegroup *F m 3 m*, in which the nitride and hydride ions randomly occupy the octahedral holes in the close packed calcium array. A slight improvement of the refinement can even be obtained when the rhombohedral spacegroup *R -3 m* is used, so possibly a small change in symmetry takes place upon lithium doping. Because of the N-D disorder, y and z in $(Ca_{1-x}Li_x)_2N_{1-y}D_{1-z}(ND)_{y+z}$ are now equal and the total imide content is very large with $y+z = 0.51$. Although this imide content seems unreasonably large, it would explain why a second imide phase develops upon Li doping. The nitride hydride phase has possibly accommodated its maximum imide ion content and consequently a second imide phase starts to build.

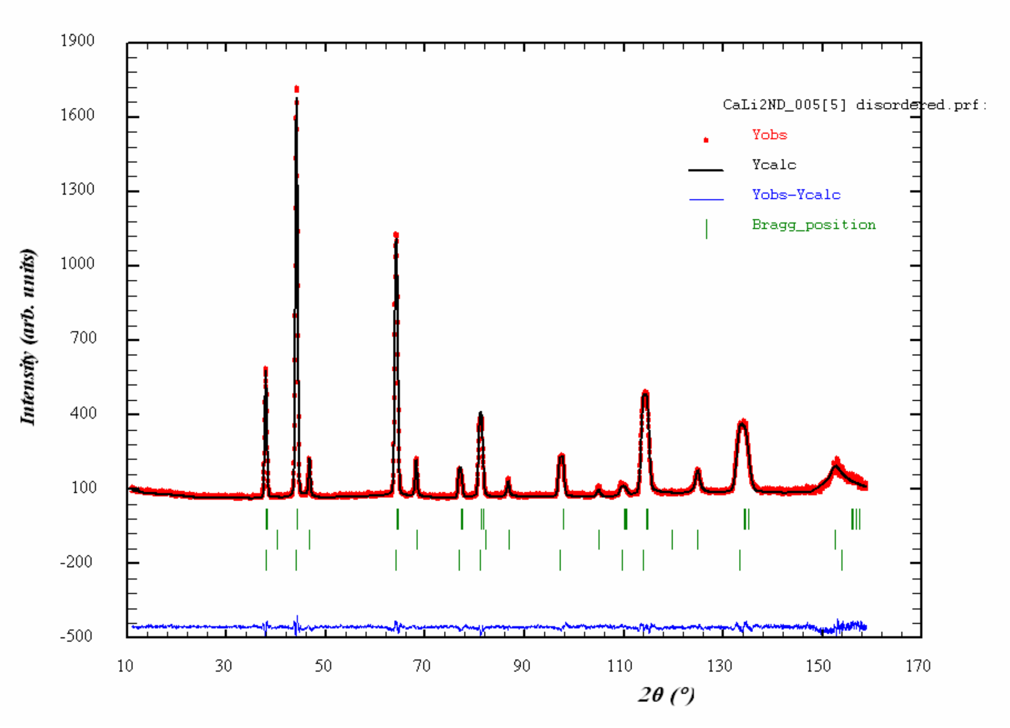

Figure 7-3: Neutron diffraction pattern of $Ca_{0.95}Li_{0.05}$-N-D; mixed imide and nitride deuteride phase (and CaO as third phase). Observed pattern in red, refinement in black, residuals after refinement in blue and reflection positions in green.

Table 7-3: Refinement results for 5 mol% Li doped Ca_2ND. Two phase system: phase 1 is $(Ca_{0.95}Li_{0.05})_2N_{1-y}D_{1-z}(ND)_{y+z}$ phase, spacegroup *F m 3 m*. Phase 2 is $Ca_{0.95}Li_{0.05}ND$ (imide), spacegroup *F m 3m*. λ = 1.9095 Å

Refinement parameter	Phase 1: $(Ca_{0.95}Li_{0.05})_2N_{1-y}D_{1-z}(ND)_{y+z}$		Phase 2: $Ca_{0.95}Li_{0.05}ND$
a (Å)	5.0675 (2)	a (Å)	5.0913 (2)
Ca/Li, 4a (0,0,0)		Ca/Li, 4a (0,0,0)	
B (Å^2)	1.84 (8)	B (Å^2)	0.7 (1)
N1/D1, 4b (½,½,½)		N1, 4b (½,½,½,)	
B (Å^2)	1.52 (6)	B (Å^2)	1.25 (9)
N2/D2, 96g (x,x,z)		D1, 96j (0,y,z)	
x	0.445 (2)	y	0.330 (5)
z	0.670 (1)	z	0.069 (13)
B (Å^2)	1.52 (6)	B (Å^2)	13 (10)
Occ	0.0058 (1)		
		d N-D (Å)	0.934 (10)
		γ (Ca-D-N)	146.0° (7)
Phase content (mol%)	39*	Phase content (mol%)	61*
R_p		4.18	
R_{wp}		5.04	
R_{exp}		4.11	
χ^2		1.50	

Table 7-4: Refinement results for 5 mol% Li doped Ca_2ND. Two phase system: phase 1 is $(Ca_{0.95}Li_{0.05})_2N_{1-y}D_{1-z}(ND)_{y+z}$ phase, spacegroup *R -3 m*. Phase 2 is $Ca_{0.95}Li_{0.05}ND$ (imide), spacegroup *F m 3m*. λ = 1.9095 Å

Refinement parameter	Phase 1: $(Ca_{0.95}Li_{0.05})_2N_{1-y}D_{1-z}(ND)_{y+z}$		Phase 2: $Ca_{0.95}Li_{0.05}ND$
a (Å)	3.5872 (4)	a (Å)	5.0922 (3)
c (Å)	8.7636 (10)		
$\frac{c}{a\sqrt{6}}$	0.9974		
V ($Å^3$)	97.66 (2)	V ($Å^3$)	132.04 (1)
Ca/Li, 3a (0,0,0)		Ca/Li, 4a (0,0,0)	
B ($Å^2$)	1.72 (7)	B ($Å^2$)	0.8 (1)
N1/D1, 3b (0,0, ½)		N1, 4b (½,½,½)	
B ($Å^2$)	1.51 (6)	B ($Å^2$)	1.23 (9)
N2/D2, 36i (x,y,z)		D1, 96j (0,y,z)	
x	0.1450 (4)	y	0.334 (5)
y	0.3006 (8)	z	0.074 (9)
z	0.520 (2)	B ($Å^2$)	12 (10)
B ($Å^2$)	1.51 (6)		
Occ	0.011 (1)		
		d N-D (Å)	0.924 (15)
		γ (Ca-D-N)	143.5 (13)
Phase content (mol%)	43*	Phase content (mol%)	57*
R_p	4.09		
R_{wp}	4.97		
R_{exp}	4.11		
χ^2	1.47		

*) CaO phase included in calculation

A good refinement is obtained when assuming two main phases are present: $(Ca_{0.95}Li_{0.05})_2ND$ and $Ca_{0.95}Li_{0.05}ND$). There is however the possibility of a third phase with very close lattice geometry, Ca doped Li_2ND. This phase will be less dominant as only 5 mol% Ca was substituted for Li. Also, Li has a negative neutron scattering length, so a possible contribution to the pattern will partly counteract those of the previous two phases. Still, a mixture of three phases, which might even form solid solutions with even closer lattice parameters, could be present, making this system very complicated and hard to analyse using diffraction techniques only.

7.5 Na doped Sr-N-D – neutron diffraction

From neutron diffraction pattern refinements, it seems that both SrND and Sr_2ND are doped with sodium. The Sr-N-D material was doped with nominally 2 mol% and 5 mol% Na by metal content. Sr_2ND shows a small volume contraction upon doping with Na, whereas the cubic lattice parameter of SrND shows a generally decreasing trend, with *a* being smallest for the nominally 2 mol% doped sample, *i.e.* a = 5.4941(6) Å as compared to 5.4997(3) Å for the undoped material. The decreases in volume and lattice parameter, respectively, are likely to be caused by the substitution of strontium with the smaller sodium ion.

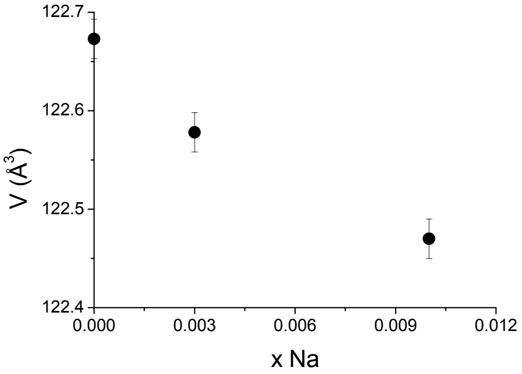

Figure 7-4: Unit cell volume of Sr_2ND vs. Na content

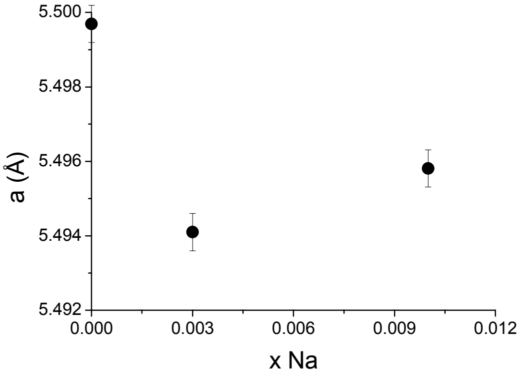

Figure 7-5: Cubic lattice parameter of SrND vs. Na content

No more SrD_2 phase could be observed after the solid state reaction with sodium. In the undoped Sr_2ND/SrND mixed phase, the nitride hydride : imide phase (molar) ratio was 37 : 63. After doping with nominally 2 and 5 mol% NaD, the imide content has increased to 68 mol% and 72 mol%, respectively. This seems counter intuitive, as the sodium is expected to have a reducing effect that would result in more nitride and hydride ions as opposed to imide ions. The process that does take place, however, is probably more like what was observed for Li doped Ca_2ND, which caused the development of a stable calcium imide phase. The alkali metals clearly prefer to be surrounded by imide ions rather than nitride and hydride ions. This effect is also seen in the Sr_2ND phase, where the Sr occupancy has now dropped to 0.60, which suggests that 67% of the nitride and hydride ions are actually substituted by imide ions. This seems very high for this phase to still be a stable nitride hydride phase, but the general trend is consistent.

Table 7-5: Refinement results for nominally 5 mol% Na doped Sr-N-D. Two phase system: phase 1 is $(Sr_{0.99}Na_{0.01})_2ND$ in spacegroup *R -3 m*, phase 2 is $Sr_{0.99}Na_{0.01}ND$ (imide) in spacegroup *F m 3 m*. λ = 1.9114 Å

	Phase 1		Phase 2
Refinement parameter	$(Sr_{0.99}Na_{0.01})_2ND$		$Sr_{0.99}Na_{0.01}ND$
a (Å)	3.8691 (6)	a (Å)	5.4958 (5)
c (Å)	9.447 (2)		-
V (Å^3)	122.47 (4)	V (Å^3)	166.00 (2)
Sr/Na, 3a (0,0,0)		Sr/Na, 4a (0,0,0)	
B (Å^2)	0.0 (1)	B (Å^2)	3.0 (2)
Occ	0.60 (1)		
N, 3b (0,0, ½)		N, 4b (½,½,½)	
B (Å^2)	5.1 (2)	B (Å^2)	2.2 (1)
Occ	0.50		
D/H, 3b (0,0, ½)		D/H, 96j (0,y,z)	
B (Å^2)	5.1 (2)	y	0.344 (4)
Occ	0.50	z	0.098 (4)
		B (Å^2)	4.4 (9)
		d (N-D) (Å)	1.01 (1)
		γ (Sr-D-N)	132.1° (7)
Phase content (mol%)	28		72
R_p		4.15	
R_{wp}		5.32	
R_{exp}		3.26	
χ^2		2.66	

7.6 Thermal analysis

7.6.1 Na doped Ca_2ND

It was shown using neutron diffraction that the stoichiometries of the Ca-N-H(D) system are very changeable and seem to depend strongly on the partial nitrogen and hydrogen (deuterium) pressures during synthesis. Also the doping has an effect on the presence of imide ions inside the nitride hydride structure and in the case of Li doped Ca_2ND, the imide phase becomes a stable secondary phase. Changes in the N and H(D) stoichiometry should be reflected in the thermal analyses of these compounds, as different amounts of hydrogen and nitrogen should be released by the compounds. It is further interesting to see whether the imide ions inside the nitride hydride structure have a different thermal stability than the nitride and hydride ions.

Figure 7-6 and Figure 7-7 show the TGAs for Na doped Ca_2ND (nominally 5 mol%) along with its undoped parent material in an argon atmosphere. A few differences can readily be seen. Firstly, a larger weight loss occurs at low temperatures, i.e. 309°C, which is too large to be due to decomposition of surface hydroxides. Very similar weight losses occur at 580 – 590°C, whereas Na doped Ca_2ND again loses more weight at 707°C. The total weight loss for Na doped Ca_2ND amounts to 2.98 wt%, which is in excellent agreement with the theoretical weight loss of a compound with composition $(Ca_{0.992}Na_{0.008})N_{0.75}D_{0.85}(ND)_{0.40}$ that decomposed fully into Ca_2N. The different weight losses along with masses of the released gases as recorded by MS are listed in Table 7-6. It can be seen that the main ion mass found for the weight loss at 309°C is m18 (m17), which could be a water molecule as expected from $Ca(OH)_2$ decomposition. The weight loss seems too large though and therefore it is thought that the ion mass represents a NDH_2 (NDH) ion, which is likely to be due to release of the imide ions in the nitride hydride structure. The weight loss would only account for a loss of 0.023 formula units of imide. The consecutive weight loss at 596°C mainly involves the loss of deuterium (HD) and is therefore believed to be simply due to deuterium loss from the Ca_2ND structure (giving $Ca_2ND_{1-\delta}$, $0.10 \leq \delta \leq 0.33$). The weight change represents a loss of 0.17 formula units of deuterium. In the last step at 707°C the remaining 2.40 wt% is released, resulting in complete decomposition into Ca_2N. It is interesting to see that when the imide ion decomposes, it is released in the form of ammonia (ND picking up H from moisture in the mass spectrometer), whereas the nitride ion is mainly released as molecular nitrogen (N_2, m28). This behaviour is not observed at higher temperatures though, as ammonia is not stable and will decompose itself into nitrogen and hydrogen/deuterium.

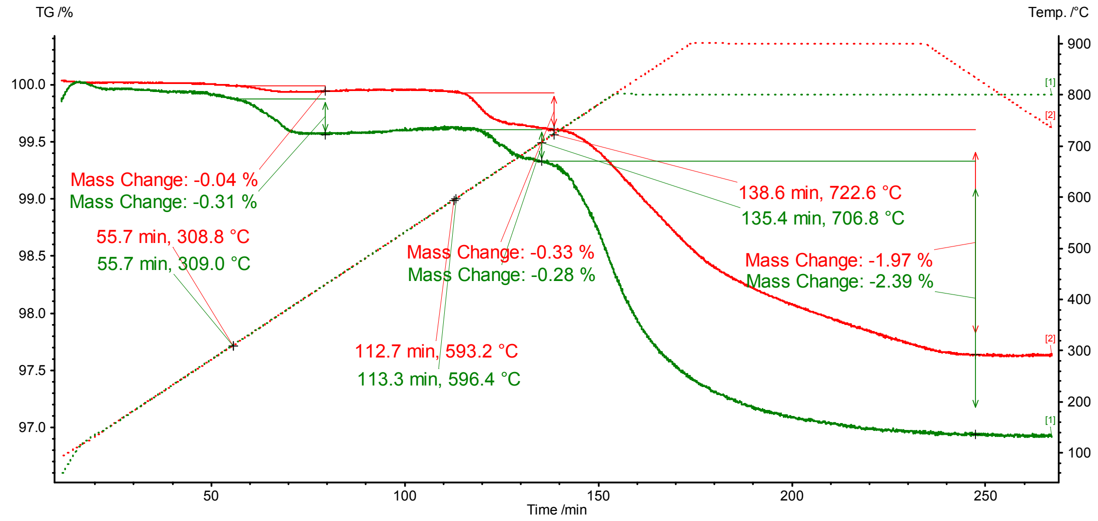

Figure 7-6: TGA for undoped $Ca_2N_{1.05}D_{0.83}$ (red) and $(Ca_{1-x}Na_x)_2N_{1.10}D_{1.10}$ (green)

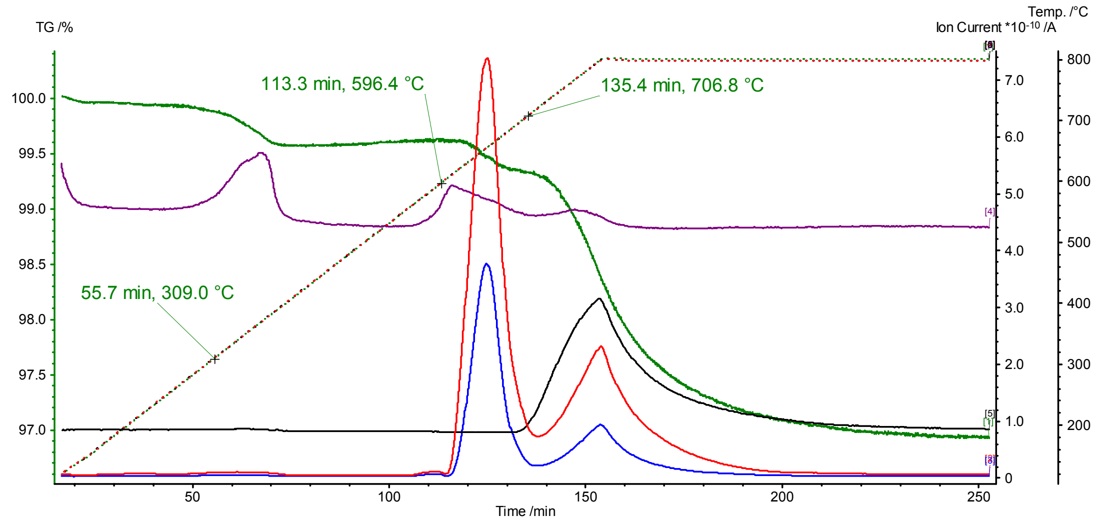

Figure 7-7: TGA for $(Ca_{1-x}Na_x)_2N_{1.10}D_{1.10}$ in argon (green), showing MS trail for m3 (red), m4 (blue), m18 (purple) and m28 (black)

Table 7-6: TGA results for $(Ca_{1-x}Na_x)_2N_{1.10}D_{1.10}$ in argon

Temperature (°C)	Weight loss (wt%)	Ion mass involved	Gas involved
309	-0.31	m18 (m17)	NDH_2
596	-0.28	m3 (m4)	HD (D_2)
707	-2.39	m3 (m4), m28	HD (D_2) & N_2

7.6.2 Li doped Ca-N-D

As described in section 7.4, doping of Ca_2ND with Li causes the development of a stable imide phase and the resulting material is a mixed phase of imide and nitride hydride. Figure 7-8 shows the TGA for both undoped and Li-doped Ca_2ND, which shows a dramatic increase in weight loss after doping. It can also be seen that the first loss of nitrogen occurs at lower temperature, i.e. 631°C for Li-doped Ca_2ND as opposed to ~760°C for undoped Ca_2ND. Clearly the imide phase is less stable than the nitride hydride and interconversion between the two takes place, as observed in the Sr-N-D system. The final weight losses of 2.59 and 4.35 wt% agree well with conversion from imide to nitride hydride with concomitant loss of overstoichiometric nitrogen and deuterium from the nitride hydride phase. The suggested decomposition mechanism is now:

$$(Ca_{1-x}Li_x)_2N_{1.04}D_{1.21} \xrightarrow{T=571^\circ C} (Ca_{1-x}Li_x)_2N_{1.04}D_{1.04} \qquad -0.16\text{ wt\%} \tag{7.1}$$

$$(Ca_{1-x}Li_x)ND \xrightarrow{T=631^\circ C} \tfrac{1}{2}(Ca_{1-x}Li_x)_2ND + \tfrac{1}{4}N_2 + \tfrac{1}{4}D_2 \qquad -6.74\text{ wt\%} \tag{7.2}$$

$$(Ca_{1-x}Li_x)_2N_{1.04}D_{1.04} \xrightarrow{T=751^\circ C} (Ca_{1-x}Li_x)_2ND + \tfrac{0.04}{2}N_2 + \tfrac{0.04}{2}D_2 \qquad -0.29\text{ wt\%} \tag{7.3}$$

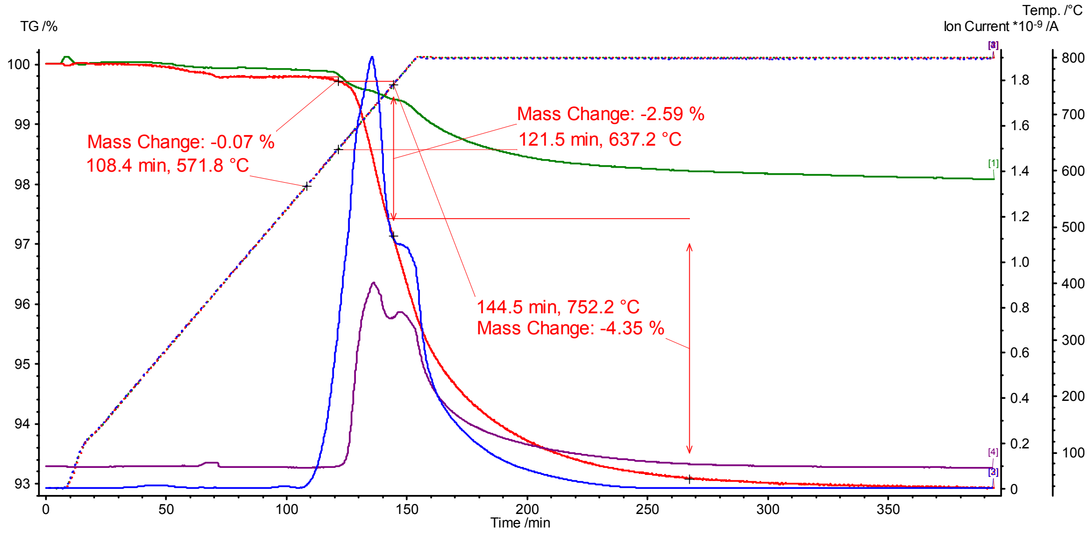

Figure 7-8: TGA for $Ca_{1-x}Li_x$-N-D in argon (red) and Ca_2ND (green), showing MS trail for m4 (blue) and m28 (purple)

Table 7-7: TGA results for $Ca_{1-x}Li_x$-N-D

Temperature (°C)	Weight loss (wt%)	Ions involved	Gases involved
213	-0.20	m18, m4	H_2O, D_2
571	-0.07	m4	D_2
631	-2.59	m4, m28	D_2, N_2
751	-4.35	m4, m28	D_2, N_2

7.6.3 Na doped Sr-N-D

The TGA for the Na doped Sr-N-D system looks similar to that of its parent material, although some differences can readily be observed. As observed for Na doped Ca_2ND, a larger weight loss can be seen at low temperatures (199°C), which is hard to attribute to decomposition of surface hydroxides alone. This is followed by a weight loss at 510°C, which is smaller than the same weight loss observed for undoped Sr-N-D, i.e. 0.11 wt%. This can be explained by the absence of a SrD_2 phase, which was present in the undoped Sr-N-D system and decomposed along with some deuterium loss from Sr_2ND to form $Sr_2ND_{1-\delta}$. For this Na doped system this weight loss now reflects the loss of 0.26 formula units of deuterium from Sr_2ND. The large final weight loss of 4.90 wt% can be ascribed to both $Sr_2ND_{1-\delta}$ and SrND decomposing into Sr_2N (theoretical weight loss of 5.32 wt% for Sr_2ND : SrND = 0.28 : 0.72). Again, as this step takes place at too high temperatures, the released imide ions are not being seen on the MS as ammonia ions, but rather as N_2 and HD (D_2).

It seems that after doping, some of the imide ions are metastable and are already released at low temperature, i.e. 199°C. It is difficult to verify this from MS data, as the related ion masses for imide release and surface hydroxide decomposition are identical (m18). If the weight loss were due to surface hydroxide decomposition alone, this would mean the sample would have picked up a lot of hydroxides inside the sealed container in the glovebox. In this case it would mean these compounds are extremely moisture sensitive, much more than for instance 'pure' hydrides.

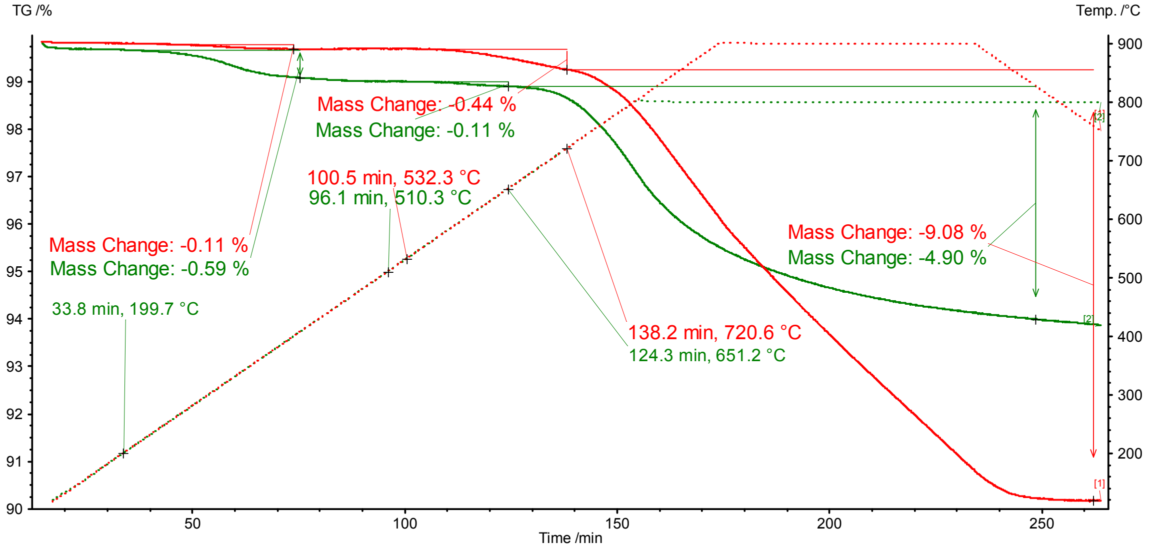

Figure 7-9: TGA for undoped Sr-N-D (red) and $(Sr_{1-x}Na_x)$-N-D (green)

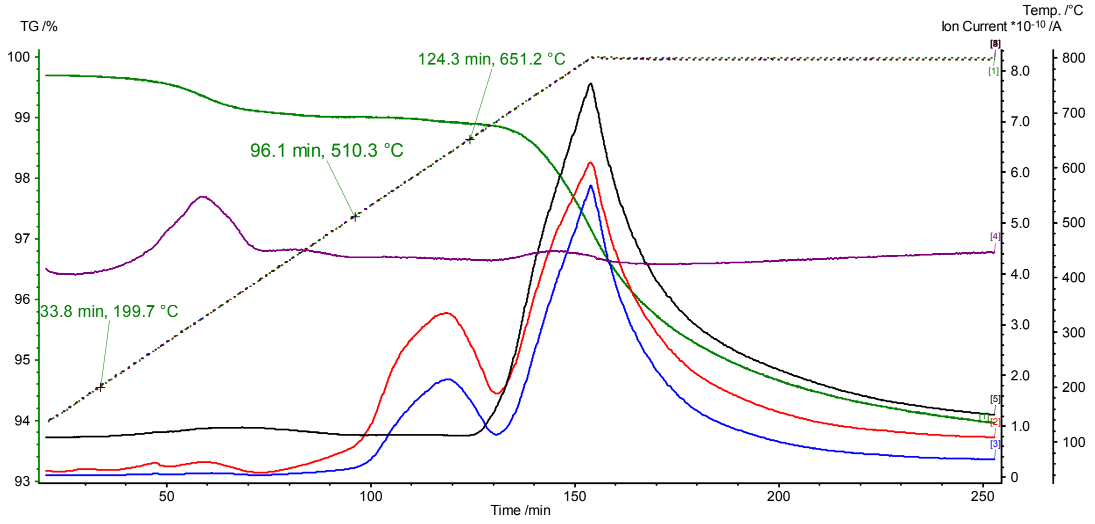

Figure 7-10: TGA for Na doped Sr-N-D (green), showing MS trail for m3 (red), m4 (blue), m18 (purple) and m28 (black)

8 Conclusions

The work in this thesis relates to the preparation and structural and electrical characterisation of calcium and strontium hydrides, imides and nitride hydrides. Conventional solid state methods in controlled atmospheres were used to synthesise these materials. Due to their highly sensitive nature towards air and moisture, special care was taken during handling, syntheses and testing to avoid decomposition reactions.

Both calcium and strontium hydride (CaH_2 and SrH_2) were successfully synthesised by reacting the metals with hydrogen gas. Neutron diffraction and thermogravimetric results suggested a small substoichiometry of hydrogen (deuterium) of the as prepared materials, which is most likely due to long equilibration times of the M – MH_2 system below the synthesis temperature. High temperature neutron diffraction data, thermal analysis and electrical testing all suggest an order – disorder transition taking place in the hydrides' structures. This transition most likely involves rapid exchange between the two hydride crystallographic sites. In the electrical properties this transition manifests itself in a lowering of the activation energy of the bulk ionic conductivity above the transition temperature. If the activation energy below the transition temperature is assumed to consist of an intrinsic defect migration and creation term, a lowering of this activation energy is to be expected above the transition temperature, due to the disappearance of the defect creation term. The conductivity is assumed to be purely ionic in nature (hydride ion conduction). This assumption seems to be validated at lower temperatures by the appearance of a Warburg type impedance, caused by a hydrogen diffusion limitation in the electrodes. The hydride ion conduction is good in these undoped materials: the total conductivity for CaH_2 at 1000K is 0.01 S/cm, whereas this is even higher for SrH_2, with 0.01 S/cm at 830K.

Upon reacting CaH_2 and SrH_2 with NaH, very little sodium enters the host materials' crystal structure (0.02%). The reaction with NaH however leads to a significant lowering of the hydrogen content in CaH_2 and SrH_2. This lowering of H-content is paralleled with the creation of electronic defect, F-centres. These extrinsic defects do not seem to have any effect on the electrical properties of CaH_2, whereas significant changes are observed for SrH_2. The low temperature conductivity of SrH_2 is increased by half an order of magnitude, whereas the high temperature regime, which is dominated by intrinsic defects, is negatively affected by the presence of these extrinsic defects [118].

The nitride hydride of calcium (Ca_2NH) could be obtained as a single phase material, by either reacting calcium metal or calcium hydride in an atmosphere of 5 – 7% H_2 and 1 – 7% N_2 in argon. The actual partial hydrogen and nitrogen pressure do affect the overall stoichiometry of the resulting compound and it is believed that imide ions (NH^{2-}) substituting for hydride and nitride ions is a major chemical defect. These imide ions are randomly distributed within the nitride hydride's crystal structure and therefore do not constitute as a separate phase. Ordering of nitride and hydride ions gives rise to a double cubic structure, in which calcium is cubic close packed, whereas nitrogen and hydrogen alternately occupy the octahedral holes. At high temperature (~600 – 650°C) disordering takes place, leading to a simple cubic structure. Upon reaction with sodium hydride (NaH), the imide content seems to be increased, which also seems to lessen the N-H ordering in Ca_2NH. Reacting calcium nitride hydride with 5 mol% lithium hydride (LiH) on the other hand induces the development of a stable secondary imide phase, whilst completely disordering the nitride hydride phase.

When applying the same reaction conditions to strontium metal, a mixture of strontium imide (SrNH) and nitride hydride (Sr_2NH) is formed. Whereas single phase strontium nitride hydride is reported to have a similar ordered structure as its calcium analogue [116], in the mixed phase its structure is fully disordered, with nitride and hydride randomly occupying the octahedral holes in the distorted strontium cubic close packing. The hydrogen position in the strontium imide phase was located using Fourier difference maps of the neutron scattering length density. Its most likely position is disordered around the nitrogen on a 96j site within the $F\ m\ 3\ m$ spacegroup. Both the nitride hydride and the imide phase are doped with Na, upon reaction with NaH. This can be concluded from the increase in lattice volume for both phases. Sodium solubilities in both Ca_2NH and Sr_2NH – SrNH are small, i.e. only 0.7 – 1%.

The disorder observed in both nitride hydrides and hydrides is due to high mobility of the hydrogen (and nitrogen) within the crystal structures. The disordering for hydrides roughly takes place around 350 – 450°C, whereas in the nitride hydrides this is at higher temperatures, i.e. 450 – 650°C. This high mobility could also be correlated with a very fast exchange of lattice hydrogen (deuterium) with the atmosphere. This process was observed when performing thermogravimetric analysis on the deuterided compounds in hydrogen containing atmospheres. Complete replacement of deuterium by hydrogen was observed within a short time. Moreover, the onset temperature of this isotope exchange process matches the nitride – hydride and hydride disordering temperatures very well, indicating that these processes are indeed related and involve rapid movement of hydrogen and nitrogen within the lattice. This high chemical mobility could be of great interest in such application as hydrogen exchange membranes. Furthermore, the rapid exchange of isotopes offers great potential in the area of nuclear fusion, where different hydrogen isotopes are used as fuels.

9 Suggestions for future work

All of the materials prepared and studied in this work have shown rapid exchange with hydrogen in the atmosphere and this is believed to be due to high mobility of the hydrogen and nitrogen ions in the materials' crystal lattices. New experiments studying the hydrogen (and possibly nitrogen) flux in these materials in typical membrane setups would be of great interest.

The electrical properties of the nitride hydrides have not been studied properly, yet. Good control of the material's stoichiometry is required before these tests are undertaken. The stoichiometry will probably affect the electrical properties drastically, as electronic defects might occur to compensate for hydride and nitride ion deficiencies. The occurrence of imide ions on the other hand will probably affect the electrical properties negatively.

More studies are needed to get a full picture on the hydride ion conduction mechanism in calcium and strontium hydride. In this work it was tried to introduce hydride ion vacancies to improve the ionic conductivity. This was however only partially successful, as the dopant was volatile and hardly soluble in the host materials. Hydride ion vacancies can also be created by doping nitride ions on the hydride ion sites. For every doped nitride ion, two hydride ion vacancies should be created. Therefore doping CaH_2 with Ca_2NH could be of interest. The effect of interstitial hydride ions has not been studied yet, either. They can be introduced by doping with trivalent elements, like lanthanum, neodymium and gadolinium.

10 References

1. Chen, P., et al., *Interaction of hydrogen with metal nitrides and imides.* Nature, 2002. **420**(6913): p. 302-304.
2. Luo, W.F., *($LiNH_2$-MgH_2): a viable hydrogen storage system.* Journal of Alloys and Compounds, 2004. **381**(1-2): p. 284-287.
3. Wu, G.T., et al., *Synthesis and characterization of a new ternary imide-$Li_2Ca(NH)_2$.* Inorganic Chemistry, 2007. **46**(2): p. 517-521.
4. Xiong, Z.T., et al., *Investigations into the interaction between hydrogen and calcium nitride.* Journal of Materials Chemistry, 2003. **13**(7): p. 1676-1680.
5. Wu, H., *Structure of ternary imide $Li_2Ca(NH)_2$ and hydrogen storage mechanisms in amide-hydride system.* Journal of the American Chemical Society, 2008. **130**(20): p. 6515-6522.
6. Gregory, D.H., *Lithium nitrides, imides and amides as lightweight, reversible hydrogen stores.* Journal of Materials Chemistry, 2008. **18**(20): p. 2321-2330.
7. Liu, Y.F., et al., *Synthesis and structural characterization of a new alkaline earth imide: $MgCa(NH)_2$.* European Journal of Inorganic Chemistry, 2006(21): p. 4368-4373.
8. Liu, Y.F., et al., *Hydrogen absorption/desorption behaviors over a quaternary Mg-Ca-Li-N-H system.* Journal of Power Sources, 2006. **159**(1): p. 135-138.
9. Hino, S., et al., *Hydrogen desorption properties of the Ca-N-H system.* Journal of Alloys and Compounds, 2005. **398**(1-2): p. 62-66.
10. Kojima, Y. and Y. Kawai, *Hydrogen storage of metal nitride by a mechanochemical reaction.* Chemical Communications, 2004(19): p. 2210-2211.
11. Kojima, Y., Y. Kawai, and N. Ohba, *Hydrogen storage of metal nitrides by a mechanochemical reaction.* Journal of Power Sources, 2006. **159**(1): p. 81-87.
12. Feng, F., M. Geng, and D.O. Northwood, *Electrochemical behaviour of intermetallic-based metal hydrides used in Ni/metal hydride (MH) batteries: a review.* International Journal of Hydrogen Energy, 2001. **26**(7): p. 725-734.
13. Reilly, J.J., et al., *The correlation between composition and electrochemical properties of metal hydride electrodes.* Journal of Alloys and Compounds, 1999. **295**: p. 569-582.
14. Bogdanovic, B. and M. Schwickardi, *Ti-doped alkali metal aluminium hydrides as potential novel reversible hydrogen storage materials.* Journal of Alloys and Compounds, 1997. **253**: p. 1-9.
15. Zuttel, A., et al., *$LiBH_4$ a new hydrogen storage material.* Journal of Power Sources, 2003. **118**(1-2): p. 1-7.
16. Blanchard, D., et al., *Desorption of $LiAlH_4$ with Ti- and V-based additives.* Materials Science and Engineering B-Solid State Materials for Advanced Technology, 2004. **108**(1-2): p. 54-59.
17. Li, Z.P., et al., *Protide compounds in hydrogen storage systems.* Journal of Alloys and Compounds, 2003. **356**: p. 469-474.
18. Schlapbach, L. and A. Zuttel, *Hydrogen-storage materials for mobile applications.* Nature, 2001. **414**(6861): p. 353-358.
19. Grochala, W. and P.P. Edwards, *Thermal decomposition of the non-interstitial hydrides for the storage and production of hydrogen.* Chemical Reviews, 2004. **104**(3): p. 1283-1315.

20. Ishihara, T., H. Matsuda, and Y. Takita, *Doped $LaGaO_3$ Perovskite-Type Oxide as a New Oxide Ionic Conductor.* Journal of the American Chemical Society, 1994. **116**(9): p. 3801-3803.

21. Abraham, F., et al., *The BiMeVOx Series - a New Family of High Performances Oxide Ion Conductors.* Solid State Ionics, 1990. **40-41**: p. 934-937.

22. West, A.R., *Solid state chemistry and its applications*. New edition ed. 1984, Blackwell: John Wiley & Sons, Ltd.

23. Norby, T., *Solid-state protonic conductors: principles, properties, progress and prospects.* Solid State Ionics, 1999. **125**(1-4): p. 1-11.

24. Teraoka, Y., et al., *Oxygen Permeation through Perovskite-Type Oxides.* Chemistry Letters, 1985(11): p. 1743-1746.

25. Yamazoe, N., Y. Teraoka, and T. Seiyama, *TPD and XPS Study on Thermal-Behavior of Absorbed Oxygen in $La_{1-x}Sr_xCoO_3$.* Chemistry Letters, 1981(12): p. 1767-1770.

26. Ten Elshof, J.E., H.J.M. Bouwmeester, and H. Verweij, *Oxidative Coupling of Methane in a Mixed-Conducting Perovskite Membrane Reactor.* Applied Catalysis A: General, 1995. **130**(2): p. 195-212.

27. Kilo, M., et al., *Nitrogen diffusion in nitrogen-doped yttria stabilised zirconia.* Physical Chemistry Chemical Physics, 2004. **6**(13): p. 3645-3649.

28. Wendel, J., M. Lerch, and W. Laqua, *Novel zirconia-based superionic conductors: The electrical conductivity of Y-Zr-O-N materials.* Journal of Solid State Chemistry, 1999. **142**(1): p. 163-167.

29. Valov, I., et al., *Electrochemical incorporation of nitrogen into a zirconia solid electrolyte.* Electrochemical and Solid State Letters, 2006. **9**(5): p. F23-F26.

30. Gellings, P.J. and H.J.M. Bouwmeester, *The CRC Handbook of Solid State Electrochemistry*. 1997, Boca Raton, Florida: CRC Press, Inc.

31. Gorelov, V.P. and S.F. Pal'guev, *Conductivity in CaH_2 - LiH and CaH_2 - CaF_2 systems.* Elektrokhimiya, 1992. **28**(10): p. 1294-1296.

32. Shriver, D.F., P.W. Atkins, and C.H. Langford, *Inorganic Chemistry*. 2nd ed. 1990, Oxford: Oxford University Press.

33. Shannon, R.D., *Revised Effective Ionic-Radii and Systematic Studies of Interatomic Distances in Halides and Chalcogenides.* Acta Crystallographica Section A, 1976. **32**(Sep1): p. 751-767.

34. Poulsen, F.W., *Speculations on the existence of hydride ions in proton conducting oxides.* Solid State Ionics, 2001. **145**(1-4): p. 387-397.

35. Libowitz, G.G., *The solid state chemistry of binary metal hydrides*. 1st ed. 1965, New York: W.A. Benjamin Inc.

36. Bergsma, J. and B.O. Loopstra, *The crystal structure of calcium hydride.* Acta Crystallographica, Short communications, 1962. **15**: p. 92-93.

37. Andresen, A.F., A.J. Maeland, and D. Slotfeldt-Ellingsen, *Calcium hydride and deuteride studied by neutron diffraction and NMR.* Journal of Solid State Chemistry, 1977. **20**: p. 93-101.

38. Morris, E., T. Groy, and K. Leinenweber, *Crystal structure and bonding in the high-pressure form of fluorite (CaF_2).* Journal of Physics and Chemistry of Solids, 2001. **62**(6): p. 1117-1122.

39. Korst, W.L. and J.C. Warf, *Rare earth-hydrogen systems. I. Structural and thermodynamic properties.* Inorganic Chemistry, 1966. **5**(10): p. 1719-1726.

40. Titcomb, C.G., A.K. Cheetham, and B.E.F. Fender, *Neutron-Diffraction Study of Hydrides of Early Lanthanide Elements at Room-Temperature.* Journal of Physics C-Solid State Physics, 1974. **7**(14): p. 2409-2416.

41. Udovic, T.J., Q. Huang, and J.J. Rush, *Characterization of the structure of* $LaD_{2.50}$ *by neutron powder diffraction.* Journal of Solid State Chemistry, 1996. **122**(1): p. 151-159.

42. Holley, C.E., et al., *The crystal structure of some rare earth hydrides.* Journal of Physical Chemistry, 1955. **59**: p. 1226-1228.

43. Ellner, M., H. Reule, and E.J. Mittemeijer, *The structure of the trihydride* GdH_3*.* Journal of Alloys and Compounds, 2000. **309**(1-2): p. 127-131.

44. Kohlmann, H., et al., *Neutron powder diffraction with (SM)-S-nat: Crystal structures and magnetism of a binary samarium deuteride and a ternary samarium magnesium deuteride.* Chemistry-a European Journal, 2007. **13**(15): p. 4178-4186.

45. Renaudin, G., P. Fischer, and K. Yvon, *Neodymium trihydride, NdH3, with tysonite type structure.* Journal of Alloys and Compounds, 2000. **313**: p. L10-L14.

46. Perkins, F.C. and C.E. Lundin, *The holmium-hydrogen system.* Journal of the Electrochemical Society, 1968. **115**(1): p. 21-24.

47. Udovic, T.J., Q. Huang, and J.J. Rush, *A neutron-powder-diffraction study of the rare-earth deuteride two-phase region.* Journal of Alloys and Compounds, 2003. **356**: p. 41-44.

48. Pebler, A. and W.E. Wallace, *Crystal stucture of some lanthanide hydrides.* Journal of Physical Chemistry, 1962. **66**(1): p. 148-151.

49. Hardcastle, K.I. and J.C. Warf, *Rare earth-hydrogen systems. III. High-pressure investigations.* Inorganic Chemistry, 1966. **5**(10): p. 1728-1735.

50. Libowitz, G.G. and J.G. Pack, *The gadolinium-hydrogen system at elevated temperatures. Vacancy interactions in gadolinium hydride.* Journal of Physical Chemistry, 1969. **73**(7): p. 2352-2356.

51. Huang, Q., et al., *Characterization of the structure of TbD2.25 at 70 K by neutron powder diffraction.* Journal of Alloys and Compounds, 1995. **231**(1-2): p. 95-98.

52. Udovic, T.J., et al., *Neutron-scattering study of the nuclear and magnetic structure of* DyD_3 *and associated vibrational and magnetic excitations.* Physical Review B, 1999. **59**(18): p. 11852-11858.

53. Warf, J.C. and K.I. Hardcastle, *Rare earth hydrogen systems: IV. The higher hydride of ytterbium, a new type of hydride.* Inorganic Chemistry, 1966. **5**(10): p. 1736-1740.

54. Auffermann, G., *High pressure synthesis and crystal structure of* $YbH_{2.67}$*.* Zeitschrift Für Anorganische Und Allgemeine Chemie, 2002. **628**(7): p. 1615-1618.

55. Sorokin, N.I. and M.W. Breiter, *Anionic conductivity and thermal stability of single crystals of solid solutions based on calcium fluoride.* Solid State Ionics, 1999. **116**(1-2): p. 157-165.

56. Shinar, J., et al., *Q-Factor Measurements of the Bulk Resistivity and Nonmetal-Metal Transitions in* LaH_x *and* CeH_x $(x \geq 2.70)$*.* Physical Review B, 1988. **37**(4): p. 2066-2073.

57. Shinar, J., et al., *Anomalous Resistivity Peaks, Localization Transitions, and the Electronic-Structure of Substoichiometric Lanthanum Trihydrides.* Physical Review Letters, 1990. **64**(5): p. 563-566.

58. Gregory, D.H., *Nitride chemistry of the s-block elements.* Coordination Chemistry Reviews, 2001. **215**: p. 301-345.

59. Marx, R., *Preparation and crystal structure of lithium nitride hydride,* Li_4NH*,* Li_4ND*.* Zeitschrift Fur Anorganische Und Allgemeine Chemie, 1997. **623**(12): p. 1912-1916.

60. Balogh, M.P., et al., *Crystal structures and phase transformation of deuterated lithium imide, Li_2ND.* Journal of Alloys and Compounds, 2006. **420**(1-2): p. 326-336.

61. Fischer, D. and M. Jansen, *Synthesis and structure of Na_3N.* Angewandte Chemie-International Edition, 2002. **41**(10): p. 1755-+.

62. Fischer, D., et al., *Synthesis and structure of K_3N.* Zeitschrift Fur Anorganische Und Allgemeine Chemie, 2004. **630**(1): p. 156-160.

63. Reckeweg, O. and F.J. DiSalvo, *Alkaline earth metal nitride compounds with the composition M_2NX (M=Ca, Sr, Ba; X=□, H, Cl or Br).* Solid State Sciences, 2002. **4**(5): p. 575-584.

64. Juza, R.v. and H. Schumacher, *Zur Kenntnis der Erdalkalimetallamide.* Zeitschrift für anorganische und allgemeine Chemie, 1963. **324**: p. 278-286.

65. Senker, J., et al., *Reorientational dynamics of amide ions in isotypic phases of strontium and calcium amide. 1. Neutron diffraction experiments.* Journal of Physical Chemistry B, 1998. **102**(6): p. 931-940.

66. Xiong, Z.T., et al., *Ternary imides for hydrogen storage.* Advanced Materials, 2004. **16**(17): p. 1522-1525.

67. Hammond, C., *The basics of crystallography and diffraction* 2nd ed. 2001, New York: Oxford University Press Inc.

68. Rodriguez-Carvajal, J., *An introduction to the program Fullprof 2000*. 2001, Gif sur Yvette.

69. Sears, V.F., *Neutron scattering lengths and cross sections.* Neutron News, 1992. **3**(3): p. 26-37.

70. Covington, E.J. and D.J. Montgomery, *Lattice constants of separated lithium isotopes.* Journal of Chemical Physics, 1957. **27**(5): p. 1030-1032.

71. Ubbelohde, A.R., *Zero point energy in the determination of the structure of solids.* Transactions of the Faraday Society, 1936. **32**: p. 525-529.

72. Anderson, J.L., et al., *Isotopic effects on the thermal expansion of lithium hydride.* Journal of Physics and Chemistry of Solids, 1970. **31**(4): p. 613-618.

73. Ruffa, A.R., *Thermal-Expansion and Zero-Point Displacement in Isotopic Lithium Hydride.* Physical Review B, 1983. **27**(2): p. 1321-1325.

74. Anderson, J.L., A.L. Bowman, and G.P. Arnold, *Low temperature neutron diffraction studies on Li(D,T).* Journal of Physics and Chemistry of Solids, 1970. **31**(5): p. 1193-1195.

75. Buschert, R.C., et al., *Effect of Isotope Concentration on the Lattice-Parameter of Germanium Perfect Crystals.* Physical Review B, 1988. **38**(8): p. 5219-5221.

76. Noya, J.C., C.P. Herrero, and R. Ramirez, *Isotope dependence of the lattice parameter of germanium from path-integral Monte Carlo simulations.* Physical Review B, 1997. **56**(1): p. 237-243.

77. MacDonald, J.R., *Impedance Spectroscopy, emphasizing solid materials and systems*. 1987, New York: John Wiley & Sons.

78. Boukamp, B.A., *A Linear Kronig-Kramers Transform Test for Immittance Data Validation.* Journal of the Electrochemical Society, 1995. **142**(6): p. 1885-1894.

79. Irvine, J.T.S., D.C. Sinclair, and A.R. West, *Electroceramics: characterization by impedance spectroscopy.* Advanced materials, 1990. **2**(3): p. 132-138.

80. Zintl, E. and A. Harder, *Constitution of the alkaline earth hydrides.* Zeitschrift für Elektrochemie und Angewandte Physikalische Chemie, 1935. **41**: p. 33-52.

81. Colognesi, D., et al., *Hydrogen self-dynamics in orthorhombic alkaline earth hydrides through incoherent inelastic neutron scattering.* Journal of Alloys and Compounds, 2007. **427**(1-2): p. 18-24.

82. Wu, H., et al., *Structure and vibrational spectra of calcium hydride and deuteride.* Journal of Alloys and Compounds, 2007. **436**(1-2): p. 51-55.

83. Brese, N.E., M. O' Keeffe, and R.B. Von Dreele, *Synthesis and Crystal-Structure of SrD_2 and SrND and Bond Valence Parameters for Hydrides.* Journal of Solid State Chemistry, 1990. **88**(2): p. 571-576.

84. Sichla, T. and H. Jacobs, *Single crystal X-ray structure determinations on calcium and strontium deuteride, CaD_2 and SrD_2.* European Journal of Solid State and Inorganic Chemistry, 1996. **33**(5): p. 453-461.

85. Bronger, W., C.C. Scha, and P. Muller, *Crystal-Structure of Barium Hydride, Determined by Neutron-Diffraction Experiments on BaD_2.* Zeitschrift Für Anorganische Und Allgemeine Chemie, 1987. **545**(2): p. 69-74.

86. Peterson, D.T. and V.G. Fattore, *Calcium-calcium hydride phase system.* Journal of Physical Chemistry, 1961. **65**: p. 2062-2064.

87. Peterson, D.T. and R.P. Colburn, *The strontium-strontium hydride phase system.* Journal of Physical Chemistry, 1966. **70**(2): p. 468-471.

88. Peterson, D.T. and M. Indig, *The barium-barium hydride system.* Journal of the American Chemical Society, 1960. **82**: p. 5645-5646.

89. Johnson, W.C., et al., *The rate of formation and the dissociation of calcium hydride.* Journal of the American Chemical Society, 1939. **61**: p. 318-329.

90. Curtis, R.W. and P. Chiotti, *Thermodynamic properties of calcium hydride.* Journal of Physical Chemistry, 1963. **67**: p. 1061-1065.

91. Peterson, D.T. and S.O. Nelson, *Equilibrium hydrogen pressure in the strontium-hydrogen system.* Journal of the Less-Common Metals, 1980. **72**: p. 251-256.

92. Gibson, I.R. and J.T.S. Irvine, *Study of the order-disorder transition in yttria-stabilised zirconia by neutron diffraction.* Journal of Materials Chemistry, 1996. **6**(5): p. 895-898.

93. Irvine, J.T.S. and A.R. West, *Sodium Phosphate-Based Solid Electrolytes.* Solid State Ionics, 1988. **28**: p. 214-219.

94. Irvine, J.T.S., et al., *Structural studies on the optimisation of fast oxide ion transport.* Solid State Ionics, 2000. **136**: p. 879-885.

95. Natsuhara, M., T. Uchida, and M. Wakihara, *Electrical-Conductivity of the CaF_2-NaF System.* Solid State Ionics, 1990. **40-1**: p. 874-877.

96. Ure, R.W., *Ionic conductivity of calcium fluoride crystals.* Journal of Chemical Physics, 1957. **26**: p. 1363-1373.

97. Irvine, J.T.S. and A.R. West, *Sodium Ion-Conducting Solid Electrolytes in the System Na_3PO_4-Na_2SO_4.* Journal of Solid State Chemistry, 1987. **69**(1): p. 126-134.

98. Cordero, B., et al., *Covalent radii revisited.* Dalton Transactions, 2008(21): p. 2832-2838.

99. Zhu, B., *CaH2 containing halide electrolytes and fuel cells.* Journal of Materials Science Letters, 1999. **18**(22): p. 1807-1809.

100. Zhu, B. and X.R. Liu, *LiF-CaH2 alumina electrolytes for intermediate temperature fuel cell applications.* Electrochemistry Communications, 2000. **2**(1): p. 10-14.

101. Zhu, B. and X.T. Yang, *Characterisation of MF-BaF2-CaH2-Al2O3 (M = Li, Na) hydrofluorides based on fuel cell studies.* Electrochemistry Communications, 1999. **1**(9): p. 411-414.

102. Wakamori, K. and A. Sawaoka, *Electrical resistance of some alkaline earth metal hydrides and alkali metal aluminium hydrides and borohydrides under high pressures.* Journal of the Less-Common Metals, 1982. **88**(1): p. 217-20.

103. Boukamp, B.A., *Electrochemical impedance spectroscopy in solid state ionics: recent advances.* Solid State Ionics, 2004. **169**(1-4): p. 65-73.

104. Boukamp, B.A., *A Nonlinear Least-Squares Fit Procedure for Analysis of Immittance Data of Electrochemical Systems.* Solid State Ionics, 1986. **20**(1): p. 31-44.

105. Sichla, T., et al., *Kristallstrukturbestimmung an einer Strontium-hydrid-imid-nitrid-Phase - $Sr_2(H)N/SrNH$ bzw. $Sr_2(D)N/SrND$ - mit Röntgen-, Neutronen- und Synchrotron-Strahlung.* Zeitschrift Für Anorganische Und Allgemeine Chemie, 1997. **623**(3): p. 414-422.

106. Wegner, B., et al., *Structure and H^--Ionic-Conductivity of Barium Hydride Nitrid, $Ba_2H(D)N$.* European Journal of Solid State and Inorganic Chemistry, 1992. **29**(6): p. 1217-1227.

107. Brice, J.F., et al., *Etude structurale de Ca_2NH par diffraction des rayons X, diffraction des neutrons et résonance magnétique nucléaire du proton dans le solide.* Journal of Solid State Chemistry, 1976. **17**(1-2): p. 135-142.

108. Andresen, A.F., M.I. Kay, and P. Fischer, *A neutron diffraction study of Ca N H.* Helvetica Physica Acta, 1964. **37**: p. 195.

109. Sichla, T. and H. Jacobs, *Synthesis and crystal structure of calcium imide, CaNH.* Zeitschrift Für Anorganische Und Allgemeine Chemie, 1996. **622**(12): p. 2079-2082.

110. Hartmann, H.v., H.J. Fröhlich, and F. Ebert, *Uber ein neues Pernitrid des Strontiums und Calciums und über die Imide der Erdalkalimetalle.* Zeitschrift für anorganische und allgemeine Chemie, 1934. **218**: p. 181-189.

111. Sichla, T. and H. Jacobs, *Synthesis and Crystal-Structure of a Calcium Nitride Deuteride Ca_2ND.* European Journal of Solid State and Inorganic Chemistry, 1995. **32**(1): p. 49-56.

112. Altorfer, F., et al., *H^--Jump Diffusion in Barium-Nitride-Hydride Ba_2NH.* Solid State Ionics, 1994. **70**: p. 272-277.

113. Ehrlich, P., W. Linz, and H.J. Seifert, *Nitride Fluorides of Heavy Alkaline Earth Metals.* Naturwissenschaften, 1971. **58**(4): p. 219-220.

114. Nicklow, R.A., T.R. Wagner, and C.C. Raymond, *Preparation and single-crystal structure analysis of Ca_2NF.* Journal of Solid State Chemistry, 2001. **160**(1): p. 134-138.

115. Chaix-Pluchery, O., et al., *Calcium Hydroxide Dehydration Early Precursor States.* Journal of Solid State Chemistry, 1983. **50**(2): p. 247-255.

116. Chemnitzer, R., et al., *$(Sr_2N)H$: On the redox-intercalation of hydrogen into Sr_2N.* Zeitschrift Für Anorganische Und Allgemeine Chemie, 2005. **631**(10): p. 1813-1817.

117. Sobolev, V.I. and G.I. Panov, *Study of hydrogen isotope exchange on calcium, strontium and barium hydride.* Reaction Kinetics & Catalysis Letters, 1985. **29**(2): p. 443-450.

118. Verbraeken, M.C., E. Suard, and J.T.S. Irvine, *Structural and electrical properties of calcium and strontium hydrides.* Journal of Materials Chemistry, 2009. **Accepted for publication**: p. DOI: 10.1039/B820173K